2018

Fabrication and Study of Gortex-based Gas Diffusion Electrodes in Hydrogen-Oxygen Fuel Cells and Electrolysers

Prerna Tiwari

UNIVERSITY OF WOLLONGONG AUSTRALIA

Fabrication and Study of Gortex-based Gas Diffusion Electrodes in Hydrogen-Oxygen Fuel Cells and Electrolysers

Prerna Tiwari

Supervisors:
Gerhard F. Swiegers, Klaudia Wagner and Gordon G. Wallace

This thesis is presented as part of the requirement for the conferral of the degree:
Doctor of Philosophy in Science

This research has been conducted with the support of the Australian Government Research Training Program Scholarship

The University of Wollongong
Intelligent Polymer Research Institute and ARC Centre of Excellence for Electromaterials Science

May 2018

Abstract

A growing imperative in the modern world is the development of new or improved technologies that: (i) can store energy efficiently, and (ii) deliver electricity on demand, at peak and off-peak times, whilst, still being (iii) compatible with the goal of sustainable development. One promising approach in this respect is to use hydrogen gas as an energy storage medium. Hydrogen can be manufactured from water, by the application of electrical energy, in an electrolyser. Hydrogen can also be converted back into water, with the production of electrical energy, in a fuel cell. However, present commercial electrolysers and fuel cells are too electrically inefficient and too costly to make such a round-trip storage and release of electrical energy, viable. In this work, a new approach to the problem has been studied using a novel class of gas diffusion electrode based on a Gortex substrate. We report the fabrication, characterization, and operation in fuel cells and electrolysers, of gas diffusion electrodes comprising of finely-pored GE Prevail™ *expanded PTFE* (*ePTFE*) ('Gortex') membranes over-coated with a wide range of precious metal and transition metal / metal oxide catalysts (PTFE=poly(tetrafluoroethylene). The coatings also incorporated carbon black and PTFE binder, with a fine Ni mesh as a current carrier. The fuel cells and electrolysers generally employed aqueous alkaline 6 M KOH as electrolyte, although selected acid systems were also examined.

The major findings of this work are summarised below.

The key distinctive features of Gortex-based gas diffusion electrodes relative to conventional gas diffusion electrodes, are as follows:

- Their gas handling pores are more uniform, more hydrophobic and may be smaller than conventional gas diffusion electrodes.
- As a result, they exhibit *Water-Entry Pressures* (water →gas side) that are ca. 20-times higher than conventional gas diffusion electrodes, which makes them, effectively, "leak-proof" and "flood-proof". This is a consequence of the water-repellent nature of Gortex.
- Their *Bubble Point Pressures* (gas →water side) are lower; this appears to be a consequence of an affinity by Gortex for gas bubbles (i.e. it is "*bubble-philic*").
- Because of the above properties, Gortex-based gas diffusion electrodes can, generally, be employed in electrochemical cells without need for an inter-electrode diaphragm / ionomer. This includes in water electrolyzers that normally require such diaphragms / ionomers to separate the hydrogen and oxygen bubbles produced (to avoid the creation of an explosive mixture).
- Gortex-based gas diffusion electrodes display high gas permeabilities, that are >2-orders of magnitude greater than would be needed in any electrochemical liquid-to-gas or gas-to-liquid transformation.
- Gortex-based gas diffusion electrodes are compatible with acid or base liquid electrolytes.
- Gortex-based gas diffusion electrodes may be capable of operating at temperatures of up to ca. 300 ^{o}C (which is the limit for *expanded PTFE*, depending on the backing material used on the Gortex).
- Gortex-based gas diffusion electrodes may generally exhibit high surface / active areas with a well-defined three-way, solid-liquid-gas interface.

The major distinctive features of alkaline water electrolysers with Gortex-based gas diffusion anodes and cathodes can be summarised as follows:

- The presence of the Gortex substrate generally acts to diminish the bubble overpotential at the electrodes, particularly as the temperature is increased to 80 ^{o}C and above.
- This may result in direct conversion of water to a product gas at the Gortex-based electrode, without the formation of gas bubbles in the electrolyte. That is, the electrodes may split water in a "bubble-free" manner.
- When operated at 80 ^{o}C and above, the activation overpotential of an oxygen-generating Gortex-based anode may decline substantially, thereby significant decreasing the cell activation overpotential. Cell activation overpotentials as low as 0.09 V were measured in some electrolysers (2-electrode).
- Electrolysers with Gortex-based gas diffusion electrodes may operate below the thermoneutral voltage for water-splitting, in an endothermic manner. Electrolysers (2-electrode) that operated at 10 mA cm^{-2} at 80 ^{o}C for 1 h at voltages as low as 1.23-1.27 V were developed.
- At 20 ^{o}C, the activity of Gortex-based water electrolysis catalysts generally followed the trends present in their equivalent volcano plots. At 80 ^{o}C, the order of catalytic activity may be different.
- Electrolysers with earth-abundant catalysts at anode and cathode performed well with 6 M KOH electrolyte. For example, the spinel catalyst, $NiCo_2O_4$, displayed a Tafel slope of 70 mV dec^{-1} at 80 ^{o}C for oxygen evolution when incorporated into a Gortex-based gas diffusion electrode. This is low in comparison to Pt in conventional electrolysers.

The major distinctive features of alkaline fuel cells with Gortex-based gas diffusion electrodes as anode and cathode can be summarised as follows:

- The presence of the Gortex substrate generally imparted fuel cell electrodes with an unusually efficient three-way solid-liquid-gas interface. This was evidenced by:
    - the ability of Gortex-based anodes to efficiently extract hydrogen gas from highly dilute mixtures (<5%) with the inert gas, methane.
    - the low Pt loadings (0.16 mg per cm^2) that could be used to achieve peak performance. (The power densities and overpotentials at such low loadings were not, however, as high as PEM fuel cells operating at peak performance with notably higher Pt loadings).
    - the low Tafel slopes exhibited by many of the tested catalysts for oxygen reduction at low current densities (<50 mA cm^{-2}). For example, an Earth-abundant perovskite catalyst displayed a Tafel slope of only 43 mV dec^{-1}, against the standard benchmark of 60 mV dec^{-1} for Pt in conventional fuel cells. At higher current densities (>50 mA cm^{-2}), Tafel slopes of >100 mV dec^{-1} were observed that were, nevertheless, lower than the Pt benchmark in conventional fuel cells under the same conditions.
    - the low charge transfer resistances (R_{CT}) (0.2-0.4 Ω cm^2) observed using electrochemical impedance spectroscopy at 20 ^{o}C for fuel cells with Gortex-based precious metal catalysts, even under conditions where the fuel was supplied in highly dilute mixtures. The charge transfer resistances were only moderately decreased at 80 ^{o}C (0.2-0.3 Ω cm^2). The use of perovskite and spinel catalysts resulted in a greater temperature dependence (R_{CT} at 20 ^{o}C 0.6-

0.8 Ω cm^2; R_{CT} at 80 °C 0.2-0.3 Ω cm^2). Under comparable conditions, PEM fuel cells appear to generally display higher charge transfer resistances that are more sensitive to changes in the temperature and concentration of the fuel.

- the capacity to mitigate the effect of supplying fuel in high dilutions by merely increasing the overall flow-through rate at which fuel was supplied.

- Fuel cells with Gortex-based gas diffusion electrodes as anode and cathode were generally resistant to CO_2 poisoning.

The major distinctive features of discrete regenerative fuel cell – electrolysers (DRFCs) employing an electrolyser unit and a fuel cell unit, each equipped with Gortex-based gas diffusion electrodes, can be summarised as follows:

- DRFCs equipped with Gortex-based gas diffusion electrodes generally displayed unusually high round-trip energy efficiencies. The best result at 80 °C and 10 mA cm^{-2} in each direction was a round-trip efficiency of 73.5%, assuming complete conservation of heat. DRFCs with round trip efficiencies of 64-72% at 80 °C and 10 mA cm^{-2} in each direction were obtained with several different catalyst combinations. The previous report highest round trip efficiency at 80 °C and 10 mA/cm^2 in each direction was 66.4% for a PEM system.
- The high round-trip efficiencies generally derived from declines in the activation overpotential for oxygen generation in the electrolyser as the temperature was increased to 80 °C and above. By contrast, the fuel cell generally exhibited a higher activation overpotential for oxygen consumption as the temperature was increased.

Acknowledgments

I would like to express my sincere gratitude to my supervisor Professor Gerhard Frederick Swiegers, his expertise, understanding, and patience, added considerably to my doctoral experience. His trust, guidance, and support inspired me in the most important moments of making the correct decisions. I would like to thank Professor Gordon Wallace for his valuable suggestions and constant guidance throughout my doctoral training. A very special thanks goes to my co-supervisor Dr Klaudia Wagner, who guided me and provided constructive feedback in this research work. Also, a special thanks to Dr. George Tsekouras for providing his sound understanding and experience in this research.

I would like to thank members of IPRI for their helpful discussions during my doctoral research and training. I am thankful to all the past and present colleagues of the IPRI for making my stay at Wollongong delightful.

Finally, I would like to dedicate this work to my husband Dr Nagesh Shukla and my parents, who has been greatly supporting me in achieving all my inspirations and ventures.

Certification

I, Prerna Tiwari, declare that this thesis submitted in fulfilment of the requirements for the conferral of the degree Doctor of Philosophy in Science, from the University of Wollongong, is wholly my own work unless otherwise referenced or acknowledged. This document has not been submitted for qualifications at any other academic institution.

_____

Prerna Tiwari

14th February 2018

Publications

Journal papers:

Alkaline Fuel Cells with Novel Gortex-Based Electrodes are Powered Remarkably Efficiently by Methane Containing 5% Hydrogen. Klaudia Wagner, Prerna Tiwari, Gerhard F. Swiegers, and Gordon G. Wallace. *Advanced Energy Materials* 2017, DOI: 10.1002/aenm.201702285

An electrochemical cell with Gortex-based electrodes capable of extracting pure hydrogen from highly dilute hydrogen–methane mixtures. Klaudia Wagner, Prerna Tiwari, Gerhard F. Swiegers and Gordon G. Wallace. *Energy and Environmental Science* 2018, 11, 172

Gortex as an Electrode Substrate: Efficient, Active Gas Diffusion Electrodes with an Unprecedented Resistance to Leaking. Prerna Tiwari, George Tsekouras, Gerhard F. Swiegers, Gordon G. Wallace. *Submitted* for publication

A Conducting Polymer Film that Amplifies Water Oxidation Catalysis by a Bare Pt Film Electrode. A Photocatalytic, Oxygen-Generating PEDOT/Nano-Ni/rGO Composite with Sustained High Activity. Mohammed Alsultan, Sivakumar Balakrishnan, Jaecheol Choi, Rouhollah Jalili, P. Tiwari, Pawel Wagner, Gerhard F. Swiegers. *Submitted* for publication

Gortex Electrode Substrates Drastically Diminish the Activation Overpotential for O_2 Formation from Water. Alkaline Electrolyzers with Remarkably Low Activation Overpotentials. Prerna Tiwari, George Tsekouras, Gerhard F. Swiegers, Gordon G. Wallace. *In preparation*

Efficient Alkaline Fuel Cells, Electrolysers, and Discrete Regenerative Fuel Cells Utilizing Gortex-based Gas Diffusion Electrodes. Prerna Tiwari, Klaudia Wagner, George Tsekouras, Gerhard F. Swiegers, Gordon G. Wallace. *In preparation*

Patent Applications:

Method and System for Efficiently Operating Electrochemical Cells. Inventors: G. F. Swiegers, E. Seymour, P. Tiwari, G. Tsekouras. Australian provisional patent application 201905158 (filed 14 December 2015). PCT International Patent Application WO2017100842 (filed 14 December 2016) and family

Electrodes with Efficient Gas Handling Properties. Inventors: G. F. Swiegers, S. Jansen, N. Schuh, J. Smith, A. Gestos, M. Greer, M. Romano, P. Tiwari. US provisional patent application 62/511574 (filed 26 May 2017).

Fuel Cell. Inventors: G. F. Swiegers, P. Tiwari, K. Wagner. US provisional patent application 62/511632 (filed 26 May 2017).

List of Names or Abbreviations

AAEM	Alkaline anion-exchange membrane
AFC	Alkaline fuel cell
AWE	Alkaline water electrolyser
BNGS	B- and N-isolated doped graphitic nanosheets
BSCF	$Ba_{0.5}Sr_{0.5}Co_{0.8}F_{0.2}O_3$
CA	Chronoamperometry
CB	Carbon black
CFP	Capillary flow porometer
CP	Chronopotentiometry
DMFC	Direct Methanol Fuel Cells
DOE	U.S. Department of energy
DRFC	Discrete regenerative fuel cell
ED	Electrodeposition
EDS	Energy dispersive X-ray spectroscopy
EEC	Equivalent electric circuit
EIS	Electrochemical impedance spectroscopy
EMF	Electromotive force
GA	Graphene aerogel
GC	Gas chromatography
GCE	Gas collection efficiency
GDE	Gas diffusion electrode
GEIS	Galvanostatic electrochemical impedance spectroscopy
HCD	High current density
HER	Hydrogen evolution reaction
HHV	Higher heating value of hydrogen
HOR	Hydrogen oxidation reaction
IPA	Isopropyl alcohol
LCD	Low current density
LEP	Liquid entry pressure
LHV	Lower heating value of hydrogen
LPI	Lines-per-inch
LSV	Linear sweep voltammetry
MCFC	Molten Carbonate Fuel Cells
NAFION™	Sulfonated tetrafluoroethylene based fluoropolymer-copolymer
NHE	Normal hydrogen electrode
NPMC	N- and P-co-doped mesoporous nanocarbon
NPMC	Non-precious metal catalysts
OCA	Optical contact angle
OCV	Open circuit voltage
OER	Oxygen evolution reaction
ORR	Oxygen reduction reaction
PAFC	Phosphoric Acid Fuel Cells
PEDOT	Poly(3,4-ethylenedioxythiophene)
PEIS	Potentiostatic electrochemical impedance spectroscopy
PEM/PEMFC	Proton Exchange Membrane Fuel Cells
PET	Polyethylene terephthalate
PGM	Platinum group catalysts
PNGF	P and N co-doped graphene framework
PTFE	Poly(tetrafluoroethylene)
PVC	Polyvinyl chloride
QCM	Quartz crystal microbalance
RFC	Regenerative fuel cell

rGO	Reduced graphene oxide
RT	Room temperature
SEM	Scanning electron microscope
SHG	N, S co-doped graphitic sheets with stereoscopic holes
SOE	Solid Oxide Electrolyte
SOFC	Solid Oxide Fuel Cells
STP	Standard temperature and presuure of 1 atm and 25 ^{o}C
SWCNTs	Single walled carbon nanotubes
TCD	Thermal conductivity detector
TEM	Transmission electron microscopy
TGA	Thermogravimetric analysis
TM	Transition metal
URFC	Unitized regenerative fuel cell
VA-BCNT	Vertically aligned boron- and nitrogen-co-doped carbon nanotubes
XPS	X-ray photoelectron spectroscopy
XRD	X-ray diffraction
YSZ	Yttria-stabilized zirconia

Table of Contents

CHAPTER 1: Introduction
1.1 Background 1
1.1.1 "The Problem" 3
1.2 Fuel Cells 4
1.2.1 Classes of Fuel Cell 5
1.2.2 The Principles and Operation of Alkaline and PEM Hydrogen-Oxygen Fuel Cells 13
1.3 Water Electrolysers 25
1.3.1 Classes of Electrolyser 26
1.3.2 The Principles and Operation of Alkaline and PEM Electrolysers 30
1.4. Reactor Designs for Alkaline Fuel Cells and Alkaline Water Electrolysers 39
1.4.1 Alkaline Fuel Cell (AFC) Designs 39
1.4.2 Alkaline Water Electrolyser (AWE) Designs 41
1.5 Catalysts Used in Alkaline Fuel Cells (AFCs) and Alkaline Water Electrolysers (AWEs) 43
1.5.1 Catalysts of the Oxygen Reduction Reaction (ORR) 44
1.5.2 Catalysts of the Oxygen Evolution Reaction (OER) 45
1.5.3 Catalysts of the Hydrogen Oxidation Reaction (HOR) 47
1.5.4 Catalysts of the Hydrogen Evolution Reaction (HER) 47
1.6 Gas Diffusion Electrodes (GDEs) used for Alkaline Fuel Cells (AFCs) and Alkaline Water Electrolysers (AWEs) 48
1.7 Proposed Research 51
1.7.1 Novel 'Gortex'-based ('ePTFE') Gas Diffusion Electrodes (GDEs) form the Key Topic of Study in this Work 51
1.7.2 Thesis Objective 55
1.7.3 Outline of the Thesis 55

CHAPTER 2: Experimental
2.1 Materials Used 65
2.2 Physical Characterisation Techniques 67
2.2.1 Four Point Probe Conductivity Measurements 67
2.2.2 Thermo-Gravimetric Analysis 68
2.2.3 Contact Angle Goniometry 69
2.2.4 Capillary-Flow Porometry 71
2.2.5 Scanning Electron Microscopy (SEM) 72
2.2.6 Energy Dispersive X-ray Spectroscopy (EDS) 72
2.2.7 X-ray Diffraction (XRD) 73
2.2.8 X-ray Photoelectron Spectroscopy (XPS) 74
2.2.9 Sputter-Coating of Metals 75
2.2.10 Probe Sonication 76
2.2.11 Centrifugation 76
2.2.12 Laser Engraving 77
2.2.13 Transmission Electron Microscopy (TEM) 78
2.2.14 Gas Chromatography (GC) 78
2.3 Electrochemical Analysis Techniques 79
2.3.1 Open Circuit Voltage (OCV) 79
2.3.2 Linear Sweep Voltammetry 80
2.3.2 Controlled Potential Techniques (Chronoamperometry) 81
2.3.3 Controlled Current Techniques (Chronopotentiometry) 82
2.3.4 Electrochemical Impedance Spectroscopy (EIS) 82
2.4 Electrode Preparation 87
2.4.1 Catalyst Attachment Methods 87

2.4.2 Electrode Preparation: Mounting of Membrane/Catalyst/Mesh Assemblies 90
2.5 Cell Construction and Assembly ……...92
2.6 Cell Configuration in Fuel Cell Mode ……..93
2.7 Cell Configuration in Electrolyser Mode ……94
2.8 Electrode Optimization …… 96
2.8.1 Nitrogen Purging……..….96
2.8.2 PTFE Fraction…….....97
2.8.3 Roller Gap……...98
2.8.4 Ohmic Resistance…….……...99
2.8.5 Metal loading……...101
2.9 Experimental Protocol ……..…….…...104

CHAPTER 3: Gortex as an Electrode Substrate: Efficient Gas Diffusion Electrodes with an Unprecedented Resistance to Flooding and Leaking
3.1 Introduction ……109
3.2 Results and Discussion..... 115
3.2.1 Conventional Gas Diffusion Electrodes 115
3.2.2 A New Approach to Fabricating 'Leak-Proof' Gas Diffusion Electrodes 118
3.2.3 Gortex as a Substrate for Gas Diffusion Electrodes..... 119
3.2.4 Characterising the Pore Structure of Gortex Using Capillary Flow Porometry 120
3.2.5 The Resistance of Gortex as a Gas Diffusion Layer to Flooding and Leaking 122
3.2.6 Fabrication and Characterisation of Gortex-Based Gas Diffusion Electrodes Coated with Sputtered Pt as Catalyst..... 123
3.2.7 Fabrication and Characterisation of Gortex-Based Gas Diffusion Electrodes Coated with 10% Pt on Vulcan XC72 Catalyst, Carbon Black, PTFE Binder and Ni Mesh. 126
3.2.8 Characterisation of Gortex-based Gas Diffusion Electrodes 128
3.2.9 Hydrophobicity of the Gortex-based Gas Diffusion Electrodes 131
3.2.10 Fuel Cells with Gortex-based Gas Diffusion Electrodes 132
3.2.11 Fuel Cells with Sputter-Coated Gortex Electrodes..... 134
3.2.12 Fuel Cells with Electro-coated Pt on Gortex Electrodes 143
3.2.13 Fuel Cells with Gortex Electrodes Coated with 10% Pt on Vulcan XC72, Carbon Black, PTFE Binder and Ni Mesh 146
3.2.14 The Significance of these Results: An Efficient Gas Diffusion Electrode that is Highly Flood-Resistant..... 149
3.3 Conclusions..... 150

CHAPTER 4: Gortex Electrode Substrates May Drastically Diminish the Activation Overpotential for O2 Formation from Water. Alkaline Electrolysers with Remarkably Low Activation Overpotentials
4.1 Introduction ……155
4.2 Results & Discussion 160
4.2.1 Use of expanded PTFE (*ePTFE*) Membrane ('Gortex') as an Electrode Substrate ……160
4.2.2 Catalyst Slurries and their incorporation as a Layer on Porous, ePTFE Membrane Electrodes 162
4.2.3 Chronoamperometry of Electrolysers with Gortex-based Gas Diffusion Electrodes ……163
4.2.4 Temperature-dependent Current-Voltage Polarization Plots of Electrolysers with Gortex-based Electrodes..... 165
4.2.5 The Energy Penalty Due to Bubble Formation and Release ……168
4.2.6 Independent Verification and Similar Effects in other Electrolysers……172
4.2.7 The Nature of the Decline in Overpotential – the Activation Overpotential for O_2 Formation is Almost Eliminated..... 173
4.2.8 The Origin of the Lowered Activation Overpotential for O_2-formation from Water ……...…175

4.2.9 A Possible Explanation: the Gortex Substrate has a Strong Capillary Action that Repels Water but Attracts Gas Bubbles....177
4.2.10 Efficient H_2/O_2 Fuel Cells Employing Gortex-based Electrodes....180
4.3 Conclusions....184

CHAPTER 5: Other Efficient Alkaline Fuel Cells, Electrolysers, and Discrete Regenerative Fuel Cells Utilizing Gortex-based Precious Metal Catalysts
5.1 Introduction....188
5.2 Experimental....193
5.2.1 Materials....193
5.2.2 Preparation of Catalyst-coated Gortex....194
5.2.3 Cell Construction....194
5.2.4 Reactant Gases and Electrochemical Testing....194
5.3 Results and discussion....194
5.3.1 The Use of *Expanded PTFE* (*ePTFE*) Membranes (‘*Gortex’*) as Electrode Substrates....194
5.3.2 Polarisation Curves....195
5.3.3 Tafel Plots....197
5.3.4 Electrochemical Impedance Spectroscopy....198
5.3.5 Bifunctional Hydrogen Catalysts (BHC)....200
5.3.6 Bifunctional Oxygen Catalysts (BOC)....200
5.3.7 Fuel Cell Performance at Room Temperature (20 ºC)....201
5.3.8 Fuel Cell Performance at 80 ºC....216
5.3.9 Some Discrete Regenerative Fuel Cells (DRFC) at 80 ºC....222
5.4 Conclusion....224

CHAPTER 6: Other Efficient Alkaline Fuel Cells, Electrolysers, and Discrete Regenerative Fuel Cells Utilizing Gortex-based Spinel and Perovskite Catalysts
6.1 Introduction....229
6.2 Experimental....233
6.2.1 Materials Used....233
6.2.2 Preparation of Catalyst-coated Gortex....234
6.2.3 Cell Construction....234
6.2.4 Reactant Gases and Electrochemical Testing....234
6.3 Results and Discussion....234
6.3.1 Perovskites as Bifunctional ORR-OER Catalysts....234
6.3.2 Spinels as Bifunctional ORR-OER Catalysts....237
6.3.3 Mechanistic Pathways for Perovskites/Spinels as ORR-OER Catalysts....238
6.3.4 Fuel Cell Performance at Room Temperature (20 ºC), using Perovskites as ORR Catalysts....242
6.3.5 Fuel Cell Performance at Room Temperature (20 ºC), using Spinels as ORR Catalyst....253
6.3.6 Fuel Cell Performance at 80 ºC using the Best Performing Perovskite and Spinel as ORR Catalyst....261
6.3.7 Electrolyser Performance at Room Temperature (20 ºC) and 80 ºC, using Perovskites and Spinels as OER catalysts....268
6.3.8 Efficient Alkaline-based Discrete Regenerative Fuel Cell....275
6.4 Conclusion....277

CHAPTER 7: Alkaline Fuel Cells with Gortex-based Electrodes May Be Powered by Hydrogen-Enriched Methane Containing as little as 5% Hydrogen
7.1 Introduction....286
7.2 Experimental....290
7.2.1 Materials....290
7.2.2 Preparation of catalyst-coated Gortex....290

7.2.3 Cell Construction . ……290
7.2.4 Reactant Gases and Electrochemical Testing . ……291
7.3 Results and Discussion ……..…292
7.3.1 Fuel Cell Operation using Hydrogen-Methane Mixtures in the Range 5%-100%. ……292
7.3.3 Polarisation Curves……294
7.3.4 Tafel Plots ……297
7.3.5 Electrochemical Impedance Spectroscopy... ……299
7.3.6 Hydrogen-Methane Mixtures in the Range 2%-5% ……304
7.3.7 Water Balance in the Fuel Cell ……306
7.4 Conclusions ……..……...……307

CHAPTER 8: Summary and Perspectives
8.1 Summary ……...…….311
8.2 Perspective ……..…..…….314

List of Figures

Figure 1.1. Schematic comparison of the working principles and operation of different classes of fuel cell. 6
Figure 1.2. Schematic cross-section of a traditional alkaline fuel cell. Reproduced with permission from reference 2. 8
Figure 1.3. Schematic diagram of an ion conducting (ionomer) membrane coated with catalysts, as used in a typical proton exchange membrane fuel cell. Reproduced with permission from reference 11. 10
Figure 1.4. Typical voltage-current density characteristics of a fuel cell 22
Figure 1.5. Activation overpotential losses in a typical voltage-current density curve of a fuel cell ..... ….23
Figure 1.6. Schematic comparison of the working principles and operation of different classes of water electrolysers 26
Figure 1.7. Compositions of the cell voltage of an example alkaline water electrolysis cell. Adapted with permission from reference 24. 34
Figure 1.8. Tafel plots for both hydrogen and oxygen evolution..... 37
Figure 1.9. Graph showing the contributions to cell voltage from the components of the cell resistance of an alkaline water electrolysis cell. Adapted from reference 24..... 38
Figure 1.10. Schematic cross-section of a typical modern-day gas diffusion electrode. 49
Figure 1.11. Cross-sectional schematic of a three phase interface formed on a Gortex electrode coated with a PEDOT conducting polymer. Reproduced with permission from reference 58. ..... ……..52
Figure 1.12. Cross-sectional schematic of a water electrolyser utilising Pt-coated Gortex electrodes at both the anode and cathode, to directly separate the hydrogen and oxygen gases produced. Reproduced with permission from reference 127. ……..53
Figure 2.1: JANDEL RM3 four-point probe instrument used for conductivity measurements…. 69
Figure 2.2: TA Instruments Q500 TGA thermogravimetric Analysis Instrument. 70
Figure 2.3: A schematic of a contact angle measurement using the sessile drop technique, showing the three phase interface where solid, liquid, and gas/vapour interact (θ= contact angle).[4] ..... …71
Figure 2.4: Dataphysics OCA Contact Angle Goniometer. 72
Figure 2.5: Sessile Drop (Left image), and Captive Bubble technique (right image) for measuring contact angle.[21] 72
Figure 2.6: CFP-1200-AEXL Capillary Flow Porometer. 73
Figure 2.7: SEM electron spatial resolution for EDS. [8] 74
Figure 2.8: JEOL7500 Field emission scanning electron microscope. 75
Figure 2.9: GBC MMA X-Ray Diffractometer. 76
Figure 2.10: Working principle of X-Ray photoelectron spectroscopy (XPS). 77
Figure 2.11: PHOIBOS 100 hemispherical energy analyser used for X-Ray photoelectron spectroscopy. 77
Figure 2.12: EDWARDS FTM6 Auto 306 sputter Coater used for catalyst coating onto Gortex membranes..... 78
Figure 2.13: Eppendorf 5702 centrifuge used in this study. 79
Figure 2.14: ULS PLS6MW Laser engraver used in this study..... 79
Figure 2.15: JEOL JEM-2010 Transmission Electron Microscopy used in this study. 80
Figure 2.16: Simadzu GC-8A Gas Chromatograph used in this study. 81
Figure 2.17: Linear sweep voltammetry 82
Figure 2.18: The principles of chronoamperometry. 83
Figure 2.19: Controlled Current Technique 84
Figure 2.20: Electrochemical Impedance Spectroscopy: the application of a sinusoidal voltage (top) generates a sinusoidal current response (bottom), showing a phase shift.[17] .. 85

Figure 2.21: Nyquist plot with impedance vector.[18] 86
Figure 2.22: Simple equivalent electric circuit with one time constant represented as a resistor (R) in parallel with a capacitor (C) .[18] 86
Figure 2.23: Bode plot with one time constant [18]..... 87
Figure 2.24: Preparation of membrane/slurry/mesh assemblies 89
Figure 2.25. The double-roll mill used for compaction of electrodes..... 91
Figure 2.26: Preparation of laminate-mounted ePTFE electrodes. 92
Figure 2.27: Precision cut lamination polymer and other components needed for mounting membrane/catalyst/mesh assemblies into electrodes for the test cells. 93
Figure 2.28: Photographs and schematics of: (a) 3D-printed plastic cell (3 mm inter-electrode gap), (b) milled stainless steel cell (10 mm inter-electrode gap), and (c) cross-section of the test cell, showing the electrical and gas connections. 94
Figure 2.29: Schematic illustration of a test cell when operating as an alkaline fuel cell. ... 95
Figure 2.30: Schematic illustration of a test cell when operating as an alkaline electrolyser.97
Figure 2.31: Gas Collection: a test cell with a 3 mm inter-electrode gap, electrical and gas connections and upturned water-filled cylinder 97
Figure 2.32: Chronoamperometry at –0.2 V of alkaline fuel cells (6 M KOH) based on Pt black catalysts showing the benefit of N_2 purging of the dry mixture of Pt black and carbon black prior to IPA addition during catalyst slurry formulation. 99
Figure 2.33: Average current at –0.2 V vs. PTFE fraction from triplicate tests of fuel cells utilizing 20% Pt-Pd (1:1) on Vulcan XC 72. Electrolyte: 6 M KOH. 100
Figure 2.34: Averaged current at –0.2 V vs. roller gap, from triplicate tests of fuel cells based on 20% Pt-Pd (1:1) on Vulcan XC 72, using electroformed Ni mesh. Electrolyte: 6 M KOH. 101
Figure 2.35: Potentiostatic electrochemical impedance spectroscopy of fuel cells based on 20% Pt-Pd (1:1) on Vulcan XC 72 at –0.4 V, demonstrating lowered ohmic resistance when using woven Ni mesh and multiple, shorter electrical leads in place of electroformed Ni mesh and a single, longer electrical lead. Electrolyte: 6 M KOH ..... …102
Figure 2.36: Metal loading as a function of the mass of catalyst employed in the catalyst slurry and the number of applied layers..... 103
Figure 2.37: Current at – 0.4 V and potential at + 10 mA cm^{-2} as functions of metal loading on the (a,b) Anode (H_2 electrode) and (c,d) Cathode (O_2 electrode), for fuel cells based on 10% Pt on Vulcan XC 72. Electrolyte: 6 M KOH..... 104
Figure 2.38: Schematic illustration of experimental protocol 106
Figure 3. 1. Schematic depiction of: (a) a typical present-day gas diffusion electrode, and (b) Gortex-based gas diffusion electrode 113
Figure 3.2. Schematic depiction of the alkaline fuel cell used to test the gas diffusion electrodes of this chapter. 116
Figure 3.3. Schematic depiction of the output “wet curve” (blue) and “dry curve” (red) measured during capillary flow porometry. The “half-dry curve” (green) is an interpolation based on the wet and dry curve profiles. Reproduced with permission.[10] 122
Figure 3.4. Scanning electron microscopy (SEM) images of Gortex electrodes sputter-coated with Pt, with nominal thicknesses (according to the internal thickness monitor of the sputter-coater) of: (a) 50 nm, (b) 200 nm, and (c) 400 nm. 125
Figure 3.5. (a) Cross-sectional view and (b) cross-sectional energy-dispersive X-ray (EDX) of the sputter-coated (200 nm nominal thickness) Gortex electrode depicted in Figure 4(b). The Pt layer is shown in red..... 127
Figure 3.6. (a) Cross-sectional view of a Gortex electrode coated with a precious metal catalyst supported on Vulcan XC72, carbon black, PTFE binder, and a Ni mesh as a current carrier; the dashed line at the top depicts the surface of the catalyst layer, and (b) transmission electron micrograph of the 10% Pt on Vulcan XC72 commercial catalyst used in this study. ..... ……129

Figure 3.7. Pore size distribution (by number) of the Gortex electrodes: (a) uncoated Gortex (control), (b)-(f) sputter-coated with Pt of 50-400 nm nominal thickness, and (g) overcoated with 10% Pt on Vulcan XC75 incorporating carbon black, PTFE binder, and Ni mesh current carrier. 131
Figure 3.8. Air permeability measurements per 1 cm^2 area of the uncoated and coated gas diffusion electrodes obtained by porometry: (◊) uncoated Gortex control, (□) Gortex sputter-coated to 50 nm nominal thickness, (Δ) Gortex sputter-coated to 100 nm nominal thickness, (○) Gortex sputter-coated to 150 nm nominal thickness, ( ) Gortex sputter-coated to 200 nm nominal thickness, (●) Gortex sputter-coated to 400 nm nominal thickness, and (+) Gortex overcoated with particulate 10% Pt on Vulcan XC72, incorporating carbon black, PTFE binder, and Ni mesh. 132
Figure 3.9. (a) Polarization Curves (left axis) and Power Curves (right axis) at 20 ºC for alkaline fuel cells containing Gortex electrodes sputter-coated with (—)Pt, (- - -) Au,& (• • •) Ag of nominal thickness of 100 nm as the anode. The cathode was a Gortex membrane sputter-coated with Pt of nominal thickness 100 nm. (b) EIS Nyquist and (c) Bode plots showing measured data at 0.8 V. 137
Figure 3.10. (a) Polarization Curves (left axis) and Power Curves (right axis) at 20 ºC for alkaline fuel cells containing Gortex electrodes sputter-coated with Pt having nominal thickness of (- - -) 50 nm, (—) 100 nm, and (•••) 150 nm. Electrolyte: 6 M KOH. (b) EIS Equivalent circuit. (c) Nyquist and (d) Bode plots showing measured data (individual data points) and modelled data (solid lines) (modelled using the equivalent circuit depicted in (b)) at 0.8V..... 139
Figure 3.11. (a) Polarization Curves (left axis) and Power Curves (right axis) at 20 ºC for alkaline fuel cells containing Gortex electrodes sputter-coated with Pt having nominal thickness of 100 nm in (—) 6 M KOH and (- - -) 1 M H_2SO_4. (b) Nyquist and (c) Bode plots showing measured data at 0.8 V. 143
Figure 3.12. Scanning electron microscopy (SEM) images of Gortex electrodes electrodeposited with Pt on an underlying layer of sputtered Pt (a) before and (b) after electrodeposition of Pt (initial pulse of -1.0 V applied for 4 s followed by cyclic voltammetry from +0.2 V to -0.58 V up to a charge density of 5 C cm^{-2})..... 146
Figure 3.13. (a) Polarization Curves (left axis) and Power Curves (right axis) at 20 ºC for alkaline fuel cells containing Gortex electrodes electrodeposited with Pt on an underlying layer of sputtered Pt before and after electrodeposition of Pt. (• • •) Pt only (nominal thickness = 100 nm) before electrodeposition, (—) Pt electrodeposited on an underlying 100nm layer of Pt. Electrolyte: 6 M KOH. (b) Nyquist plots showing measured data at 0.8 V. 146
Figure 3.14. (a) Polarization Curves (left axis) and Power Curves (right axis) at 10 mA cm^{-2} and 20 ºC for alkaline fuel cells containing Gortex electrodes coated with 10% Pt on Vulcan XC72, carbon black, PTFE, and woven Ni mesh. Electrolyte: 6 M KOH. (b) EIS equivalent circuit. (c) Nyquist and (d) Bode plots showing measured data (individual data points) and modelled data (solid line) (modelled using the equivalent circuit depicted in (b)). 147
Figure 3.15. Chronopotentiogram measured over 24 h at + 10 mA cm^{-2} for a symmetrical fuel cell utilizing Gortex electrodes incorporating 10% Pt on Vulcan XC 72 catalyst. The small variations observed in the measured voltage appear to coincide with small temperature variations in the environment, including due to the fume cupboard turning on and off. Carbon black used in the catalyst slurry was treated with ascorbic acid prior to use. 149
Figure 4.1. Cell potentials for water electrolysis as a function of temperature.[2(b)] 157
Figure 4.2. Schematic depiction of an electrolyser cell used for the studies in this Chapter….. 160
Figure 4.3. Chronoamperograms at 10 mA cm^{-2} of electrolysers operating at 80 ºC and comprising of: (a) Raney Ni+CB+PTFE+Ni-mesh/Gortex (cathode) and $NiCo_2O_4$+PTFE+Ni-mesh/Gortex (anode), and (b) 10% Pt/CB+PTFE+Ni-mesh/Gortex (cathode) and $NiCo_2O_4$+PTFE+Ni-mesh/Gortex (anode)..... 164

Figure 4.4. Current-voltage curves for the Raney Ni+CB+PTFE+Ni-mesh/Gortex (cathode) and $NiCo_2O_4$+PTFE+Ni-mesh/Gortex (anode) electrolyser (6M KOH electrolyte) at different temperatures. The inset graph depicts the data at 80 °C (solid line) compared to interpolations of the most active reported alkaline[8] (dashed line) and PEM[13] (dotted line) electrolysers at the same temperature..... 167
Figure 4.5. Current-voltage curves for a test water electrolyser that was independently fabricated by AquaHydrex Pty Ltd, and that contained Plasma-nano-Ni+CB+PTFE+Ni-mesh/Gortex (cathode) and Plasma-nano-Ni+PTFE+Ni-mesh/Gortex (anode) electrolyser (6 M KOH electrolyte) at different temperatures..... 170
Figure 4.6. Overpotential as a function of current density and temperature for Raney Ni+CB+PTFE+Ni-mesh/Gortex (cathode) and $NiCo_2O_4$+PTFE+Ni-mesh/Gortex (anode) electrolyser (6M KOH electrolyte; 80 °C) at: (a) the hydrogen-generating cathode, and (b) the oxygen-generating anode. 172
Figure 4.7. Sequence of events in an attempt to measure the contact angle, using the "Captive Bubble" technique, of an air bubble on a Gortex surface immersed in water. The Gortex was tight up against a glass backing plate (shown at the very top of each photograph). In (a), an air bubble is carefully placed on the Gortex surface. Before a contact angle can be measured however, the Gortex draws the air bubble into it, as shown in (b) and then in (c). Within a matter of seconds, the air bubble is almost totally taken up by the Gortex. 174
Figure 4.8. Polarisation curve after 1 h of cells in fuel cell mode at 80 °C (6 M KOH electrolyte; 10 mm inter-electrode gap) having: (a) Fuel cell 1 containing 20% Pd-Pt/CB+PTFE+Ni-mesh/Gortex at both the H_2 and O_2 electrodes; (b) Fuel cell 2 containing 20% Pd-Pt/CB+PTFE+Ni-mesh/Gortex at the H_2 electrode and $La_{0.8}Sr_{0.2}MnO_3$/CB+PTFE+Ni-mesh/Gortex at the O_2 electrode; and (c) Fuel cell 3 containing 20% Pd-Pt/CB+PTFE+Ni-mesh/Gortex at the H_2 electrode and carbon black+Ni-mesh/Gortex at the O_2 electrode. Inset shows fitted straight lines of the ohmic regions, which have the general formula y=mx+c, where the value of c accords with the onset potential of the fuel cell. The activation overpotential (η_{cell}) is difference between the onset potential and 1.18 V, which is the E^o of the cell at 80 °C. .. …178
Figure 4.9. Overpotential (hydrogen (a) and oxygen (b)) as a function of current density for 20% Pd-Pt/CB+PTFE+Ni-mesh/Gortex at the H_2 electrode and $La_{0.8}Sr_{0.2}MnO_3$/CB+PTFE+Ni-mesh/Gortex at the O_2 electrode in fuel cell 2(6M KOH electrolyte) at 80 °C. 180
Figure 5.1. Schematic diagram for discrete regenerative fuel cell (DRFC)..... 190
Figure 5.2. Typical polarization curves during fuel cell operation, showing: (a) uncorrected data (….), and data corrected by taking into account: (b) the resistance due to the electrical contacts (-- -- --), (c) the resistance due to the electrolyte (- - -), and (d) the total resistance, as measured using EIS ( ). 197
Figure 5.3. (a) Nyquist and (b) Bode plots of symmetrically supplied hydrogen (H_2/H_2, black line), oxygen (O_2/O_2, grey line) and (H_2/O_2, dotted line), at the two electrodes of a fuel cell having two 20% Pd-Pt on Vulcan XC32+CB+PTFE+Ni mesh/Gortex gas diffusion electrodes, at open circuit potential (OCV); (c) table with charge transfer resistance (R_{ct}), double layer capacitance (C_{ct}); (d) equivalent electrical circuit . 199
Figure 5.4. (a) Volcano plot for oxygen reduction reaction (ORR) activity as a function of oxygen binding energy on metals,[21] (b) Volcano plot for oxygen reduction reaction (ORR) activity as a function of oxygen binding energy on Pt-based transition metal alloys.[22] Reproduced with permission from references 21 and 22. 202
Figure 5.5. Polarization curves (left axis) and power density curves (right axis) at 20 °C for alkaline fuel cells containing Gortex electrodes coated with (1) ▲-20% Pt-Pd (2) ■-10% Pt (3) ▬-20% Pt-Ru (4) □-Pt black (5) ♦ -20% Pt-Co (6) ●-20% Pt-Ni (7) X -20% Pt-Ir (8) +-IrO_2 as cathode (O_2 catalyst). Gortex coated with 10% Pt served as the anode (H_2 catalyst) in all cases. Electrolyte: 6 M KOH. 205
Figure 5.6. Straight line fits of the ohmic regions (iR-corrected) for the alkaline fuel cells, at 20 °C, containing Gortex electrodes coated with (1) ▲-20% Pt-Pd (2) ■-10% Pt (3) ▬-

20% Pt-Ru (4) □-Pt black (5) ♦ -20% Pt-Co (6) ●-20% Pt-Ni (7) X -20% Pt-Ir (8) +-IrO_2 as cathode (O_2 catalyst). Gortex coated with 10% Pt served as the anode (H_2 catalyst) in all cases. The fitted straight lines have the general formula y=mx+c, where the value of c accords with the onset potential of the fuel cell. The activation overpotential is the difference between the onset potential and 1.23 V, which is the E^o of the cell at 20 ^oC. Electrolyte: 6 M KOH. The cell potential was iR-corrected for resistance due to electrical contacts..... 206

Figure 5.7. Chronopotentiograms (CP) at 10 mA cm^{-2} for alkaline fuel cells, at 20 ^oC, containing Gortex electrodes coated with (1) ▬20% Pt-Pd (2) ▬10% Pt (3) ▬20% Pt-Ru (4) ▬20% Pt-Ir (5) ▬ IrO_2 (6) ▬20% Pt-Ni (7) ▬ 20% Pt-Ir, as cathode (O_2 catalyst). Gortex coated with 10% Pt served as the anode (H_2 catalyst) in all cases. Electrolyte: 6 M KOH. 207

Figure 5.8. Chronopotentiogram (CP) at 10 mA cm^{-2} for a fuel cell with 10% Pt/CB+PTFE+Ni-mesh/Gortex at both the anode and cathode, at 20 ^oC. Electrolyte: 6 M KOH 207

Figure 5.9. iR-corrected Tafel plots for the alkaline fuel cells, at 20 ^oC, containing Gortex electrodes coated with (1) ▲-20%Pt-Pd (2) ■-10%Pt (3) ▬-20%Pt-Ru (4) □-Pt black (5) ♦ -20%Pt-Co (6) ●-20%Pt-Ni (7) X -20%Pt-Ir (8) +-IrO_2 as cathode (O_2 catalysts). Gortex coated with 10% Pt served as the anode (H_2 catalyst). Electrolyte: 6 M KOH. 210

Figure 5.10. iR-corrected Tafel plots at (a) Low Current density (LCD) (b) High Current Density (HCD) for the alkaline fuel cells, at 20 ^oC, containing Gortex electrodes coated with (1) ▲-20%Pt-Pd (2) ■-10%Pt (3) ▬-20%Pt-Ru (4) X -20%Pt-Ir (5) +-IrO_2 as cathode (O_2 catalysts). Gortex coated with 10% Pt served as the anode (H_2 catalyst). The fitted straight lines have the general formula y=mx+c, where m is the Tafel slope and c is the imputed exchange ciurrent density, i_o. Electrolyte: 6 M KOH. 211

Figure 5.11. (a) Nyquist plot and inset showing an enlargement of the high frequency impedance region, (b) Bode plots; at 10 mA cm^{-2}, showing measured data (individual data points) and modelled data (solid line). The modelled data used the equivalent circuit shown in (c). Alkaline fuel cells, at 20 ^oC, containing Gortex electrodes coated with (1) ▲-20%Pt-Pd (2) ■ -10%Pt (3) ▬ -20%Pt-Ru (4) □ -Pt black (5) ♦ -20%Pt-Co (6) ○ -20%Pt-Ni (7) X -20%Pt-Ir (8) + -IrO_2 as cathode (O_2 catalysts). Gortex coated with 10% Pt served as the anode (H_2 catalyst). Electrolyte: 6 M KOH..... 213

Figure 5.12. Parameters obtained from equivalent electric circuit fitted to electrochemical impedance of different precious catalyst: charge transfer resistance $R_{(ct)}$, diffusional resistance $Z_{(d)}$. ..... …215

Figure 5.13. (a) Equivalent circuit before chronopotentiometry (CP) at 10 mA/cm^2 for10 min, (b) Equivalent circuit after chronopotentiometry (CP) at 10 mA/cm^2 for10 min, (c) Nyquist and (d) Bode plots at 10 mA cm^{-2}, showing measured data (individual data points) and modelled data (solid line). The modelled data used the equivalent circuit shown in (a) for before chronopotentiometry (CP) at 10 mA/cm^2 for10 min, and (b) for after chronopotentiometry (CP) at 10 mA/cm^2 for10 min. Alkaline fuel cells, at 20 ^oC, containing Gortex electrodes coated with (1) □-20%Pt-Ni before (2) □-20%Pt-Ni after (3) ○-20%Pt-Co before (4) ○-20%Pt-Co after, as the cathode (O_2 catalysts). Gortex coated with 10% Pt served as the anode (H_2 catalyst). Electrolyte: 6 M KOH. ... 217

Figure 5.14. Polarization curves (left axis) and power density curves (right axis) for alkaline fuel cells containing Gortex electrodes coated with (1)○● -20%Pt-Pd; (2)□■ -10%Pt and (3) Δ▲ -IrO_2 as the cathode (O_2 catalysts). Gortex coated with 10% Pt served as the anode (H_2 catalyst). Empty and filled markers denote 20 ^oC and 80 ^oC data respectively. Electrolyte: 6 M KOH. 218

Figure 5.15. iR-corrected Tafel plots for alkaline fuel cells containing Gortex electrodes coated with (1) ○● -20%Pt-Pd; (2) □■ -10%Pt and (3) Δ▲ -IrO_2 as cathode (ORR catalysts). Gortex coated with 10% Pt served as the anode (HOR catalyst) in all cases. Empty and filled markers denote 20 ^oC and 80 ^oC data respectively. Electrolyte: 6 M KOH…… 220

Figure 5.16. (a) Plots of cell potential vs current density (iR-corrected) showing straight line fits of the ohmic region (with formula y=mx+c, where the intercept of that line with the y-axis, c, is the onset potential. The activation overpotential is the difference between the onset potential and E_{cell}^o (E_{cell}^o =1.23 V at 20 ^oC, E_{cell}^o =1.18 V at 80 ^oC); (b) Tafel plots (iR-corrected), at Low Current density (LCD), showing straight-line fits (with formula y=mx+c, where m is the Tafel slope and c is the exchange current density, i_o); for the alkaline fuel cells containing Gortex electrodes coated with (1) ○● -20%Pt-Pd; (2) □■ -10%Pt and (3)Δ▲ -IrO_2 as cathode (ORR catalysts). Gortex coated with 10% Pt served as the anode (H_2 catalyst) in all cases. Empty and filled markers denote 20 ^oC and 80 ^oC data respectively. Electrolyte: 6 M KOH. 220

Figure 5.17. Nyquist plot at 10 mA cm^{-2}, (inset: equivalent electrical circuit) showing measured data (individual data points) and modelled data (solid line). The modelled data used the equivalent circuit shown in (a). Alkaline fuel cells containing Gortex electrodes coated with (1) ○● -20%Pt-Pd; (2) □■ -10%Pt and (3) Δ▲ -IrO_2 as cathode (ORR catalysts). Gortex coated with 10% Pt served as the anode (HOR catalyst) in all cases. Empty and filled markers denote 20 ^oC and 80 ^oC data respectively. Electrolyte: 6 M KOH. 221

Figure 5.18. (a) Polarization curves (iR-corrected) and (b) chronopotentiograms (iR-corrected) for alkaline fuel cells containing Gortex electrodes coated with (1) ●-20%Pt-Pd (2)▲-IrO_2 at 80 ^oC, as O_2-catalysts and alkaline water electrolyzers containing Goretex electrodes coated with ▲-IrO_2 as O_2-catalysts at 80 ^oC. Alkaline fuel cell cathodes contained either of 20%Pt-Pd or IrO_2 as O_2-catalyst along with carbon black. Alkaline water electrolysers contained only IrO_2 as O_2 catalyst, without any addition of carbon black. 20%Pt-Pd was not chosen as O_2 catalyst for electrolyser as it contained carbon black as a support. The H_2-catalysts in all cells were 10% Pt/CB+PTFE+Ni-mesh on Gortex. Electrolyte: 6 M KOH. 224

Figure 6.1. Schematic diagram for discrete regenerative fuel cell (DRFC)..... 231

Figure 6.2. Volcano plot for Oxygen Reduction activity as a function of oxygen binding energy on perovskites.[61] Reproduced with permission from reference 61. 240

Figure 6.3. Polarization curves (left axis) and power density curves (right axis) at 20 ^oC for alkaline fuel cells containing Gortex electrodes coated with (1) ▲-$La_{0.8}Sr_{0.2}MnO_3$ (2) ■-$LaMnO_3$ (3) ♦- $La_{0.7}Ca_{0.3}CoO_3$ (4) +-$LaNi_{0.6}Fe_{0.4}O_3$ (5) X –$Ba_{0.5}Sr_{0.5}Co_{0.2}Fe_{0.8}O_3$ as cathode (O_2 catalyst). Gortex coated with 10% Pt served as the anode (H_2 catalyst) in all cases. Electrolyte: 6 M KOH. 242

Figure 6.4. Chronopotentiograms (CP) at 10 mA cm^{-2} for alkaline fuel cells, at 20 ^oC, containing Gortex electrodes coated with (1) ▬ $La_{0.8}Sr_{0.2}MnO_3$ (2) ▬ $LaMnO_3$ (3) ▬ $La_{0.7}Ca_{0.3}CoO_3$ (4) ▬ $LaNi_{0.6}Fe_{0.4}O_3$ (5) ▬ $Ba_{0.5}Sr_{0.5}Co_{0.2}Fe_{0.8}O_3$ as cathode (O_2 catalyst). Gortex coated with 10% Pt served as the anode (H_2 catalyst) in all cases. Electrolyte: 6 M KOH. 243

Figure 6.5. Straight line fits of the ohmic regions (iR-corrected) for the alkaline fuel cells containing Gortex electrodes coated with (1) ▲-$La_{0.8}Sr_{0.2}MnO_3$ (2) ■-$LaMnO_3$ (3) ♦-$La_{0.7}Ca_{0.3}CoO_3$ (4) +-$LaNi_{0.6}Fe_{0.4}O_3$ (5) X –$Ba_{0.5}Sr_{0.5}Co_{0.2}Fe_{0.8}O_3$ as cathode (O_2 catalyst). Gortex coated with 10% Pt served as the anode (H_2 catalyst) in all cases. The fitted straight lines have the general formula y=mx+c, where the value of c accords with the onset potential of the fuel cell. The activation overpotential (η_{act}) is the difference between the onset potential and 1.23 V, which is the E^o of the cell at 20 ^oC. Inset: Tafel plots for Oxygen Reduction activity on perovskites; reproduced with permission from reference 61. Solid and open symbols represent activities of perovskites (LSMO- $La_{0.8}Sr_{0.2}MnO_{3-\delta}$, LMO- $LaMnO_{3\pm\delta}$, LCO- $LaCoO_3$, and BSCF-$Ba_{0.5}Sr_{0.5}Co_{0.8}Fe_{0.2}O_{3-\delta}$) tested in the form of thin films and powders respectively. Electrolyte: 6 M KOH. 247

Figure 6.6. iR-corrected Tafel plots at 20 ^oC of: (a) b_1 at Low Current density (LCD), (b) b_2 at High Current Density (HCD) for alkaline fuel cells containing Gortex electrodes coated with (1) ▲-$La_{0.8}Sr_{0.2}MnO_3$ (2) ■-$LaMnO_3$ (3) ♦- $La_{0.7}Ca_{0.3}CoO_3$ (4) +-$LaNi_{0.6}Fe_{0.4}O_3$ (5) X –$Ba_{0.5}Sr_{0.5}Co_{0.2}Fe_{0.8}O_3$, as cathode ($O_2$ catalyst). Gortex coated

with 10% Pt served as the anode (H_2 catalyst) in all cases. The fitted straight lines have the general formula y= $b_{(1\ or\ 2)}$ x+c, where $b_{(1\ or\ 2)}$ is the Tafel slope and c is the imputed exchange current density, i_o. Electrolyte: 6 M KOH. 248

Figure 6.7. (a) Nyquist and (b) Bode plots at 10 mA cm^{-2}, (c) Equivalent electric circuit used to model Nyquist impedance data, for alkaline fuel cells, at 20 °C, containing Gortex electrodes coated with (1) ▲-$La_{0.8}Sr_{0.2}MnO_3$ (2) ■-$LaMnO_3$ (3) ♦- $La_{0.7}Ca_{0.3}CoO_3$ (4) +-$LaNi_{0.6}Fe_{0.4}O_3$ (5) X –$Ba_{0.5}Sr_{0.5}Co_{0.2}Fe_{0.8}O_3$ as cathode (O_2 catalyst). Gortex coated with 10% Pt served as the anode (H_2 catalyst) in all cases. Electrolyte: 6 M KOH.. ……250

Figure 6.8. Polarization curves (left axis) and power density curves (right axis) at 20 °C of alkaline fuel cells containing Gortex electrodes coated with (1) ▲-$NiCo_2O_4$ (2) ■-$Mn_{1.5}Co_{1.5}O_4$ (3) ♦- $NiFe_2O_4$ (4) +-$Co_{0.5}Ni_{0.5}Fe_2O_4$ (5) X –Co_3O_4, as cathode (O_2 catalyst). Gortex coated with 10% Pt served as the anode (H_2 catalyst) in all cases. Electrolyte: 6 M KOH. 253

Figure 6.9. Straight line fits of the ohmic regions (iR-corrected) at 20 °C for the alkaline fuel cells containing Gortex electrodes coated with: (1) ▲-$NiCo_2O_4$ (2) ■-$Mn_{1.5}Co_{1.5}O_4$ (3) ♦- $NiFe_2O_4$ (4) +-$Co_{0.5}Ni_{0.5}Fe_2O_4$ (5) X –Co_3O_4 as cathode (O_2 catalyst). Gortex coated with 10% Pt served as the anode (H_2 catalyst) in all cases. The fitted straight lines have the general formula y=mx+c, where the value of c is the onset potential of the fuel cell. The activation overpotential (η_{act}) is the difference between the onset potential and 1.23 V, which is the E^o of the cell at 20 °C. Electrolyte: 6 M KOH. 254

Figure 6.10. Chronopotentiograms (CP) at 10 mA cm^{-2} for alkaline fuel cells, at 20 °C , containing Gortex electrodes coated with (1) ▬ $NiCo_2O_4$ (2) ▬ $Mn_{1.5}Co_{1.5}O_4$ (3) ▬ $NiFe_2O_4$ (4) ▬ $Co_{0.5}Ni_{0.5}Fe_2O_4$ (5) ▬ Co_3O_4, as cathode (O_2 catalyst). Gortex coated with 10% Pt served as the anode (H_2 catalyst) in all cases. Electrolyte: 6 M KOH. ..... …254

Figure 6.11. iR-corrected Tafel plots for alkaline fuel cells, at 20 °C, containing Gortex electrodes coated with (1) ▲-$NiCo_2O_4$ (2) ■-$Mn_{1.5}Co_{1.5}O_4$ (3) ♦- $NiFe_2O_4$ (4) +-$Co_{0.5}Ni_{0.5}Fe_2O_4$ (5) X –Co_3O_4, as cathode (O_2 catalyst). Gortex coated with 10% Pt served as the anode (H_2 catalyst) in all cases. Electrolyte: 6 M KOH..... 256

Figure 6.12. iR-corrected Tafel plots at: (a) Low Current density (LCD), and (b) High Current Density (HCD) for alkaline fuel cells, at 20 °C, containing Gortex electrodes coated with (1) ▲-$NiCo_2O_4$ (2) ■-$Mn_{1.5}Co_{1.5}O_4$ (3) ♦- $NiFe_2O_4$ (4) +-$Co_{0.5}Ni_{0.5}Fe_2O_4$ (5) X –Co_3O_4, as cathode (O_2 catalyst). Gortex coated with 10% Pt served as the anode (H_2 catalyst) in all cases. The fitted straight lines have the general formula y=$b_{1/2}$x+c, where $b_{1/2}$ is the Tafel slope. Electrolyte: 6 M KOH. 257

Figure 6.13. (a) Nyquist and (b) Bode plots at 10 mA cm^{-2}, (c) Equivalent electric circuit used to model the Nyquist impedance data, for alkaline fuel cells, at 20 °C, containing Gortex electrodes coated with (1) ▲-$NiCo_2O_4$ (2) ■-$Mn_{1.5}Co_{1.5}O_4$ (3) ♦- $NiFe_2O_4$ (4) +-$Co_{0.5}Ni_{0.5}Fe_2O_4$ (5) X –Co_3O_4, as cathode (O_2 catalyst). Gortex coated with 10% Pt served as the anode (H_2 catalyst) in all cases. Electrolyte: 6 M KOH..... 258

Figure 6.14. Polarization curves (left axis) and power density curves (right axis) for alkaline fuel cells containing Gortex electrodes coated with: (1) □■ - $La_{0.8}Sr_{0.2}MnO_3$ and (2) ◊♦ - $NiCo_2O_4$ as cathode (O_2 catalyst). Gortex coated with 10% Pt served as the anode (H_2 catalyst) in all cases. Empty and filled markers denote 20 °C and 80 °C data respectively. Electrolyte: 6 M KOH. 260

Figure 6.15. Plots of cell potential vs current density (iR-corrected) showing straight line fits of the ohmic region for the alkaline fuel cells containing Gortex electrodes coated with (1) □■ - $La_{0.8}Sr_{0.2}MnO_3$ and (2) ◊♦ - $NiCo_2O_4$ as cathode (O_2 catalyst). Gortex coated with 10% Pt served as the anode (H_2 catalyst) in all cases. Empty and filled markers denote 20 °C and 80 °C data respectively. The straight lines fits have formula y=mx+c, where the intercept of the straight line with the y-axis, c, is the onset potential. The activation overpotentials (η_{act}) provided on the graph are the difference between the

onset potential and E_{cell}^{o} (E_{cell}^{o} =1.23 V at 20 ºC, E_{cell}^{o} =1.18 V at 80 ºC). Electrolyte: 6 M KOH. 261
Figure 6.16. Chronopotentiogram (CP) at 10 mA cm^{-2} and 80 ºC for alkaline fuel cell containing Gortex electrode coated with ▬ $La_{0.8}Sr_{0.2}MnO_3$, as cathode (O_2 catalyst). Gortex coated with 10% Pt served as the anode (H_2 catalyst). Electrolyte: 6 M KOH. ... 263
Figure 6.17. iR-corrected Tafel plots and inset showing Tafel slopes calculated at low current density (LCD) for the alkaline fuel cells containing Gortex electrodes coated with (1) □■ - $La_{0.8}Sr_{0.2}MnO_3$ and (2) ◊♦ - $NiCo_2O_4$ as cathode (O_2 catalyst). Gortex coated with 10% Pt served as the anode (H_2 catalyst) in all cases. Empty and filled markers denote 20 ºC and 80 ºC data respectively. The straight line fits of the ohmic region shown in the inset have the formula $y=b_1x+c$, where m is Tafel slope. Electrolyte: 6 M KOH. 264
Figure 6.18. Nyquist plot and inset showing the equivalent circuit used to model the data, for alkaline fuel cells containing Gortex electrodes coated with (1) □■ - $La_{0.8}Sr_{0.2}MnO_3$ and (2) ◊♦ - $NiCo_2O_4$ as cathode (O_2 catalyst). Gortex coated with 10% Pt served as the anode (H_2 catalyst) in all cases. Empty and filled markers denote 20 ºC and 80 ºC data respectively. Electrolyte: 6 M KOH. 265
Figure 6.19. Volcano plot for Oxygen Evolution activity as a function of oxygen binding energy on metal oxides.[85] Reproduced with permission from reference 85. 266
Figure 6.20. Volcano plot for oxygen evolution activity as a function of oxygen binding energy on perovskites. BSCF stands for $Ba_{0.5}Sr_{0.5}Co_{0.8}Fe_{0.2}O_{3-\delta}$.[61] Reproduced with permission from reference 61. 267
Figure 6.21. iR-corrected current-voltage curves at 20 ºC for alkaline electrolysers containing Gortex anodes (O_2 catalysts) coated with (1) □ - $La_{0.8}Sr_{0.2}MnO_3$ (2) ◊ - $NiCo_2O_4$ and (3) Δ - $Ba_{0.5}Sr_{0.5}Co_{0.2}Fe_{0.8}O_3$. Gortex coated with 10% Pt served as the cathode (H_2 catalyst) in all cases. Inset shows Tafel plots for oxygen evolution activity on perovskites; reproduced with permission from reference 61. Solid and open symbols represent activities of perovskites (LSMO- $La_{0.8}Sr_{0.2}MnO_{3-\delta}$, LMO- $LaMnO_{3\pm\delta}$, LCO- $LaCoO_3$, and BSCF- $Ba_{0.5}Sr_{0.5}Co_{0.8}Fe_{0.2}O_{3-\delta}$) tested in the form of thin films and powders respectively. Electrolyte: 6 M KOH. 269
Figure 6.22. iR-corrected current-voltage curves for alkaline electrolysers containing Gortex anodes coated with (1) □■ - $La_{0.8}Sr_{0.2}MnO_3$ (2) ◊♦ - $NiCo_2O_4$ and (3) Δ▲- $Ba_{0.5}Sr_{0.5}Co_{0.2}Fe_{0.8}O_3$. Gortex coated with 10% Pt served as the cathode (H_2 catalyst) in all cases. Empty and filled markers denote 20 ºC and 80 ºC data respectively. Inset shows straight line fits of the ohmic region, with formula $y=mx+c$, where the intercept of that line with the y-axis, c, is the onset potential. The activation overpotential (η_{act}) is the difference between the onset potential and E_{cell}^{o} (E_{cell}^{o} =1.23 V at 20 ºC, E_{cell}^{o} =1.18 V at 80 ºC). Electrolyte: 6 M KOH. 270
Figure 6.23. Chronopotentiogram (CP) at 10 mA cm^{-2} and 80 ºC for alkaline electrolysers containing Gortex anodes coated with ▬ $La_{0.8}Sr_{0.2}MnO_3$ and ▬ $NiCo_2O_4$. Gortex coated with 10% Pt served as the cathode (H_2 catalyst) in all cases. Electrolyte: 6 M KOH. 271
Figure 6.24. Nyquist plot and inset showing the equivalent circuit used to model the data for alkaline electrolysers containing Gortex anodes coated with (1) □■ - $La_{0.8}Sr_{0.2}MnO_3$, (2) ◊♦ - $NiCo_2O_4$ and (3) Δ▲ -IrO_2. Gortex coated with 10% Pt served as the cathode (H_2 catalyst) in all cases. Empty and filled markers denote 20 ºC and 80 ºC data respectively. Electrolyte: 6 M KOH. 272
Figure 6.25. (a) Current-voltage curves (iR-corrected) and (b) chronopotentiograms (iR-corrected) at 80 ºC for alkaline fuel cells containing Gortex electrodes coated with ■ - $La_{0.8}Sr_{0.2}MnO_3$ at 80 ºC, as cathode (O_2 catalyst) and alkaline water electrolysers containing Goretx electrodes coated with ♦ - $NiCo_2O_4$ as anode (O_2 catalyst). Gortex coated with 10% Pt served as the H_2 catalyst in both cases. Electrolyte: 6 M KOH. 275

Figure 7.1. (a) Principle of “Power-to-Gas”, in which hydrogen manufactured from excess renewable energy, is injected in existing natural gas pipelines. Natural gas is mainly methane. (b) Schematic diagram of a fuel cell in the present chapter. 284
Figure 7.2. Cross-sectional schematic of the test cell, showing the electrical and gas connections. 287
Figure 7.3. Current density – voltage curves, (j-V) on left axis and current density–power density (j-P) curves, on right axis for a fuel cell operating between 5% and 100% of hydrogen in a gas mixture. 290
Figure 7.4. Polarization curves for pure hydrogen, uncorrected data (dash line), corrected by: (i) taking into account the electrolyte resistance (black line) and (ii) using EIS (grey line)). 292
Figure 7.5. Tafel plots for the fuel cell operating between 5% and 100% of hydrogen in methane..... 293
Figure 7.7. Nyquist spectrum of impedance measurements for cell (1 cm^2) supplied with pure hydrogen and 50%, 40%, 30%, 20%, 10%, and 5% hydrogen and methane mixture. (a) The total flow was kept constant at 20 ml min^{-1}, constant current density of 10 mA cm^{-2} was applied; (b) the equivalent circuit. 298
Figure 7.8. (j-V), j-P) (a) and GEIS at 10 mA cm^{-2}, (b) characteristics for a fuel cell operating with pure hydrogen before (solid lines, black for j-V and grey for j-P) and after measurements with hydrogen and methane mixtures. 300
Figure 7.9. (j-V) and (j-P) characteristics (a) fuel utilization (b) and GEIS at 10 mA cm^{-2} for the cell (1 cm^2) operating with: 100%, 5%, 4%, 3% and 2% hydrogen in the gas mixture. 302

List of Tables

Table 2.1: Chemicals, Reagents and Materials used..... 67
Table 2.2. Example compositions of catalyst slurries..... 88
Table 3.1. Capillary flow analysis of Gortex-based gas diffusion electrodes.[9] 129
Table 3.2. Contact angles for varying thickness of sputtered Pt on ePTFE membrane 132
Table 3.3. Combinations of sputter-coated metals on Gortex, tested as alkaline fuel cell gas diffusion anodes and cathodes. 134
Table 3.4. Data from Electrochemical Impedance Spectroscopy (EIS) of alkaline fuel cells containing Gortex electrodes sputter-coated with Pt, modelled using the equivalent circuit in Figure 3.10(b) (ohmic resistance (R_Ω), pore resistance (R_{pore}), charge transfer resistance (R_{ct}), diffusional resistance (Z_d), and capacitance expressed in terms of constant phase element[17] (Pore: $Q_{CPE,pore}$, $n_{CPE,pore}$, and C_{pore}) (Charge transfer: $Q_{CPE,ct}$, $n_{CPE,ct}$, and C_{ct})). Electrolyte: 6 M KOH. ..... …….139
Table 3.5. Electrochemical Impedance Spectroscopy modelling data for ohmic resistance (R_Ω), charge transfer resistance (R_{ct}), charge transfer capacitance (C_{ct}) and diffusion resistance (Z_d) of the alkaline fuel cell containing Gortex electrodes coated with 10% Pt on Vulcan XC72, carbon black, PTFE, and Ni mesh. Electrolyte: 6 M KOH. The equivalent circuit in Figure 3.13(b) was used to model the EIS data. 149
Table 5.1. Comparison, at 20 °C, of alkaline fuel cells containing Gortex anode electrodes coated with different precious metal catalysts. Gortex coated with 10% Pt served as the anode (H_2 catalyst) in all cases. Symbols: activation overpotential (η_{act}), Voltage at 10 mA cm^{-2} ($V_{@10mAcm-2}$), Tafel slope (b_1) (at lower current density (LCD)), Tafel slope (b_2) (at higher current density (HCD)); from electrochemical impedance, ohmic resistance (R_Ω), charge transfer resistance $R_{(ct)}$, double-layer capacitance within the catalyst layer $C_{(ct),}$ diffusional resistance $Z_{(d)}$. 200
Table 5.2: Data from Tafel plots and modelling of EIS data for alkaline fuel cells containing Gortex electrodes coated with different precious metal catalysts at 20 °C vs 80 °C. Gortex coated with 10% Pt served as the anode (H_2 catalyst) in all cases. Showing: (from Tafel plots) activation overpotential (η_{act}), voltage at 10 mA cm^{-2} ($V_{@10mAcm-2}$), Tafel slope (b_1) (at lower current density (LCD)); (from EIS) ohmic resistance (R_Ω), charge transfer resistance $R_{(ct)}$, double-layer capacitance within the catalyst layer $C_{(ct),}$ diffusional resistance $Z_{(d)}$. 215
Table 6.1. Comparison, at 20 °C, of alkaline fuel cells containing Gortex cathode electrodes coated with perovskite catalysts. Gortex coated with 10% Pt served as the anode (H_2 catalyst) in all cases. Symbols: activation overpotential (η_{act}), Voltage at 10 mA cm^{-2} ($V_{@10mAcm-2}$), Tafel slope (b_1) (at lower current density (LCD)), Tafel slope (b_2) (at higher current density (HCD)); from electrochemical impedance, ohmic resistance (R_Ω), charge transfer resistance (R_{ct}), double-layer capacitance within the catalyst layer (C_{ct}), diffusional resistance (Z_d). 244
Table 6.2. Comparison, at 20 °C, for alkaline fuel cells containing Gortex cathode electrodes coated with spinel catalysts. Gortex coated with 10% Pt served as the anode (H_2 catalyst) in all cases. Symbols: activation overpotential (η_{act}), Voltage at 10 mA cm^{-2} ($V_{@10mAcm-2}$), Tafel slope (b_1) (at lower current density (LCD)), Tafel slope (b_2) (at higher current density (HCD)); from electrochemical impedance, ohmic resistance (R_Ω), charge transfer resistance (R_{ct}), double-layer capacitance within the catalyst layer (C_{ct}), diffusional resistance(Z_d). 244
Table 6.3. Parameters for a comparison of electrochemical activity for alkaline fuel cells containing Gortex electrodes coated with $La_{0.8}Sr_{0.2}MnO_3$ and $NiCo_2O_4$ as cathode (O_2 catalyst) at 20 °C and 80 °C. Gortex coated with 10% Pt served as the anode (H_2 catalyst) in all cases. Column titles: activation overpotential (η_{act}), Voltage at 10 mA cm^{-2} ($V_{@10mAcm-2}$), Tafel slope (b_1) (at lower current density (LCD)); from electrochemical impedance, ohmic resistance (R_Ω), charge transfer resistance (R_{ct}), double-layer capacitance within the catalyst layer (C_{ct}), diffusional resistance (Z_d). 260

Table 6.4. Parameters for a comparison of electrochemical activity for alkaline electrolysers containing Gortex electrodes coated with IrO_2, $La_{0.8}Sr_{0.2}MnO_3$ and $NiCo_2O_4$ as anode (O_2 catalyst) at 20 ^oC and 80 ^oC. Gortex coated with 10% Pt served as the cathode (H_2 catalyst) in all cases. Column titles: activation overpotential (η_{act}), Voltage at 10 mA cm^{-2} ($V_{@10mAcm-2}$), Tafel slope b; from electrochemical impedance, ohmic resistance (R_Ω), polarisation resistance of the catalysts (R_p), double-layer capacitance (C_p), charge transfer resistance (R_{ct}), and constant phase element of the catalysts layer ($C_{CPE,ct}$). ……...……..260

Table 7.1. Flow parameters of H_2 and CH_4 in examined mixtures. Columns: open circuit voltage (V_{oc}), potential upon applying current density of 10 mA cm^{-2} ($V_{@10mAcm-2}$), the highest power density (P_{max}) and ohmic resistance (R_{slop_unc}) from uncorrected polarization curves. 289

Table 7.2. Parameters obtained from the Tafel plots: slope A, and the exchange current density i_o; from electrochemical impedance, double-layer capacitance within the catalyst layer $C_{(ct),}$ charge transfer resistance $R_{(ct),}$ diffusional resistance $Z_{(d)}$. 294

Table 7.3. Parameters obtained after fitting data from Nyquist and Bode plots to equivalent circuit (Nyquist, Bode plots and equivalent circuit shown in Figure 5.2); charge transfer resistance (R_{ct}), double layer capacitance (C_{ct}), exchange current density (i_o) and relaxation time t_o calculated from R_{ct}. Electrochemical cells were supplied with symmetrically supplied hydrogen (H_2/H_2), oxygen (O_2/O_2) and (H_2/O_2), at the two electrodes of the cell, at open circuit potential (OCV). 296

Table 7.4. Parameters of the flow of H_2 and CH_4 in examined mixtures, and obtained: open circuit voltage (V_{oc}), potential upon applying current density of 10 mA cm^{-2}($V_{@10mAcm-2}$), the highest power density (P_{max}) and ohmic resistance (R_{slop_unc}) from uncorrected polarization curves……..301

CHAPTER 1

Introduction

1.1 Background

Worldwide, importance is being placed on the development of new technologies that: (i) can store energy efficiently, (ii) deliver electricity on demand, at peak and off-peak times, and, (iii) are compatible with the goal of sustainable development. Energy produced or consumed, in the form of electricity, is an indication of a country's economic development. Particular importance is being placed on alternative energy storage systems due to: (i) uncertainties in the future availability of fossil fuels; (ii) costly infrastructure requirement for pumped hydro and nuclear power; and (iii) concerns about climate change to limit the use of fossil fuels. For these reasons, researchers are increasingly focusing on hydrogen as a potential storage medium for electricity. Hydrogen is suitable as a long term electricity storage medium because of its high energy content per unit mass, the highest of any fuel.

One class of hydrogen production system (based on water) involves an electrochemical cell known as an '*electrolyser*'. Within an *electrolyser*, water is split into oxygen (O_2) at the anode electrode and hydrogen (H_2) at the cathode electrode by the following overall reaction:

$$2\ H_2O \rightarrow O_2 + 2\ H_2 \qquad E^o_{cell} = -1.23\ V\ vs\ NHE \qquad \ldots (1.1)$$

The negative sign of E^{o}_{cell} indicates that the water-splitting reaction is thermodynamically unfavourable and must be driven by an input of electrical energy. This is achieved by applying a voltage across the anode and cathode that is greater than 1.23 V (at Standard Temperature and Pressure (STP) of 1 atm and 25 ^{o}C). Using an *electrolyser*, electricity is therefore converted into, and stored in the form of hydrogen gas.

The reverse reaction, involving re-combining hydrogen (H_2) at the anode and oxygen (O_2) at the cathode to generate water (H_2O), is carried out in an electrochemical device known as a '*fuel cell*', which facilitates the overall reaction:

$$O_2 + 2\ H_2 \rightarrow 2H_2O \qquad E^{o}_{cell} = 1.23\ V\ vs\ NHE \qquad \ldots (1.2)$$

The positive sign of E^{0}_{cell} for this overall reaction indicates that it is thermodynamically favourable, meaning that a *fuel cell* of this type spontaneously generates a voltage across the anode and cathode, and an electrical current if the circuit is closed. In this way, the stored electrical energy in the hydrogen may be recovered, at least in part.

During periods of low demand for electricity, when electricity is cheap, hydrogen (and oxygen) may therefore be produced using an *electrolyser*. The hydrogen (and oxygen) could then be stored and used to generate electricity within a *fuel cell* during periods of peak electricity demand, when electricity is expensive. In some parts of North America, off-peak electricity may, at certain times, have a negative price, meaning that a user will be paid by the utility to take the electricity. A potential commercial proposition would be to use such electricity to generate hydrogen in an *electrolyser*. At peak periods of electrical demand, the stored hydrogen from the *electrolyser* could then be converted back into water within a *fuel cell* to regenerate the electricity, at least in part.

1.1.1 "The Problem"

While the above scenario may seem attractive, one of the major challenges with implementing it is that, at the present time, commercial *electrolysers* and *fuel cells* are electrically inefficient, typically achieving 44-75% electrical efficiency in the forward direction and less in the reverse direction. Moreover, there is a thermodynamic limit which has the effect that more energy needs to be put into making hydrogen than can be obtained out of it, at least electrically.

The minimum theoretical energy required to generate 1 kg of hydrogen is 39.41 kWh.[1] This quantity is known as the Higher Heating Value (HHV) and includes the heat energy present in the hydrogen (6.08 kWh/kg hydrogen). However, a fuel cell cannot harvest the heat energy in hydrogen, so that the maximum theoretical energy it can generate from 1 kg of hydrogen is 33.33 kWh.[1] This quantity is known as the Lower Heating Value (LHV) of hydrogen.

An electrolyser operating at, say, 50% overall energy efficiency will, consequently, require 39.41/0.5 = 78.82 kWh to manufacture 1 kg of hydrogen. However, a fuel cell operating at 50% energy efficiency will only be able to harvest 33.33 x 0.5 = 16.665 kWh from the same 1 kg of hydrogen. As a result, the '*round-trip*' energy efficiency of the forward and the reverse process would then be: 16.665 / 78.82 x 100 = 21.14%. That is, only 21.14% of the electrical energy originally put into the electrolyser will be recovered as electrical energy from the fuel cell.

This compares poorly with other storage systems such as '*pumped hydro*', where 'round-trip' electrical efficiencies of 70-75% are routinely achieved. Pumped hydro involves pumping water uphill into a dam using unwanted, low-cost, off-peak electricity, and then allowing this

water to run downhill to generate hydroelectricity at later periods of high electrical demand. Pumped hydro has the disadvantage however, that it requires massive and expensive infrastructure, including two dams (one at a lower and one at a higher elevation) as well as connecting piping and pumps. As such, it may not be suitable for small-scale electricity storage, as may be needed to smooth out the peaks and troughs of electricity generation by renewable electricity generators, like wind and sunlight. Because, for example, the wind blows only intermittently, wind turbines cannot provide a constant flow of electricity. They need a technique that can efficiently store the electricity generated when the wind blows strongly and release it when the wind is weak. A small-scale hydrogen-based system would be ideal, but only if it could be made sufficiently energy- and cost-efficient.

Given the long-standing imperatives to move the modern economy to a hydrogen-based economy based on renewable energy, the development of an energy- and cost-effective hydrogen-based system could also help achieve this aim.

In the following sections we will discuss electrolysers and fuel cells, with a special emphasis on their operation and how that creates the above-mentioned limitations. We will start with fuel cells, as these represent, in some respects, the more challenging problem.

1.2 Fuel Cells

Fuel cells convert chemical energy into electrical energy, where the electrical current is produced according to two half reactions that occur at the anode and at cathode respectively, with electrons transported between them through an external circuit. The anode half-reaction usually involves oxidation of a fuel such as hydrogen or methanol. The cathode reaction usually involves reduction of oxygen, typically in the form of air-oxygen. Of these two half-reactions, the oxygen reduction half-reaction at the cathode is generally the more

energetically demanding, meaning that it is most critical to have a good catalyst at this electrode (although effective catalysts are needed at both the anode and cathode in order to achieve overall high efficiency).

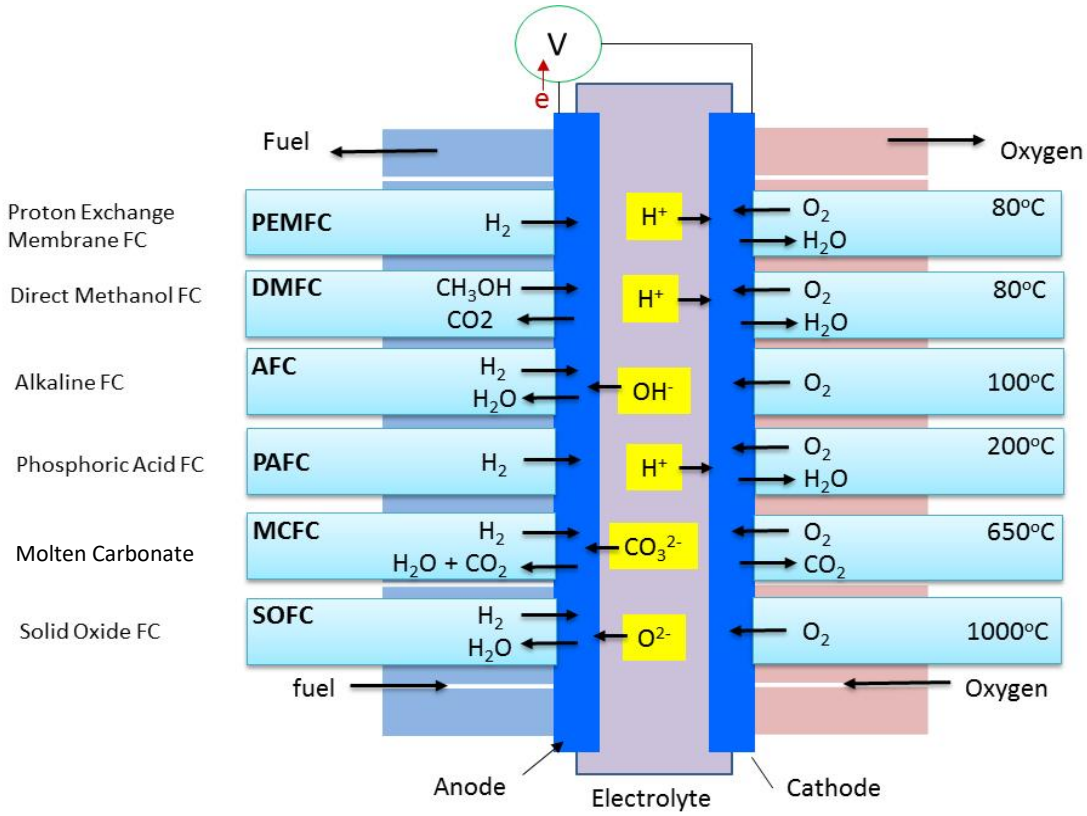

Figure 1.1. *Schematic comparison of the working principles and operation of different classes of fuel cell.*

1.2.1 Classes of Fuel Cell

Several classes of fuel cell have been developed. These are shown schematically in Figure 1.1, which depicts:

- The reactants and products at the anode of each class of fuel cell (shown on the left of the left-hand vertical blue line in Figure 1.1),

- the reactants and products at the cathode of each class of fuel cell (shown on the right of the right-hand vertical blue line in Figure 1.1), and
- the ions that move between the electrodes for each class of fuel cell (shown with a yellow highlight, between the two vertical blue lines in Figure 1.1).

1.2.1.1 Alkaline Fuel Cells (AFC)

In alkaline fuel cells (AFCs), oxygen gas is fed into the cathode, where it is converted to hydroxide ions (OH^-) as shown below. The hydroxide ions migrate through the electrolyte to the anode, which is fed with hydrogen that reacts to produce water as shown below:

Cathode:	$O_2 + 2H_2O + 4e^- \rightarrow 4OH^-$	E_{red}^o = 0.40 V … (1.3)
Anode:	$2H_2 + 4OH^- \rightarrow 4H_2O + 4e^-$	E_{ox}^o = 0.83 V … (1.4)
	---	---
Overall:	$2H_2 + O_2 \rightarrow 2H_2O$	E_{cell}^o = 1.23 V … (1.5)

Note that the overall E_{cell} is positive, meaning that the overall reaction is thermodynamically favoured and will occur spontaneously, to thereby generate voltage and current.

AFCs generally employ porous electrodes known as gas diffusion electrodes (GDEs). A schematic of an AFC GDE is depicted in Figure 1.2. As can be seen, AFC GDEs traditionally comprise of a porous "catalytic" layer incorporating a catalyst as well as a nickel mesh current carrier, backed by a gas-porous poly(tetrafluoroethylene) (PTFE) "white PTFE" gas diffusion layer, through which the reactant gas permeates.[2] The space between the electrodes is filled by a strongly alkaline electrolyte ("KOH electrolyte").

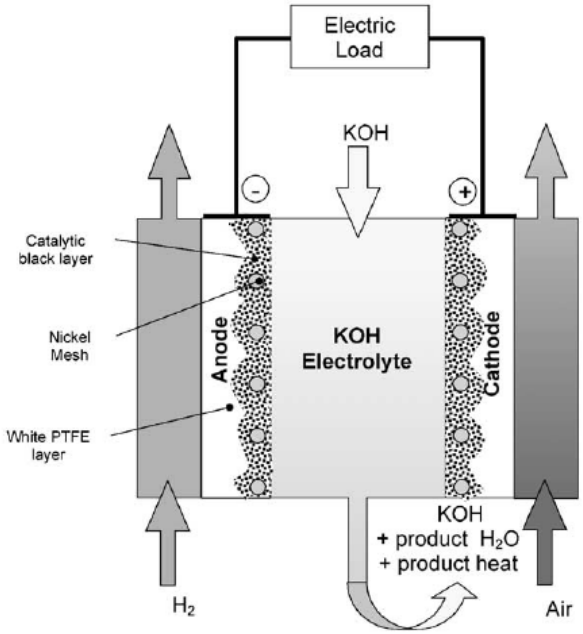

Figure 1.2. *Schematic cross-section of a traditional alkaline fuel cell. Reproduced with permission from reference 2.*

Catalysts at the anode electrode have generally been less studied than catalysts at the cathode because the cathode electrode is directly linked to the power output and lifetime of alkaline fuel cells. This is because the sluggish oxygen reduction reaction at the cathode (compared with the hydrogen oxidation at anode) typically limits the performance.

At the anode, studies[3-4] have shown that Pt-group metals such as Pt and Pd, deliver good performance and stability when used as catalysts.[5-6] Nickel may also offer a potentially low-cost catalyst for AFC anodes, especially Raney Ni, which provides a high surface area and has been shown to be one of the most active catalysts for hydrogen oxidation in alkaline media. Ni may, however, be subject to deactivation as reported in references,[7-9] which can reportedly be improved by the addition of copper[10] or treatment with H_2O_2.

We will discuss the catalysts used in AFCs in greater detail in a later section of this chapter.

In general, alkaline fuel cells display the highest electrical efficiencies of any class of "*low temperature*" fuel cell (i.e. fuel cells that normally operate below 110 ^{o}C). This is because they typically employ a highly basic aqueous electrolyte, such as 6 M potassium hydroxide (KOH), which strongly favours the more demanding half-reaction, namely, oxygen reduction at the cathode. The kinetics of oxygen reduction in alkaline electrolyte is much faster than in acid, which makes for a more efficient system.[2] The operating temperatures of AFCs are normally low compared to other types of fuel cells, being below 110 $^{\circ}$C. High temperatures are not needed to improve the oxygen reduction kinetics, as is the case in other types of fuel cell.

AFCs suffer from one significant drawback: the problem of insoluble carbonate formation.[2] Alkaline solutions, like 6 M KOH, have the property that they spontaneously extract carbon dioxide (CO_2) from the atmosphere. In so doing, they form insoluble carbonate precipitates which typically interfere with the operation of the AFC. Such precipitates may also arise from oxidation of the carbon support material used in the electrodes under open circuit and operational conditions. The insoluble carbonates usually form in the pores of the gas diffusion electrodes used in AFCs, blocking them and resulting in degraded cell performance.

1.2.1.2 Proton Exchange Membrane Fuel Cells (PEMFC, or PEM Fuel Cells)

Proton exchange membrane fuel cells are distinguished by the fact that they employ a solid-state proton-conducting polymer membrane as the electrolyte in the fuel cell. Catalysts, typically Pt and/or Ir/Ru oxides, are deposited on opposite sides of the membrane. On one side, the anode, hydrogen gas (H_2) is oxidized by the catalyst to generate protons (H^+), as shown below. The protons then migrate along the proton conduction pathways through the PEM membrane to the catalyst on the other side, at the cathode, where they react with

oxygen (O_2) to form water (H_2O), as shown below. The proton exchange membrane most widely used in PEMFCs is Nafion, manufactured by DuPont. The half-reactions are:

Cathode:	$O_2 + 4H^+ + 4e^- \rightarrow 2H_2O$	$E_{red}^o = 1.23$ V	… (1.6)
Anode:	$H_2 \rightarrow 2H^+ + 2e^-$	$E_{ox}^o = 0.00$ V	… (1.7)
	---	---	
Overall:	$2H_2 + O_2 \rightarrow 2H_2O$	$E_{cell}^o = 1.23$ V	… (1.8)

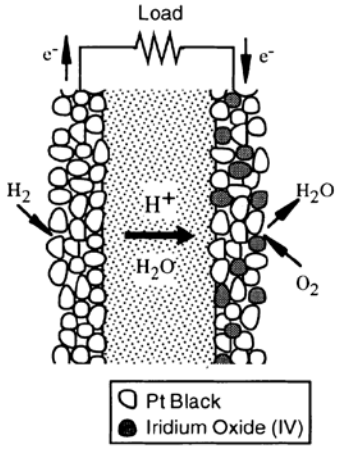

Figure 1.3. *Schematic diagram of an ion conducting (ionomer) membrane coated with catalysts, as used in a typical proton exchange membrane fuel cell. Reproduced with permission from reference 11.*

Porous, gas diffusion layers are employed on the outsides of PEM fuel cells, as depicted in Figure 1.3, to allow for diffusion of the reactant H_2 and O_2 gases to their respective anode and cathode active surface areas, where the catalysts are in contact with the PEM ion conductor.

PEM fuel cells also operate at relatively low temperatures of 85-105 ˚C. Due to the low operating temperature and the intrinsically acidic nature of proton exchange membranes, the

catalyst loading must typically be high in order to compensate for the slow kinetics of oxygen reduction under such conditions. For practical reasons, commercial PEM fuel cells use air oxygen for the cathode gas supply. Because of the low partial pressure of oxygen in air, the catalytic activity is diminished compared to pure oxygen, so that many commercial PEM fuel cells use air compressors to improve performance.[2]

To maintain high proton conductivity, the PEM membranes in PEM fuel cells must generally be kept close to saturated with water. To avoid drying out of the membrane, with an accompanying decline in the rate of proton conduction, input gases generally have to be humidified. The need to keep the PEM membrane humid makes water management a major challenge in PEM fuel cell technology. The precious metal catalysts in PEM fuel cells are also very sensitive to CO poisoning, so that the feedstock gases, particularly hydrogen, must be extremely pure.

1.2.1.3 Direct Methanol Fuel Cells (DMFC)

DMFCs are a special form of low temperature fuel cell based on PEM technology. Methanol is fed directly into the DMFC anode, either in a gaseous or liquid form, with oxygen – typically air oxygen – fed into the cathode (see Figure 1.1). Protons formed at the anode, migrate through the PEM membrane to the cathode. The reactions are:

Cathode: $\frac{3}{2}O_2 + 6H^+ + 6e^- \rightarrow 3H_2O$ $E_{red}^o = 1.229$ V … (1.9)

Anode: $CH_3OH + H_2O \rightarrow CO_2 + 6H^+ + 6e^-$ $E_{ox}^o = 0.02$ V … (1.10)

Overall: $CH_3OH + \frac{3}{2}O_2 \rightarrow CO_2 + 2H_2O$ $E_{cell}^o = 1.249$ V … (1.11)

A vapour fed methanol fuel cell can improve overall cell performance in combination with gas diffusion electrodes. Using a liquid feed arrangement for methanol, however, simplifies the design, as no humidification system is necessary.

1.2.1.4 Phosphoric Acid Fuel Cells (PAFC)

The PAFC is one of the most advanced systems when it comes to commercial development. In this fuel cell, phosphoric acid is used as the electrolyte. This allows the use of higher operating temperatures than is possible in, for example, PEM fuel cells, where water management is an issue. The reactions in PAFCs are the same as in PEM fuel cells; however the reaction at the cathode is faster due to the higher operating temperatures (150-200 ˚C).

Cathode:	$O_2 + 4H^+ + 4e^- \rightarrow 2H_2O$	$E_{red}^o = 1.23$ V	… (1.12)
Anode:	$H_2 \rightarrow 2H^+ + 2e^-$	$E_{ox}^o = 0.00$ V	… (1.13)
	---	---	
Overall:	$2H_2 + O_2 \rightarrow 2H_2O$	$E_{cell}^o = 1.23$ V	… (1.14)

PAFCs have the advantage of simple construction, as well as thermal, chemical, and electrochemical stability, and low electrolyte volatility, at the operating temperatures used. The high concentration of acid increases the conductivity of the electrolyte and reduces corrosion of carbon-supported electrodes. In PAFCs, it is extremely important to have a hydrophobic backing layer, which prevents loss of the liquid electrolyte.[12]

1.2.1.5 Molten Carbonate Fuel Cells (MCFC)

In this type of fuel cell, carbonaceous materials are melted at ca. 650 ˚C and used as the electrolyte. The reactions that occur are:

Cathode: $\frac{1}{2}O_2 + CO_2 + 2e^- \rightarrow CO_3^{2-}$ … (1.15)

Anode: $H_2 + CO_3^{2-} \rightarrow H_2O + CO_2 + 2e^-$ … (1.16)

Overall: $2H_2 + O_2 \rightarrow 2H_2O$ $E_{cell}^o = 1.23$ V … (1.17)

In contrast to other types of fuel cells, MCFCs operate at high temperatures of about 600-700 ˚C. This has the effect of increasing the oxygen reduction kinetics dramatically. Fast oxygen reduction kinetics eliminates the need for high metal catalyst loading. As can be seen above, CO_2 poisoning is not a problem for MCFCs as was the case with AFCs.

The high temperatures are also used in MCFCs to internally reform methane into hydrogen. The fuel supplied to the fuel cell may therefore be methane from a natural gas network, rather than pure hydrogen, which is difficult and expensive to store and transport.

Some of the disadvantages of MCFCs include the fact that the molten carbonate is stabilized in a matrix. This makes it necessary to find an electrolyte matrix with optimum capillary pressures to maintain the interfacial boundaries necessary between electrodes and electrolyte. The materials used for the electrodes, as well as the cell materials also require costly fabrication to prevent degradation in cell performance.

1.2.2.6 Solid Oxide Fuel Cells (SOFC)

Solid oxide fuel cells (SOFCs) operate at very high temperatures (700-1000 ˚C) using a solid oxide electrolyte, through which oxygen ions generated at the cathode readily migrate to the anode to form water. The migration occurs *via* oxygen vacancies in the crystal structure of the solid oxide electrolyte. The reactions are:

Cathode: $\frac{1}{2}O_2 + 2e^- \rightarrow O^{2-}$ … (1.18)

Anode: $H_2 + O^{2-} \rightarrow H_2O + 2e^-$ … (1.19)

Overall: $2H_2 + O_2 \rightarrow 2H_2O$ $E_{cell}^o = 1.23$ V … (1.20)

The use of a solid electrolyte renders SOFCs leak-free. They also tend to be more stable than MCFCs. The high operating temperature leads to enhanced oxygen reduction kinetics. Like MCFCs, SOFCs use their high operating temperatures for internal reforming of the fuel feed as well as to eliminate CO poisoning and the need for high loadings of expensive metal catalysts. Major challenges faced in the development of SOFCs include the need for thermally and chemically stable materials capable of handling the high temperatures and energy losses deriving from the high temperatures.

1.2.2 The Principles and Operation of Alkaline and PEM Hydrogen-Oxygen Fuel Cells

We will now narrow our focus to the operation of alkaline and PEM fuel cells that are based on the reaction of hydrogen and oxygen.

1.2.2.1 Half-Reaction at the Anode: The Hydrogen Oxidation Reaction (HOR)

The Hydrogen Oxidation Reaction, or HOR, is a relatively fast electrochemical reaction that occurs at the anode in a hydrogen-oxygen fuel cell. The HOR half-reaction in alkaline solution is:

$H_2 + 2OH^- \rightarrow 2H_2O + 2e^-$ $E_{ox}^o = 0.83$ V vs NHE … (1.21)

In acid solution, the HOR half-reaction is:

$$H_2 \rightarrow 2H^+ + 2e^- \qquad E_{ox}^{o} = 0.00 \text{ V vs NHE} \qquad \ldots (1.22)$$

In both of these processes, adsorption of hydrogen (H_2) occurs at the catalyst surface, where it then dissociates and undergoes an electrochemical reaction. Using a catalyst such as Pt, for example, the electrochemical reactions in alkaline solution are:[13]

$$H_{2(g)} + 0H^- + Pt_{(s)} \rightleftharpoons Pt - H_{ads} + H_2O + e^- \qquad \ldots (1.23)$$

$$H_2 + 2Pt_s \rightleftharpoons 2Pt - H_{ads} \qquad \ldots (1.24)$$

$$Pt - H_{ads} + 0H^- \rightleftharpoons H_2O + e^- + Pt_{(s)} \qquad \ldots (1.25)$$

where: $Pt_{(s)}$ is a free surface site and $Pt - H_{ads}$ is adsorbed H-atom on the free surface site.[13]

Although, the above-mentioned overall reaction is relatively fast, it requires pure hydrogen, which is expensive and difficult to store. Hydrogen may be, alternatively, obtained *via* on-site reformation of hydrogen from vectors such as natural gas and alcohols, although contaminants, such as CO, may still be present. Such contaminants would typically block and poison the active surface sites of precious metal catalysts like Pt, thereby hindering reaction.

1.2.2.2. Half-Reaction at the Cathode: The Oxygen Reduction Reaction (ORR)

The oxygen reduction reaction, or ORR, involves a direct 4-electron reaction in which oxygen (O_2) is converted into water (H_2O). In acid electrolyte, the ORR half-reaction is:

$$O_2 + 4H^+ + 4e^- \rightarrow 2H_2O \qquad E_{red}^{o} = 1.23 \text{ V vs NHE} \qquad \ldots (1.26)$$

In alkaline electrolyte the ORR half-reaction is:

$$O_2 + 2H_2O + 4e^- \rightarrow 4OH^- \qquad E_{red}^o = 0.40 \text{ V vs NHE} \qquad \ldots (1.27)$$

An undesired side-reaction that may occur is the 2-electron reduction of oxygen (O_2) to hydrogen peroxide (H_2O_2) or the hydroperoxy anion (HO_2^-). The hydroperoxy anion (HO_2^-) is the stable form of hydrogen peroxide (H_2O_2) in basic solution. These species are intermediates in the 4-electron reduction of O_2 to H_2O, so that this side-reaction can be considered to be an incomplete ORR. In acid electrolyte, this half-reaction is:

$$O_2 + 2H^+ + 2e^- \rightarrow H_2O_2 \qquad E_{red}^o = 0.70 \text{ V vs NHE} \qquad \ldots (1.28)$$

In alkaline electrolyte this half-reaction is:

$$O_2 + H_2O + 2e^- \rightarrow HO_2^- + OH^- \qquad E_{red}^o = -0.065 \text{ V vs NHE} \qquad \ldots (1.29)$$

The peroxy intermediates may react further according to the half-reactions:

In alkaline electrolyte

$$HO_2^- + H_2O + 2e^- \rightarrow 3OH^- \qquad E_{red}^o = 0.867 \text{ V vs NHE} \qquad \ldots (1.30)$$

or in an acidic electrolyte

$$H_2O_2 + 2H^+ + 2e^- \rightarrow 2H_2O \qquad E_{red}^o = 1.76 \text{ V vs NHE} \qquad \ldots (1.31)$$

Generally, the 4-electron pathway is desired due to its greater charge efficiency and the fact that it avoids the unwanted involvement of an unstable intermediate peroxide species. However, due to the intrinsically slow kinetics of the ORR and the poor durability of electrodes under severe operating environment, peroxides may be formed, at least in some part. For this reason, extensive studies have been carried out to discover highly active and stable ORR electro-catalysts that do not generate peroxide products. A feature of catalysis research on the ORR is measurements of the ratio of 4-electron: 2-electron reaction products by candidate catalysts. The higher that ratio, the more desirable the catalyst is in respect of the ORR.

1.2.2.3. Fuel Cell Thermodynamics

A. Open Circuit Voltage (OCV)

The open circuit voltage (OCV) of a fuel cell is the voltage it generates between its electrodes when the electrical circuit is open, not closed. The OCV may be used to measure the electrical output and efficiency of a fuel cell. The OCV is theoretically created by the Gibbs free energy, which is the energy available from the fuel cell to do external work (i.e. move electrons around the electrical circuit). The Gibbs free energy ($\Delta\bar{g}_f$) of a fuel cell is the difference in the Gibbs free energy of the products ($(\bar{g}_f)_{H_2O}$) generated by the cell and that of the reactants ($(\bar{g}_f)_{H_2}, \frac{1}{2}(\bar{g}_f)_{O_2}$) consumed by the cell.[14] For a fuel cell, the Gibbs free energy is determined as:

$$H_2 + \tfrac{1}{2}O_2 \rightarrow H_2O \quad \ldots (1.32)$$

$$\Delta\bar{g}_f = (\bar{g}_f)_{H_2O} - (\bar{g}_f)_{H_2} - \tfrac{1}{2}(\bar{g}_f)_{O_2} \quad \ldots (1.33)$$

For a fuel cell (assuming all of the Gibbs free energy is converted to electrical energy), the reversible OCV can be calculated. Based on the fuel cell reaction, two electrons will pass through the circuit for every molecule of H_2 that is converted into H_2O. The total charge flowing through the fuel cell (for 1 mole of H_2) can be represented by:

$$Total\ charge = -2Ne = -2F \quad \ldots (1.34)$$

Where, *N* is Avogadro's number (molecules in a mole), *F* is the Faraday constant (the charge on one mole of electrons), and *–e* is the charge on one electron.

The electrical work done by the fuel cell is:

$$W = charge \times voltage = -2FE_{cell} \quad \ldots (1.35)$$

Where, E_{cell} is the voltage of the fuel cell. As the Gibbs free energy of the fuel cell is assumed to be completely converted into electrical work, $W = \Delta\bar{g}_f$. The electromotive force (EMF) or the reversible open circuit voltage (OCV) (E^0) of the fuel cell is then:

$$E^0 = \frac{-\Delta\bar{g}_f^{\,0}}{2F} \quad \ldots (1.36)$$

B. The Nernst Equation

The Gibbs free energy changes with variations in the pressure and concentration of the reactants. The activities of water, hydrogen and oxygen affect the Gibbs free energy. For an ideal gases, activity (α) is defined as:[14]

$$\alpha = \frac{P}{P^0} \quad \ldots (1.37)$$

where, P^0 is standard pressure (0.1 MPa) and P is the partial pressure of the gas. The Gibbs free energy, based on the changes in activity, at any given temperature T, is given by:[14]

$$\Delta\bar{g}_f = \Delta\bar{g}_f^{\,0} - RTln\left(\frac{a_{H_2}.a_{O_2}^{\frac{1}{2}}}{a_{H_2O}}\right) \quad \ldots (1.38)$$

The abovementioned equation shows that higher energy is released when the activities of the reactants are high and less energy is released when the activities of the products are high. Combining Equation 1.36 with Equation 1.38, the Nernst equation for the fuel cell reaction is obtained:[14]

$$E_f = E_f^{\,0} - \frac{RT}{2F}ln\left(\frac{a_{H_2}.a_{O_2}^{\frac{1}{2}}}{a_{H_2O}}\right) \quad \ldots (1.39)$$

The Nernst equation shows that the cell potential depends on the activities of the products and reactants. This equation can also be also expressed as a function of gas pressure. This is done by replacing the activities in the above equation with their equivalent partial pressures, measured in bar. When a fuel cell is operated below 100 ^oC, the partial pressure of water is considered to be unity. Under this condition, the above equation can be expressed as:[14]

$$E_f = E_f^{\,0} - \frac{RT}{2F}ln\left(\frac{1}{p_{H_2}p_{O_2}^{1/2}}\right) \quad \ldots (1.40)$$

The Nernst equation also describes the dependence of the fuel cell potential on the temperature as shown below:[14]

$$E_f = E_f^0 + \frac{\Delta S}{2F}(T - T^0) - \frac{RT}{2F} ln\left(\frac{a_{H_2}.a_{O_2}^{\frac{1}{2}}}{a_{H_2O}}\right) \quad \ldots (1.41)$$

Where, ΔS is the change in entropy and T^0 is a reference temperature. As per the above equation, the potential of the cell will decrease as the temperature increases when the fuel cell is running on hydrogen. In case of an alkaline fuel cell running on hydrogen at 25 °C, E_f^0 is 1.23 V whereas a solid oxide fuel cell at 1000 °C exhibits an E_f^0 of 1.0 V.

C. Efficiency

In general, fuel cells are not completely reversible, and it is therefore impossible to have W = $\Delta \bar{g}_f$ or an efficiency of 100%. The ratio of the electrical energy produced ($W = \Delta \bar{g}_f$) and the total energy produced by burning the fuel ($\Delta \bar{h}_f$) gives a maximum efficiency:[15]

$$Maximum\ efficiency = \frac{-\Delta \bar{g}_f}{\Delta \bar{h}_f} \quad \ldots (1.42)$$

As the Gibbs free energy varies with temperature, the efficiency of a fuel cell also changes with temperature. There are two types of $\Delta \bar{h}_f$ that can be used. One comes from the combustion of hydrogen gas to produce steam (-241.83 kJ/mol), which corresponds to the Lower Heating Value (LHV) of hydrogen (33.33 kWh/kg hydrogen). The second comes from the same reaction but with the product being condensed to liquid (-285.84 kJ/mol), which corresponds to the Higher Heating Value (HHV) of hydrogen (39.41 kWh/kg hydrogen). These values or acronyms should be specified when efficiency values are calculated. For a 100% efficient fuel cell, the EMF would be 1.48 V if using the higher heating value, and 1.25 V if using the lower heating value. Therefore, the efficiency of a cell with a measured voltage E^0 can be calculated from the equations:

$$Efficiency\ (\%)(LHV) = \frac{E^0}{1.23} \times 100 \quad \ldots (1.43)$$

$$Efficiency\ (\%)(HHV) = \frac{E^0}{1.48} \times 100 \quad \ldots (1.44)$$

In fuel cell research, the efficiency of a fuel cell is generally given as a percentage based on the LHV equation above. Electrolyser efficiencies are generally quoted in terms of the HHV value.

1.2.2.4 Fuel Cell Voltage Losses based on Electrochemical Kinetics

Fuel cell performance is commonly characterised using current-voltage (I-V) 'polarisation' curves. Such curves display current (in mA) on the x-axis and voltage (V) on the y-axis. The current values are usually normalized by the geometric active area of the electrode (and then expressed as current density, in mA/cm^2) to compare results from electrodes with different areas. Also, a complementary power curve is often plotted alongside the I-V curve.

An example of an I-V curve for a typical low temperature fuel cell is shown in Figure 1.4. The theoretical voltage of the fuel cell is a function of the Gibbs free energy of the overall reactions. In practise, the fuel cell voltage is less than the theoretical value due to irreversible losses. As can be seen from Figure 1.4, the more current that is produced, the lower the voltage of the cell, limiting the total power that can be delivered.

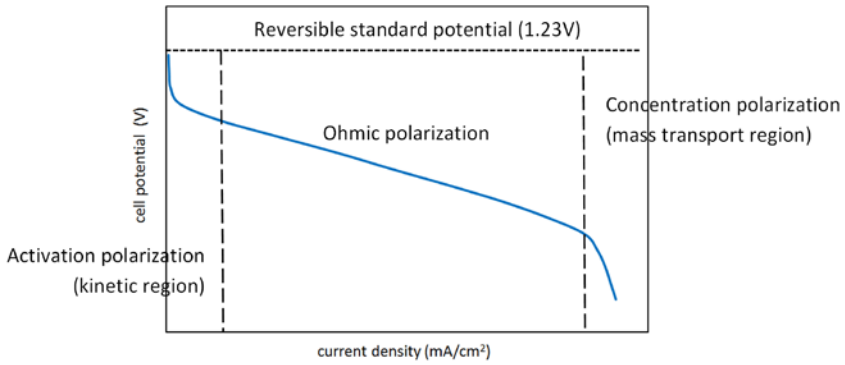

Figure 1.4. *Typical voltage-current density characteristics of a fuel cell*

In Figure 1.4, three different regions can be considered to be present, namely: (a) a kinetic (activation polarisation) region, (b) an ohmic polarisation region, and (c) a mass transport (concentration polarisation) region. In the kinetic region (shown as the non-linear voltage drop at low current density), a significant proportion of the produced energy is used to start the chemical reactions on both electrodes. In this region, activation losses dominate the cell behaviour.

In the ohmic region, ohmic losses dominate although kinetic, ohmic, and mass transport losses all occur. This results in a linear polarization curve.

In the mass transport region, losses occur due to an insufficient supply of reactant/s. That is the cell is, effectively, starved of reactants, resulting in a nonlinearity. The real voltage of a fuel cell (E_{cell}) is derived by subtracting all of the voltage losses from the thermodynamically reversible open circuit voltage (E^0).[15] This is expressed as:

$$E_{cell} = E^0 - \eta_{act} - \eta_{ohmic} - \eta_{diffusion} \quad \ldots (1.45)$$

A. Kinetic Region: Activation

Electrochemical kinetics is characterised by the activation overpotential, η_{act}, which is defined as the potential difference between the theoretical and actual cell potential at zero current as shown in Figure 1.5:

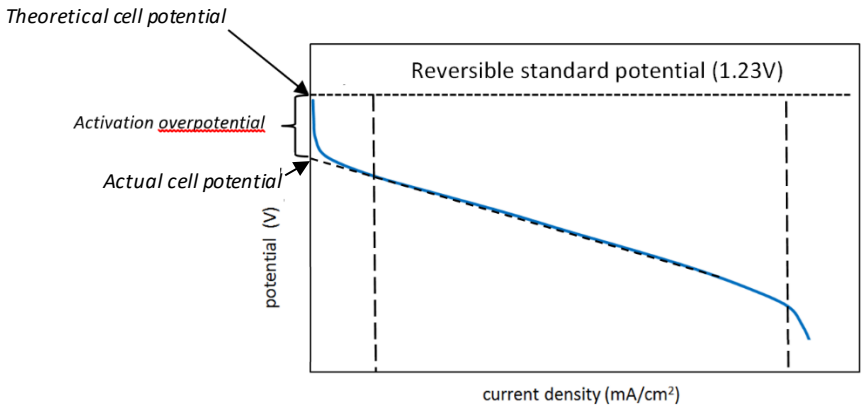

Figure 1.5. *Activation overpotential losses in a typical voltage-current density curve of a fuel cell*

Activation overpotential, η_{act} can be expressed as:

$$\eta_{act} = E_{cell} - E^0 \quad \ldots (1.46)$$

Equivalent expressions exist for the anode and cathode, each of which also have their own activation overpotentials.

The activation overpotential controls the rate of the cell reaction. The expression linking the rate (current density) of an electrochemical reaction to overpotential is called the Butler–Volmer equation, and is stated as follows:[15]

$$j = j_{anode} - |j_{cathode}| = j^0 \left(\left(e^{\frac{\alpha_a n F \eta_a}{RT}} \right)_{anode} - \left(e^{\frac{-\alpha_c n F \eta_c}{RT}} \right)_{cathode} \right) \quad \ldots (1.47)$$

where, j is the current density, j^0 the exchange current density, α_a and α_c are the charge transfer coefficient of anode and cathode respectively, η_a and η_c are the activation overpotential of anodic and cathode half reactions respectively, and n the number of electrons involved. The above relation indicates an exponential decline in the produced voltage with increasing current, which corresponds to activation losses (η_{act}) associated with the kinetics of the reactions occurring at the electrode surfaces.

B. Ohmic Region: Charge Transfer

Charge transfer, including both electron and ions in an electrochemical reaction, is driven by the gradient of the IV curve in the ohmic region. The voltage (η_{ohmic}), which drives charge transfer in fuel cells, is represented as follows:

$$\eta_{ohmic} = iR \quad \ldots (1.48)$$

where, R represents the overall ionic as well as electronic resistance. The ionic resistance derives from ion migration in the supporting electrolyte (R_{el}) and it depends on various factors such as the charge-transport length (d), cross-sectional area of charge transport (A) and the ionic conductivity (σ). This is represented as:

$$R_{el} = \frac{d}{\sigma A} \quad \ldots (1.49)$$

The electronic resistance (R_{er}) represents the sum of all ohmic resistances from the electrodes, current collectors and electrical contacts. It can be expressed as:

$$R_{er} = \sum \frac{l}{A\kappa_g} \quad \ldots (1.50)$$

where, κ is the electrical conductivity (in Ω^{-1} m^{-1}) and subscript g stands for each component of the circuit (e.g. wires, connectors and the electrode). As this resistance is proportional to

the length of the resistors, electronic resistance can be reduce by shortening the length of the wires, connectors, and the like, or by increasing the cross-sectional area and using more conductive materials.

In general, for a well-constructed fuel cell, ionic resistance is the main source of losses (being four to eight orders of magnitude greater than the electronic resistance).[15]

C. Mass Transport Region: Diffusion

Close to equilibrium, i.e. when $\eta_{act} = 0$, the electrochemical reaction rates are very small. However, at large overpotentials (that is, where electrochemical reactions occur far from the equilibrium state), mass transfer limitations occur due to depletion of reactants at the electrochemical interface. Hindrances in removing reaction products may also lead to accumulation in close proximity of the electrode surface. In non-agitated electrolyte, mass transfer usually only involves diffusion. This mass transfer affects both thermodynamic and kinetic reactions. Using the Butler–Volmer equation, one can account for the actual concentration of the rate-limiting reactants c_R and rate-limiting products c_P, where c_R^O & c_P^O is the reference reactant and product concentration respectively, at the electrode–electrolyte interface. The modified equation is expressed as:[15]

$$j = j^0 \left(\left(\frac{c_R}{c_R^O} e^{\frac{\alpha_a n F \eta_a}{RT}} \right)_{anode} - \left(\frac{c_P}{c_P^O} e^{-\frac{\alpha_c n F \eta_c}{RT}} \right)_{cathode} \right) \quad \ldots (1.51)$$

D. Adsorption

Another important feature that influences electrode kinetics is adsorption interactions between the electrode surface and the molecules or ions in the solutions. Various kinds of adsorption are possible and one of these may determine the rate of electrochemical reaction. It is usually necessary to find a good trade-off between the strength of the adsorption which is accompanied by a high adsorption rate and the ability of the adsorbed species to be

removed from the surface. That is, the adsorption interaction should be good enough to guarantee high adsorption and low enough to guarantee ready desorption. This is the basis for *Sabatier's Principle*[16] which determines the so-called volcano plots that will be discussed in more detail in Chapter 5 and 6 for the hydrogen and oxygen oxidation and reduction reactions.

1.3 Water Electrolysers

Hydrogen, being the fuel with the highest energy density per unit weight, is not only environmentally friendly but also easy to manufacture. In general, there are two ways to produce hydrogen: (1) steam reforming of natural gas (which is mainly methane, CH_4), gasification of coal, petroleum coke and heavy oil,[17] which dominates industrial hydrogen production, and (2) water electrolysis, which also produces oxygen and comes with the inherent advantage of producing extremely pure hydrogen. Different types of water electrolysers are depicted in Figure 1.6.

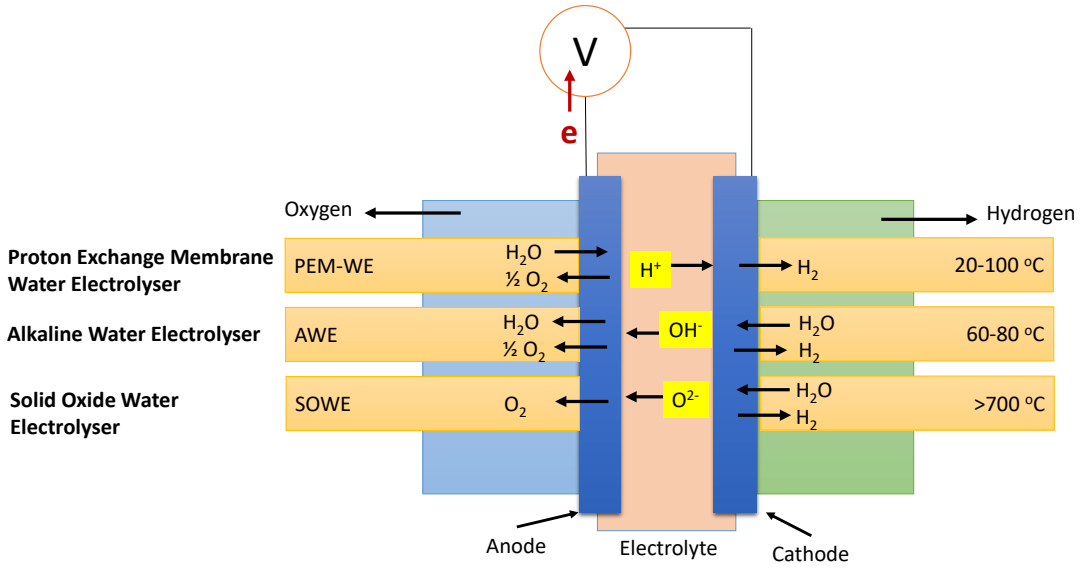

Figure 1.6. *Schematic comparison of the working principles and operation of different classes of water electrolysers*

In water electolysers, an application of direct current between two electrodes separated by an electrolyte, yields hydrogen at one electrode (the cathode) and oxygen at the other electrode (the anode). The electrons produced at the anode during oxygen formation flow from the negative terminal of the current source to the cathode where they are consumed to produce hydrogen. Water molecules or ionic species simultaneously migrate through the electrolyte between the electrodes. How that occurs varies in the different classes of electrolyser, which are discussed in the following section. To have the highest possible ion conductivities, the electrolytes used in water electrolysers typically involve high mobility ions.[18]

1.3.1 Classes of Electrolyser

1.3.1.1 Alkaline Electrolysers

Alkaline water electrolysers are widely recognised to be the most developed technology for water electrolysis. The chemical reactions that occur in an alkaline electrolyser are as follows:

Cathode: $2H_2O + 2e^- \rightarrow H_2(g) + 2OH^-$ E_{red}^o = -0.83 V … (1.52)

Anode: $2OH^-(aq.) \rightarrow \frac{1}{2}O_2(g) + H_2O\ (l) + 2e^-$ E_{ox}^o = -0.40 V … (1.53)

---------- ----------

Overall: $H_2O \rightarrow H_2(g) + \frac{1}{2}O_2(g)$ E_{cell}^o = -1.23 V … (1.54)

These cells generally use aqueous solutions of 20-40% KOH, which has a higher ionic conductivity than NaOH. In alkaline water electrolysis, an ion-permeable, gas-impermeable "diaphragm" separates the two electrodes, which are each immersed in a liquid electrolyte. At the cathode hydrogen is formed when water is reduced to hydroxide ions (OH^-). The

hydroxide ions thereafter migrate through the diaphragm towards the anode. At the anode, the hydroxide ions are converted to oxygen and water molecules as depicted above. Water needs to be continuously supplied to all electrolysers, including alkaline electrolysers, to replace the water that is consumed (as shown in the overall cell reaction above). The gases are produced in the form of gas bubbles. The diaphragm is needed between the electrodes to keep the oxygen and hydrogen bubbles from mixing, which could result in the formation of an explosive mixture. The gas bubbles are separately transported via circulating electrolyte (catholyte and anolyte) to gas-separation tanks where they are separated and collected in bulk form.

Although widely used, alkaline water electrolysers suffer from some limitations. Because the diaphragms are typically somewhat permeable to gases, diffusion of oxygen from the anode to the cathode, and of hydrogen from the cathode to the anode (through the diaphragm) may occur. Oxygen that reaches the cathode and hydrogen that reaches the anode will typically be converted back into water or hydroxide ions, meaning that electrons are wasted in, first, forming these gases and then in converting them back into their starting materials. This phenomenon is known as “crossover” and it is observed as a decline in the Faradaic efficiency of the cell. Faradaic efficiency is a measure of the rate of gas generation by an electrolyser relative to the expected rate of gas generation according to the electrical current passing through the cell. Crossover may also cause the collected oxygen and hydrogen to be contaminated with the other gas; that is, it is detrimental to the purity of the gases produced by each electrode.

This type of electrolyser also exhibits ohmic losses across the electrolyte and diaphragm, limiting the maximum current density. Because of the use of liquid electrolytes, the stack designs for alkaline water electrolyser are normally bulky.

The biggest advantages of alkaline electrolysis systems are their robustness, their long lifetime and the lower costs due to cheaper electrode materials. They account for the majority of the installed water electrolysers worldwide. In general, commercial alkaline electrolyser system size varies between 1.8 and 5300 kW. The hydrogen production capacities for these systems range from 0.25 to 760 $Nm^3\ h^{-1}$.[19] Due to the use of high concentrations of KOH, these cells are also susceptible to corrosion.

1.3.1.2 Proton Exchange Membrane (PEM) Electrolysers

In PEM electrolysers, a thin proton conducting membrane is employed as a polymer electrolyte instead of the liquid electrolytes used in alkaline water electrolysers. The polymer electrolyte membranes are mechanically strong and acidic in nature. The most commonly used membrane is Nafion™. The chemical reactions at the cathode and anode are as follows:

Cathode: $2H^+(aq.) + 2e \rightarrow H_2(g)$ $E_{red}^o = 0.00$ V … (1.55)

Anode: $H_2O\ (l) \rightarrow \frac{1}{2}O_2(g) + 2H^+(aq.) + 2e^-$ $E_{ox}^o = -1.23$ V … (1.56)

---------- ----------

Overall: $H_2O \rightarrow H_2(g) + \frac{1}{2}O_2(g)$ $E_{cell}^o = -1.23$ V … (1.57)

Deionised water is supplied to the anode side. Water reaches the anode catalyst layer and decomposes to produce oxygen which travels against water flow to the separator plates and exits the cell. The electrons however travel from the anodic catalytic layer towards the cathode side to combine with the protons to form hydrogen gas. The resulting hydrogen gas purity is higher than that of alkaline water electrolysers. PEM is commercially well suited for medium to small-scale applications.[19]

The rate of gas diffusion between the electrodes is less severe in the case of PEM electrolysers than in alkaline water electrolysers. Increasing pressure can cause adverse gas cross permeation in PEM electrolysers. Due to the solid PEM electrolyte, these electrolysers respond quickly in situations of input power variations. This allows PEM electrolysers to be operated in a more dynamic fashion compared to alkaline counterpart. PEM electrolysers also have a more compact system design due to the solid membrane.

PEM electrolysers typically have higher economic costs due to the material requirements deriving from the corrosive low pH conditions of the polymer electrolyte membrane. They also have shorter lifetimes when compared to alkaline water electrolysers, because of the degradation of conducting membranes used in PEM electrolysers, which then has detrimental effect on the long-term membrane stability. Costly and scare platinum-group metals are used as catalysts. Titanium separator plates are needed to reduce corrosion in PEM electrolysers.[20]

1.3.1.3 Solid Oxide Electrolyte (SOE) Electrolysers

Solid oxide electrolyte (SOE) electrolysers are the least mature technology when compared to PEM and alkaline electrolysers. SOE electrolysers operate at very high temperature (>700 ^{o}C) and utilize solid-state, ceramic electrolytes, within which oxygen anions (O^{2-}) are able to form and migrate from the cathode to the anode at the operating temperatures. The ceramic electrolytes are usually, yttria-stabilized zirconia (YSZ).[21] The chemical reactions that occur at the cathode and anode are as follows:

Cathode: $H_2O\ (g) + 2e^- \rightarrow H_2(g) + O^{2-}$ … (1.58)

Anode: $O^{2-} \rightarrow \frac{1}{2}O_2(g) + 2e^-$ … (1.59)

Overall: $H_2O \rightarrow H_2(g) + \frac{1}{2}O_2(g)$ E_{cell}^{o} = -1.23 V … (1.60)

Water vapour (steam) is supplied to the cathode where it is reduced to hydrogen gas and oxide ions. These ions travel through the ceramic electrolyte to the anode where they recombine to produce oxygen gas.

SOEs achieve higher efficiencies in water electrolysis (typically over 90%)[21] than alkaline and PEM electrolysers thanks to the higher operating temperatures. SOEs are often referred to as "steam electrolysers". At such high temperatures, the electrolyser components require frequent maintenance and replacement due to high rates of degradation. As such, this technology is still largely in the research and development stage.

1.3.2 The Principles and Operation of Alkaline and PEM Electrolysers

1.3.2.1. Half-Reaction at the Cathode: The Hydrogen Evolution Reaction (HER)

The Hydrogen Evolution Reaction, or HER, is a relatively fast electrochemical reaction that occurs at the cathode in a water electrolyzer. In acid electrolyte, the HER half-reaction is:

$2H_{(aq)}^{+} + 2e^{-} \rightarrow H_{2(g)}$ E_{red}^{o} = 0.00 V … (1.61)

In basic solution, the HER half-reaction is:

$2H_2O_{(l)} + 2e^{-} \rightarrow H_{2(g)} + 2OH_{(aq)}^{-}$ E_{red}^{o} = -0.83 V … (1.62)

The process of the HER typically takes place in steps of adsorption and desorption. In the case of an alkaline electrolyte, as shown below, water is reduced to an adsorbed atomic

hydrogen species, that then either reacts with another such species, or reacts with a second water molecule, to form di-hydrogen, H_2. The product H_2 thereafter dissociates through desorption.[13] Using a catalyst such as Pt, the electrochemical reactions in alkaline solution are:

$$H_2O + e^- + Pt_{(s)} \rightleftharpoons Pt - H_{ads} + OH^- \quad \ldots (1.63)$$

$$2\,Pt - H_{ads} \rightleftharpoons 2Pt_{(s)} + H_2 \quad \ldots (1.64)$$

$$Pt - H_{ads} + H_2O + e^- \rightleftharpoons H_2 + OH^- + Pt_{(s)} \quad \ldots (1.65)$$

where: $Pt_{(s)}$ is a free surface site and $Pt - H_{ads}$ is an adsorbed H-atom on the free surface site. The slowest of these steps becomes the rate determining step. For example, in acid electrolyte, desorption (equation 1.64 or 1.65) is rate determining with a Pt catalyst, whereas adsorption (equation 1.63) is rate determining for a MoS_2 catalyst.[22]

1.3.2.2. Half-Reaction at the Anode: The Oxygen Evolution Reaction (OER)

The oxygen evolution reaction, or OER, involves a direct 4-electron reaction in which water (H_2O) is converted into oxygen (O_2). In acid electrolyte, the OER half-reaction is:

$$2H_2O_{(l)} \rightarrow O_{2(g)} + 4H^+ + 4e^- \qquad E_{ox}^o = 1.23\ V \quad \ldots (1.66)$$

In alkaline electrolyte the OER half-reaction is:

$$4OH^- \rightarrow O_{2(g)} + 2H_2O_{(l)} + 4e^- \qquad E_{ox}^o = 0.40\ V \quad \ldots (1.67)$$

The OER can take place in either of four ways: (1) -*OH* adsorption and interaction (equation 1.69), (2) –*O* adsorption and interaction (equation 1.70), or (3) -*OOH* adsorption and

interaction (equation 1.71), (4) $–OO^-$ adsorption and interaction (equation 1.72), with the active catalyst site. Equation 1.69 shows the OER mechanism when *–OH* adsorption is dominant,[23] that is, when the surface coverage of the catalyst (Pt) is predominantly by *–OH* species. Similarly, equations 1.70, 1.71 and 1.72 indicate *–O, -OOH, –OO*$^-$ respectively as the dominant surface coverage species for other three OER mechanisms.[13]

$$Pt_{(s)} + OH^- \rightleftharpoons PtOH_{ads} + e^- \quad \ldots (1.68)$$

$$PtOH_{ads} + OH^- \rightleftharpoons PtO_{ads} + H_2O + 2e^- \quad \ldots (1.69)$$

$$PtO_{ads} + OH^- \rightleftharpoons PtOOH_{ads} + e^- \quad \ldots (1.70)$$

$$PtOOH_{ads} + OH^- \rightleftharpoons PtOO^-_{ads} + H_2O \quad \ldots (1.71)$$

$$PtOO^-_{ads} \rightleftharpoons Pt_{(s)} + O_2 + e^- \quad \ldots (1.72)$$

The surface coverage by either of *–OH, –O, -OOH, –OO*$^-$ species depends, in turn, on the electrochemical potential applied. This switch in mechanistic pathways of the OER in response to the change in electrochemical potential is reflected as a change in Tafel slopes (discussed in section 1.3.2.4 and chapter 5).

1.3.2.3. Electrolyser Thermodynamics

A. Cell Potential of a Water Electrolysis Cell

The reversible open circuit potential (E^0) of a water electrolysis cell may be calculated using the Nernst equations as described in section 1.2.2.3. E^0_{cell}, the reversible potential (namely the theoretical voltage of electrolysis) is given b:

$$E^0_{cell} = E^0 - \frac{RT}{2F} ln \frac{P}{P_0} \quad \ldots (1.73)$$

where E^0 is the standard equilibrium potential, R is the gas constant, T is the absolute temperature, and P and P_0 are the vapour pressure of pure water and electrolyte respectively.

Under standard conditions, the total reversible cell voltage E^0 is 1.23 V, independent of the pH of the electrolyte. In practice, this is never achieved because an overpotential must be applied to drive the process. The actual cell voltage differs from the reversible cell voltage because of the several system-related inefficiencies. The actual cell voltage is a combination of the contributing factors shown below:

$$E_{cell} = E^0_{cell} + \eta_{anode} + \eta_{cathode} + iR_{cell} \quad \ldots (1.74)$$

where, η_{anode} is the overpotential at the anode, $\eta_{cathode}$ the overpotential at the cathode, i is the current and R_{cell} is the cell resistance.

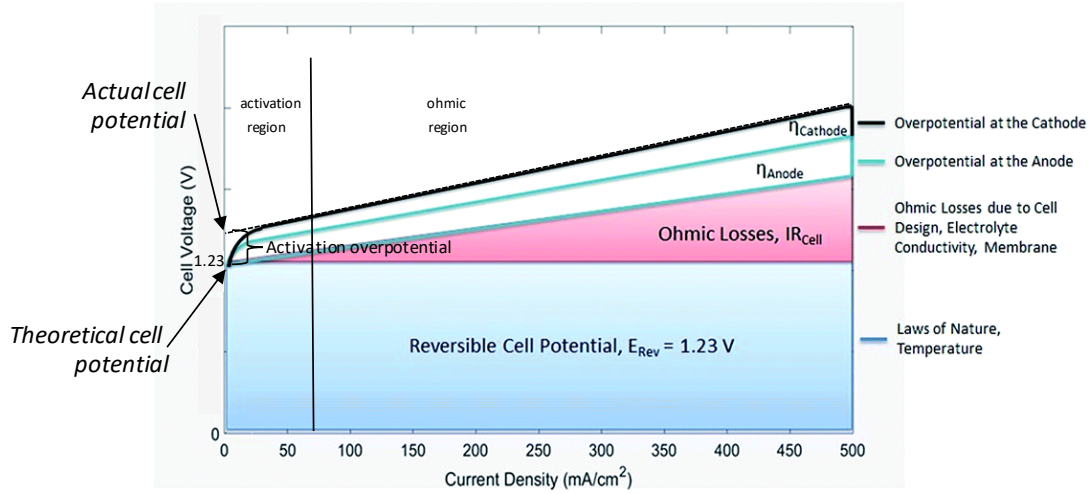

Figure 1.7. *Compositions of the cell voltage of an example alkaline water electrolysis cell. Adapted with permission from reference 24.*

Figure 1.7 shows the contributions to cell voltage, as a function of current density, as previously calculated for an example alkaline electrolyser. As can be seen, the contribution

from ohmic losses increases with current density until it becomes dominant at high current density values. Also, the overpotential at the anode is greater than at the cathode.

The activation overpotential is the energy that must be supplied to get the reaction started. It can be calculated by extrapolating (as a straight line), the VI curve in the ohmic region back to the y-axis at zero current as shown in Figure 1.7. The activation overpotential is then expressed as:

$$\eta_{act} = E_{cell} - E^0 \quad \ldots (1.78)$$

Equivalent expressions exist for the anode and cathode, each of which also have their own activation overpotentials.

B. Efficiency

Typically, the *energy efficiency* of water electrolysis is defined as the percentage of the total energy input that is stored in the hydrogen generated. This may be defined in terms of the electrical energy (excluding the thermal energy) that is present in the hydrogen; that is, it may be defined as the *energy efficiency relative to the lower heating value (LHV) of hydrogen*. Alternatively, and more conventionally, energy efficiency in an electrolyser is defined as the percentage of the input energy relative to the total electrical and heat energy stored in the hydrogen produced; that is, as the *energy efficiency relative to the higher heating value (HHV) of hydrogen*. The latter may also be termed the *thermal efficiency*. These definitions can be expressed as:

$$Efficiency_{LHV}(\%) = \frac{1.23}{E_{cell}} \times 100 \quad \text{at } 25\ ^{o}\text{C} \quad \ldots (1.75)$$

$$Efficiency_{HHV}(\%) = \frac{1.48}{E_{cell}} \times 100 \quad \text{at } 25\ ^{o}\text{C} \qquad \ldots (1.76)$$

Another way to express the latter is:

$$Efficiency_{Thermal} = \frac{energy\ content\ of\ 1\ mole\ of\ hydrogen}{energy\ required\ to\ produce\ 1\ mole} = \frac{283.8\ (kJ)}{E_{cell}it} \quad \ldots (1.77)$$

where 283.8 kJ is the higher heating value of one mole of hydrogen, *i* is the current and *t* is the time taken for one mole of hydrogen to be produced.

1.3.2.4. Electrolyser Voltage Losses based on Electrochemical Kinetics

The rate of the electrode reaction depends on (i) the nature and pre-treatment of the electrode surfaces (ii) the composition of the electrolyte solution near the electrode surface, and (iii) the electrode potential, characterised by the reaction overpotential. The electrode kinetics affects the relationship between current density, the surface overpotential and the composition of electrolytic solution near the electrode surface.[17]

A. Overpotential Loses

Electrolyser kinetics is characterised by the activation overpotential, η_{act}, which is caused by the electrode kinetics (as discussed above). The charge between the reactants and the electrodes has to be overcome and this depends on the catalytic properties of the electrode materials. Similar to overpotential losses in fuel cells, the overpotential in an electrolyser is nonlinear with respect to the electric current passing through the cell, and can be calculated from the potential difference between the theoretical and actual cell potential.

The Tafel equation describes the rate of the hydrogen evolution reaction (HER) as well as the oxygen evolution reaction (OER), in terms of the current density, *j*:

$$\eta_{cathode} = 2.3\,\frac{RT}{\alpha F} log\,\frac{j}{j_0} \quad \ldots (1.79)$$

$$\eta_{anode} = 2.3\,\frac{RT}{(1-\alpha)F} log\,\frac{j}{j_0} \quad \ldots (1.80)$$

These equations can be simplified as:

$$log|j| = \log j_0 + \left|\frac{\eta}{\beta}\right| \quad \ldots (1.81)$$

where, j_0 is the exchange current density which may also be defined as the equal anodic and cathodic current densities at the equilibrium potentials, η is the applied overpotential (= E_{cell} - E^0) and β is the Tafel slope. It should be also noted that the kinetics of the hydrogen and oxygen evolution reactions vary significantly with catalyst material used. A typical Tafel plot involves graphing the overpotential as a function of the log of the current density (as shown in Figure 1.8).

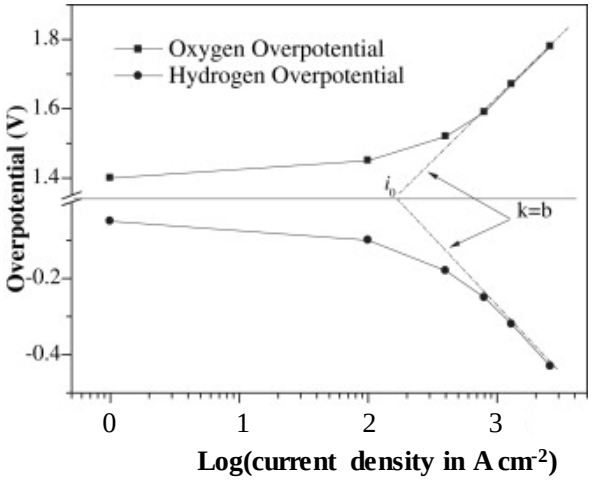

Figure 1.8. *Tafel plots for both hydrogen and oxygen evolution.*

The kinetics of the HER[25,26] and OER[27] have been previously discussed and explained in detail. In particular, the kinetics of the HER can be rapid, which means that the reaction can take place at many surfaces with only a small overpotential. However, the kinetics of the OER is sluggish and therefore requires a substantial overpotential. The higher overpotential in the case of the OER is the main cause of the relative inefficiency of water electrolyser cells.

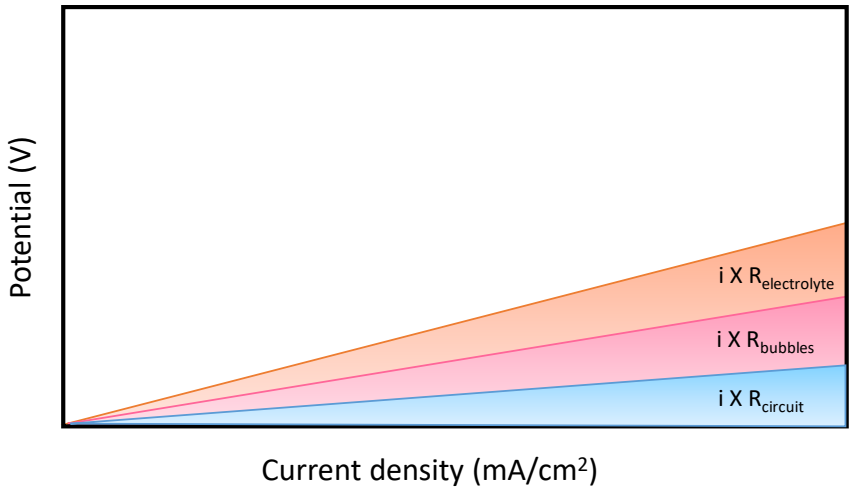

Figure 1.9. *Graph showing the contributions to cell voltage from the components of the cell resistance of an alkaline water electrolysis cell. Adapted from reference 24.*

B. Ohmic Loses

Water electrolysis processes generally produce heat due to the electrical resistances according to ohms law. The electrical resistance in water splitting is due to three major components: (i) resistances in the system circuits (depicted as $R_{circuit}$ in Figure 1.9); (ii) mass transport phenomena including ion migration in the electrolyte (depicted as $R_{electrolyte}$ in Figure 1.9) and, (iii) gas bubbles covering the electrode surfaces (depicted as $R_{bubbles}$ in

Figure 1.9). The resistance in the system circuits and mass transport phenomena are calculated as discussed in section 1.2.2.4.

The third component of electrical resistance arises from the formation of hydrogen and oxygen gas bubbles on the surfaces of the cathode and anode, respectively. Gas bubbles are non-conducting voids that increase resistance to ionic conductance between the electrodes. The greater the volume of bubbles present, the greater the resistance. This effect, which is referred to as "voidage", can be estimated based on the following theoretical equation:[28]

$$\kappa_g = \kappa\,(1 - 1.5f) \qquad \ldots (1.82)$$

where κ is the electrical conductivity of the gas-free electrolyte solution; f is the volume fraction of gas in the solution.

Gas bubbles also form on, and only detach from electrode surfaces when they grow big enough. This coverage of electrode surfaces by gas bubbles, which is known as the "bubble curtain effect", adds to the electrical resistance of the water electrolysis cell by reducing the contact surface area between the electrolyte and electrode. The bubble curtain blocks reactant access to the electrode and thereby increases the resistance of water electrolysis cells. The electrical resistance due to the bubble curtain effect on the electrode surface can be represented as:[29]

$$\rho = \rho_0\,(1 - \theta)^{-\frac{3}{2}} \qquad \ldots (1.83)$$

where, ρ_0 is the specific resistivity of the gas-free electrolyte solution and θ represents the percentage of the electrode surface covered by the bubbles.

1.4. Reactor Designs for Alkaline Fuel Cells (AFCs) and Alkaline Water Electrolysers (AWEs)

1.4.1 Alkaline Fuel Cell (AFC) Designs

As noted above, in an AFC, hydroxide ions (OH^-) are produced at the cathode and migrate to the anode where they react with hydrogen gas (H_2) to form water. Water molecules formed at the anode similarly diffuse to the cathode, where they react with oxygen to form OH^-, thereby closing the cycle. In the overall reaction, water and heat is produced, with 4-electrons (per mole of oxygen) generated. These electrons travel *via* the external circuit, producing the electrical current.

At least five different designs of AFC have been demonstrated. We will only summarise them here; further information on the principles and operation of each of these AFCs are presented elsewhere.[30] The different types of AFC include:

(i) "*Free liquid electrolyte cells*", in which a liquid electrolyte (e.g. 6 M KOH) is maintained between the electrodes. This liquid solution is typically circulated through the stack, to thereby allow for: (a) optimum thermal and water management control; (b) improved electrolyte sensitivity to CO_2 uptake and the formation of insoluble carbonates; (c) maintenance of a uniform OH^- concentration; and (d) minimum build-up of gas bubbles in the gap between the electrodes.[31] However, this class of electrolyte systems are prone to challenges such as electrolyte leakage (into the gas lines) and parasitic losses. The AFC cells that form the basis of the present proposal are of this type.

An alternative is the use of so-called “immobilized” electrolyte systems, which have been widely used in spacecraft applications.[32] Examples in this respect include:

(ii) “*Pore system cells*”, where liquid electrolyte is immobilized in a pore-system (e.g. electrolyte absorbed in a sheet of micro-porous asbestos; and

(iii) “*Matrix cells*”, where the electrolyte is fixed in the electrode matrix itself;

In some cells of this type, the electrode pair are each porous and disposed tightly against a thin porous separator in a so-called “*zero-gap*” arrangement. Another cell design involving a zero-gap design is:

(iv) *“Alkaline anion-exchange membrane (AAEM) cells”*, which employ a solid-state polymer membrane to transport hydroxide ions (OH^-) from the cathode to the anode in much the same way as proton exchange membranes transport protons in PEMFCs. Such cells offer several advantages over other AFCs, including:[33-35]

a. no carbonate precipitates are formed as there are no mobile cations,
b. no electrolyte “weeping” is observed which occurs in AFCs due to loss in hydrophobicity and mechanical strength of the electrodes,
c. reduced fuel crossover,
d. simplified water management (as water is produced at the anode and consumed at the cathode),
e. a larger selection of effective catalyst materials are available for use, and
f. potentially reduced corrosion due to the absence of a corrosive alkaline electrolyte.

All of the above designs are characterised by the presence of an inter-electrode diaphragm or ionomer between the electrodes. A design that sought to eliminate this element was:

(v) "*Falling film cells*", in which a liquid electrolyte is configured to flow between the electrodes from top to bottom in such a way that the hydrodynamic pressure of the electrolyte compensates the hydrostatic pressure drop thereby eliminating the need for an inter-electrode diaphragm.

1.4.2 Alkaline Water Electrolyser (AWE) Designs

One of aspects of alkaline water electrolysers (AWEs) still being researched is the separators/diaphragms used to separate the hydrogen and oxygen gases produced. Such a separator should demonstrate high ionic conductivity and low susceptibility to gas crossover, as well as long life. Three main classes of separators have been developed:[36]

(i) *Porous Spacers*. A porous spacer provides a physical barrier between electrodes and has an open structure, such as a plastic mesh. This type of separator may offer: (i) dimensional support for a fragile electrode, (ii) prevention of direct electrode-to-electrode contact (which could result in electrical shorting) and (iii) promotion of turbulent motion in a liquid electrolyte next to an electrode in order to enhance mass transfer.

(ii) *Microporous Spacers, also known as "Diaphragms"*. A second type of separator is microporous in nature. The liquid electrolyte fills the pores and is held in the pores by capillary forces. The presence of the electrolyte allows for ion transport across the diaphragm, however the capillary forces

prevent bubble formation in the pores. The diaphragm therefore allows transport of ions due to its hydraulic permeability, however gas transport across the diaphragm is generally blocked. Some of the separators in this class include porous ceramics (e.g. asbestos, glass frits) and porous polymers (e.g. porous polyvinyl chloride (PVC), polyolefins, and PTFE). In its initial years of development, asbestos-based membranes for AWEs were commercially popular. However, it was later found that these types of membrane are not very resistant to corrosion due to the strong alkaline electrolyte at higher temperatures and lead to severe adverse health effect. Therefore asbestos based membranes were gradually replaced by other materials.

(iii) *Ion-Exchange Membranes*. A third type of separator includes ion exchange membranes which divide the cell into two hydraulically separate compartments. The main function of an ion exchange membrane in an AWE is that it selectively allows the ions to pass through but not the gases. This maintains separation of the produced hydrogen and oxygen in the AWE with some limitation on the ionic transfer. It has been established that the benefits of using a membrane to separate hydrogen and oxygen outweigh the ohmic resistance brought by the ionomer. In past three decades, a wide range of membranes based on perfluorinated hydrocarbon backbones have been developed and introduced.[17]

In recent AWEs, development has focussed on 'zero-gap' electrode design to reduce the gap between electrodes. Traditional electrolysers of conventional designs used to have *solid* electrodes placed a few millimetres away from the separator which resulted in a high ohmic resistance as the electrolyte (between the electrodes and diaphragm) gets filled with gas bubbles during electrolysis. By contrast, zero-gap AWEs have the diaphragm and *porous*

electrodes closely packed in such a way that the gas bubbles evolve on the back of the electrode, thereby reducing the cell voltage in alkaline water electrolysis.[37]

In more recent work,[38] "membrane-less" electrolyzers based on flow-induced hydrogen and oxygen separation and increased mass transfer, have been investigated. This technology involves flowing liquid electrolyte through angled mesh flow-through electrodes, which then produces flow-induced separation of gases with low gas crossover.

1.5 Catalysts Used in Alkaline Fuel Cells (AFCs) and Alkaline Water Electrolysers (AWEs)

Catalysts are materials that accelerate chemical reactions without taking part in them, or being changed by them. Catalysts play a crucial role in determining the cost, efficiency and effectiveness of AFCs & AWEs. This is because of the significant amount and cost of the catalysts required to facilitate the half-reactions. In particular, the oxygen electrodes suffer from relatively slow ORR/OER kinetics. Therefore, research efforts in the field of AFC catalysts have focused on the ORR/OER.

Platinum (Pt)-based materials are known to offer the most active catalysts for ORR/OER in AFCs/AWEs. However, their use in large scale commercialization is largely restricted by their high cost, often poor durability, and the scarce availability of platinum group metals.[39] Therefore, development of high performing non-precious metal catalysts (NPMC) is increasingly of interest, both commercially and from a research viewpoint. The following section provides a review of precious metal catalysts followed by NPMCs used for AFCs/AWEs.

1.5.1 Catalysts of the Oxygen Reduction Reaction (ORR)

The most commonly used and active ORR catalysts are based on platinum (Pt). All of the Pt-group metals facilitate reduction of oxygen in alkaline media by a direct 4-electron process.[40-43] Numerous Pt-based alloys have been studied. Several of these exhibit higher catalytic activities[44] and greater stabilities[45] than Pt alone. Due to the high cost of Pt, several techniques have been developed to reduce the loadings of Pt metal in fuel cells.[46-50] Other noble metals have also been studied to replace Pt based catalysts, for example Pd-based catalysts[51-52] and Ag-based catalysts[53].

Various non-precious metal catalysts (NPMC) were developed to replace Pt-based catalysts in AFCs. In 1964, Jasinski[54] first introduced cobalt pthalocyanine as a catalyst for the ORR. After that, NPMC materials[55-58] including N-coordinated transition metal (TM) macromolecules, chalcogenides, oxynitrides, carbonitrides, and transition metal-doped conductive polymers, were evaluated as potential substitutes for Pt-based catalysts.

Among these, recent studies have shown that the use of metal-free carbon materials doped with heteroatoms (e.g. nitrogen (N), boron (B), phosphorus (P), sulphur (S), or selenium (Se)) also give excellent electrocatalytic performance for the ORR at near neutral pHs.[59-61] In addition to their low cost, they exhibit good durability and are environment friendly. It has been suggested that the presence of a C-N-M (M= Fe or Co or Ni) structure may be the origin of the high electrocatalytic activity of these NPMCs in the ORR.[39, 62]

The development of carbon materials doped with dual or multi heteroatoms has been also investigated as a means of improving the electrocatalytic performance of carbon materials. Various electrocatalysts such as vertically aligned B and N co-doped carbon nanotubes (VA-BCNT)[63], B- and N-isolated doped graphitic nanosheets (BNGS)[64], N,S dual-doped

mesoporous graphene[65], ternary (N, B, P)-doped carbon[66] have been reported as alternative, metal free catalyst for the ORR in alkaline medium.

Surface transfer doping, where electrons are exchanged between a semiconductor and dopants, have also been used for catalyst development for the ORR.[67-68] Composites based on heteroatom-doped carbon nanomaterials significantly improved activities and kinetics for the ORR. Some of these materials involve nitrogen enriched core-shell structured species comprising iron-based (Fe/Fe_3C) composite nanorods as the core and graphite carbon as the shell (N-Fe/Fe_3C@C),[69] 3D N-doped graphene aerogel- (GAs) supported Fe_3O_4 nanoparticles[70], or MnO-m-N-C nanocomposites.[71]

Various researchers have examined oxygen reduction on perovskites,[72-76] since their first development by Meadowcroft.[77] Spinels, ternary metal oxides with an AB_2O_4 structure, have been also used as an ORR catalyst. The nature of the B cations have been found to offer a potentially useful (and crucial) element for creating (and amplifying) an ability to act as useful catalysts.[78-79] A wide range of spinel catalysts have been reported previously.

1.5.2 Catalysts of the Oxygen Evolution Reaction (OER)

An activity trend of Ru>Ir>Rh>Pt>Au in electrochemically oxidised metals has been reported for catalysts of the OER at a current density of 5 mA cm^{-2}.[80] Trasatti et al. reported that IrO_2 and RuO_2 are among the most active catalysts to date.[81] In general, studies have relied on optimising synthesis condition and the substitution of Ru/Ir by cations (e.g. fluorine) for improving OER catalysts performance.[82]

Carbon catalysts doped with N atoms also enhanced the performance of the OER.[83-84] N-doped graphene/single wall carbon nanotubes (SWCNTs) have been used for the OER.[85] A study involving N-doped graphene, prepared by pyrolysis of graphene oxide with

polyaniline, has demonstrated higher OER electrocatalytic activity compared to Pt/C catalyst.[84] Zhang et al.[86] prepared highly ordered N-doped mesoporous carbon/graphene frameworks (N-MCF/N-MGF). The N-MGF also exhibited low or negligible mass transfer resistance, good durability and bifunctionality for the ORR and OER.

Dual or triple-doped carbon nanomaterials may also be used for the OER. N- and P-co-doped mesoporous nanocarbon (NPMC) foams have been developed by pyrolysis of polyaniline aerogels synthesised with phytic acid.[87] The NPMC showed good OER activities which was reflected in low onset potentials and higher currents than Pt/C catalyst. A recent study synthesised N, P, F tri-doped graphene catalysts which was used as an efficient tri-functional electrocatalyst for OER and HER for electrochemical water splitting.[88] Along the same lines, N, S co-doped graphitic sheets with stereoscopic holes (SHG)[89], P and N co-doped graphene framework (PNGF)[90] were developed for obtaining better OER performances.

Perovskite oxides have also received a lot of attention recently as OER electrocatalysts in alkaline media. This is largely due to their low cost, high efficiency and flexible structures. $Ba_{0.5}Sr_{0.5}Co_{0.8}F_{0.2}O_3$ (BSCF) has been reported to show high activity for OER greater than that of IrO_2.[91] Along similar lines, several other catalysts were successfully developed to enhance OER activity, such as $La_{0.7}(Ba_{0.5}Sr_{0.5})_{0.3}Co_{0.8}Fe_{0.2}O_{3-\delta}$,[92] $La_{0.6}Ca_{0.4}Mn_xCo_{1-x}O_{3-\delta}$,[93] $Ca_2Mn_2O_5$, [94] and $CaCu_3Fe_4O_{12}$.[95]

In the case of spinels, $NiCo_2O_4$ has received lot of attention recently as an efficient and low-potential electrocatalyst. Various $NiCo_2O_4$ nanostructures have been developed, such as nanowire arrays,[96] core-ring nanoplatelets,[97] hexagonal nanosheets,[98] nanorods,[99] and various $NiCo_2O_4$ nanocomposites with aerogels,[100] graphene[101] to improve OER. There has been considerable interest to study the performance of $NiCo_2O_4$ nanostructures towards ORR and OER.[102-103]

1.5.3 Catalysts of the Hydrogen Oxidation Reaction (HOR)

Researchers have historically mostly focused on studying and improving ORR catalysts in alkaline medium over the past several years. However, hydrogen HOR catalysts for alkaline fuel cells (AFCs) have received growing interest. The HOR activity of platinum group catalysts (PGMs) in alkaline medium is significantly lower than that in acidic medium.[104-105] Pt-based catalysts, normally used for the HOR and ORR reactions, have high costs and limited elemental availability which limits the commercialization of fuel cells.

Other HOR catalysts that have been developed include: Pt-coated Cu nanowires[106], Pt-Ru alloys[107], and Pt/Ru core/shell nanoparticles.[108] Raney Ni has been used as the anode catalyst in case of commercial AFCs.[109] Pt NWs (nanowires) were also alloyed with metals such as: Fe, Co, Ru, Cu, Au to decrease the platinum metal loading without compromising HOR electroactivity in alkaline medium.[110-111]

1.5.4 Catalysts of the Hydrogen Evolution Reaction (HER)

Several studies have demonstrated the HER activity of PGM-free catalysts in alkaline medium. For instance, Ni alloys such as NiMo nanoparticles (NP)[112] exhibited high HER activity in concentrated KOH electrolyte. Other studies also reported high HER activity under low alkaline conditions for NiO/Ni heterostructures on carbon nanotubes (CNTs)[113], cobalt-cobalt oxide/N-doped carbon nanotube hybrids (CoO_x@CN).[114]

Among transition metals (such as Fe, Co, Ni), widely used on electrolyser cathodes in alkaline medium[115-117], Ni-based catalysts are the most promising. Due to the low activity of

pure Ni, several studies in the past decades have focused on developing Ni-based alloys and high-surface-area Raney-Ni type electrodes.[117-118]

Heteroatom-doped graphitic carbon materials have been also tested for the HER.[119] Carbon materials with N, B, S, P dopants exhibit good HER activity due to the resulting large surface areas, better electrical conductivity and strong activation effects.[120]

1.6 Gas Diffusion Electrodes (GDEs) used for Alkaline Fuel Cells (AFCs) and Alkaline Water Electrolysers (AWEs)

Traditionally, the gas diffusion electrodes (GDEs) used in AFCs employ a polytetrafluroethylene (PTFE)-bonded, carbon-multilayer construction. This assembly has been designed to accommodate the various physical and chemical properties needed in AFCs. In a typical GDE there are at least two layers designed for gas diffusion and catalytic activity. Figure 1.10 depicts the cross-sectional arrangement of a typical modern-day gas diffusion electrode.

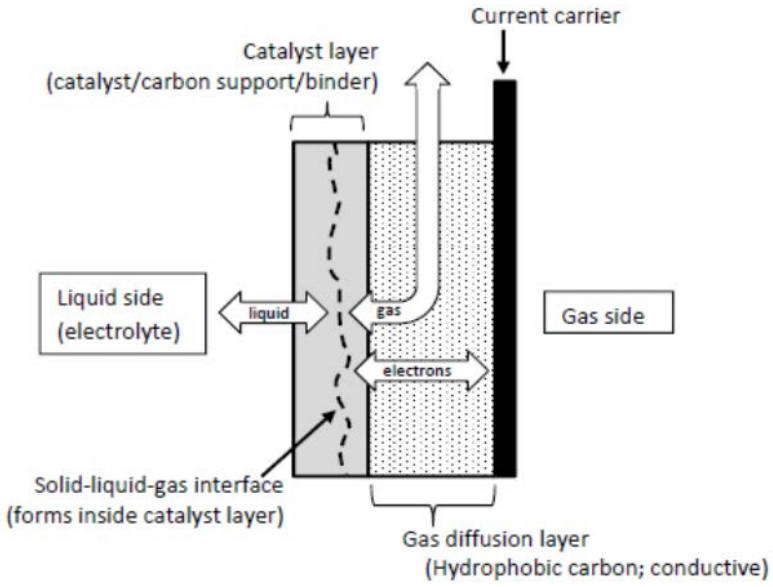

Figure 1.10. *Schematic cross-section of a typical modern-day gas diffusion electrode.*

The catalyst layer is typically made somewhat hydrophobic by the inclusion of materials such as 2 - 25% PTFE with carbon. This creates an environment for partial wetting of the carbon and electrocatalyst particles.[121] In the catalyst layer, a three-phase, interfacial solid-liquid-gas reaction zone is formed (shown as the dashed line in the Figure 1.10). Within this zone, the fuel, electrolyte, and carbon supported electrocatalyst are combined and controlled.

The gas diffusion layer of GDEs includes gas channels to feed or supply reactants to the catalyst layer. This diffusion layer has hitherto been made by combining a mixture that includes 25-60% PTFE with carbon in form of carbon black, acetylene black, and Vulcan XC-72R. The PTFE ensures hydrophobicity by blocking penetration of the aqueous electrolyte into the diffusion layer.

A current carrier layer is generally also present. This layer may require high gas permeability, structural and mechanical strength, corrosion resistance, and high conductivity. This layer has typically been created using metals, metal screens, teflonized metal plaques, carbon cloth, carbon paper, or other carbon materials.

The method of preparing such GDEs involves mixing carbon black with PTFE in order to achieve appropriate wettability and to maximise the activity and stability of the resulting electrode. One of the requirements of the catalytic layer is to generate high performance through the presence of a fine network of gas channels. These gas channels allow for diffusion of reactant gases, which need to penetrate to the catalytic sites; the absence of such networks can limit high current generation. However, creating and controlling the three phase boundary and the fine network of gas channels is not easy because the initial porous structure and chemical surface properties of the active carbon are difficult to control. When poorly achieved, lower electrochemical performance of electrodes is realised. The nature and morphology of initial porous structures are mainly dependant on the fabrication process.[122]

Other limitations of AFC GDEs include CO_2 poisoning, corrosion due to the alkaline electrolyte, weeping and flooding.

CO_2 is generally regarded as having a harmful effect on the performance of AFCs. This is due to the formation of carbonate species which cause degradation of the ion conductivity. CO_2 is highly soluble in strongly alkaline aqueous solutions like the 6 M KOH that is often used. It reacts to form carbonate species by following reaction:

$$CO_2 + 2OH^- \rightarrow CO_3^{2-} + H_2O \text{ and/or} \quad \ldots (1.84)$$

$$CO_2 + 2KOH \rightarrow K_2CO_3 + H_2O \quad \ldots (1.85)$$

Since the conductivity of CO_3^{2-} is lower than that of OH^-, the ionic resistance of the electrolyte increases. Moreover, carbonate formation often occurs in the pores of the electrode active layer, causing them to become blocked, and potentially also destroying the structure due to expansion of the precipitate.[123]

Corrosion of carbon and PTFE degradation caused by the strongly alkaline electrolyte are the main reasons behind the reduced electrochemical performance of AFC electrodes over time.[122] An increase in current density, temperature and OH^- concentration may further accelerate corrosion.

Carbon corrosion is even more of a problem when modern-day GDEs are used as the electrodes in water electrolyser cells. At the anode in such cells, the oxygen produced reacts with the carbon materials in the electrode, which may cause complete electrode structural failure.[124] For this reason, modern-day gas diffusion electrodes cannot be sustainably used as the anode in a water electrolyser cell.

Another effect that reduces the performance of GDEs in AFCs over time is known as weeping or flooding. This is caused when the fine network of channels in the GDE electrode structure becomes filled with the electrolyte, thereby destroying the 3-way solid-liquid-gas interface and limiting the access of the reactant gases to the reacting, catalytic sites in the

GDE. Liquid electrolyte then also passes through the electrode into the gas side. Modern-day gas diffusion electrodes typically flood and leak at very moderate overpressures (<0.1 bar)[125] on the liquid side of the electrode relative to the gas side (although GDEs that only leak at 0.2 bar have recently been claimed).[126]

1.7 Proposed Research

This section describes the foundation of the present study and provides a summary of the proposed contribution to the field. This contribution is intended to partially overcome some of the limitations that have existed in the field and fill in some of the research gaps that have been identified, at least in part.

1.7.1 Novel 'Gortex'-based ('ePTFE') Gas Diffusion Electrodes (GDEs) form the Key Topic of Study in this Work

In order to minimize the above mentioned problems associated with AFC GDEs, this thesis will not employ traditional GDEs of the type described above. Instead, it aims to study a new and potentially more effective type of GDE, comprising of a GORE-TEX® membrane, coated with the desired electrocatalyst and conductor.

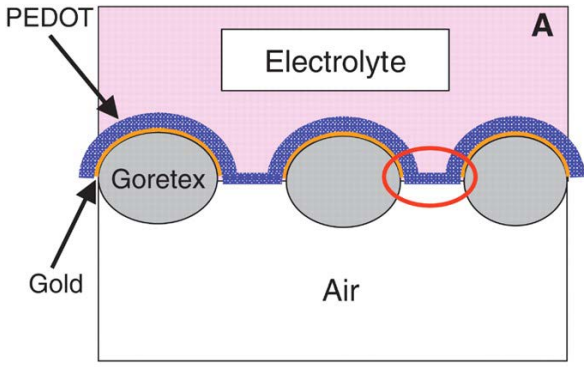

Figure 1.11. *Cross-sectional schematic of a three phase interface formed on a Gortex electrode coated with a PEDOT conducting polymer. Reproduced with permission from reference 58.*

In recent work, Winther-Jensen et.al.[58] described an air electrode based on a GORE-TEX® substrate coated with a conducting polymer, PEDOT, which reduced oxygen at rates comparable to those of Pt-catalyzed electrodes of similar geometry. The high rates were ascribed to an unusually high active surface area, created by the Gortex substrate. Pertinently, the electrode did not appear to be sensitive to CO_2 poisoning. This type of GDE also seemed to have a very well defined three phase interface, as shown in the Figure 1.11, suggesting it to be less prone to flooding.

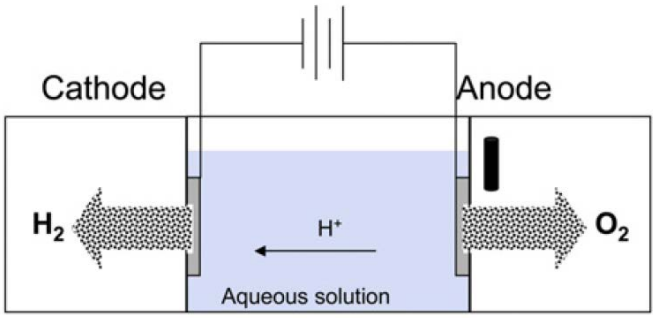

Figure 1.12. *Cross-sectional schematic of a water electrolyser utilising Pt-coated Gortex electrodes at both the anode and cathode, to directly separate the hydrogen and oxygen gases produced. Reproduced with permission from reference 127.*

In later work, the same authors showed that a similar, Gortex-based electrode design could be used at both the anode and cathode of a water electrolyser. The Gortex electrodes facilitated *direct separation* of the gases and improved efficiency in the water splitting reactions.[127] Figure 1.12 schematically depicts their cell. Upon the application of a suitable voltage to the electrodes, the cell generated oxygen at the anode and hydrogen at the cathode, both of which gases passed directly into the gas side of their respective gas diffusion electrodes without bubble formation in the aqueous electrolyte. That is, the cell split water in a *bubble-free* manner. The ability to directly separate the two gases, eliminated the need

for a diaphragm or ionomer between the electrodes and decreased gas cross-over, enhancing the coloumbic efficiency of the cell.

While water electrolysers with gas diffusion electrodes have been studied before over short periods of time,[17] they have always generated some gas bubbles in the water electrolyte. Moreover, the electrodes have always before leaked liquid electrolyte into the gas sides of the electrodes, creating a potential safety hazard (given the corrosive nature of the strongly alkaline electrolyte used).[128] For this reason, along with the fact that the oxygen produced at the anode rapidly corrodes carbon substrates, water electrolysers with gas diffusion electrodes have, to date, been widely considered to be practically un-feasible.

The above, *bubble-free* water-splitting cell employing Gortex-based gas diffusion electrodes appeared to be significant in multiple ways that did not appear to have been recognized by the authors at the time of the above work.

Firstly, Gortex comprises of chemically inert poly(tetrafluoroethylene) (PTFE). In fact, Gortex is a generic or brand name for a class of materials known as *expanded PTFE* (or ePTFE). The relevance of this is that Gortex is not susceptible to corrosion by oxygen gas that may be supplied (in an AFC) or generated (in an AWE). That is gas diffusion electrodes fabricated from Gortex can potentially be sustainably used in both alkaline fuel cells and alkaline electrolysers.

Moreover, the Gortex substrate can be chosen from a wide variety of commercially available membranes, each with its own, well-defined pore structure. To obtain a desired and distinct three phase liquid-gas interface at a particular differential pressure, Gortex with an optimum pore size can be selected by using Washburn's Equation:

$$P_c = \frac{2\gamma}{r} cos\phi \quad \ldots(1.86)$$

where, P_c is the desired capillary pressure, r is the pore radius, γ is the surface tension of the liquid, and ϕ is the contact angle of the liquid with the material.

Gortex substrates that remain leak-free up to very high overpressures of >4 bar on the liquid side relative to the gas side are routinely available. This presents the possibility of fabricating gas diffusion electrodes that are highly flood and leak-resistant, thereby potentially overcoming the problem of leaking that has generally be-devilled the use of gas diffusion electrodes in water electrolysers.

In other words, the used of a Gortex-based gas diffusion electrodes could potentially overcome all of the impediments observed in gas diffusion electrodes in AFCs and AWEs. Additionally, their large three-phase contact area are of great interest because they could potentially yield high power and operating current densities in AFCs and AWEs.

A further feature of interest was that all of the previously studied Gortex-based electrodes had employed very simple or unconventional catalysts, such as sputter-coated Pt (which is a relatively poor catalyst compared to other forms of Pt) and the conducting polymer poly(3,4-ethylenedioxythiophene (PEDOT) (which was, at best, not generally considered to be a catalyst at all). As such, an opening existed to study the incorporation of well-known, conventional, powerful catalysts in Gortex-based gas diffusion electrodes. This is a key objective of the present thesis.

1.7.2 Thesis Objective

This research aimed to study hydrogen-oxygen fuel cells and electrolysers for energy storage that employed gas diffusion electrodes based on Gortex membranes. It was anticipated that the use of Gortex-based gas diffusion electrodes would reduce or eliminate the above mentioned problems associated with the use of GDEs. The studies aimed to examine whether this was, in fact, the case and, if so, to what extent could the above problems be alleviated?

The project aimed to examine a range of available, high-performing catalysts and catalytic systems for their ability to efficiently and inexpensively catalyse the fuel cell and/or water electrolysis reactions. Additionally, the project sought to consider catalysts capable of facilitating both the forward (electrolyser) and the reverse (fuel cell) reactions, so as to thereby enable to fabrication of a reversible fuel cell – electrolyser, or a combination of a fuel and electrolyser that could achieve efficient energy storage.

The overall aim of the work was to identify, characterise, and quantify alkaline fuel cells and electrolysers utilizing Gortex-based gas diffusion electrodes.

1.7.3 Outline of the Thesis

Chapter 2 summarizes the chemicals, equipment, and electrochemical techniques used in this research. It also describes the various optimisation techniques that were used to prepare the Gortex-based GDEs.

Chapter 3 examines the fabrication, characterization, and operation of a novel GDE comprising of GE Prevail^{TM} ePTFE ('Gortex') membranes in desktop *alkaline fuel cells*

(AFCs). The catalysts tested included sputtered metals, as well as particulate catalytic coatings. The electrodes were characterised for hydrophobicity, conductivity, permeability, liquid entry pressure and active surface area.

Chapter 4 examines the utility of GDEs comprising of Gortex substrates layered with several well-known, conventional water-splitting catalysts in *alkaline water electrolysers* (AWEs). It describes how the use of Gortex based GDEs eliminated the formation of gas bubbles on the electrode interface and drastically improved the efficiency of AWEs. The effect of temperature was also studied for these Gortex-based AWEs to demonstrate the improvement of kinetic properties of the GDEs. The AWE cells were later combined with an equivalent alkaline fuel cell to evaluate round trip efficiency.

Chapter 5 analyses a range of commercially available precious metals and precious oxides as catalysts on Gortex substrates as GDEs for *alkaline fuel cells and electrolysers.* The effect of temperature was also studied as a means of improving the kinetic properties of the GDEs, as were Gortex-based *reversible alkaline fuel cell-electrolyzer*.

Chapter 6 analyses a range of commercially available perovskites and spinels as catalysts on Gortex substrates as GDEs for *alkaline fuel cells and electrolysers*. The effect of temperature was also studied as a means of improving the kinetic properties of the GDEs, as were Gortex-based *reversible alkaline fuel cell-electrolyzer*.

Chapter 7 examines the novel use of Gortex-based electrodes in AFCs for power generation from mixtures of hydrogen-enriched methane containing as little as 5% hydrogen. The performance of the AFCs was studied over a wide range of hydrogen to methane ratios and the extent of fuel utilization evaluated.

References:

1. Ludwig, B. S. http://www.h2data.de/ (accessed 29/12/2017).
2. McLean, G. F.; Niet, T.; Prince-Richard, S.; Djilali, N., *Int. J. Hydrogen Energy* **2002,** *27* (5), 507-526.
3. Kiros, Y.; Myrén, C.; Schwartz, S.; Sampathrajan, A.; Ramanathan, M., *Int. J. Hydrogen Energy* **1999,** *24* (6), 549-564.
4. Kiros, Y.; Schwartz, S., *J. Power Sources* **2000,** *87* (1–2), 101-105.
5. Al-Saleh, M. A.; Gültekin, S.; Al-Zakri, A. S.; Celiker, H., *J. Appl. Electrochem.* **1994,** *24* (6), 575-580.
6. Schulze, M.; Gülzow, E.; Steinhilber, G., *Appl. Surf. Sci.* **2001,** *179* (1–4), 251-256.
7. Gultekin, S.; Al-Saleh, M. A.; Al-Zakri, A. S.; Abbas, K. A. A., *Int. J. Hydrogen Energy* **1996,** *21* (6), 485-489.
8. Kenjo, T., *Bull. Chem. Soc. Jpn.* **1981,** *54* (9), 2553-2556.
9. Schultze, K.; Bartelt, H., *Int. J. Hydrogen Energy* **1992,** *17* (9), 711-718.
10. Al-Saleh, M. A.; Gultekin, S.; Al-Zakri, A. S.; Khan, A. A. A., *Int. J. Hydrogen Energy* **1996,** *21* (8), 657-661.
11. Ioroi, T.; Kitazawa, N.; Yasuda, K.; Yamamoto, Y.; Takenaka, H., *J. Electrochem. Soc.* **2000,** *147* (6), 2018-2022.
12. Hara, N.; Tsurumi, K.; Watanabe, M., *J. Electroanal. Chem.* **1996,** *413* (1), 81-88.
13. Shinagawa, T.; Garcia-Esparza, A. T.; Takanabe, K., **2015,** *5*, 13801.
14. Lavacchi, A.; Miller, H.; Vizza, F., Springer New York: New York, NY, 2013; pp 25-61.
15. Bidault, F.; Brett, D. J. L.; Middleton, P. H.; Brandon, N. P., *J. Power Sources* **2009,** *187* (1), 39-48.
16. Laursen, A. B.; Varela, A. S.; Dionigi, F.; Fanchiu, H.; Miller, C.; Trinhammer, O. L.; Rossmeisl, J.; Dahl, S., *J. Chem. Educ.* **2012,** *89* (12), 1595-1599.
17. Zeng, K.; Zhang, D., *Prog. Energy Combust. Sci.* **2010,** *36* (3), 307-326.

18. Oldham, K. B.; Myland, J. C., Academic Press: San Diego, 1994; pp 63-111.
19. Bertuccioli, L. C., A; Hart, D; Lehner, F; Madden, B; Standen, E., Fuel Cells and Hydrogen Joint Undertaking (EU): 2014.
20. Carmo, M.; Fritz, D. L.; Mergel, J.; Stolten, D., *Int. J. Hydrogen Energy* **2013,** *38* (12), 4901-4934.
21. Lehner, M.; Tichler, R.; Steinmüller, H.; Koppe, M., Springer International Publishing: Cham, 2014; pp 41-61.
22. Wang, H.; Lu, Z.; Xu, S.; Kong, D.; Cha, J. J.; Zheng, G.; Hsu, P.-C.; Yan, K.; Bradshaw, D.; Prinz, F. B.; Cui, Y., *Proceedings of the National Academy of Sciences of the United States of America* **2013,** *110* (49), 19701-19706.
23. Lyons, M.; Brandon, M., 2008; Vol. 3, p 1386-1424.
24. Phillips, R.; Dunnill, C., *RSC Advances* **2016,** *6* (102), 100643-100651.
25. Trasatti, S., Wiley-VCH Verlag GmbH: 2008; pp 1-85.
26. Breiter, M. W., John Wiley & Sons, Ltd: 2010.
27. L'Her, M., Wiley-VCH Verlag GmbH & Co. KGaA: 2007.
28. Schmidt, H.-J., Reports of Bunsen Society for Physical Cheistry **1995,** *99* (8), 999-999.
29. Hine, F.; Murakami, K., *J. Electrochem. Soc.* **1980,** *127* (2), 292-297.
30. Gülzow, E., *J. Power Sources* **1996,** *61* (1–2), 99-104.
31. Cifrain, M.; Kordesch, K. V., *J. Power Sources* **2004,** *127* (1–2), 234-242.
32. Markgraf, S.; Hörenz, M.; Schmiel, T.; Jehle, W.; Lucas, J.; Henn, N., *J. Power Sources* **2012,** *201*, 236-242.
33. Merle, G.; Wessling, M.; Nijmeijer, K., *J. Membr. Sci.* **2011,** *377* (1–2), 1-35.
34. Agel, E.; Bouet, J.; Fauvarque, J. F., *J. Power Sources* **2001,** *101* (2), 267-274.
35. Xu, T.; Liu, Z.; Yang, W., *J. Membr. Sci.* **2005,** *249* (1-2), 183-191.
36. Santos, D. M. F.; Sequeira, C. A. C.; Figueiredo, J. L., *Química Nova* **2013,** *36*, 1176-1193.
37. Manabe, A.; Kashiwase, M.; Hashimoto, T.; Hayashida, T.; Kato, A.; Hirao, K.; Shimomura, I.; Nagashima, I., *Electrochim. Acta* **2013,** *100* (Supplement C), 249-256.

38. Esposito, D. V., *Joule*.

39. Lefèvre, M.; Proietti, E.; Jaouen, F.; Dodelet, J. P., *Science* **2009,** *324* (5923), 71-74.

40. Anastasijević, N. A.; Dimitrijević, Z. M.; Adžić, R. R., *J. Electroanal. Chem.* **1986,** *199* (2), 351-364.

41. Pattabiraman, R., *Applied Catalysis A: General* **1997,** *153* (1-2), 9-20.

42. Yang, Y. F.; Zhou, Y. H.; Cha, C. S., *Electrochim. Acta* **1995,** *40* (16), 2579-2586.

43. Sepa, D. B.; Vojnovic, M. V.; Stojanovic, M.; Damjanovic, A., *J. Electroanal. Chem.* **1987,** *218* (1-2), 265-272.

44. Ramesh, K. V.; Shukla, A. K., *J. Power Sources* **1987,** *19* (4), 279-285.

45. Chatenet, M.; Aurousseau, M.; Durand, R.; Andolfatto, F., *J. Electrochem. Soc.* **2003,** *150* (3), D47-D55.

46. Giordano, N.; Passalacqua, E.; Alderucci, V.; Staiti, P.; Pino, L.; Mirzaian, H.; Taylor, E. J.; Wilemski, G., *Electrochim. Acta* **1991,** *36* (5-6), 1049-1055.

47. Lima, F. H. B.; Ticianelli, E. A., *Electrochim. Acta* **2004,** *49* (24), 4091-4099.

48. Vukmirovic, M. B.; Zhang, J.; Sasaki, K.; Nilekar, A. U.; Uribe, F.; Mavrikakis, M.; Adzic, R. R., *Electrochim. Acta* **2007,** *52* (6), 2257-2263.

49. Giordano, N.; Passalacqua, E.; Recupero, V.; Vivaldi, M.; Taylor, E. J.; Wilemski, G., *Electrochim. Acta* **1990,** *35* (9), 1411-1421.

50. Sasaki, K.; Mo, Y.; Wang, J. X.; Balasubramanian, M.; Uribe, F.; McBreen, J.; Adzic, R. R., *Electrochim. Acta* **2003,** *48* (25-26), 3841-3849.

51. Lima, F. H. B.; Zhang, J.; Shao, M. H.; Sasaki, K.; Vukmirovic, M. B.; Ticianelli, E. A.; Adzic, R. R., *J. Phys. Chem. C* **2007,** *111* (1), 404-410.

52. Erikson, H.; Sarapuu, A.; Solla-Gullón, J.; Tammeveski, K., *J. Electroanal. Chem.* **2016,** *780*, 327-336.

53. Lima, F. H. B.; de Castro, J. F. R.; Ticianelli, E. A., *J. Power Sources* **2006,** *161* (2), 806-812.

54. Jasinski, R., *Nature* **1964,** *201* (4925), 1212-1213.

55. Bashyam, R.; Zelenay, P., *Nature* **2006,** *443* (7107), 63-66.

56. Gong, K.; Yu, P.; Su, L.; Xiong, S.; Mao, L., *J. Phys. Chem. C* **2007,** *111* (5), 1882-1887.

57. Collman, J. P.; Devaraj, N. K.; Decréau, R. A.; Yang, Y.; Yan, Y.-L.; Ebina, W.; Eberspacher, T. A.; Chidsey, C. E. D., *Science* **2007,** *315* (5818), 1565-1568.

58. Winther-Jensen, B.; Winther-Jensen, O.; Forsyth, M.; MacFarlane, D. R., *Science* **2008,** *321* (5889), 671-674.

59. Sheng, Z. H.; Gao, H. L.; Bao, W. J.; Wang, F. B.; Xia, X. H., *J. Mater. Chem.* **2012,** *22* (2), 390-395.

60. Liu, Z.; Peng, F.; Wang, H.; Yu, H.; Tan, J.; Zhu, L., *Catal. Commun.* **2011,** *16* (1), 35-38.

61. Yang, Z.; Yao, Z.; Li, G.; Fang, G.; Nie, H.; Liu, Z.; Zhou, X.; Chen, X.; Huang, S., *ACS Nano* **2012,** *6* (1), 205-211.

62. Wu, G.; More, K. L.; Johnston, C. M.; Zelenay, P., *Science* **2011,** *332* (6028), 443-447.

63. Wang, S.; Iyyamperumal, E.; Roy, A.; Xue, Y.; Yu, D.; Dai, L., *Angew. Chem. Int. Ed.* **2011,** *50* (49), 11756-11760.

64. Wang, L.; Yu, P.; Zhao, L.; Tian, C.; Zhao, D.; Zhou, W.; Yin, J.; Wang, R.; Fu, H., *Sci. Rep.* **2014,** *4*.

65. Liang, J.; Jiao, Y.; Jaroniec, M.; Qiao, S. Z., *Angew. Chem. Int. Ed.* **2012,** *51* (46), 11496-11500.

66. Choi, C. H.; Park, S. H.; Woo, S. I., *ACS Nano* **2012,** *6* (8), 7084-7091.

67. Wang, S.; Yu, D.; Dai, L., *J. Am. Chem. Soc.* **2011,** *133* (14), 5182-5185.

68. Wang, S.; Yu, D.; Dai, L.; Chang, D. W.; Baek, J. B., *ACS Nano* **2011,** *5* (8), 6202-6209.

69. Wen, Z.; Ci, S.; Zhang, F.; Feng, X.; Cui, S.; Mao, S.; Luo, S.; He, Z.; Chen, J., *Adv. Mater.* **2012,** *24* (11), 1399-1404.

70. Wu, Z.-S.; Yang, S.; Sun, Y.; Parvez, K.; Feng, X.; Müllen, K., *J. Am. Chem. Soc.* **2012,** *134* (22), 9082-9085.

71. Tan, Y.; Xu, C.; Chen, G.; Fang, X.; Zheng, N.; Xie, Q., *Adv. Funct. Mater.* **2012,** *22* (21), 4584-4591.

72. van Buren, F. R.; Broers, G. H. J.; Boesveld, C.; Bouman, A. J., *J. Electroanal. Chem.* **1978,** *87* (3), 381-388.

73. Karlsson, G., *Electrochim. Acta* **1985,** *30* (11), 1555-1561.

74. Kahoul, A.; Hammouche, A.; Nâamoune, F.; Chartier, P.; Poillerat, G.; Koenig, J. F., *Mater. Res. Bull.* **2000,** *35* (12), 1955-1966.

75. El Baydi, M.; Tiwari, S. K.; Singh, R. N.; Rehspringer, J.-L.; Chartier, P.; Koenig, J. F.; Poillerat, G., *J. Solid State Chem.* **1995,** *116* (1), 157-169.

76. Hammouche, A.; Kahoul, A.; Sauer, D. U.; De Doncker, R. W., *J. of Power Sources* **2006,** *153* (2), 239-244.

77. Meadowcroft, D. B., *Nature* **1970,** *226* (5248), 847-848.

78. Ortiz, J.; Gautier, J. L., *J. Electroanal. Chem.* **1995,** *391* (1-2), 111-118.

79. Ríos, E.; Reyes, H.; Ortiz, J.; Gautier, J. L., *Electrochim. Acta* **2005,** *50* (13), 2705-2711.

80. Danilovic, N.; Subbaraman, R.; Chang, K.-C.; Chang, S. H.; Kang, Y. J.; Snyder, J.; Paulikas, A. P.; Strmcnik, D.; Kim, Y.-T.; Myers, D.; Stamenkovic, V. R.; Markovic, N. M., *J. Phys. Chem. Lett.* **2014,** *5* (14), 2474-2478.

81. Trasatti, S., *J Electroanal Chem Interfacial Electrochem.* **1980,** *111* (1), 125-131.

82. Kadakia, K.; Datta, M. K.; Jampani, P. H.; Park, S. K.; Kumta, P. N., *J. Power Sources* **2013,** *222*, 313-317.

83. Zhao, Y.; Nakamura, R.; Kamiya, K.; Nakanishi, S.; Hashimoto, K., *Nat. Commun.* **2013,** *4*, 2390.

84. Lin, Z.; Waller, G. H.; Liu, Y.; Liu, M.; Wong, C., *Carbon* **2013,** *53*, 130-136.

85. Tian, G.-L.; Zhao, M.-Q.; Yu, D.; Kong, X.-Y.; Huang, J.-Q.; Zhang, Q.; Wei, F., *Small* **2014,** *10* (11), 2251-2259.

86. Zhang, C.; Wang, B.; Shen, X.; Liu, J.; Kong, X.; Chuang, S. S. C.; Yang, D.; Dong, A.; Peng, Z., *Nano Energy* **2016,** *30*, 503-510.

87. Zhang, J.; Zhao, Z.; Xia, Z.; Dai, L., *Nat Nano* **2015,** *10* (5), 444-452.

88. Zhang, J.; Dai, L., *Angew. Chem. Int. Ed.* **2016,** *55* (42), 13296-13300.

89. Hu, C.; Dai, L., *Adv. Mater.* **2017,** *29* (9), 1604942-n/a.

90. Chai, G.-L.; Qiu, K.; Qiao, M.; Titirici, M.-M.; Shang, C.; Guo, Z., *Energy Environ. Sci* **2017,** *10* (5), 1186-1195.

91. Suntivich, J.; May, K. J.; Gasteiger, H. A.; Goodenough, J. B.; Shao-Horn, Y., *Science* **2011,** *334* (6061), 1383-1385.

92. Jung, J.-I.; Risch, M.; Park, S.; Kim, M. G.; Nam, G.; Jeong, H.-Y.; Shao-Horn, Y.; Cho, J., *Energy Environ. Sci* **2016,** *9* (1), 176-183.

93. Malkhandi, S.; Trinh, P.; Manohar, A. K.; Manivannan, A.; Balasubramanian, M.; Prakash, G. K. S.; Narayanan, S. R., *J. Phys. Chem. C* **2015,** *119* (15), 8004-8013.

94. Kim, J.; Yin, X.; Tsao, K.-C.; Fang, S.; Yang, H., *J. Am. Chem. Soc* **2014,** *136* (42), 14646-14649.

95. Yagi, S.; Yamada, I.; Tsukasaki, H.; Seno, A.; Murakami, M.; Fujii, H.; Chen, H.; Umezawa, N.; Abe, H.; Nishiyama, N.; Mori, S., **2015,** *6*, 8249.

96. Lu, B.; Cao, D.; Wang, P.; Wang, G.; Gao, Y., *Int. J. of Hydrogen Energy* **2011,** *36* (1), 72-78.

97. Cui, B.; Lin, H.; Li, J.-B.; Li, X.; Yang, J.; Tao, J., *Adv. Funct. Mater.* **2008,** *18* (9), 1440-1447.

98. Yang, J.; Li, J.; Lin, H.; Yang, X.; Tong, X.; Guo, G., *J. Appl. Electrochem.* **2006,** *36* (8), 945-950.

99. Garg, N.; Basu, M.; Upadhyaya, K.; Shivaprasad, S. M.; Ganguli, A. K., *RSC Advances* **2013,** *3* (46), 24328-24336.

100. Chien, H.-C.; Cheng, W.-Y.; Wang, Y.-H.; Wei, T.-Y.; Lu, S.-Y., *J. Mater. Chem.* **2011,** *21* (45), 18180-18182.

101. Srivastava, M.; Elias Uddin, M.; Singh, J.; Kim, N. H.; Lee, J. H., *J. Alloys Compd.* **2014,** *590*, 266-276.

102. Lee, D. U.; Kim, B. J.; Chen, Z., *J. Mater. Chem. A* **2013,** *1* (15), 4754-4762.

103. Prabu, M.; Ketpang, K.; Shanmugam, S., *Nanoscale* **2014,** *6* (6), 3173-3181.

104. Neyerlin, K. C.; Gu, W.; Jorne, J.; Gasteiger, H. A., *J. Electrochem. Soc.* **2007,** *154* (7), B631-B635.

105. Durst, J.; Siebel, A.; Simon, C.; Hasche, F.; Herranz, J.; Gasteiger, H. A., *Energy Environ. Sci* **2014,** *7* (7), 2255-2260.

106. Alia, S. M.; Pivovar, B. S.; Yan, Y., *J. Am. Chem. Soc.* **2013,** *135* (36), 13473-13478.

107. Wang, Y.; Wang, G.; Li, G.; Huang, B.; Pan, J.; Liu, Q.; Han, J.; Xiao, L.; Lu, J.; Zhuang, L., *Energy Environ. Sci* **2015,** *8* (1), 177-181.

108. Elbert, K.; Hu, J.; Ma, Z.; Zhang, Y.; Chen, G.; An, W.; Liu, P.; Isaacs, H. S.; Adzic, R. R.; Wang, J. X., *ACS Catalysis* **2015,** *5* (11), 6764-6772.

109. Jenseit, W.; Khalil, A.; Wendt, H., *J. Appl. Electrochem.* **1990,** *20* (6), 893-900.

110. Subbaraman, R.; Tripkovic, D.; Strmcnik, D.; Chang, K.-C.; Uchimura, M.; Paulikas, A. P.; Stamenkovic, V.; Markovic, N. M., *Science* **2011,** *334* (6060), 1256.

111. Scofield, M. E.; Zhou, Y.; Yue, S.; Wang, L.; Su, D.; Tong, X.; Vukmirovic, M. B.; Adzic, R. R.; Wong, S. S., *ACS Catalysis* **2016,** *6* (6), 3895-3908.

112. Wang, Z.-L.; Hao, X.-F.; Jiang, Z.; Sun, X.-P.; Xu, D.; Wang, J.; Zhong, H.-X.; Meng, F.-L.; Zhang, X.-B., *J. Am. Chem. Soc.* **2015,** *137* (48), 15070-15073.

113. Gong, M.; Zhou, W.; Tsai, M.-C.; Zhou, J.; Guan, M.; Lin, M.-C.; Zhang, B.; Hu, Y.; Wang, D.-Y.; Yang, J.; Pennycook, S. J.; Hwang, B.-J.; Dai, H., *Nat. Commun.* **2014,** *5*, 4695.

114. Jin, H.; Wang, J.; Su, D.; Wei, Z.; Pang, Z.; Wang, Y., *J. Am. Chem. Soc* **2015,** *137* (7), 2688-2694.

115. Danilovic, N.; Subbaraman, R.; Strmcnik, D.; Chang, K.-C.; Paulikas, A. P.; Stamenkovic, V. R.; Markovic, N. M., *Angew. Chem. Int. Ed.* **2012,** *51* (50), 12495-12498.

116. Nelson, A.; Fritz, K. E.; Honrao, S.; Hennig, R. G.; Robinson, R. D.; Suntivich, J., *J. Mater. Chem. A* **2016,** *4* (8), 2842-2848.

117. Safizadeh, F.; Ghali, E.; Houlachi, G., *Int. J. Hydrogen Energy* **2015,** *40* (1), 256-274.

118. Rosalbino, F.; Delsante, S.; Borzone, G.; Angelini, E., *Int. J. Hydrogen Energy* **2008,** *33* (22), 6696-6703.

119. Jiao, Y.; Zheng, Y.; Jaroniec, M.; Qiao, S. Z., *Chem. Soc. Rev* **2015,** *44* (8), 2060-2086.

120. Duan, J.; Chen, S.; Jaroniec, M.; Qiao, S. Z., *ACS Catalysis* **2015,** *5* (9), 5207-5234.

121. Tomantschger, K.; Kordesch, K. V., *J. of Power Sources* **1989,** *25* (3), 195-214.

122. Tomantschger, K.; Findlay, R.; Hanson, M.; Kordesch, K.; Srinivasan, S., *Journal of Power Sources* **1992,** *39* (1), 21-41.

123. Rolla, A.; Sadkowski, A.; Wild, J.; Zóltowski, P., *J. of Power Sources* **1980,** *5* (2), 189-196.

124. Pletcher, D.; Li, X., *Int. J. Hydrogen Energy* **2011,** *36* (23), 15089-15104.

125. Moussallem, I.; Jörissen, J.; Kunz, U.; Pinnow, S.; Turek, T., *J. Appl. Electrochem.* **2008,** *38* (9), 1177-1194.

126. Gulla, A. F.; Krasovic, J. L. WO2013037902, 2013.

127. Winther-Jensen, O.; Chatjaroenporn, K.; Winther-Jensen, B.; MacFarlane, D. R., *Int. J. Hydrogen Energy* **2012,** *37* (10), 8185-8189.

128. Kjartansdóttir, C. K.; Nielsen, L. P.; Møller, P., *Int. J. Hydrogen Energy* **2013,** *38* (20), 8221-8231.

CHAPTER 2

Experimental

2.1 Materials Used

All chemicals and reagents used in this research study are listed in Table 2.1.

Reagent Name	Grade/Batch	Supplier (Company)
Polypropylene backed Preveil™ expanded PTFE (ePTFE) membranes (also generically referred to as "*Gortex*" membranes)		General Electric Energy
Carbon black	Ketjenblack EC-600 JD	AkzoNobel
Carbon black <100 nm particle size		Sigma-Aldrich
Carbon glassy, spherical powder, 2-12 µm		Sigma-Aldrich
Polytetrafluoroethylene 60 wt% dispersed in water		Sigma-Aldrich
Iso-Propyl Alcohol		Chem-Supply
10% Pt on Vulcan XC 72		Premetek
20% Ir on Vulcan XC 72		Premetek
20% Pt-Pd (1:1) on Vulcan XC 72		Premetek
20% Pt-Ir (1:1) on Vulcan XC 72		Premetek
20% Pt-Ru (1:1) on Vulcan XC 72		Premetek
20% Pt-Ni (1:1) on Vulcan XC 72		Premetek
20% Pt-Co (1:1) on Vulcan XC 72		Premetek

Pt black Surface area: 45-52 m^2/g		Premetek
IrO_2 powder Surface area: 10-20 m^2/g		Premetek
Co_3O_4		SkySpring Nanomaterials
Mn_2O_3		SkySpring Nanomaterials
Nickel nanopowder/nanoparticles (20 nm)		SkySpring Nanomaterials
"Wet" Nickel nanoparticles (25 nm)		SkySpring Nanomaterials
Raney-Nickel, slurry in H_2O	W.R Grace and Co. Raney 4200	Sigma-Aldrich
$CoFe_2O_4$		Sigma-Aldrich
$BaTiO_3$		Sigma-Aldrich
$LiCoO_2$		Sigma-Aldrich
$La_{0.6}Sr_{0.4}Co_{0.2}Fe_{0.8}O_3$		American Elements
$LaNi_{0.6}Fe_{0.4}O_3$		American Elements
$Ba_{0.5}Sr_{0.5}Co_{0.2}Fe_{0.8}O_3$		American Elements
$La_{0.7}Ca_{0.3}CoO_3$		American Elements
$LaMnO_3$		American Elements
$La_{0.8}Sr_{0.2}MnO_3$		American Elements
$Co_{0.5}Ni_{0.5}Fe_2O_4$		American Elements
$Mn_{1.5}Co_{1.5}O_4$		American Elements
$NiFe_2O_4$		American Elements
$NiCo_2O_4$		American Elements
MoS_2 (99% metals basis)		Alfa Aesar
KOH (90% flakes)	Reagent grade	Sigma-Aldrich
5 wt% Liquion™ Nafion™		Ion Power
HCL 36% (w/v) solution in water	Analytical grade	Univar
Multi-walled nanotubes –COOH functionalized MWCNTs 95% <8nm		SkySpring Nanomaterials

Single-walled nanotubes –COOH functionalized SWCNTs 90%		SkySpring Nanomaterials
Sodium dodecyl sulphate		
Sodium Sulfate (Na_2SO_4) anhydrous		Sigma-Aldrich
Dihydrogen hexachloroplatinate (IV) $H_2PtCl_6.6H_2O$		Pressure Chemical
Sodium tetrachloropalladate (II) Na_2PdCl_4		Sigma-Aldrich
Ethylene Glycol anhydrous $HOCH_2CH_2OH$		Sigma-Aldrich
Polyvinypyrrolidone average mol wt 10,000 $(C_6H_9NO)_n$		Sigma-Aldrich
Potassium bromide KBr	FT-IR grade	Sigma-Aldrich
Potassium borohydride KBH_4		Sigma-Aldrich
L(+)-Ascorbic acid	Analytical reagent	VWR
Ruthenium (III) chloride hydrate $RuCl_3.3H_2O$ hygroscopic		Precious Metals Online
Cobalt(II) chloride hexahydrate $Cl_2Co.6H_2O$		Alfa Aesar
Nickel(II) chloride hexahydrate $Cl_2Ni.6H_2O$		Alfa Aesar
Potassium tetrachloroplatinate(II), K_2PtCl_4		Precious Metals Online
Sodium sulfate, anhydrous 99%, Na_2SO_4		Sigma-Aldrich
Ni mesh, 200 LPI		Precision Eforming LLC (Cortland, NY) (flat, non-woven)
Ni mesh, 200 LPI		Century Woven (Beijing) (woven)

Table 2.1: *Chemicals, Reagents and Materials used*

2.2 Physical Characterisation Techniques

2.2.1 Four Point Probe Conductivity Measurements

The sheet resistance of all fabricated electrodes were measured using a JANDEL RM3 four-point probe (Figure 2.1). This technique utilises four probes. The outer pair of probes supplies the current, while the inner pair measures the voltage. Through the use of four terminals, the impedance contribution of the wiring and contact resistance is eliminated (as compared to a two point probe, where the current and voltage are measured using a single wire). This increases the accuracy of this measurement.[1]

Figure 2.1: *JANDEL RM3 four-point probe instrument used for conductivity measurements.*

2.2.2 Thermo-Gravimetric Analysis

Thermogravimetric analysis (TGA) is a thermal analysis technique wherein changes in the mass of a sample in response to changes in temperature, are measured. A precision balance is used to monitor the changes in mass. An inert gas is used as the atmosphere in the sample chamber (furnace). The temperature profile (i.e. the heating rate) can be modified by the user, depending on the desired data and the material being tested. Changes in sample mass may be used to quantify water content and/or chemical functionalities in the material being tested.[2] TGA was done on the fabricated ePTFE membranes in air with a heating rate of 10 ^{o}C/min, from room temperature to 800 ^{o}C using a TA Instruments Q500 TGA (Figure 2.2).

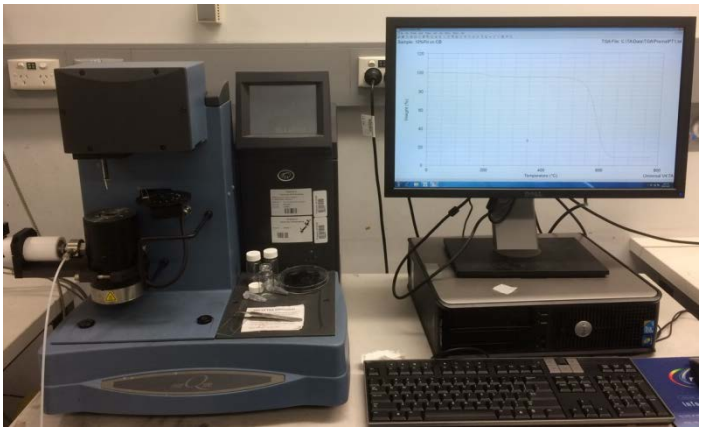

Figure 2.2: *TA Instruments Q500 TGA thermogravimetric Analysis Instrument.*

2.2.3 Contact Angle Goniometry

The contact angle (θ_c) is used to quantitatively measure the wettability of a solid surface. The most widely used method of contact angle measurement is called the "*sessile drop*" technique.[4] In this approach, the contact angle is measured through the liquid at the three-phase boundary where solid, liquid and gas interface each other (Figure 2.3).[3] The contact angle is strongly dependent on the interfacial tensions between the three phases involved. It can be mathematically expressed as:

$$\gamma_{SV} = \gamma_{SL} + \gamma_{LV}\cos(\theta) \qquad \ldots (2.1)$$

where, γ_{SV} is the interfacial tension between solid and vapour, γ_{SL} is the interfacial tension between solid and liquid, γ_{LV} is the interfacial tension between liquid and vapour, and $\theta$is the contact angle. A lower contact angle indicates a greater degree of hydrophilicity of the solid surface.

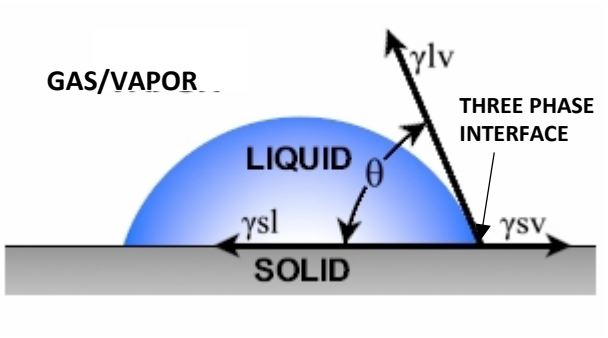

Figure 2.3: *A schematic of a contact angle measurement using the sessile drop technique, showing the three phase interface where solid, liquid, and gas/vapour interact (θ = contact angle).*[4]

A contact angle goniometer from Dataphysics OCA (Figure 2.4) was used to measure the static contact angle of water on the surface of the ePTFE electrodes used in the experiments.

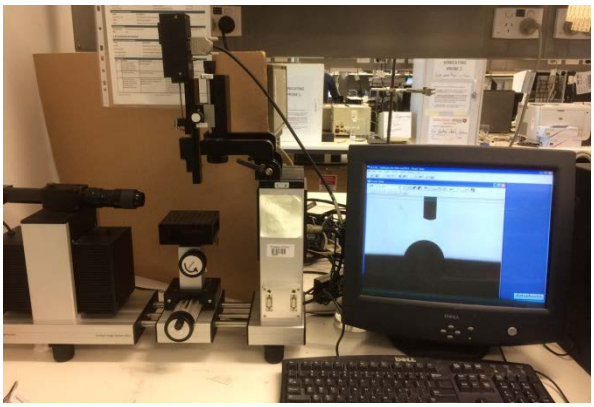

Figure 2.4: *Dataphysics OCA Contact Angle Goniometer.*

Another method of measuring the contact angle is the "*captive bubble*" technique.[21] In this approach, an air bubble is placed beneath and at the surface of the solid sample, which is immersed in water (see Figure 2.5, right image). This method has the advantage over the sessile drop technique that it ensures that the surface is in contact with a saturated gaseous atmosphere. It also reduces the chances of contamination of the solid-vapour interface from sources such as airborne oil droplets.

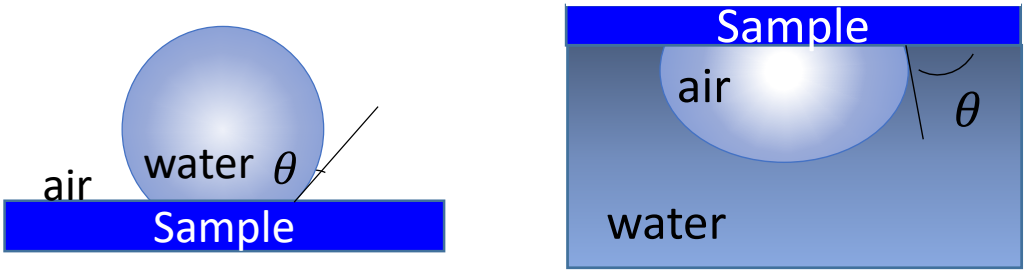

Figure 2.5: *Sessile Drop (Left image), and Captive Bubble technique (right image) for measuring contact angle.*[21]

2.2.4 Capillary-Flow Porometry

A CFP-1200-AEXL Capillary Flow Porometer from PMI Porous Materials Inc, integrated with PMI Capwin software, was used to measure the following properties of the fabricated electrodes (Figure 2.6):

(i) Mean Flow Pore pressure and Mean Flow Pore diameter,

(ii) Bubble Point pressure and Bubble Point pore diameter,

(iii) pore size distribution, and

(iv) Liquid Entry Pressure (LEP; also known colloquially as the "wetting pressure", or the "water entry pressure").

Bare and sputter-coated membranes were cut into 9 mm diameter circles. A wetting liquid, isopropanol (IPA), was used for tests (i)-(iii) above. Milli-Q water was used for test (iv). For tests (i)-(iii) above, the wetting liquid was, first, soaked into and allowed to fill the pores of the Gortex electrode. A non-reacting gas (compressed air) was then used to systematically displace the wetting liquid from the pores, with the pressure required in this respect plotted against the air flow rate through the membrane.[5]

Figure 2.6: *CFP-1200-AEXL Capillary Flow Porometer.*

2.2.5 Scanning Electron Microscopy (SEM)

A scanning electron microscope (SEM) uses a beam of electrons to image a sample's surface morphology and composition.[6] The beam is scanned in a raster pattern over the sample. Signals generated from the interaction between the electrons and the atoms of the sample are collected and used to produce an image.[7]

A JEOL7500 field emission scanning electron microscope (Figure 2.8) was used to study the morphology of the various ePTFE electrodes made. Typical settings involved an accelerating voltage of 3 kV, probe current of 8 mA and a working distance of 8 mm. Samples were adhered to the sample holder using double-sided, conductive carbon tape and silver paste.

2.2.6 Energy Dispersive X-ray Spectroscopy (EDS)

Energy Dispersive X-ray Spectroscopy (EDS) displays characteristic signals (x-rays) that are detected after electrons from the probe tip of an SEM have interacted with the specimen as shown in Figure 2.7.[8] EDS spectra were taken on a JEOL JSM-6490LA with 20 kV accelerating voltage, an emission current of 10 μA and a working distance of 10 mm.

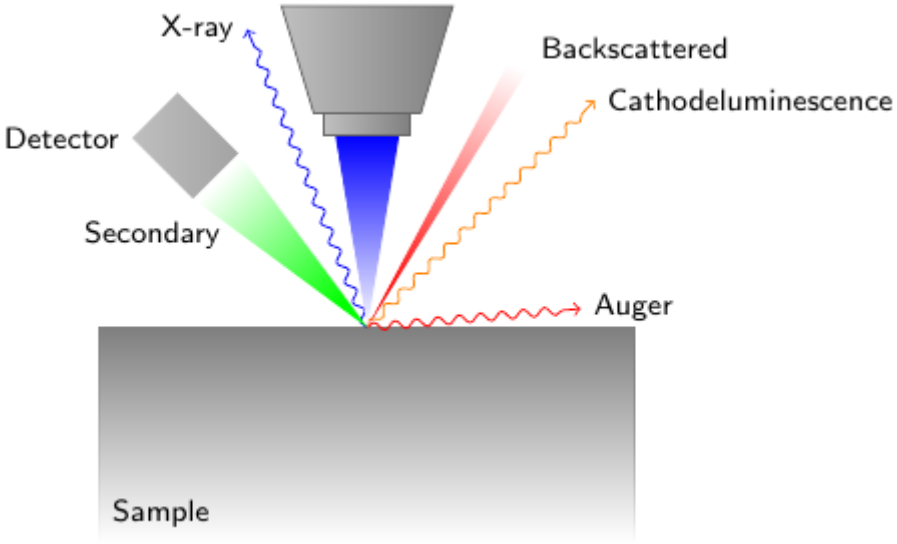

Figure 2.7: *SEM electron spatial resolution for EDS.*[8]

Figure 2.8: *JEOL7500 Field emission scanning electron microscope.*

2.2.7 X-ray Diffraction (XRD)

X-rays are electromagnetic waves with wavelengths ranging from 0.01 nm to a few nanometres, which is comparable to that of inter-planar spacing in crystals. This makes X-rays useful in structure determination.[9] In XRD, the X-ray beam is incident on a surface of a sample, interacting with the planes of atoms in the crystal. A portion of the X-ray beam will become scattered/diffracted due to interaction with the crystal structure. This diffracted beam

falls at a well-defined 2θ to the incident beam. The diffraction pattern for each element or compound is unique, which allows a user to assess the structure of different materials under investigation. XRD was carried out on a GBC MMA XRD (λ=1.54 Å) with the voltage and current at -40 kV and 25 mA, respectively (Figure 2.9).

Figure 2.9: *GBC MMA X-Ray Diffractometer.*

2.2.8 X-ray Photoelectron Spectroscopy (XPS)

XPS is a spectroscopic technique which is used to conduct quantitative elemental analysis of samples (Figure 2.10). The spectra is obtained when the sample under investigation is irradiated with a beam of X-rays which emits electrons from 1s, 2s, 2p, 3s, etc. orbitals.[10] A detector records the kinetic energy and the number of electrons emitted based on this interaction. The energy of the emitted electron is characteristic of the sample and the resulting spectra are therefore unique. This technique helps to characterise any change in surface chemistry between different samples.[10]

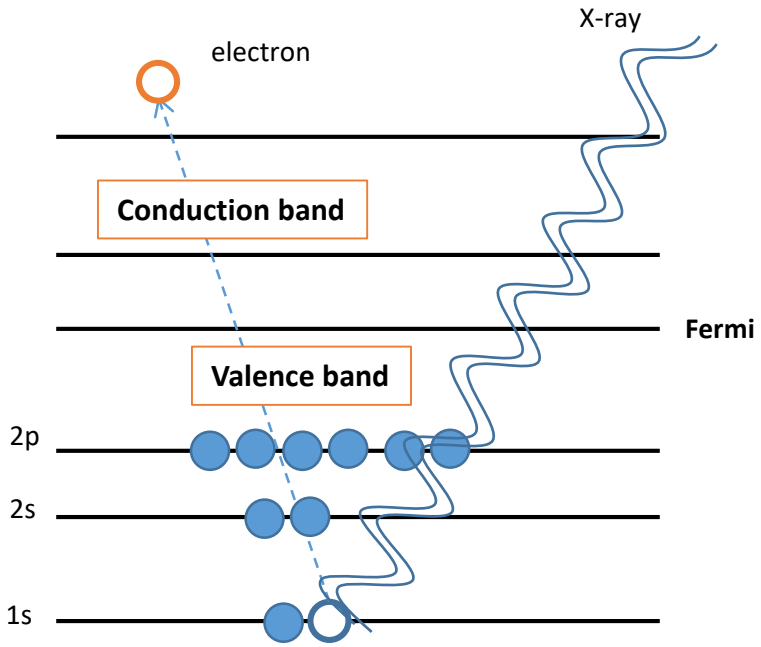

Figure 2.10: *Working principle of X-Ray photoelectron spectroscopy (XPS).*

XPS was performed on a PHOIBOS 100 hemispherical energy analyser from SPECS (Figure 2.11), using Al, K_α radiation (1486.6 eV) in fixed analyser transmission mode.

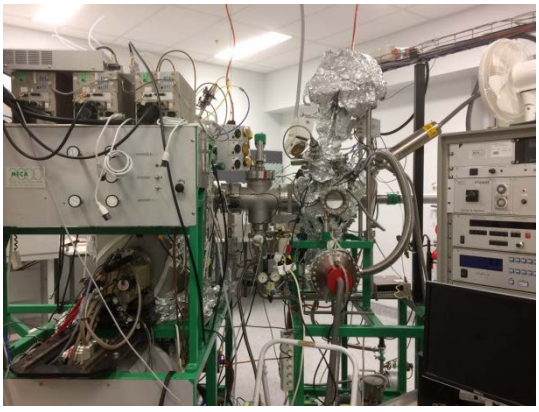

Figure 2.11: *PHOIBOS 100 hemispherical energy analyser used for X-Ray photoelectron spectroscopy.*

2.2.9 Sputter-Coating of Metals

Sputter-coating of metals was performed using an EDWARDS FTM6 Auto 306 (Figure 2.12). Pt, Au, and Ag nanolayers of different loadings were sputter-coated onto ePTFE under an argon atmosphere, using suitable targets. The rate of deposition of the metal coating was controlled by a thickness monitor, which employed a QCM crystal to determine the build-up of material within the sputter chamber.[11] Sputter conditions were 40 W for Pt and 30 W for Au and Ag, with argon flow maintained at ~100 kPa.

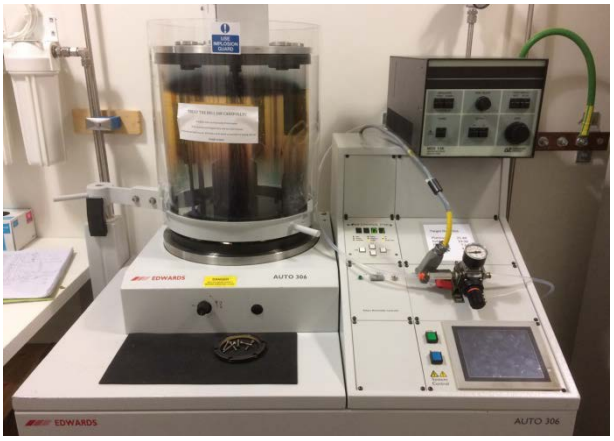

Figure 2.12: *EDWARDS FTM6 Auto 306 sputter Coater used for catalyst coating onto Gortex membranes.*

2.2.10 Probe Sonication

Catalyst slurries were dispersed using a Branson Digital Sonifier Model 102C at 450 W, 20 Hz in a pulsed method (2 s on, 1 s off).

2.2.11 Centrifugation

Centrifugation of synthesized carbon/CNT supported precious catalysts dispersed in solvents was performed using an Eppendorf centrifuge 5702 (Figure 2.13).

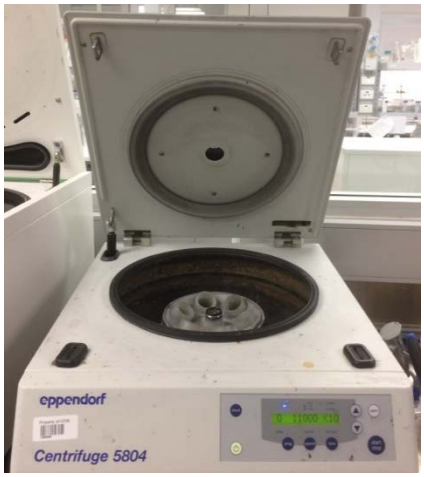

Figure 2.13: *Eppendorf 5702 centrifuge used in this study.*

2.2.12 Laser Engraving

A ULS PLS6MW laser engraver (Figure 2.14) was used for precision cutting of membranes, membrane laminates, metal meshes, and the like. The engraver employed a thermal separation process in which it produced a controlled heat entry that was optimum for fine cutting (as the laser beam can be focussed on a very small diameter for high precision). The high energy depth-in-focus point of the laser beam caused material to melt and evaporate.[12] Under an inert process gas (nitrogen), unwanted material was blown out. When cutting fine designs, the precision and dynamics of the cutting machine were of extreme importance.

Figure 2.14: *ULS PLS6MW Laser engraver used in this study.*

2.2.13 Transmission Electron Microscopy (TEM)

TEM is used to image samples at the nanometer scale by illuminating the sample with a beam of electrons, focussed by electromagnetic lenses, within a high vacuum, and detecting the electrons that are transmitted through the sample. Depending on the density of the material present, some of the electrons are scattered and disappear from the beam. At the bottom of the microscope, the unscattered electrons hit a fluorescent screen, which produces a shadow image of the specimen with its different parts displayed in varying thicknesses, according to their density.[13] The TEM used in this research was a JEOL JEM-2010 and is shown in Figure 2.15.

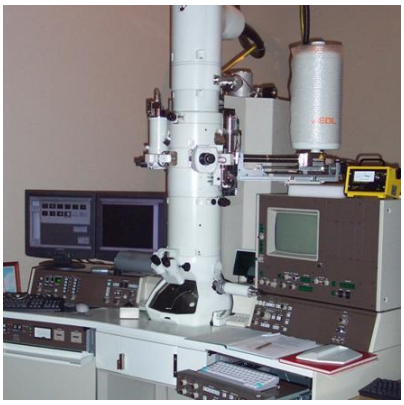

Figure 2.15: *JEOL JEM-2010 Transmission Electron Microscopy used in this study.*

2.2.14 Gas Chromatography (GC)

GC is a common analytical technique for detection of very small quantities of gases. This technique requires a mobile phase, a stationary phase and a detector. The mobile phase (=carrier gas) comprises of an inert gas, argon. The stationary phase consisted of a packed 6-foot column, which contained 5 Å Molecular Sieves. A thermal conductivity detector (TCD) was used and the column was kept at 90 ^{0}C; the detector was at 100 ^{0}C. The time taken for a particular gas product to travel through the column to the detector ("retention time") was

monitored. The stronger the interaction of the gas product with the stationary phase, the longer it takes to migrate through the column (=longer retention time).[14] Gas products were identified using calibration curves generated by injecting standard calibration gas mixture of CO and H_2 into the GC. The GC used in this research was a Simadzu GC-8A as shown in Figure 2.16.

Figure 2.16: *Simadzu GC-8A Gas Chromatograph used in this study.*

2.3 Electrochemical Analysis Techniques

All electrochemical analysis was done with a BioLogic potentiostat/galvanostat/EIS (SP-300) and EC – Lab V10.40 software. The hydrogen electrode was typically connected as the working electrode and the oxygen electrode as a combined auxiliary/reference electrode.

2.3.1 Open Circuit Voltage (OCV)

The open circuit voltage (OCV) of a cell is recorded when no current and no voltage is applied to the cell. During the period of OCV measurements, the cell reaches a thermodynamic equilibrium.

2.3.2 Linear Sweep Voltammetry

In linear sweep voltammetry (LSV), the voltage is scanned from a lower limit to an upper limit of a fixed potential range, as shown in Figure 2.17(a). The scan rate at which the potential changes is typically between 1 mV s^{-1} and 100 mV s^{-1}. When the voltage is swept between V_1 and V_2, the current is recorded. An example is shown in Figure 2.17 (a) where faradaic process is taking place. The current increases until it eventually reaches a peak before declining as shown in Figure 2.17(b). The initial rise in current is due to an increase in the conversion of reactants to products. Later the current peaks and starts decreasing due to a reduced concentration of reactants to the electrode surface.[15]

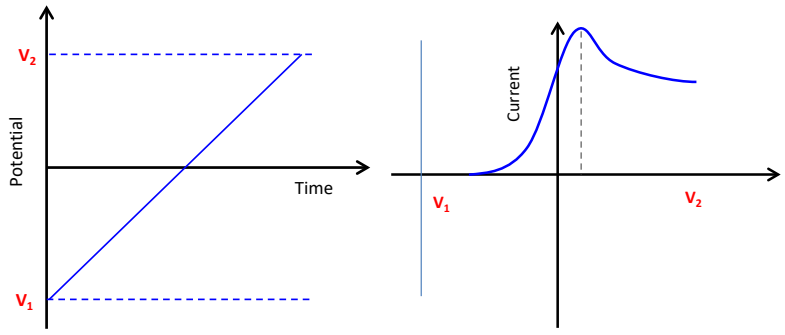

(a) (b)

Figure 2.17: *Linear sweep voltammetry*

The characteristics of a linear sweep voltammogram depend on:

- The rate of the electron transfer reaction(s)
- The chemical reactivity of the electroactive species
- The rate of the change in voltage (scan rate).

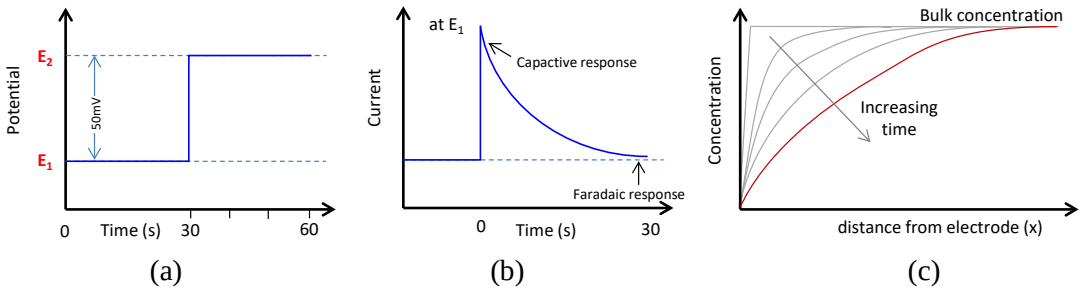

Figure 2.18: *The principles of chronoamperometry.*

2.3.2 Controlled Potential Techniques (Chronoamperometry)

Controlled-potential techniques involve the measurement of the current response to a step change in the applied potential. For example, as shown in Figure 2.18(a), a constant potential E_1 may be applied for a duration t_1 (30 s), and is then stepped up by 50 mV to E_2 and held again for 30 s. The current-time response is shown in Figure 2.18(b) and reflects the change in concentration gradient in the vicinity of the electrode surface. This process may be repeated for a range of potentials with the corresponding current measured over time, so that the technique is called chronoamperometry (CA).

Chronoamperometry is often used to measure the diffusion coefficients of electroactive species or the surface area of the working electrode. In the current-time (i-t) graph (Figure 2.17(b)), there will initially be an increase in current due to background and/or capacitive currents. The capacitive currents are caused by the electrode solution interface behaving like an electrical capacitor, storing charge. However, as soon as the reactant is converted to product, fresh reactants diffuse to the electrode surface. The surface concentration of the reactant species near the electrode therefore decreases and comes to depend solely on diffusion (in case of stagnant electrolyte solutions). As a result, the current, decreases until it reaches a constant value (as shown in Figures 2.17 (b) & (c)).[16] To record only the Faradaic current responses to an applied potential change, the last 90% of the 30 seconds step of the i-t graph is considered; this avoids capacitive currents altogether.

Chronoamperometry has been used instead of linear sweep voltammetry for the majority of the electrochemical characterisations in this work because the scan rate of LSVs are such that they are typically unable to separate capacitive currents from faradaic currents. The current-potential (I-V) graphs reported here have therefore involved chronoamperometry at different potentials (stepped at 50 mV), with each step being held for 30 s.

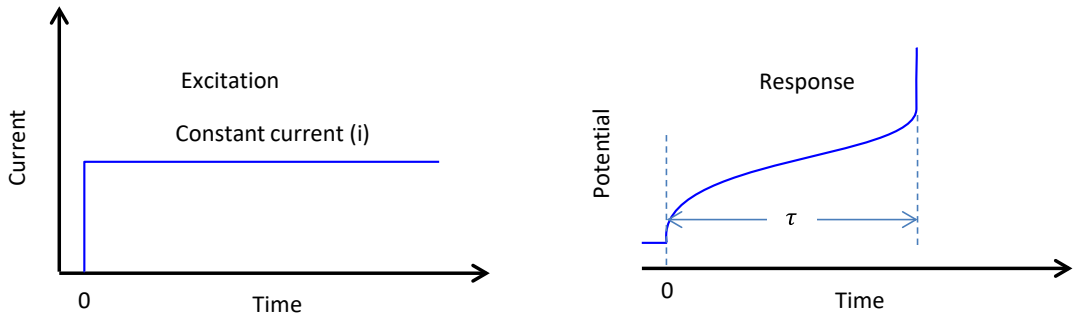

(a) (b)

Figure 2.19: *Controlled Current Technique*

2.3.3 Controlled Current Techniques (Chronopotentiometry)

In these techniques, current is controlled and the potential becomes the dependent variable (as opposed to voltammetric techniques, where the voltage is controlled and the current is monitored). These techniques are generally called chronopotentiometry (CP) as the potential is determined as a function of time.

Figure 2.19 illustrates chronopotentiometry. In Figure 2.19(a), a steady current (i) is applied to the electrode, which causes the reactant to be reduced at a constant rate. As a result, the potential of the electrode (Figure 2.19(b)) increases with time, as the concentration ratio (of reactant/product) changes at the electrode surface.[16]

2.3.4 Electrochemical Impedance Spectroscopy (EIS)

Electrochemical Impedance Spectroscopy was used to analyse the fundamental components and performance of the fuel cells and electrolysers studied in this work. EIS involves applying a small AC perturbation on top of an underlying DC bias to the cell. If the AC perturbation is applied in form of a sinusoidal potential superimposed on the DC potential, then the technique is called *Potentiostatic Electrochemical Impedance Spectroscopy* (PEIS). If the AC perturbation is applied in form of a sinusoidal current superimposed on the DC current, the technique is called *Galvanostatic Electrochemical Impedance Spectroscopy* (GEIS). The frequency of the AC perturbation is normally varied between 100 MHz and 10 kHz and the resulting system response is measured. The following equations describe the sinusoidal response of the system:

$$Z = Z_0 \frac{\cos(\omega t)}{\cos(\omega t - \varphi)} \tag{2.2}$$

$$Z = Z_0 \, (\cos \varphi + j \sin \varphi) \tag{2.3}$$

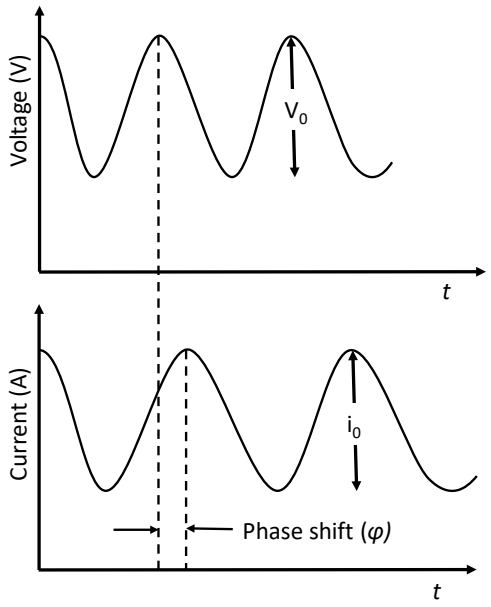

Figure 2.20: *Electrochemical Impedance Spectroscopy: the application of a sinusoidal voltage (top) generates a sinusoidal current response (bottom), showing a phase shift.*[17]

The expression Z is composed of a real ($Z = Z_0 \cos\varphi$) and an imaginary part ($Z = Z_0 \sin\varphi\, j$). If the real part is plotted on the X-axis and the imaginary part is plotted on the Y-axis of a chart, one gets a "Nyquist Plot" (Figure 2.21). The Y-axis is negative and each point on the Nyquist Plot is the impedance at one frequency. Low frequency data are on the right side of the plot and higher frequencies are on the left.

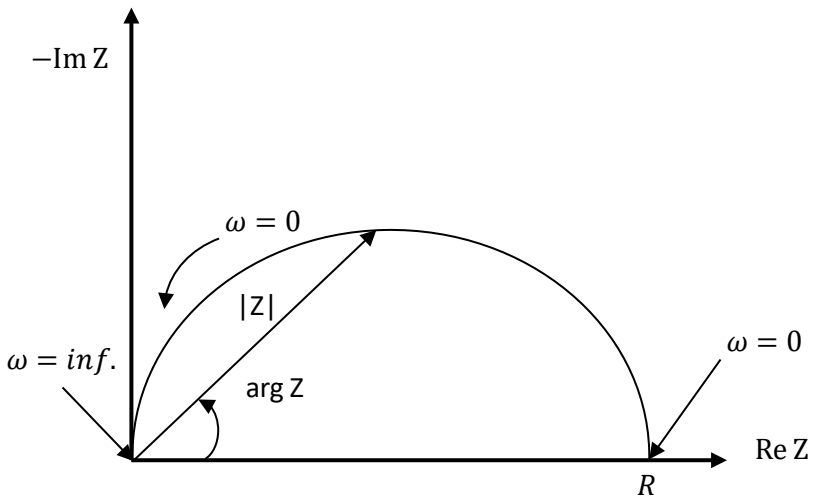

Figure 2.21: *Nyquist plot with impedance vector.*[18]

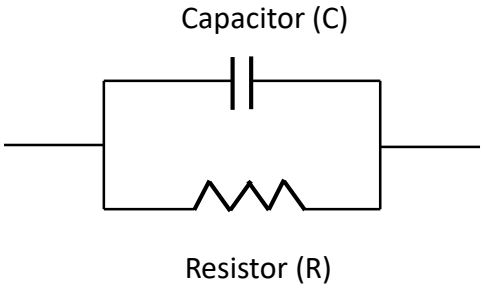

Figure 2.22: *Simple equivalent electric circuit with one time constant represented as a resistor (R) in parallel with a capacitor (C) .*[18]

On the Nyquist Plot in Figure 2.21, the impedance can be represented as a vector (arrow) of length |Z| is the angle between this vector and the X-axis, commonly called the "phase angle", is ϕ (=argZ). The semicircle arc in a Nyquist Plot (Figure 2.21) is characteristic of a

single “time constant”. This time constant is a physical representation of an electrochemical reaction interface (electrolye-catalyst-gas). So, the impedance behaviour of this interface can be fitted to an equivalent electric circuit (EEC) comprising of a resistor and a capacitor as shown in Figure 2.22. Electrochemical impedance plots often contain several semicircle arcs but usually, only a portion of a semicircle is seen. Thus, several time constants can be combined in series to obtain an EEC for a full impedance spectrum.

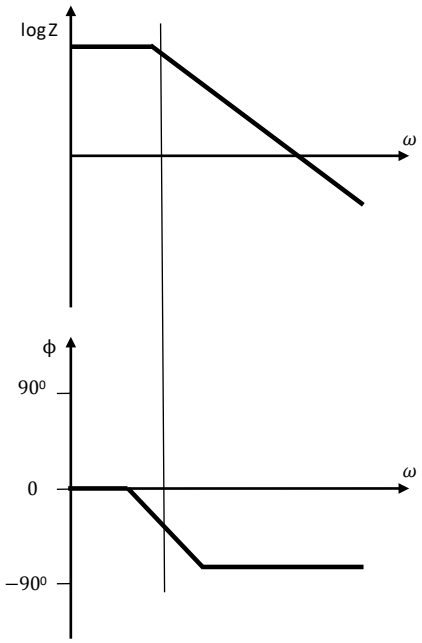

Figure 2.23: *Bode plot with one time constant* [18]

Nyquist plots have one major shortcoming. At any data point on the plot, there is no information about the frequency that was used to record that point. To provide information about the frequency, another popular presentation method is employed: the Bode plot, depicted in Figure 2.23. The impedance is plotted with log frequency on the X-axis and both the absolute values of the impedance ($|Z| = Z_0$) and the phase-shift on the Y-axis. The Bode plot in Figure 2.23 is representative of a single time constant shown in an EEC in Figure 2.22. As can be seen from Figure 2.23, at low frequencies, impedance sits at a constant magnitude as the current flows almost completely through the resistor and the phase angle

sits at 0°. At higher frequencies, the current divides to flow through the capacitor. Unlike the resistor, in which passage of current is always proportional to the magnitude of voltage, in the capacitor, the passage of current is proportional to the voltage gradient, which introduces a phase shift between voltage and current, as shown in Figure 2.20. In the case of a pure capacitor, the current is 90° out of phase with the voltage thereby forcing the phase angle to shift towards -90° in the Bode plot at lower frequencies.[18]

Typical EEC's used in this research involved combinations of ohmic resistances (R_Ω), interfacial charge transfer (in terms of charge transfer resistance, R_{ct}, and capacitance, expressed as double layer capacitance (C_{ct}) or a constant phase element (CPE), involving $Q_{CPE,ct}$, $n_{CPE,ct}$, and $C_{CPE,ct}$)[22], and diffusional resistance (Z_d). R_Ω is recognized as the sum of the contributions from uncompensated contact resistances and the ohmic resistance of cell components such as the electrolyte (electrolyte ionic resistivity) and electrodes. R_{ct} models the kinetics of the electrochemical reaction at the three phase interface (electrolyte-catalyst-gas). C_{ct} reflects the capacitive nature of the three phase interface and models the charge separation between ions and electrons across the interface; however, instead of using a pure capacitor C_{ct}, a CPE is used to fit the experimental data to improve the quality of fit. CPE behaviour is mainly due to surface inhomogeneity, roughness, reactivity, porosity, and current and potential distributions associated with the electrode geometry. The estimated values of CPE can help to estimate the double layer capacitance (C_{ct}) by following the Brug equation (shown below in equation 2.4) for normal distribution of time constants for electrode elements.

$$Q^{-1} = C_0^{1-\alpha}\left[R_\Omega^{-1} + R_{ct}^{-1}\right]^{\alpha} \qquad (2.4)$$

where, Q corresponds to $Q_{CPE,ct}$, α corresponds to $n_{CPE,ct}$ ($0 < n_{CPE,ct} \leq 1$), and C_0 corresponds to $C_{CPE,ct}$ in this research. Z_d models the mass transfer/diffusion resistance and tends to dominate overall impedance at lower frequencies.

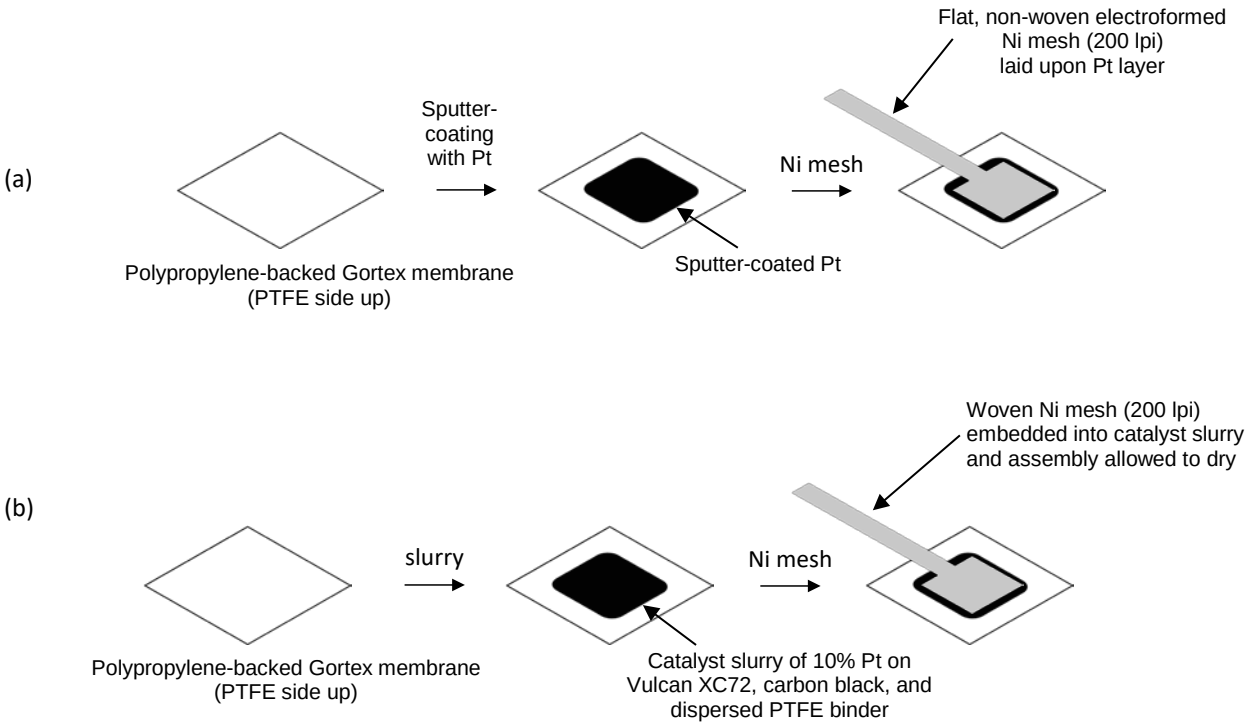

Figure 2.24: *Preparation of membrane/slurry/mesh assemblies*

2.4 Electrode Preparation

2.4.1 Catalyst Attachment Methods

In this research, two techniques, namely, sputter coating and slurry-coating, were employed to attach catalysts to the surface of Gortex membranes. The steps involved in preparing electrodes using the above-mentioned techniques are described below and depicted in Figure 2.24(a) (sputter-coating) and Figure 2.24(b) (slurry-coating).

Preparation of Gortex Sputter-Coated with Metals: Metal nanolayers of different loadings were sputter-coated onto the ePTFE membranes under Ar atmosphere, using suitable targets. The rate of deposition of the metal coating was controlled by a thickness monitor, which used a QCM crystal to determine the build-up of material within the sputter chamber. The catalyst loading was calculated from the thickness of the metal coating sputtered onto the

Gortex membrane. The current collector employed was an electroformed Ni mesh which had been laser cut to dimensions 12 mm x 12 mm for the square part with an attached 4 mm x 34 mm neck. The current collector was laid on top of the sputtered Gortex membrane (as shown in Figure 2.24(a)) and pushed down gently to ensure even contact with the membrane. During mounting of the electrodes (described in a following section), the current collector mesh became tightly wedged against the sputtered Gortex membrane.

Preparation of Gortex Slurry-Coated with Particulate Catalyst: A catalyst slurry was prepared by weighing out catalyst and carbon black (pre-treated with ascorbic acid) into a 20 mL vial, with isopropyl alcohol (IPA) and water then added. The resulting mixture was purged with N_2 for ca. 2 min to remove air. The mixture was then sheared using a homogeniser (IKA T25) with dispersing element (IKA S 25 N – 18 G) at 10,000 rpm for 5 min. PTFE aqueous dispersion was thereafter added dropwise, with continuous shearing. After all of the PTFE was added, shearing at 10,000 rpm was continued for another 5 min. Table 2.2 shows example compositions used in the preparation of catalyst slurries.

Catalyst	Catalyst (g)	Carbon black (g)	aq. 60% PTFE dispersion (mL)	Isopropyl alcohol (g)	H_2O (g)
10% Pt on Vulcan XC72	0.06	0.18	0.202	11.16	3.6
$NiCo_2O_4$	1.0	0.18	0.303	11.16	3.5

Table 2.2. *Example compositions of catalyst slurries.*

The resulting catalyst slurry was drop-cast onto the Teflon side of a Gortex membrane (24 mm x 24 mm membrane pieces) and spread out into a square shape measuring ca. 12 mm x 12 mm as shown in Figure 2.24(b). The current collector, which was a woven Ni mesh in the case of Gortex membranes coated with particulate catalysts, had been laser cut to dimensions 12 mm x 12 mm for the square part with an attached 4 mm x 34 mm neck. The

current collector was laid on top of the wet slurry (see Figure 2.24(b)) and pushed down gently using tweezers to embed the mesh in the wet catalyst layer. The resulting membrane/slurry/mesh assemblies were allowed to dry under ambient conditions.

Figure 2.25. *The double-roll mill used for compaction of electrodes.*

The dried membrane/slurry/mesh assemblies were compacted using a double-roll mill, having metal rollers shown in Figure 2.25. After drying, membrane/slurry/mesh assemblies were rolled three-times through a gap equal to 0.1 mm plus the mesh thickness. For the woven mesh used, a roller gap of 0.1 mm + 0.15 mm= 0.25 mm was set when using precious metal catalysts. As the membrane was ca. 0.2 mm thick, the membrane/slurry/mesh assemblies were compressed by 0.1 mm during rolling. However for perovskite and spinel catalysts, a roller gap of 0.35 mm was used as their respective loadings was more than that of precious metal catalysts.

After rolling, the membrane/slurry/mesh assemblies were weighed. These values were used, together with the weight of the membrane (pre-measured before applying catalyst) and the weight of the mesh (pre-measured before use) to calculate the catalyst loading.

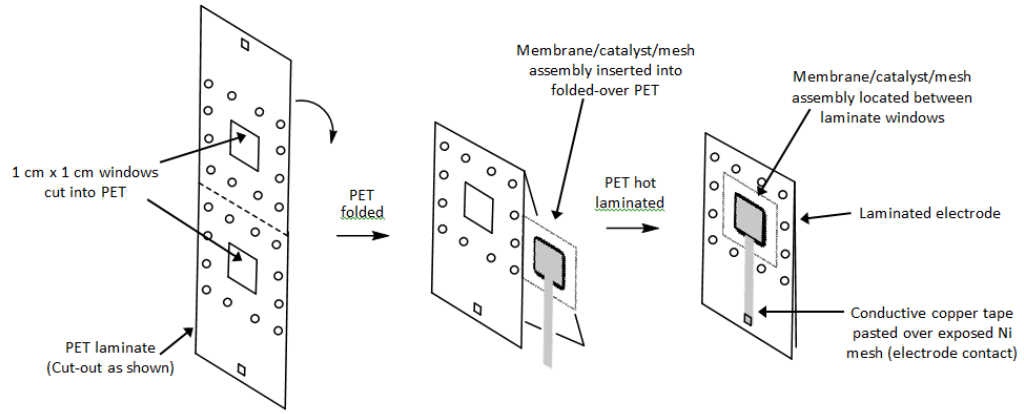

Figure 2.26: *Preparation of laminate-mounted ePTFE electrodes.*

2.4.2 Electrode Preparation: Mounting of Membrane/Catalyst/Mesh Assemblies

Electrodes were prepared by mounting the coated Gortex membranes, with associated Ni mesh, in a plastic (PET) laminate that became rigid after hot lamination by passing through a stationery-store laminator.

After weighing, each dried electrode was mounted in a pre-cut, folded PET laminate of the type available in stationery stores. The laminate was first cut, using a laser cutter, to the design depicted in Figure 2.26, which included a 1 cm x 1 cm window in each side.

Membranes that had been sputter-coated with Pt were, first, cut into 1.5 cm x 1.5 cm pieces and then laminated with a 200 line-per-inch (LPI) flat, electroformed Ni mesh current collector (as shown in Figure 2.24(a)), into the folded-over laminate such that the membrane/ mesh was located in the middle of the window (as depicted in Figure 2.26). The lamination process caused the Ni mesh, which was slightly larger than the laminate window, to become tightly wedged against the Pt coating on the Gortex membrane.

Membranes that had been coated with particulate catalyst, binder and Ni mesh, were placed inside the folded-over laminate such that the membrane/catalyst/mesh was located in the middle of the window (as depicted in Figure 2.26). The resulting assembly was then fixed in place by carefully passing it through a commercial hot laminator of the type found in stationery stores.

Using the above technique, both sides of the catalyst-coated Gortex membrane remained open and exposed, within the window in the laminate. A small piece of conductive copper tape was attached over the terminus of the neck of the Ni mesh as an electrode contact (see Figure 2.26). Photographs of the laser-cut laminate, Gortex membrane, current collector and copper tab are provided in Figure 2.27. The 10 mm x 10 mm window in the laminate limited the geometric area of the electrode to 1 cm^2.

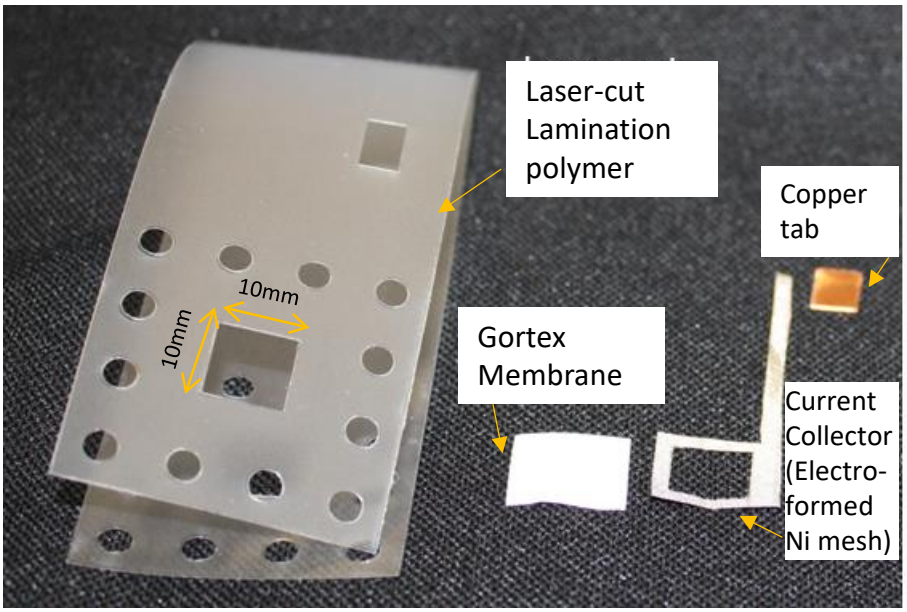

Figure 2.27: *Precision cut lamination polymer and other components needed for mounting membrane/catalyst/mesh assemblies into electrodes for the test cells.*

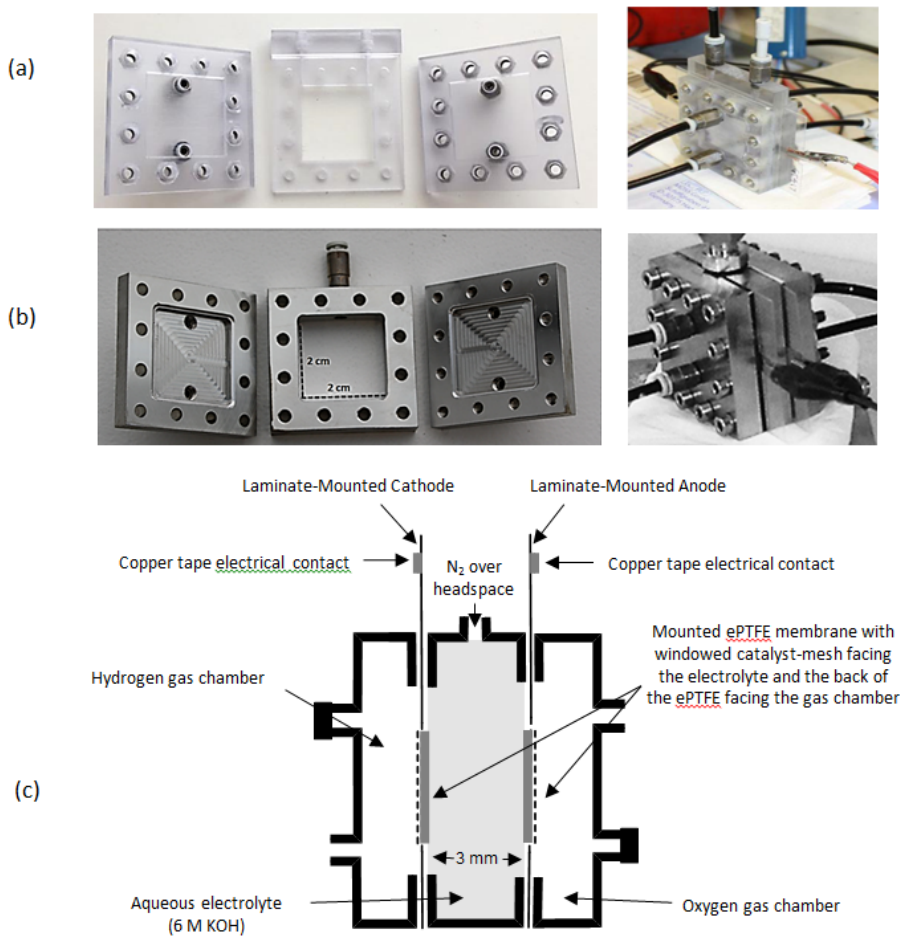

Figure 2.28: *Photographs and schematics of: (a) 3D-printed plastic cell (3 mm inter-electrode gap), (b) milled stainless steel cell (10 mm inter-electrode gap), and (c) cross-section of the test cell, showing the electrical and gas connections.*

2.5 Cell Construction and Assembly

Test cells were custom-built to match the dimensions of the laminated electrodes. Figure 2.28 depicts photographs and schematics of: (a) a 3D-printed plastic cell with a 3 mm inter-electrode gap, (b) a milled stainless steel cell having a 10 mm inter-electrode gap, and (c) a cross-section of a test cell, showing how the laminate-mounted electrodes were placed between the three components of the cell, which were then bolted together using twelve, edge-arrayed screws / bolts. Each of the laminate-mounted electrodes were placed in the cell

such that the exposed, windowed catalyst-mesh side faced the opposing electrode, while the uncoated back of the ePTFE faced outwards toward the respective gas chamber behind the electrode (Figure 2.28(c)). The gas connections were made using gas-tight fittings. The central cavity of the cell was filled with electrolyte, which was typically 6 M KOH.

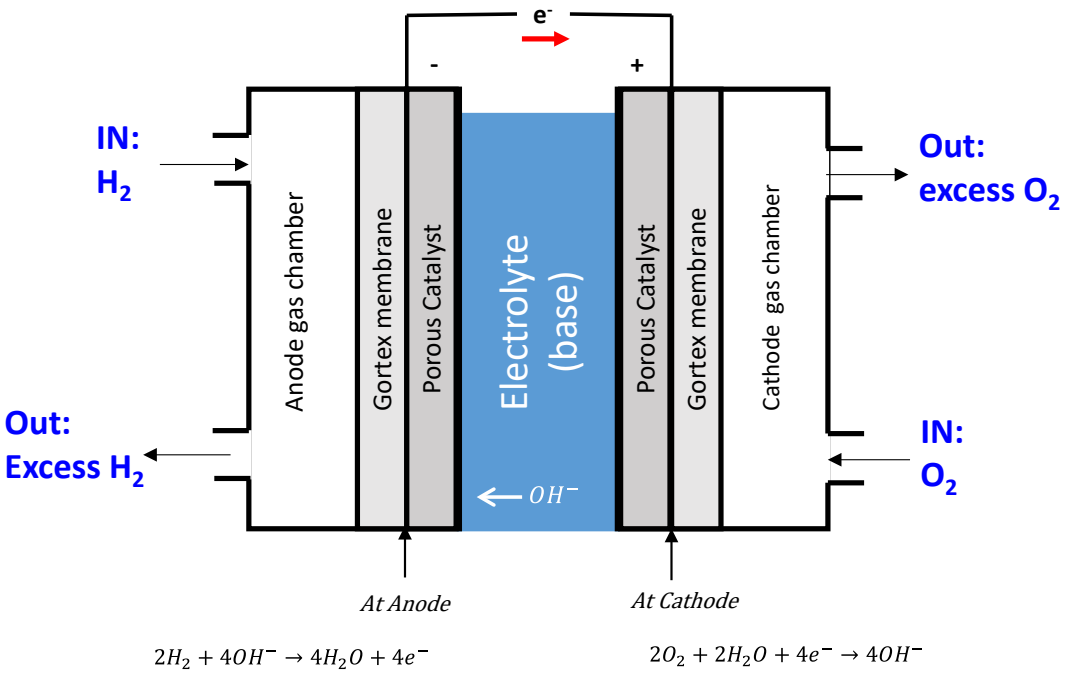

Figure 2.29: *Schematic illustration of a test cell when operating as an alkaline fuel cell.*

2.6 Cell Configuration in Fuel Cell Mode

A schematic illustration of a test cell during operation in fuel cell mode is shown in Figure 2.29. The catalyst layers of two mounted electrodes were located in facing dispositions in the cell, with the central cavity of the cell, between the electrodes, filled with aqueous electrolyte. In an alkaline fuel cell, the electrolyte was basic. Because of the water repellency properties of the Gortex-based electrodes (discussed in Chapter 3), aqueous electrolyte was unable to pass through the gas diffusion electrodes at atmospheric pressure and the central cavity of the cell was liquid-fast. Behind each electrode in the cell was a

sealed gas chamber, through which high-purity cylinder hydrogen (at the anode) and oxygen (at the cathode), both at atmospheric pressure, were slowly passed, as shown in Figure 2.29. As can be seen, both the chambers were continuously flushed with gases to avoid build-up of any gas pressure inside the chambers and consequently at the back of electrodes. Because of the porosity of the Gortex substrate, both of the gases, hydrogen and oxygen, were able to pass through the electrodes from the back, and access the catalyst layers that were facing each other across the electrolyte. No inter-electrode diaphragm was needed in the cell because of the relatively high bubble point pressures of the Gortex membranes. Stray gas bubbles that formed within the liquid electrolyte, at either of the electrodes, rose and exited the cell through the liquid headspace, which was filled with nitrogen at the start of each experiment but thereafter left open to the air.

During operation as an alkaline fuel cell, oxygen gas (O_2) is reduced to OH^- at the three phase interface (electrolyte-catalyst-gas) which migrates to anode where they react with hydrogen gas (H_2) to form water, thereby closing the cycle. In the overall reaction, water and heat is produced, with 4-electrons (per mole of oxygen) generated. These electrons travel via the external circuit, producing electrical current. Half reactions for oxygen reduction at cathode and simultaneous oxidation of hydrogen to water at anode is shown in Figure 2.20.

2.7 Cell Configuration in Electrolyser Mode

A schematic illustration of a test cell during operation as an alkaline electrolyzer is shown in Figure 2.30. In this case, hydrogen is formed at cathode when water is reduced and hydroxide ions migrate to the anode where they are oxidised to generate oxygen. Each of these gases exit through their respective mounted Gortex electrode into the sealed gas chamber behind; that is, hydrogen exits through the Gortex electrode at the cathode into the

cathode gas chamber and oxygen exits through the Gortex electrode at the anode into the anode gas chamber.

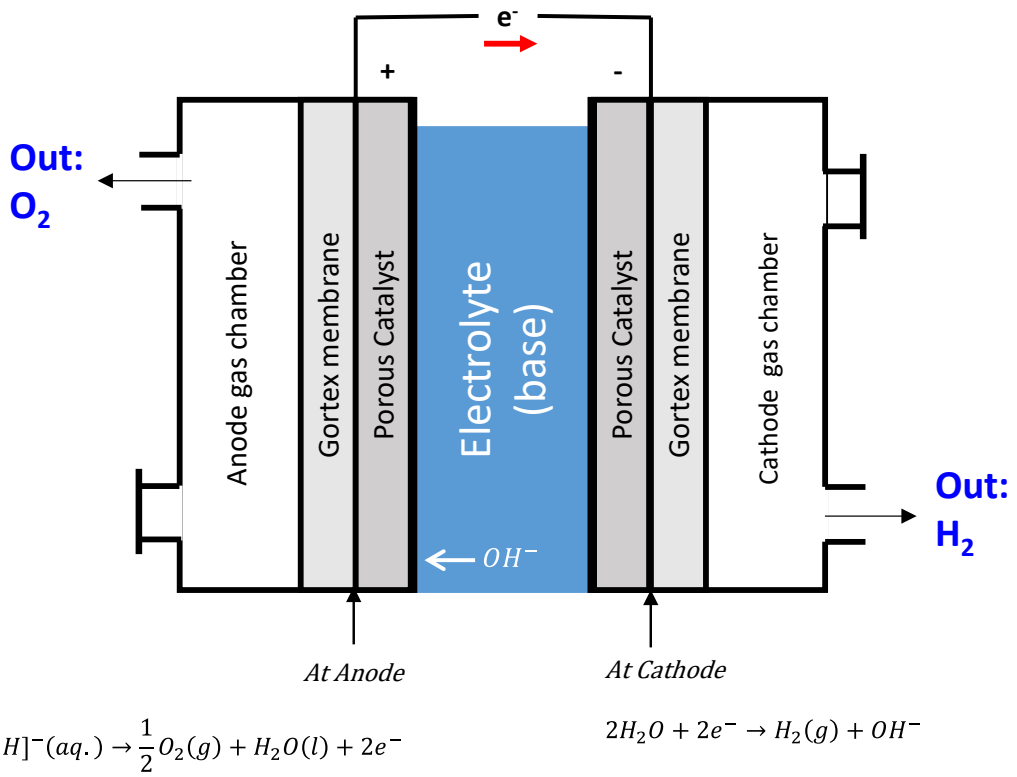

Figure 2.30: *Schematic illustration of a test cell when operating as an alkaline electrolyser.*

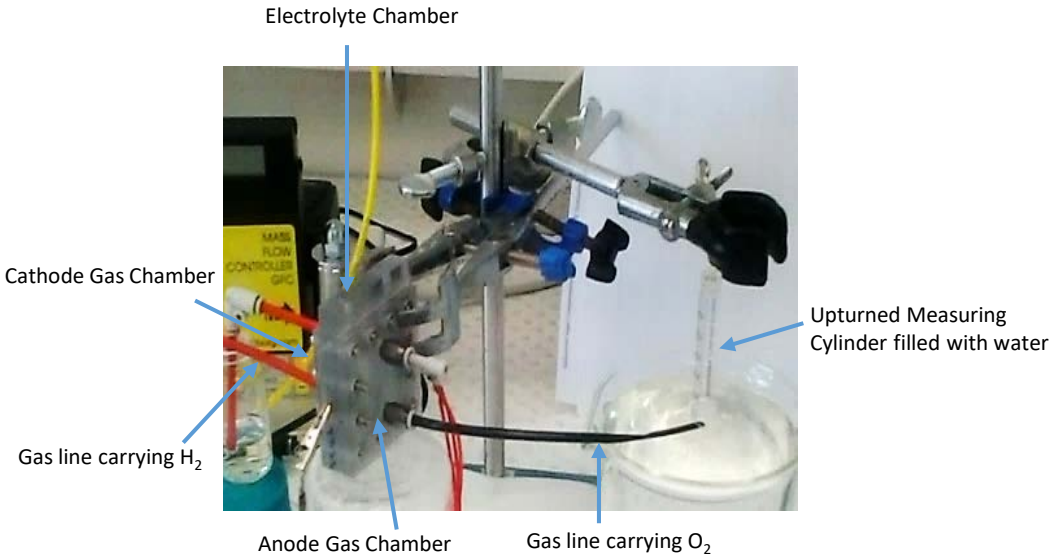

Figure 2.31: *Gas Collection: a test cell with a 3 mm inter-electrode gap, electrical and gas connections and upturned water-filled cylinder*

As reported previously,[20] the overwhelming majority of gas produced by Gortex electrodes pass through the Gortex, without forming bubbles in the aqueous electrolyte, into the gas chamber behind them. The gases were separately collected in upturned measuring cylinders filled with water, within a small water bath as shown in Figure 2.31. The volume of water displaced by the gases in the upturned measuring cylinders was recorded over a period of time at different current densities and compared to the volume of gas that would theoretically have been generated if all of the current was converted into gas. The "*Gas Collection Efficiency*" (GCE) is determined using equation 2.5 below.

$$\text{Gas Collection Efficiency (\%)} = \frac{\text{actual volume per unit time}}{\text{theoretical volume per unit time}} \times 100 \qquad (2.5)$$

2.8 Electrode Optimization

In order to obtain the best electrocatalytic activity from the electrodes in fuel cell mode, we optimized their fabrication. The following approaches were followed in optimizing the electrodes.

2.8.1 Nitrogen Purging

As mentioned earlier in section 2.4, catalyst slurries were prepared by mixing catalyst with carbon black. However, it came to our notice that a dry mixture of precious metal-based catalysts and carbon black would typically spark when IPA was added. Therefore, to avoid sparking, the dry mixture of catalysts with carbon black was purged with N_2 for ca. 2 min prior to addition of the IPA solvent.

Two fuel cells were employed to study the impact of N_2 purging during catalyst slurry formulation. One fuel cell comprised of an anode and cathode fabricated from slurry

(containing Pt black and carbon black) that was not purged with N_2, while the other fuel cell comprised of an anode and cathode fabricated from the same slurry as above but purged with N_2 during fabrication.

As can be seen in Figure 2.32, N_2 purging substantially improved fuel cell performance. The lower performance when N_2 purging was not employed, might be due to a loss of electrochemical active area from sintering of the finely dispersed noble metal nanoparticles on the surface of the carbon support. Following these studies, all electrodes were prepared using the N_2 purging technique.

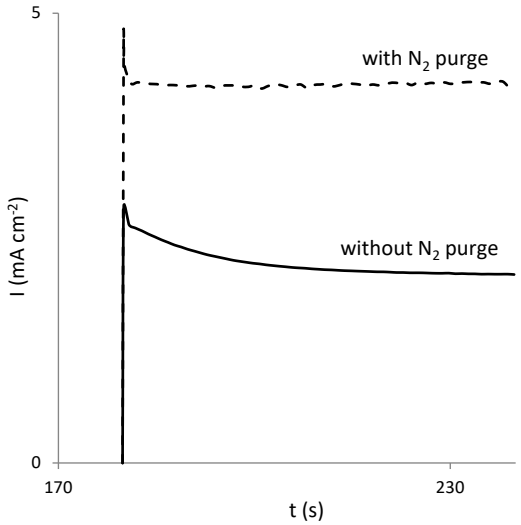

Figure 2.32: *Chronoamperometry at –0.2 V of alkaline fuel cells (6 M KOH) based on Pt black catalysts showing the benefit of N_2 purging of the dry mixture of Pt black and carbon black prior to IPA addition during catalyst slurry formulation.*

2.8.2 PTFE Fraction

The fraction of PTFE used in a catalyst slurry determines the hydrophobicity of the electrode produced and must strike a balance between access to the catalyst for reactant gases and the aqueous electrolyte. Catalyst slurries based on 20% Pt-Pd (1:1) on Vulcan XC 72 containing PTFE fractions of 0.4, 0.5 and 0.6 (vs. solids - i.e. carbon black + catalyst) were used to

prepare a total of 18 electrodes, from which three test fuel cells were prepared. Each fuel cell contained identical electrodes fabricated from 20% Pt-Pd (1:1) on Vulcan XC 72 as anode and cathode. Averaged currents at –0.2 V from triplicate fuel cell tests are presented in Figure 2.33. They show that a 0.5 PTFE fraction (vs. solids) to be optimum. Following these studies, all electrodes employed in this work were prepared with a 0.5 PTFE fraction.

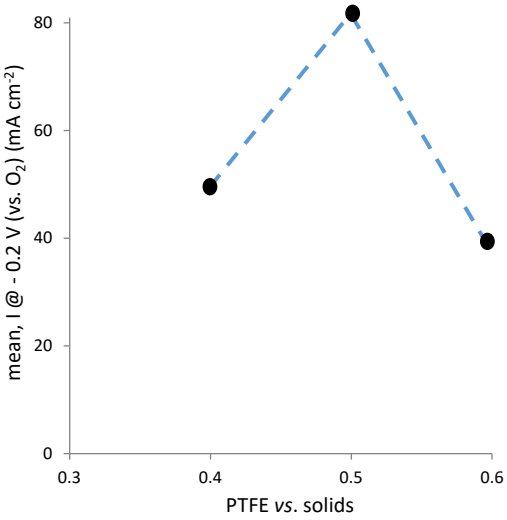

Figure 2.33: *Average current at –0.2 V vs. PTFE fraction from triplicate tests of fuel cells utilizing 20% Pt-Pd (1:1) on Vulcan XC 72. Electrolyte: 6 M KOH.*

2.8.3 Roller Gap

To obtain optimum electrical contact between the Ni meshes and the particulate catalysts, the dried membrane/catalyst/mesh assemblies were rolled following the procedure described in section 2.4. Electroformed Ni meshes were initially used as they have a negligible thickness when compared to the roller gap. We tested a narrow range of roller gaps (0.10, 0.13 and 0.15 mm).

To study the effect of the different roller gaps on membrane/catalyst/mesh assemblies, each of the above assemblies were incorporated as anode and cathode in a fuel cell. For each

roller gap, three fuel cells were tested, thereby giving a total of 9 fuel cells and 18 electrodes. All the electrodes were formulated with one catalyst, 20% Pt-Pd (1:1) on Vulcan XC 72. Figure 2.34 presents averaged currents at –0.2 V results for triplicate tests on the fuel cells. As can be seen, a roller gap of 0.10 mm delivered a higher mean current density, suggesting 0.10 mm to be an optimum roller gap.

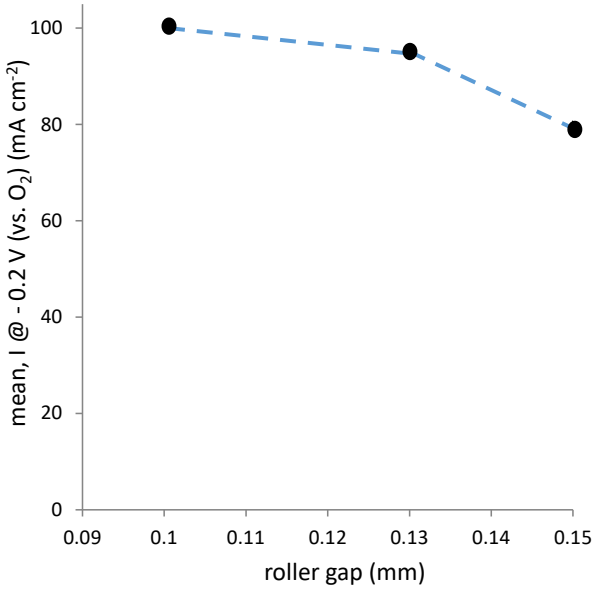

Figure 2.34: *Averaged current at –0.2 V vs. roller gap, from triplicate tests of fuel cells based on 20% Pt-Pd (1:1) on Vulcan XC 72, using electroformed Ni mesh. Electrolyte: 6 M KOH.*

2.8.4 Ohmic Resistance

Concerted efforts were made to minimise the ohmic resistance, as it contributes to the overall impedance of the cell. Two different current collectors, electroformed Ni mesh and woven Ni mesh, were tested. A single, longer electrical lead (from the potentiostat to the electrochemical cell) was also replaced with multiple, shorter electrical leads. The long electrical lead had been supplied with the potentiostat.

As in the above optimisation techniques, fuel cells were employed to study the effect of the different current collectors in the electrodes. All of the electrodes were formulated with one catalyst, 20% Pt-Pd (1:1) on Vulcan XC 72, but a first pair of electrodes (for fuel cell 1) employed the electroformed Ni mesh, while a second pair of electrodes (for fuel cell 2) employed the woven Ni mesh during fabrication. The effect of the supplied long leads was also compared to three short leads.

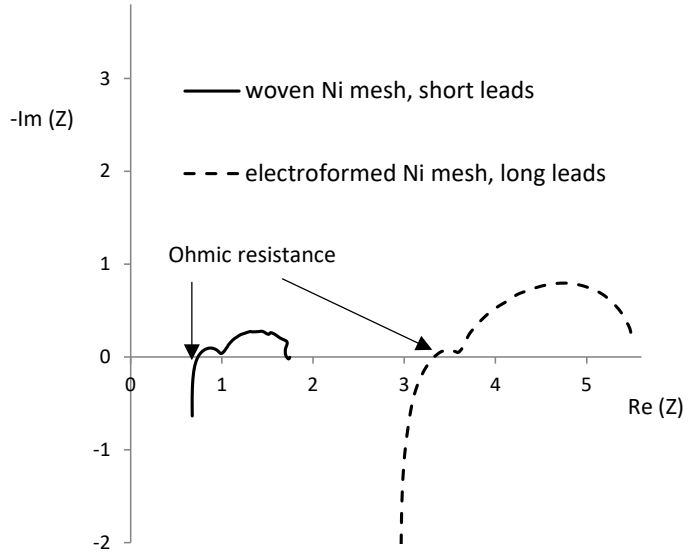

Figure 2.35: *Potentiostatic electrochemical impedance spectroscopy of fuel cells based on 20% Pt-Pd (1:1) on Vulcan XC 72 at –0.4 V, demonstrating lowered ohmic resistance when using woven Ni mesh and multiple, shorter electrical leads in place of electroformed Ni mesh and a single, longer electrical lead. Electrolyte: 6 M KOH*

The Ohmic resistance for each of the cells was compared by applying potentiostatic electrochemical impedance spectroscopy (PEIS) at -0.4V. Nyquist plots thus obtained are shown in Figure 2.35. The ohmic resistance is the intercept on the x-axis made by the real part (Z) of impedance. As can be seen, the impedance spectrum of fuel cell 2 is shifted to lower real impedance when compared to fuel cell 1, indicating lowered ohmic resistance. Thus, woven Ni meshes proved to be better current collectors and were used for subsequent

electrodes involving particulate catalysts. Weaved meshes could not be successfully used with the sputter-coated electrodes because they achieved poor contact with the deposited Pt.

2.8.5 Metal loading

High cost of catalysts hinders the large-scale application of alkaline fuel cells and electrolyzers. So, catalyst loadings were optimized with the intention of obtaining maximum performance at lower loadings.

A systematic experiment was performed to optimise metal loading in fuel cell electrodes based on 10% Pt on Vulcan XC 72. To optimize catalyst loading on electrodes used for anode, the cathode electrodes had relatively higher catalyst loadings so that the anode electrodes with lower catalyst loading would be the limiting factor. A similar approach was applied to optimize loading on cathode electrode as well.

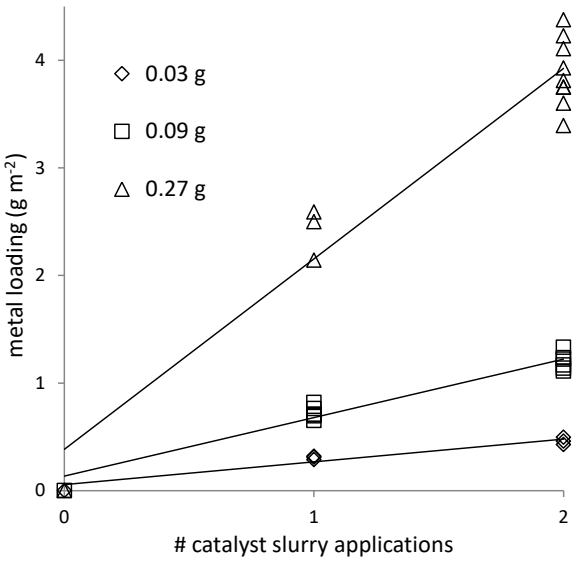

Figure 2.36: *Metal loading as a function of the mass of catalyst employed in the catalyst slurry and the number of applied layers.*

Catalyst loadings were either increased by putting more catalysts in the slurry or by applying 1 to 2 layers of the slurry onto the Gortex membrane. Figure 2.36 shows increase in metal loadings as a function of applied layers (1 or 2) and as a function of increase in amount of catalyst added in the slurry (0.03g, 0.09g and 0.27 g of 10% Pt on Vulcan XC 72).

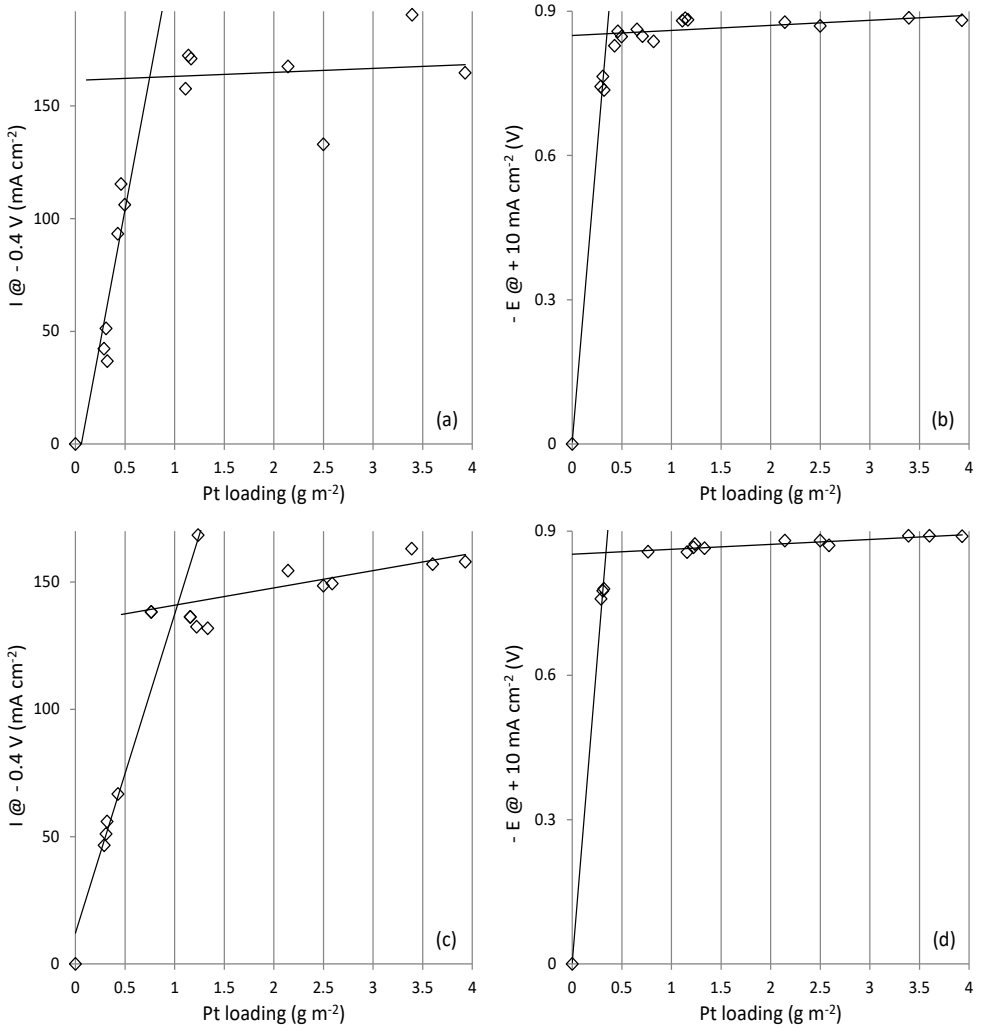

Figure 2.37: *Current at – 0.4 V and potential at + 10 mA cm^{-2} as functions of metal loading on the (a,b) Anode (H_2 electrode) and (c,d) Cathode (O_2 electrode), for fuel cells based on 10% Pt on Vulcan XC 72. Electrolyte: 6 M KOH*

Experiments which involved optimizing anode electrodes, had their catalyst loading ranging from 0 to 4 g m^{-2}, and corresponding cathodes had an average catalyst loading of 4.23 g m^{-2}. While, the experiments which involved optimizing cathode electrodes, had their catalyst loading ranging from 0 to 4 g m^{-2}, and corresponding anodes had an average catalyst loading of 3.8 g m^{-2}. Figure 2.37 shows the effect of metal loading within anode (H_2) and cathode (O_2) electrodes on fuel cell performance using two metrics, namely the current at –0.4 V and the potential at +10 mA cm^{-2}. For anode and cathode electrodes, fuel cell performance reached plateaus, beyond which the addition of further catalyst carried only modest benefit. For example, from Figure 2.36 (a) and (b) where catalyst loadings have been varied on anode, the current drawn at -0.4 V plateaus at around a catalyst loading of 0.8 g m^{-2} and voltage generated at 10 mA cm^{-2} plateaus at around a catalyst loading of 0.4 g m^{-2}. Similar results are seen from Figure 2.37 (c) and (d) when catalyst loadings are varied on cathode. The crossover point between rapidly improving and plateaued performance occurred at ca. 0.8 – 1.0 g m^{-2} metal loading according to the current at – 0.4 V, and at ca. 0.4 g m^{-2} metal loading according to the potential at + 10 mA cm^{-2}. This suggests that catalyst loadings on both anode and cathode, must be in between 0.4 g m^{-2} and 0.8 g m^{-2} to obtain optimum fuel cell performance. Such data is important when considering the technoeconomics of the technology.

2.9 Experimental Protocol

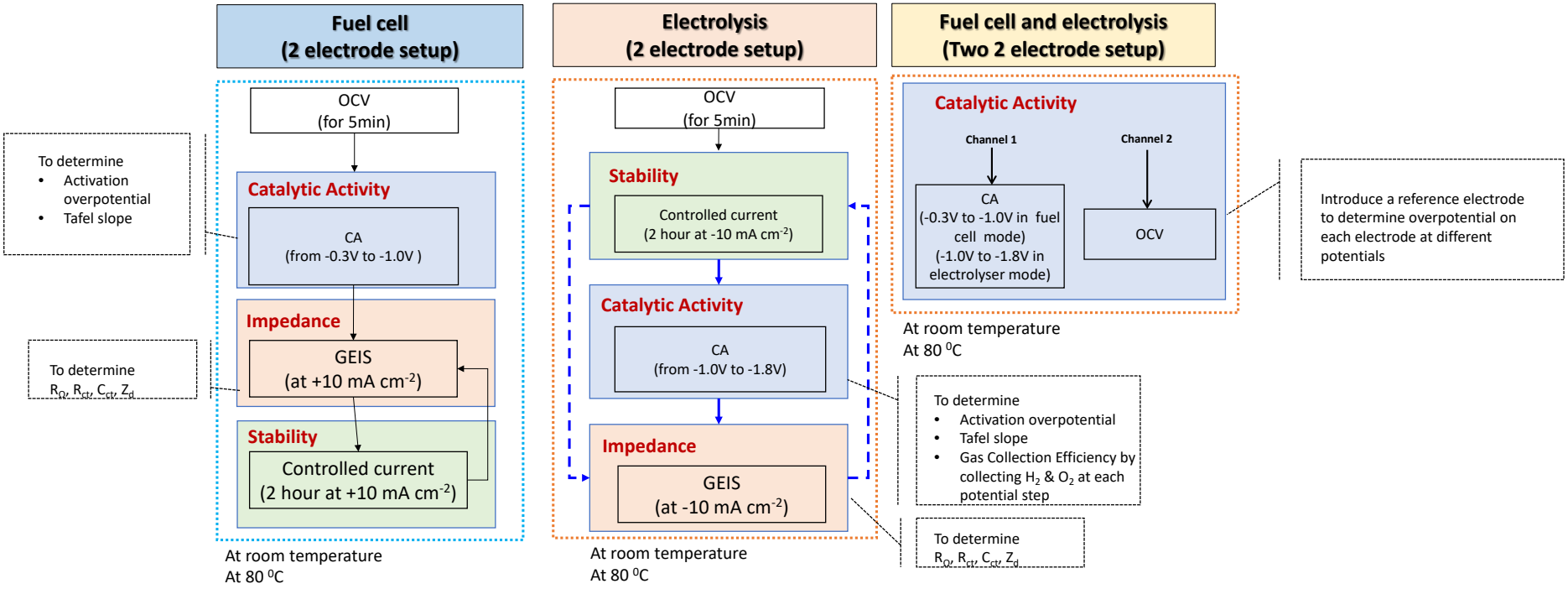

Figure 2.38: *Schematic illustration of experimental protocol (⟶ steps done first, - - - - - ->steps done after)*

Figure 2.38 shows an overview of the experimental protocol followed in this research. In the fuel cell mode, the electrochemical cell was tested in a two electrode setup, both at room temperature (RT) and at 80 ^{0}C. The anode was connected to the working electrode while the cathode was connected as a combined auxiliary/reference electrode. Therefore, all the voltages are recorded versus the cathode (O_2). Open-circuit-voltage is monitored for 5 minutes and as soon as hydrogen and oxygen is supplied to the electrodes, OCV swiftly reaches – 1 V, which is close to the thermodynamic reversible potential of 1.23 V, typical of alkaline fuel cell. Fuel cells were then characterised by chronoamperometry, electrochemical impedance spectroscopy (PEIS and GEIS), and chronopotentiometry measurements. I-V curve measurements were achieved by applying multiple chronoameprograms at potentials from -0.3 V to -1.0 V to the working electrode, stepped at 50 mV and held for 30 s, with the current taken from 90% of 30s time step. I-V curves thus obtained was then used to generate power curves (current vs power) and to calculate factors, which determine the catalytic activity of the catalysts used in the fuel cell like activation overpotentials and tafel slopes. PEIS was performed using a – 0.4 V DC component and superimposed ± 10 mV AC component; and GEIS was performed using a + 10 mA cm^{-2} DC component and superimposed ± 1 mA cm^{-2} AC. Both PEIS and GEIS were performed in the frequency range of 200 kHz to 100 mHz. Stability data of the fuel cell for long-term tests was done by applying chronopotentiometry at + 10 mA cm^{-2} for 2 h; few stability tests were done for longer times. PEIS and GEIS were repeated after stability to determine the change in the electrode from impedance elements like interfacial charge transfer resistance (R_{ct}), double layer capacitance (C_{ct}) and diffusional resistance (Z_d). To determine individual overpotentials on anode and cathode, two two-electrode setups were used on different channels on potentiostat. The cell was connected in a two electrode configuration to channel 1 on potentiostat as described above. The electrode on which the overpotential was to be determined (whether anode or cathode) was connected to the working electrode and the reference electrode (Ag/AgCl/3M NaCl(not saturated)) was connected as combined auxiliary electrode and reference electrode. This second two-electrode setup was connected to channel

2 on potentiostat. The Ag/AgCl reference electrode was added in the electrolyte spacer between anode and cathode. Thus, on channel 1 the cell was run in a fuel cell mode generating current under multiple CA's, while on channel 2, the individual potential on electrode (under investigation) vs Ag/AgCl was recorded via OCV.

In the electrolyzer mode, the electrochemical cell was tested in a two electrode setup, both at room temperature (RT) and at 80 ^{0}C. The cathode was connected to the working electrode while the anode was connected as a combined auxiliary/reference electrode. Therefore, all the voltages were recorded versus the cathode (O_2). As discussed in section 2.7, when operating our cell as an electrolyser, water is being be split to generate hydrogen and oxygen gases, however, at the start of the operating the cell as electrolyser, hydrogen and oxygen was being supplied to cathode and anode to monitor the OCV as done in fuel cell mode. This was done to get a common reference point. Similar OCV value (~-1 V) was obtained as in the case of fuel cell. Later, both gas supplies are turned off. Electrolysers were then characterised by similar techniques as used for fuel cell mentioned above. A chronopotentiograph (CP) of - 10 mA cm^{-2} is applied for 2 h to activate both anode and cathode catalysts for electrolyser operation. After this initial activation step, I-V curve measurements were achieved by applying multiple chronoameprograms at potentials from -1.0 V to -1.8 V to the working electrode, stepped at 50 mV and held for 30 s, with the current taken from 90% of 30s time step. These I-V curves were used to determine the catalytic activity of catalysts, used in electrolysers, in the same way as described for fuel cells. However, an additional experiment was performed to collect the gases (hydrogen and oxygen) generated during I-V curve measurements to extract information about gas collection efficiency of our novel Gortex-based electrolysers. GEIS was performed using similar settings as described for fuel cell above, however; a - 10 mA cm^{-2} DC component was superimposed on ± 1 mA cm^{-2} AC component. A stability test, - 10 mA cm^{-2}, is performed subsequently for 2 h followed by another GEIS. Individual overpotentials on anode and cathode were determined following the same procedure as for fuel cell.

References

1. Four point probe measurement. Available from: http://www.mdc-europe.com/product/0/Four-Point-Probe-Resistivity-Measurements?ad=1&gclid=EAIaIQobChMIwMXc6r6w1QIVHgUqCh2EFQyiEAEYASAAEgIryvD_BwE
2. Perkin Elmer. TGA-A beginners Guide. Available from: http://www.perkinelmer.com/CMSResources/Images/44-74556GDE_TGABeginnersGuide.pdf
3. Associates, O.R. Contact Angle Measurement System. Available from: http://www.orbitresearch.org/contact-angle-measurement-system.html
4. Rame-hart contact angle goniometers and tensiometers. Available from: http://www.ramehart.com/glossary.htm
5. The PMI Capillary Flow Porometer. Available from: http://www.pmiapp.ru/brochures2013/Capillary%20Flow%20Porometer.pdf
6. Schweitzer, J. Scanning Electron Microscope. Available from: https://www.purdue.edu/ehps/rem/rs/sem.htm
7. Mogk, D. Scanning Electron Microscopy. Available from: http://serc.carleton.edu/research_education/geochemsheets/techniques/SEM.html
8. Jensen, E. Example: Mechanism of Scanning Electron Microscopy. **2012**. Available from: http://www.texample.net/tikz/examples/scanning-electron-microscopy/
9. Kasap, S.O. *Principles of Electronic materials and devices 3rd ed* **2006**, New York: McGraw-Hill.
10. Heide, P. X-*ray Photoelectron Spectroscopy. An Introduction to Principles and Practices.* **2011**, New Jersey:Wiley.
11. AUTO 306 Vacuum Coater with Turbomolecular Pumping System. Available from: http://mfc.engr.arizona.edu/documents/E-beam/E090-03-860.pdf

12. Universal Laser Systems. Available from: https://www.ulsinc.com/products/platforms/pls6mw
13. Transmission Electron Microscope with LaB_6 emitter. Available from: http://files.instrument.com.cn/bbs/upfile/2007121075245.pdf
14. Practical Aspects of Gas Chromatography. Available from: http://www.chem.ucla.edu/~bacher/General/30BL/gc/practice.html
15. Linear Sweep and Cyclic Voltametry: The Principles. Available from: http://www.ceb.cam.ac.uk/research/groups/rg-eme/teaching-notes/linear-sweep-and-cyclic-voltametry-the-principles
16. Joseph Wang, *Analytical electrochemistry* 3rd Ed., Wiley, **2006**, ISBN-13 978-0-471-67879-3.
17. Instruments, G. Basics of Electrochemical Impedance Spectroscopy. **2010**. Available from: http://www.gamry.com/assets/Application-Notes/Basics-of-EIS.pdf
18. Ryan O'Hayre, Suk-Won Cha, Whitney Colella, Fritz B. Prinz, *Fuel Cell Fundamentals, 2nd Ed.*, John Wiley & Sons, ISBN: 978-1-119-11380-5.
19. B. Winther-Jensen, O. Winther-Jensen, M. Forsyth and D. R. MacFarlane Science **2008**, *321*, 671-674
20. O. Winther-Jensen, K. Chatjaroenporn, B. Winther-Jensen and D. R. MacFarlane *Int. J. Hydrog. Energy* **2012**, *37*, 8185-8189.
21. Duc, C.; Vlandas, A.; Malliaras, G. G.; Senez, V. Soft Matter **2016**, *12*, 5146-5153.
22. Brug, G. J.; van den Eeden, A. L. G.; Sluyters-Rehbach, M.; Sluyters, J. H., *J. Electroanal. Chem.* **1984**, *176*, 275-295.

CHAPTER 3

Gortex as an Electrode Substrate: Efficient Gas Diffusion Electrodes with an Unprecedented Resistance to Flooding and Leaking

3.1 Introduction

The use of gas diffusion electrodes is widely considered to be practically unfeasible in numerous electrochemical cells because such electrodes tend to leak liquid electrolyte into their gas sides. For example: gas diffusion electrodes have been said to be unsuitable for long-term operation in water electrolysers because they constantly weep electrolyte across the liquid-gas interface.[1(a)] This limitation is, arguably, most troublesome in electrochemical manufacturing processes, like chlor-alkali and electrowinning cells, where the counter electrode produces an unwanted product that must be disposed of, usually at some cost. A potential option in such cases is often to bathe the counter-electrode in a so-called *"depolarizing"* gas, like oxygen (O_2) or hydrogen (H_2), using a gas diffusion electrode.[1] This may favour a different half-reaction at the counter electrode that generates a more useful species, whilst simultaneously diminishing the cell voltage by 1.23 V.[1]

For example, in a standard chlor-alkali cell, the anode (which generates chlorine gas (Cl_2) according to equation (3.1)) is paired with a cathode that produces unwanted hydrogen (H_2) gas as shown in equation (3.2).[1]

anode:	$2\ Cl^- \rightarrow Cl_2 + 2\ e^-$	$E^o_{ox} = -1.36$ V	…(3.1)
cathode:	$2\ H_2O + 2\ e^- \rightarrow H_2 + 2\ OH^-$	$E^o_{red} = -0.83$ V	…(3.2)
	Standard chlor-alkali process:	$E^o_{cell} = -2.19$ V	

If, however, the cathode was instead a gas diffusion electrode that was fed with (air) oxygen, then it would produce more useful hydroxide ions (OH^-) according to equation (3.3). In the process, the cell voltage would also be cut by more than half, from -2.19 V to -0.96 V, with an accompanying, decline in the energy requirement per kg of chlorine produced.[1]

anode:	$2\ Cl^- \rightarrow Cl_2 + 2\ e^-$	$E^o_{ox} = -1.36$ V	…(3.1)
cathode:	$O_2 + 2\ H_2O + 4\ e^- \rightarrow 4\ OH^-$	$E^o_{red} = 0.40$ V	…(3.3)
	Chlor-alkali with O_2-depolarised cathode:	$E^o_{cell} = -0.96$ V	

Given that the chlor-alkali process is one of the most energy-intensive industrial processes in the world and consumes about 2% of the USA's electricity,[1] a capacity to readily and efficiently "gas-depolarize" counter-electrodes in industrial electrochemical processes (through the use of gas diffusion electrode technology) is of potentially enormous importance.

In the same way a zinc electrowinning cell would normally employ the half-reactions (3.4) and (3.5):

cathode:	$Zn^{2+}(SO_4^{2-}) + 2\ e^- \rightarrow Zn$	$E^o_{red} = -0.763$ V	…(3.4)
anode:	$H_2O \rightarrow 2H^+(SO_4^{2-}) + 0.5\ O_2 + 2e^-$	$E^o_{ox} = -1.229$ V	…(3.5)
	Standard Zn electrowinning process:	$E^o_{cell} = -1.992$ V	

However, if the anode were instead a gas diffusion electrode fed with hydrogen gas, then the anode reaction would become that in equation (3.6), with a 1.23 V decrease in cell voltage:

cathode:	$Zn^{2+}(SO_4^{2-}) + 2\ e^- \rightarrow Zn$	E^o_{red}=-0.763 V	…(3.4)
anode:	$H_2 \rightarrow 2H^+ (SO_4^{2-}) + 2e^-$	E^o_{ox} = -1.229 V	…(3.6)
Zn electrowinning with H_2-depolarised anode:		E^o_{cell}=-0.763 V	

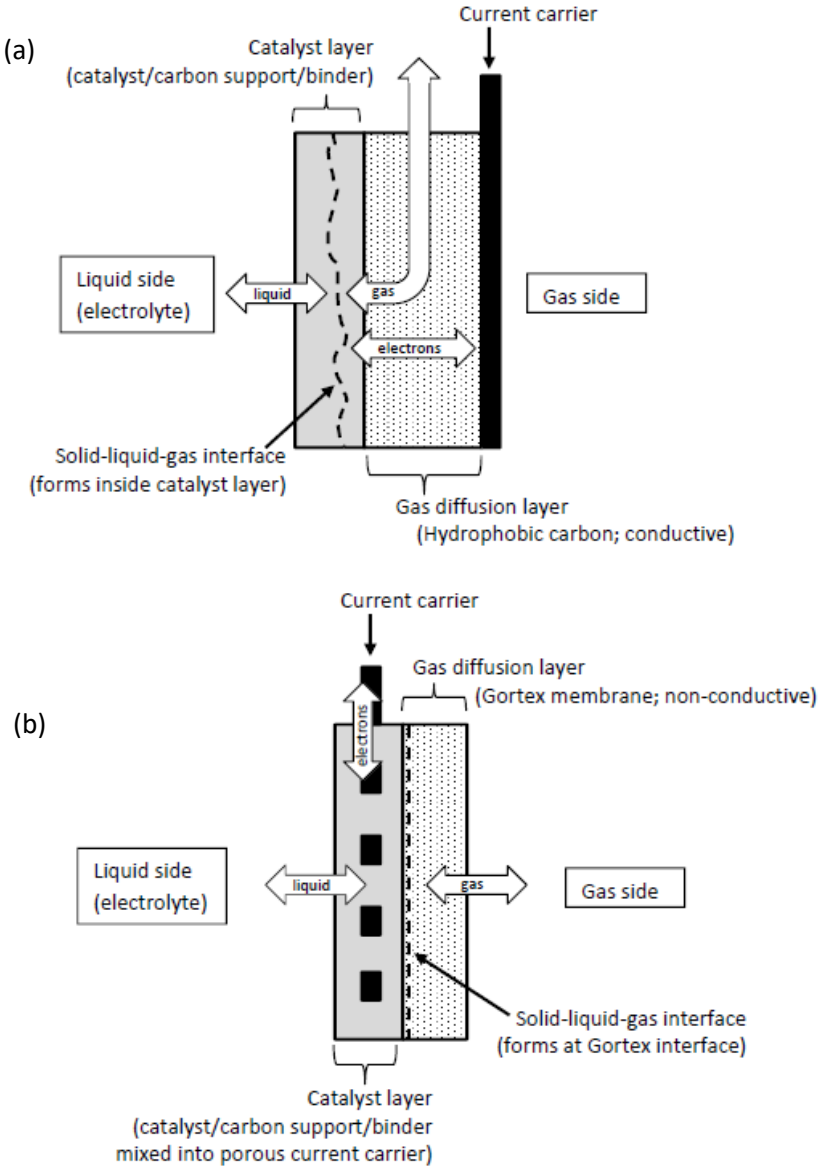

Figure 3. 1. *Schematic depiction of: (a) a typical present-day gas diffusion electrode, and (b) Gortex-based gas diffusion electrode*

Figure 3.1(a) schematically depicts the cross-sectional structure of a typical modern-day gas diffusion electrode (as previously shown in Chapter 1).

While the potential advantages of gas diffusion electrodes are well-known, they are, in fact, deployed in only a very few industrial electrochemical cells.[1] Almost all industrial electrochemical processes that could benefit from gas diffusion electrodes do not make use of them. This is largely because of the problem of leaking that exists in modern-day gas diffusion electrodes. That is, even a relatively small excess of pressure (typically <0.1 bar) on the liquid side of the gas diffusion electrode over its gas side, will cause liquid electrolyte to penetrate through the electrode, causing it to flood, with the electrode then leaking liquid electrolyte into the gas side.[1] This may be caused even by a hydraulic head of electrolyte that exerts less than 0.1 atm overpressure. Thus, for example, most industrial chlor-alkali cells are more than 1 m high, meaning that their hydraulic head of water alone generates 0.1 bar pressure at the base of the cell.[1] If a gas diffusion electrode were used as the cathode, comprising one wall of such a cell, then it would flood at its bottom, causing the caustic electrolyte to leak out of the cell.[1]

This constraint has had a huge impact on industrial electrochemistry and numerous attempts have been made to overcome it.[1] Patent applications and publications have described various approaches to the problem that have included:[1] (i) a clever, but cumbersome *"gas pocket"* electrode design that, effectively, splits up the hydraulic head (developed by Eltech Systems, Dow Chemical and Bayer, amongst others), (ii) a "*falling film*" or *"percolating"*-type gas diffusion electrode, which avoids the problem but creates a large inter-electrode voltage drop (pioneered by Hoechst), (iii) the use of a cell design in which the gas diffusion electrode is located tight against a water-fast ion-exchange membrane (developed, most prominently, by Permelec), and (iv) the use of a horizontally disposed gas diffusion electrode involving a liquid mercury covering. Most recently, in 2013, De Nora patented a sintered and cast gas

diffusion electrode with a high elastic modulus, that is capable of withstanding a 0.2 bar excess liquid-side pressure over the gas-side pressure during depolarisation with oxygen gas, without leaking.[1(b)] As in all of the above approaches however, this electrode requires special manifolding to balance the pressure differential over its liquid and gas side, and any defect may produce a leak.

The archetypal electrochemical cell in respect of gas depolarisation is a hydrogen-oxygen fuel cell, which, effectively, involves a hydrogen-depolarized anode paired with an oxygen-depolarized cathode, utilizing the reactions (in the case of an alkaline fuel cell):

anode:	$2\ H_2 + 4\ OH^- \rightarrow\ 4\ H_2O + 4\ e^-$	$E^o_{ox} = 0.83$ V	…(3.7)
cathode:	$O_2\ + 2\ H_2O\ + 4\ e^- \rightarrow 4\ OH^-$	$E^o_{red} = 0.40$ V	…(3.3)
	Alkaline fuel cell	$E^o_{cell} = 1.23$ V	

In its simultaneous use of both hydrogen and oxygen depolarization, a fuel cell, like an alkaline fuel cell, provides potentially the best-available test-bed with which to assess the practical utility of novel gas diffusion electrodes as “leak-proof” carriers of depolarising gases.

For many years up to the 1990’s, Alkaline Fuel Cells (AFCs) were regarded as the most promising of the fuel cell technologies.[2] During that decade however, Proton Exchange Membrane Fuel Cells (PEMFCs) came to dominate the field. Several of the technical challenges associated with AFCs contributed to that change. Key amongst them were:[2] (i) the difficulty of producing a well-defined, uniform pore system and evenly distributed catalyst in AFC electrodes, (ii) the excessive cost of the electrodes and the difficulty of fabricating them reproducibly in large scale, (iii) the non-availability, due to the phasing out of asbestos, of ion-permeable, gas-impermeable inter-electrode diaphragms that were alkaline-stable, and

(iv) the problem of CO_2 intolerance in air-breathing AFCs, which saw crystallites of insoluble carbonates forming within, and blocking the electrode pores.

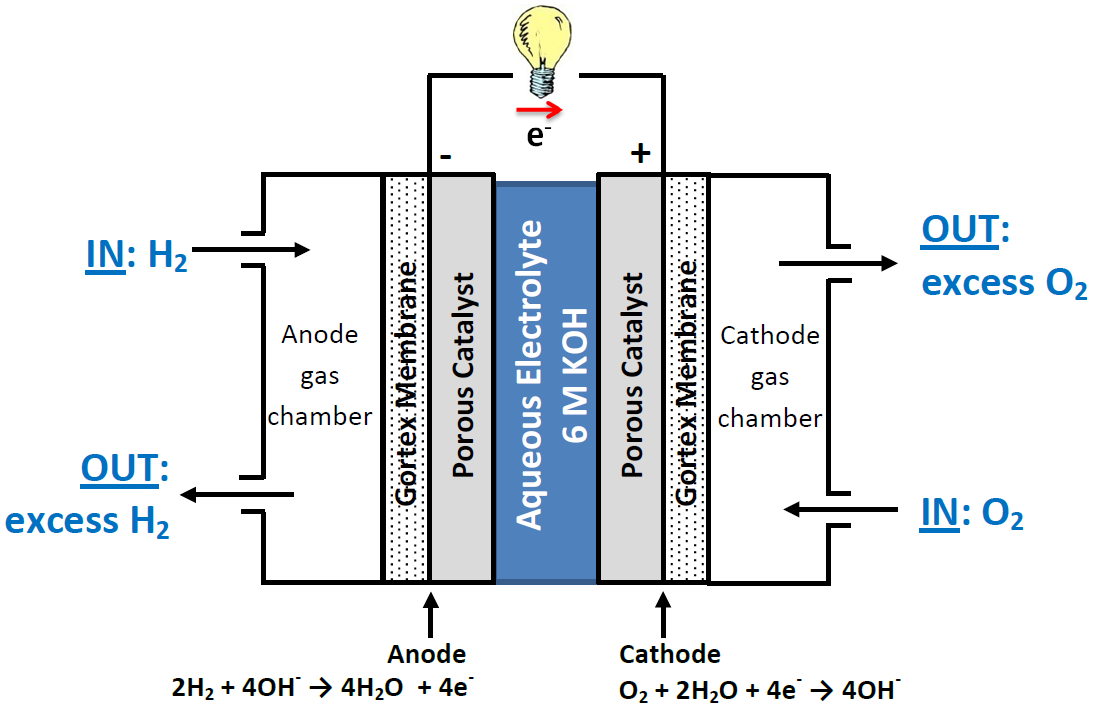

Figure 3.2. *Schematic depiction of the alkaline fuel cell used to test the gas diffusion electrodes of this chapter.*

In this chapter we describe the fabrication, characterization, and operation of novel, leak-proof gas diffusion electrodes comprising of finely-pored *Gortex* membranes over-coated with porous, conductive catalyst layers that incorporate a metal mesh current carrier. Figure 3.1(b) schematically depicts the cross-sectional structure of the Gortex-based electrodes. Two different catalyst layers have been studied: (1) sputter-coated metals of various thicknesses (including Pt, Ti, Ni and other metals) wedged tight against a fine, flat, non-woven Ni mesh, and (2) an optimized mixture of 10% Pt on Vulcan XC72 commercial catalyst incorporating carbon black and dispersed poly(tetrafluoroethylene) (PTFE), with a fine, woven Ni mesh. Capillary flow porometry indicated that the resulting gas diffusion electrodes only flooded / leaked when the excess of the liquid-side pressure over the gas-side

was >4 bar. When employed in bench-scale alkaline fuel cells utilizing 6 M KOH electrolyte and having the structure schematically illustrated in Figure 3.2, the particulate-coated Gortex electrodes operated efficiently over extended periods, without need for an ion-permeable, gas-impermeable diaphragm between the electrodes. They also proved robustly tolerant of CO_2.

The high activity of the cathode in the fuel cell is significant insofar as its half-reaction is identical to that of an oxygen-depolarised cathode in a chlor-alkali cell, which also operates under strongly alkaline conditions (typically 35% wt/wt OH^-). It can be concluded that the cathode electrode will most likely also have high activity and practical utility for O_2-depolarisation of chlor-alkali cells. (This has not been verified here because it is outside the scope of this study and because of the safety issues associated with chlor-alkali cells). The high activity of the anode in the fuel cell is significant insofar as its half-reaction is comparable to that of a hydrogen-depolarised anode in a zinc electrowinning cell. Given that that reaction takes place in an acid environment, it cannot be directly concluded that the anode electrode developed here will have high activity and practical utility for H_2-depolarisation of a zinc electrowinning cell.

The unprecedented resistance to flooding and leaking exhibited by these gas diffusion electrodes, as well as their high activity and utility for O_2- and H_2-depolarisation, provide an important advance with potentially far-reaching implications for industrial electrochemistry.

3.2 Results and Discussion

3.2.1 Conventional Gas Diffusion Electrodes

The structures and construction of modern-day *gas-diffusion electrodes* (GDEs) date back to a series of patents in the early 1960s by Varta, Siemens-Schuckert, and Brown-Boveri.[5] Gas

diffusion electrodes typically comprise of porous layers of carbon particles of varying size, with or without catalysts, fused together with particular proportions of poly(tetrafluoroethylene) (PTFE) as a binder. The resulting layers are electrically conductive and usually attached, on one side, to a metallic current carrier.[5] Figure 3.1(a) schematically depicts the cross-sectional structure of a typical modern-day gas diffusion electrode. On one side (the 'liquid side'), the electrode is in direct contact with the aqueous electrolyte. On the other side (the 'gas side'), the reaction gas flows into or out of the electrode.

The *catalyst* layer, which lies on the liquid side, normally comprises of carbon particles of smaller dimensions, fused with catalyst and sufficient PTFE binder to make this layer *partially* permeable to the liquid electrolyte. The pores in the catalyst layer are typically relatively small and may involve a mixture of hydrophobic and hydrophilic structures.[5,6]

By contrast, the *gas diffusion layer*, which lies on the gas side of the electrode, normally contains larger and/or more hydrophobic carbon particles, along with enough PTFE to make this layer maximally impermeable to the liquid electrolyte, whilst still maintaining permeability to the reaction gas. The gas diffusion layer is generally more porous but also more hydrophobic than the catalyst layer. Multiple other conductive, carbon-based layers of intermediate porosity/hydrophobicity may be incorporated between the catalyst layer and the gas diffusion layer.

The intention of this gradation in particle size, porosity, and hydrophobicity is to create, within the catalyst layer, a three-way solid-liquid-gas boundary where the liquid electrolyte interfaces with the reactant gas in the presence of the solid catalyst. That is, the catalyst layer is typically designed to allow the liquid electrolyte to penetrate some way, but not all the way, into it. The extent of this penetration may vary along the length of the electrode, depending on vagaries in the local pore structure and hydrophobicity of the catalyst layer.

The solid-liquid-gas interface is therefore illustratively depicted in Figure 3.1(a) as an irregular, dashed line. On the liquid side of the line is the electrolyte. On the gas side is the reaction gas, which flows through the gas diffusion layer as shown. At the solid-liquid-gas interface, catalyst turnover drives the reaction, with the catalyst continuously re-generated by electron flow to or from the current carrier, through the conductive catalyst and gas diffusion layers. That is, electrical current (electrons) flow through the body of the electrode, perpendicular to its liquid side surface, to or from the current carrier. For maximum electrode performance, the catalyst layer and the gas diffusion layer should be as conductive as possible.

A problem with modern-day gas diffusion electrodes however, is the fact that the hydrophobicity, as well as the size and uniformity of the pore structures of the different layers cannot be controlled to a very high degree of precision. Thus, as noted earlier, such electrodes are prone to flooding, which typically involves the solid-liquid-gas interface progressively re-locating itself into the gas diffusion layer, causing partial or complete filling with liquid. Gas transport in the gas diffusion layer and/or ion transport through the electrolyte in the catalyst layer, may then be interrupted, causing a decline or halt to the reaction. Liquid electrolyte may also leak through the electrode into the gas side.

One measure of the capacity of a gas diffusion electrode to resist flooding is to determine the overpressure on the liquid side that is needed to drive electrolyte (water) into and through the gas diffusion layer. As noted earlier, most gas diffusion electrodes flood at an overpressure of <0.1 bar,[1] although, as noted above, GDEs that flood only at 0.2 bar when depolarised with oxygen are the subject of a recent patent application.[1(b)]

3.2.2 A New Approach to Fabricating 'Leak-Proof' Gas Diffusion Electrodes

A potential solution to the problem of flooding and leaking involves developing a gas diffusion electrode in which less is asked of the gas diffusion layer. That is, instead of seeking to simultaneously optimize the gas diffusion layer for maximum conductivity (for electron transport), porosity (for gas transport), and water-repellence (for flood-resistance), one could optimize it only for porosity and water-repellence and provide conductivity to the catalyst layer by another means. That is, instead of trying to concurrently optimize three variables, which has clearly proved not entirely successful, one could optimise for two variables and provide the third by other means.

That other means may conceivably involve incorporating metallic mesh current carriers within the catalyst layer, as was done, for example, in some early alkaline fuel cell electrodes.[2(a),7] The meshes transported electrons along the respective catalyst layers, parallel to their liquid-side surface.

Recent studies have examined electrodes based on a *Gortex* substrate coated with conducting polymers.[8] Gortex has the reputation of displaying near-ideal porosity and water-repellence. If one were to optimise only for porosity and water-repellence, then Gortex would clearly be an excellent candidate for a gas diffusion layer.

To explore and more fully develop these concepts, we have prepared and studied various Gortex-based gas diffusion electrodes in which the Gortex membrane was coated with catalysts that incorporate or contact Ni meshes as conductive current carriers. The resulting gas diffusion electrodes had the cross-sectional structure shown schematically in Figure 3.1(b). In its contrast with Figure 3.1(a), Figure 3.1(b) condenses and summarises the alternative gas diffusion electrode architecture that has been studied in this Chapter. To the best of our knowledge, Gortex has thus far only been subjected to very limited studies as an

electrode substrate in its own right,[8] and has not previously been examined as a substrate for the gas diffusion electrodes in an alkaline fuel cell.

3.2.3 Gortex as a Substrate for Gas Diffusion Electrodes

Gortex is a common name for a group of membranes known as "*expanded PTFE"*, or *ePTFE,* which comprise a network of microscopically-small, hydrophobic Teflon filaments with overall porosities of 80% or less (PTFE = polytetrafluoroethylene, or Teflon).[9] Since its discovery in 1969, Gortex has been used as a water-resistant textile, a filter, a sealant, a polymer coating, and in medical devices. Gortex is unique in that it has a structure that is both highly porous and highly hydrophobic. It therefore allows gases to pass through, but not liquid water. As a textile, for example, Gortex permits the exit of water vapour from a wearer's body, but not the entrance of liquid rain.

A key, promising feature of Gortex is that it may be manufactured to reliably exhibit an exceedingly well-defined pore structure of small average size and narrow distribution. The pores are additionally highly hydrophobic. Moreover, a wide range of different Gortex membranes, each with their own particular pore structure, are commercially available at low cost and in large scale from the filtration industry. A potential advantage of using Gortex as the base for a gas diffusion electrode is therefore that it becomes possible to tailor the pore structure of the gas diffusion layer by simply selecting a particular, desired type of Gortex membrane. The narrow engineering specifications of Gortex membranes also overcome the problem of reproducibility in fabricating gas diffusion electrodes in large volumes. Finally, Gortex membranes are available in large physical size, making them suitable for fabricating gas diffusion electrodes of large dimensions.

3.2.4 Characterising the Pore Structure of Gortex Using Capillary Flow Porometry

The pore structure of Gortex membranes is routinely characterised in the filtration industry using the technique of *capillary flow porometry*.[9] By contrast, most studies of gas diffusion layers / electrodes to date have employed mercury intrusion porosimetry[11] and / or nitrogen sorption to measure macroscopic (>10 µm) and microscopic (<10 µm) pores respectively.[12(a)] Capillary flow porometry differs from these techniques in that it is skewed towards much smaller pores of the type that would be needed in gas diffusion layers if they were optimized for porosity and water-repellence.[12] To the best of our knowledge, conventional gas diffusion layers / electrodes have never been studied using capillary flow porometry. For this reason, we now briefly describe the technique and how it applies to Gortex-based gas diffusion electrodes.

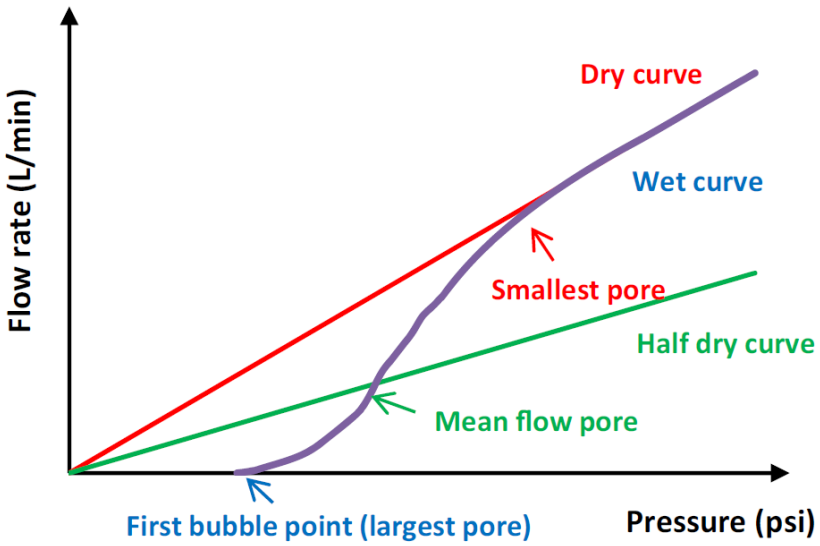

Figure 3.3. *Schematic depiction of the output "wet curve" (blue) and "dry curve" (red) measured during capillary flow porometry. The "half-dry curve" (green) is an interpolation based on the wet and dry curve profiles. Reproduced with permission.*[10]

Capillary flow porometry involves the displacement of a "wetting" liquid from the pores of a sample by applying, on one side, a gas at systematically increasing pressures.[9] The Gortex membrane must first be soaked in a liquid that completely fills and "*wets*" its pores. Isopropanol is typically used. This wetting liquid is then progressively displaced and pushed out of the pores by subjecting one side of the wetted membrane to a gas source (typically compressed air) under steadily increasing pressure.[9] In the process, a plot of gas flow rate (through the membrane) vs. gas pressure is obtained. Such a curve is known as the "*wet curve*" and is shown, illustratively, in blue in Figure 3.3.

Starting from zero pressure and zero flow rate (i.e. the origin of the graph in Figure 3.3), the wetted membrane initially resists the increasing gas pressure and retains the incorporated IPA. During this phase, the plot runs along the bottom axis of the graph, producing zero flow rate with increasing pressure. At a particular pressure however, the wetting liquid is driven out of the largest pores in the Gortex, causing the graph to divert upwards. This point, which is known as the "*first bubble point*", characterises the largest pores in the membrane (i.e. the pores that "de-wet" first).[9] Thereafter, as the gas pressure continues to increase, the liquid is progressively driven out of the other pores in the order of their size, from the larger pores first to the smaller pores last. When the smallest pores in the membrane have been de-wetted, the flow rate plot overlaps a curve that is separately but similarly measured using the membrane in a completely dry state. That curve is known as the "*dry curve*" and is shown in Figure 3.3 in red.[9] The point at which the wet curve and the dry curve first overlap characterises the smallest pore size within the membrane and is marked as such in Figure 3.3. The point half way between the largest pore (the first bubble point) and the smallest pore, characterises the "mean" pore and is termed the "*mean flow pore*".[9] A straight line, interpolated from the origin of the graph through the mean flow pore, provides a hypothetical line known as the "*half dry curve*" (depicted in green in Figure 3.3).

3.2.5 The Resistance of Gortex as a Gas Diffusion Layer to Flooding and Leaking

A similar procedure can be carried out using a liquid that does not wet (fill) the pores of Gortex, like water. In such measurements, a pool of water is placed on the one side of the dry membrane. The water is then subjected to a methodical increase in pressure until it penetrates and passes through the membrane to the other side.[9] The pressure at which that occurs is known as the "*water-entry pressure*" (or the "*liquid-entry pressure*").[9] Because Gortex membranes have pore structures that are highly repellent to water, the water tends to burst through the membrane suddenly once the water-entry pressure is reached.

When thought of as a potential gas diffusion layer, the water-entry pressure is, effectively, the overpressure on the liquid side relative to the gas side, at which a putative Gortex gas diffusion layer would flood and leak. Gortex membranes with a wide range of water-entry pressures are commercially available. For the purposes of this study, we selected as our Gortex substrate, a finely pored *Prevail^{TM} expanded PTFE* (ePTFE) membrane supported by a fibrous polypropylene backer, supplied by GE Energy, that had a water-entry pressure of >4 bar. That is, the membrane was manufactured to resist penetration by water (flooding / leaking) until the overpressure on the water side of the membrane over the gas side, exceeded 4 bar.

As noted earlier, conventional gas diffusion layers / electrodes do not seem to have ever been studied using capillary flow porometry. Conventional gas diffusion electrodes result in hydrophilic and hydrophobic pores and often pore symmetry on these materials is compared with a hydrophobic and hydrophilic liquid to highlight the distribution of these two distinct phases whereas, capillary flow porometry measures homogeneous properties. The fact that modern-day gas diffusion electrodes flood and leak aqueous electrolyte at low overpressures on their liquid side (<0.2 bar),[1] indicates that their pore structures and/or hydrophobicities

are likely too ill-defined or too broadly distributed for measurement using capillary flow porometry. They may, additionally, be insufficiently robust, leading them to be damaged by the capillary flow porometry technique.

In selecting the above *Prevail*^{TM} membrane as a substrate for gas diffusion electrodes, we were therefore aiming to drastically improve upon the pore structures and/or hydrophobicities of modern-day gas diffusion layers.

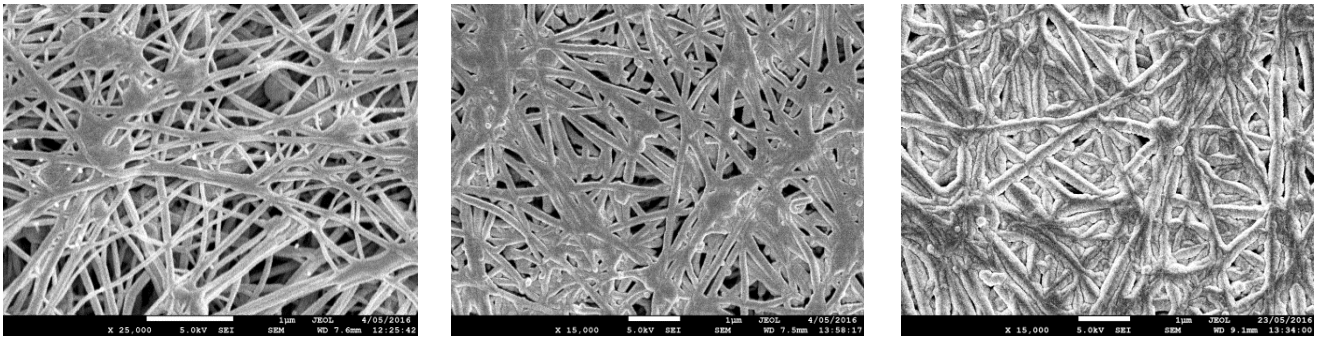

(a) (b) (c)

Figure 3.4. *Scanning electron microscopy (SEM) images of Gortex electrodes sputter-coated with Pt, with nominal thicknesses (according to the internal thickness monitor of the sputter-coater) of: (a) 50 nm, (b) 200 nm, and (c) 400 nm.*

3.2.6 Fabrication and Characterisation of Gortex-Based Gas Diffusion Electrodes Coated with Sputtered Pt as Catalyst

In the first experiments, we prepared a set of gas diffusion electrodes comprising of the above Gortex membrane sputter-coated on its PTFE side, with various thicknesses of Pt. The method of fabrication is described in the experimental section 2.4.1. Figure 3.4 shows magnified views of the Gortex membrane after sputter-coating with varying loadings of Pt. As can be seen, the membranes comprised of fine 3D fibrous networks with high internal surface area. Figure 3.4(a) depicts a membrane after deposition of 0.083 g of Pt per m^2 of

geometric area. QCM measurements indicated that this loading was equivalent to a uniform layer of Pt that was ca. 50 nm thick when deposited on a non-porous, solid substrate. As can be seen in Figure 3.4(a), the fibrous network of the membrane remained relatively unchanged after deposition, with each of the fibres coated with a thin layer of Pt. The metallized membrane was conductive, albeit with a high sheet resistance (~60-80 Ω/square). However, increasing the Pt loading by five-fold, to 0.42 g of Pt per m^2 of geometric area, provided a continuous conductive layer of Pt with a lower sheet resistance (in the order of ~10 Ω/square). This loading equated to a nominal thickness of 100 nm on a non-porous, solid substrate, according to the internal thickness monitor of the sputter-coater.

Figure 3.4(b) depicts the Gortex membrane after deposition of 2.03 g of Pt per m^2 of geometric area. This loading equated to a thickness of ca. 200 nm when deposited on a non-porous, solid substrate. As can be seen, in Figure 3.4(b), the fibres of the membrane were noticeably thickened by the deposition process, with "knots" of Pt visible. The pore structure, porosity and high internal surface area of the membrane remained essentially intact however. Because of the thicker Pt coating, the conductance of the membrane surface was enhanced, with a sheet resistance of <3 Ω/square.

Figure 3.4(c) depicts the Gortex membrane after the deposition of 6.47 g of Pt per m^2 of geometric area. This loading equated to a thickness of ca. 400 nm when deposited on a non-porous, solid substrate. As can be seen, in Figure 3.4(c), the fibres in the fibrous network of the membrane became so thickened by the deposition process that, in many places the surface of the membrane was almost completely covered.

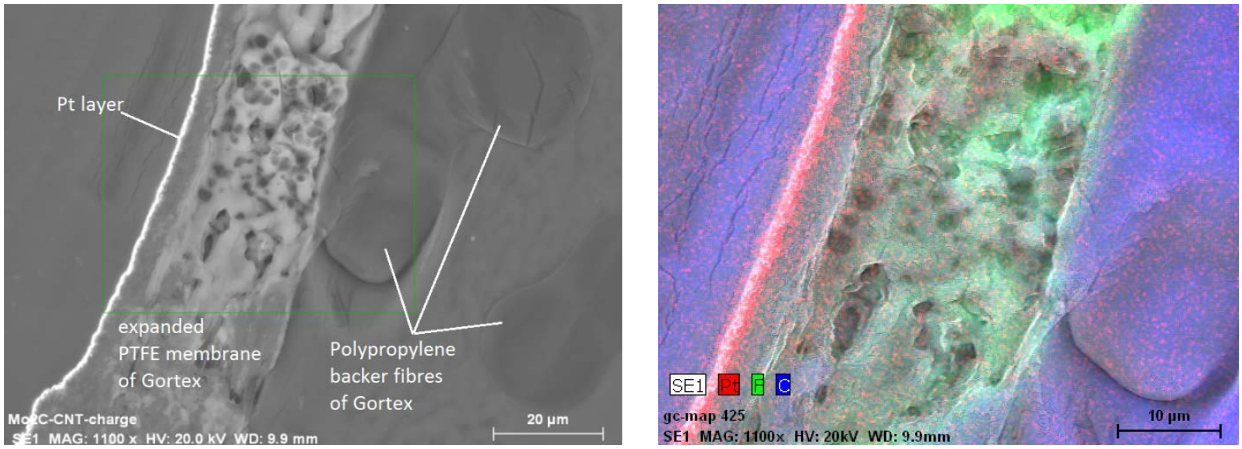

(a) (b)

Figure 3.5. *(a) Cross-sectional view and (b) cross-sectional energy-dispersive X-ray (EDX) of the sputter-coated (200 nm nominal thickness) Gortex electrode depicted in Figure 4(b). The Pt layer is shown in red.*

To determine how far the Pt coating penetrated into the ePTFE membrane, the Pt-coated membrane in Figure 3.4(b) was cryogenically frozen, cracked, and a cross-section at the fracture was examined using scanning electron microscopy (SEM). Figure 3.5(a) shows an SEM image of the cross-section, viewed from laterally above the top surface of the exposed edge. As can be seen, the cross-sectional thickness of the Gortex expanded PTFE membrane was ca. 20 µm. The cross-section displayed the same complex fibrous network observed in the earlier figures. Below the membrane, on the opposite side to the Pt coating, could be seen the polypropylene fibres that make up the backing material of the Gortex. The polypropylene backer is needed to give the Gortex "hand", by which is meant that without such a backer, the expanded PTFE membrane alone is difficult to handle due to its lack of rigidity.

Figure 3.5(b) was generated using Energy-Dispersive X-rays (EDX), tuned to image only specific atoms. The Pt atoms appear as red areas with C atoms coloured blue and F atoms

green. As can be seen, the sputter-coated Pt was limited to the top ca. 0.85 μm of the Gortex membrane. It could not be ascertained whether the entire 0.85 μm displayed sheet conductivity.

Excluding the polypropylene backer layer, metallized Gortex electrodes of this type therefore comprise two layers: (i) a porous, metallized, and at least partially conductive Pt layer that penetrated ca. 0.85 μm into the Gortex, and (ii) an underlying layer of virgin, uncoated Gortex of ca. 19.15 μm thickness. Except for locations where the Pt heavily overcoated the Gortex, the pore structures of the conductive and non-conductive layers appeared very similar. The boundary between them was therefore largely a boundary of electrical conductivity and surface metallisation.

3.2.7 Fabrication and Characterisation of Gortex-Based Gas Diffusion Electrodes Coated with 10% Pt on Vulcan XC72 Catalyst, Carbon Black, PTFE Binder and Ni Mesh

In the second set of experiments, we prepared a set of gas diffusion electrodes comprising of the Gortex membrane overcoated on its PTFE side, with a homogeneous mixture of 10% Pt on Vulcan XC72 commercial catalyst, carbon black (CB), dispersed poly(tetrafluoroethylene) (PTFE) as a binder, and a Ni mesh as current carrier. The method of fabrication is described in section 2.4.1.

Figure 3.6(a) depicts, using optical microscopy, a cross-sectional view of a Gortex electrode of this type, that had been overcoated with a Vulcan-supported catalyst, carbon black, PTFE binder, and a woven Ni mesh current carrier. As can be seen, the gas-facing side of the electrode (depicted at the bottom of the figure) comprised of Gortex, which was made up of the thin ePTFE membrane (ca. 20 μm thick) backed by a thicker, fibrous polypropylene

backing layer. The liquid-facing side (depicted at the top of the figure) comprised of the commercial catalyst, incorporating carbon black and PTFE binder, enveloping the Ni mesh current carrier.

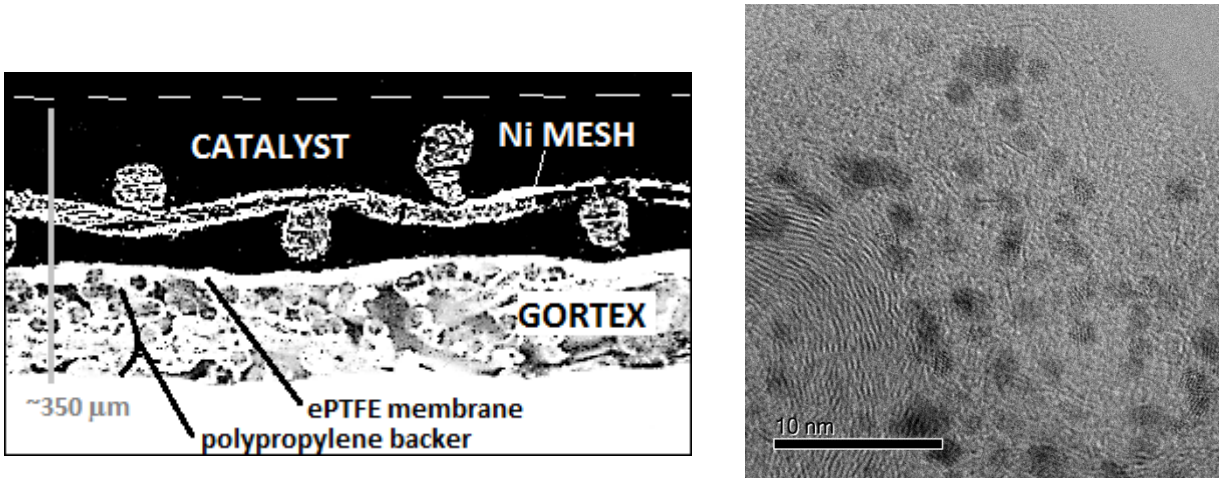

Figure 3.6. *(a) Cross-sectional view of a Gortex electrode coated with a precious metal catalyst supported on Vulcan XC72, carbon black, PTFE binder, and a Ni mesh as a current carrier; the dashed line at the top depicts the surface of the catalyst layer, and (b) transmission electron micrograph of the 10% Pt on Vulcan XC72 commercial catalyst used in this study.*

Figure 3.6(b) provides a transmission electron micrograph of the 10% Pt on Vulcan XC72 catalyst used in this study. The catalyst exhibited a rather ideal morphology, comprising of 2-4 nm Pt nanoparticles evenly dispersed over the carbon support.

Gas Diffusion Electrode	Nominal thickness of catalyst layer on Gortex (nm/μm)	Mean flow pressure (IPA)[a] (bar)	Mean flow pore diameter (IPA)[a] (μm)	Bubble point pressure (IPA)[a] (bar)	Bubble point pore diameter (IPA)[a] (μm)	Liquid-entry pressure (H_2O) (bar)
Pt sputter-coated on Gortex	0 nm	1.1204	0.5695	1.0331	0.6176	4.2558
	50 nm	1.9474	0.3276	1.8948	0.3367	4.7047
	100 nm	1.9323	0.3302	1.8945	0.3368	4.4852
	150 nm	1.8638	0.3423	1.8193	0.3507	4.2939
	200 nm	1.2556	0.5082	1.2025	0.5306	3.991
	400 nm	1.1822	0.5397	1.1345	0.5624	3.508
10% Pt on Vulcan XC72, carbon black, PTFE and Ni mesh on Gortex	~200 μm	1.1708	0.5450	1.0969	0.5817	5.702

[a] wetting liquid was IPA (= *i*-propanol)

Table 3.1. *Capillary flow analysis of Gortex-based gas diffusion electrodes.*[9]

3.2.8 Characterisation of Gortex-based Gas Diffusion Electrodes

To characterise the gas diffusion electrodes that had been fabricated, capillary flow porometry was carried out on them. Table 3.1 summarizes the data obtained.

The most significant data in Table 3.1 is, undoubtedly, the *liquid entry pressure* / *water-entry pressure*. As noted above, this is, effectively, the pressure at which a catalyst-coated Gortex gas diffusion electrode becomes "flooded" with water (electrolyte), causing it to leak. As can be seen in Table 3.1, the water-entry pressure was measured to be >4 bar for all electrodes that had been sputter-coated with a Pt layer of nominal thickness <200 nm, as well as for the electrode coated with 10% Pt on Vulcan XC72, carbon black, PTFE and Ni mesh. The latter was measured to be a remarkable 5.702 bar, which is more than an order of magnitude larger than the 0.2 bar reported for the earlier-mentioned De Nora gas diffusion electrode under O_2-depolarisation.[1(b)]

The mean flow pore pressures and the bubble point pressures of the electrodes generally followed the respective trends in pore diameter that are evident in Table 3.1. It is noticeable however, that for the electrode coated with the particulate catalyst layer and Ni mesh, these quantities were similar to those of the uncoated Gortex membrane, suggesting that they were set by the Gortex gas diffusion layer, with the catalyst layer having little influence.

Figure 3.7 depicts the computed distribution (by number) of the average pore diameter of the Gortex electrodes. As can be seen, 90% of the pores of the uncoated Gortex fell in the range 0.5-0.6 μm (Figure 3.7(a)). By contrast, 70%-95% of the pores of the Gortex that had been sputter-coated with Pt of 50-150 nm nominal thickness fell in the 0.3-0.4 μm size (Figure 3.7(a)). More thickly sputter-coated membranes (200 and 400 nm nominal thickness) had 65%-95% of their pores in the 0.5-0.6 μm diameter range. The Gortex electrode coated with 10% Pt on Vulcan XC72, incorporating carbon black, PTFE and Ni mesh, had 65% of its pores in the range 0.5-0.6 μm diameter, with declining numbers of pores at lower diameters.

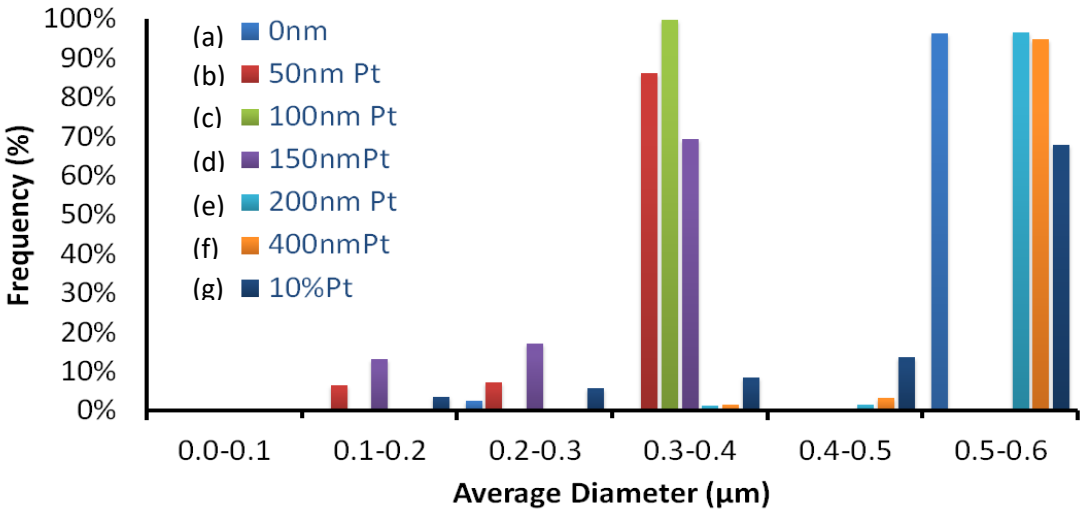

Figure 3.7. *Pore size distribution (by number) of the Gortex electrodes: (a) uncoated Gortex (control), (b)-(f) sputter-coated with Pt of 50-400 nm nominal thickness, and (g) overcoated with 10% Pt on Vulcan XC75 incorporating carbon black, PTFE binder, and Ni mesh current carrier.*

Figure 3.8 shows air permeability data (the *dry curve*) obtained by porometry for the Gortex electrodes. To obtain these measurements, air was passed through 1 cm^2 of the dry electrodes and the flow rate was measured as a function of the applied pressure. As can be seen, the electrodes displayed highly porous structures that each exhibited approximately linearly increasing flow rates with applied pressure. The almost parallel slopes of their air permeability data relative to and below the control, uncoated Gortex membrane, indicated that their overall porosity decreased as a result of the coating. The porosity of the sputter-coated electrodes generally declined with an increase in the loading of Pt. The Gortex electrode that had been sputter-coated with Pt of nominal 400 mm thickness displayed the lowest porosity as shown by the filled circles (●) in Figure 3.8. By contrast, the electrodes coated with 10%Pt/carbon black/PTFE/Ni mesh ((+) in Figure 3.8) displayed an intermediate flow rate, indicating an intermediate porosity in its catalytic layer.

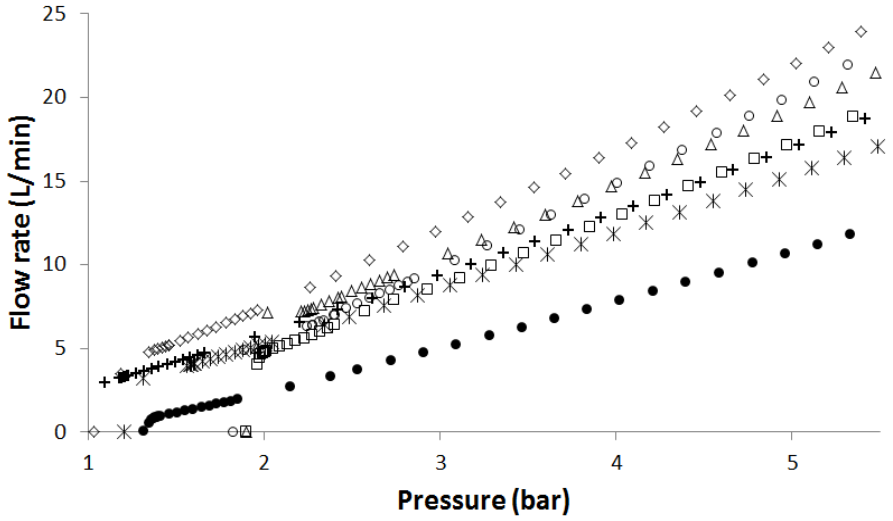

Figure 3.8. *Air permeability measurements per 1 cm^2 area of the uncoated and coated gas diffusion electrodes obtained by porometry: (◊) uncoated Gortex control, (□) Gortex sputter-coated to 50 nm nominal thickness, (Δ) Gortex sputter-coated to 100 nm nominal thickness, (○) Gortex sputter-coated to 150 nm nominal thickness, (✳) Gortex sputter-coated to 200 nm nominal thickness, (●) Gortex sputter-coated to 400 nm nominal thickness, and (+) Gortex overcoated with particulate 10% Pt on Vulcan XC72, incorporating carbon black, PTFE binder, and Ni mesh.*

It should be noted however that, even for the poorest performing of the above electrodes, a very substantial flow of air, equal to ca. two litres per min, passed through a 1 cm^2 area of electrode at a 0.5 bar pressure differential. Clearly there was no significant hindrance to gas transport into or out of the electrodes.

3.2.9 Hydrophobicity of the Gortex-based Gas Diffusion Electrodes

The extent to which water penetrates a porous electrode typically depends on the hydrophibicity of its catalyst layer surface. To establish the hydrophobicity of the gas diffusion electrodes, we sought to measure their contact angles and compare them to that of the uncoated, control Gortex membrane. The catalyst surface of electrodes coated with 10% Pt/carbon black/PTFE/Ni mesh wetted completely when a droplet of water was placed on it, meaning that they were essentially hydrophilic. No contact angle could be measured. However, water droplets beaded on the catalyst surface of the Gortex electrodes that had been sputter-coated with Pt. Table 3.2 lists the contact angles of these samples. As can be seen, the surface of the control, uncoated membrane was strongly hydrophobic, with a contact angle of ca. 117^o. However, when coated with increasing loadings of Pt, the contact angle and the hydrophobicity of the surface progressively declined, to 98.8^o at 100 nm nominal thickness, 78.2^o at 200 nm, and 74.5^o at 400 nm. A contact angle below 90^o formally indicates a loss of hydrophobicity, with wetting of the surface.

Nominal thickness of sputtered Pt on ePTFE membrane (nm)	Contact angle (water 5µL @ 0.5µL/s)
0	117.2
50	106.7
100	98.8
150	92.5
200	78.2
400	74.5

Table 3.2. *Contact angles for varying thickness of sputtered Pt on ePTFE membrane*

3.2.10 Fuel Cells with Gortex-based Gas Diffusion Electrodes

In order to study the performance of the Gortex gas diffusion electrodes, they were tested in a desktop alkaline fuel cell. The procedure of mounting the Gortex membrane/catalyst/mesh assembly into a useable electrode assembly is described in experimental section 2.4.2.

Two such mounted electrodes were then placed in a facing disposition, a few millimeters apart, within a custom-built cell that contained sealed gas chambers behind each of the anode and the cathode electrodes. Figure 3.2 depicts the resulting cell. Experimental sections 2.5 and 2.6 elaborate cell construction and configuration when operated in fuel cell mode.

For all electrodes tested, the fuel cell was operated in open air over periods of days, including periods of using air oxygen, without any difficulties arising from CO_2 uptake with accompanying carbonate precipitation. The liquid electrolyte was either maintained at the same atmospheric pressure as the respective gas chambers (i.e. 1 bar pressure), or overpressured by 0.5 bar relative to the gas chambers (i.e. 1.5 bar pressure for the liquid electrolyte and 1 bar pressure in the gas chambers). In general the data collected for these two situations was essentially identical, indicating the presence of an overpressure of 0.5 bar on the liquid electrolyte had little effect on the performance of the cells tested.

S.No.	Anode [H_2 electrode] (nominal thickness of layer)	Cathode [O_2 electrode] (nominal thickness of layer)	Aqueous Electrolyte	KOH Concentration (M)	Maximum Power ($mW\ cm^{-2}$)	Current at Maximum Power ($mA\ cm^{-2}$)	Voltage at Maximum Power (V vs O_2)	Open Circuit Voltage, OCV (V vs O_2)
1.	Pt (100 nm)	Pt (100 nm)	KOH	6	5.369	10.162	-0.528	-1.033
2.	Pt (50 nm)	Pt (50 nm)	KOH	6	4.281	8.052	-0.532	-1.025
3.	Pt (150 nm)	Pt (150 nm)	KOH	6	4.225	8.533	-0.495	-1.002
4.	Pt (100 nm)	Pt (100 nm)	KOH	6	5.226	10.141	-0.515	-1.025
5.	Pt (100 nm)	Ag (100 nm)	KOH	6	3.977	9.541	-0.417	-1.035
6.	Ag (100 nm)	Pt (100 nm)	KOH	6	-	-	-	OCV not established
7.	Pt (100 nm)	Au (100 nm)	KOH	6	4.288	9.808	-0.437	-0.959
8.	Au (100 nm)	Pt (100 nm)	KOH	6	-	-	-	OCV not established
9.	Pt (100 nm)	Pt (top, 50nm) + Ag (100nm)	KOH	6	2.701	6.263	-0.431	-1.007
10.	Pt (100 nm)	Pt (top, 100nm) + Au (50nm)	KOH	6	5.238	10.738	-0.488	-1.034
11.	Pt (100 nm)	Au (top, 50nm) + Pt (50nm)	KOH	6	5.021	10.654	-0.471	-1.009
12.	Pt (100 nm)	Pt (top, 50nm) + Ag (100nm)	KOH	6	4.039	9.895	-0.408	-1.002
13.	Pt (top, 50nm) + Ag (100nm)	Pt (100 nm)	KOH	6	1.312	2.743	-0.478	-1.024
14.	Pt (100 nm)	Pt (top, 100nm) + Au (50nm)	KOH	6	2.823	6.605	-0.427	-1.190
15.	Pt (100 nm)	Pt (top, 100nm) + Au (50nm)	KOH	6	2.875	7.069	-0.407	-1.032
16.	Pt (top, 100nm) + Au (50nm)	Pt (100 nm)	KOH	6	3.052	6.537	-0.467	-1.012
17.	Ti (100 nm)	Pt (100 nm)	KOH	6	0.120	0.200	-0.601	-1.011
18.	Pt (100 nm)	Ti (100 nm)	KOH	6	-	-	-	OCV not established
19.	Pt (100 nm)	Ni (100 nm)	KOH	6	0.969	2.377	-0.408	-0.861
20.	Ni (100 nm)	Pt (100 nm)	KOH	6	0.040	0.075	-0.538	-1.193
21.	Ni (100 nm)	Au (100 nm)	KOH	6	0.386	0.601	-0.643	-0.941
22.	Ni (100 nm)	Ag (100 nm)	KOH	6	0.183	0.281	-0.651	-1.020
23.	Ti (top, 100nm)+ Au (50nm)	Ag (100 nm)	KOH	6	0.057	0.127	-0.446	-1.001

Table 3.3. *Combinations of sputter-coated metals on Gortex, tested as alkaline fuel cell gas diffusion anodes and cathodes.*

3.2.11 Fuel Cells with Sputter-Coated Gortex Electrodes

Electrodes having sputter-coated catalyst layers have previously been studied in PEM fuel cells.[13] In order to achieve high performance, it was concluded that a sputter-coated catalyst layer should generally exhibit the following properties:[13] (i) ready availability of the three-phase zone, in order to maximise the activity of the catalyst, (ii) low diffusion losses, (iii) ready water removal, (iv) low ohmic losses, and (v) an ability to withstand high mechanical stresses. A thin layer thickness minimises the gas diffusion losses and facilitates water removal.

To determine and compare the performance of the sputter-coated gas diffusion electrodes, fuel cells incorporating them as anodes and cathodes were tested. The electrochemical activity of several metals, namely Pt, Au, Ag, Ni & Ti were tested as fuel cell electrodes. Table 3.3 describes the various combinations of metals tested as anode and cathode in fuel cell. As can be seen from Table 3.3, only when metals like Pt, Ni and Ti were used as anode catalyst, could we obtain an open circuit potential of ~ 1 V (close to the thermodynamic potential of 1.23 V). However, when the anodes were switched to metals like Au and Ag, no open circuit potential was established. Thus, for all fuel cell tests, the anode electrode composition was fixed and consisted of sputtered Pt. A nominal thickness of 100 nm of Pt was chosen to obtain optimum hydrophobicity as demonstrated by the contact angles in Table 3.2. As can be seen from Table 3.3 only three metals namely, Pt, Au and Ag, each sputtered to a nominal thickness of 100 nm, when coupled as cathode electrodes with Pt anodes delivered reasonable fuel cell performances.

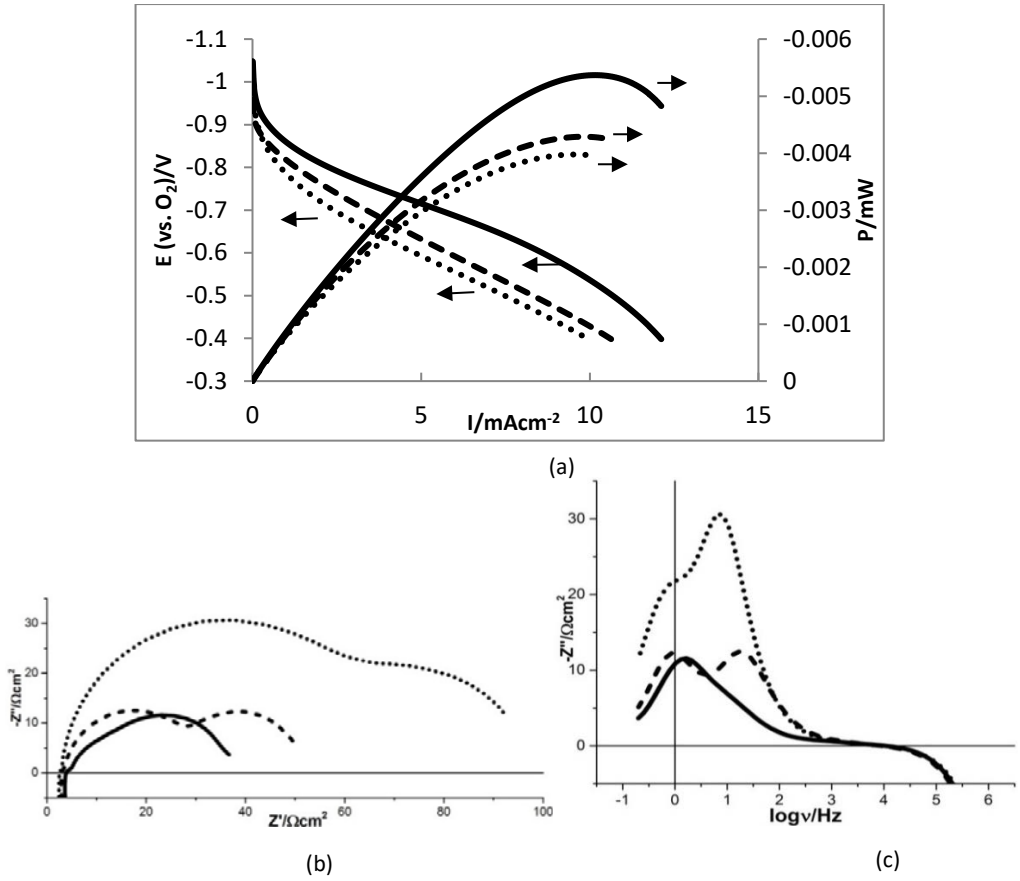

Figure 3.9. *(a) Polarization Curves (left axis) and Power Curves (right axis) at 20 ^{o}C for alkaline fuel cells containing Gortex electrodes sputter-coated with (—)Pt, (- - -) Au,& (• • •) Ag of nominal thickness of 100 nm as the anode. The cathode was a Gortex membrane sputter-coated with Pt of nominal thickness 100 nm. (b) EIS Nyquist and (c) Bode plots showing measured data at 0.8 V.*

Figure 3.9(a) illustrates the polarisation curves of fuel cells consisting of sputter-coated Pt (100 nm nominal thickness) on Gortex at the cathode and sputter-coated Pt, Au or Ag of 100 nm nominal thickness on Gortex at the anode. As can be seen, the Pt coated anode outperformed the Au and Ag coatings.

Figure 3.9(b) and (c) depicts the Nyquist and Bode plots for these fuel cells, which can be explained on the basis of the binding energy of these metals with oxygen. Ag and Au, with higher oxygen binding energies than Pt, have a higher activation barrier for dissociation of

oxygen, leading to higher overpotentials for the ORR. Thus, Pt has the smallest overpotential for the ORR.[14] Comparing the three metal coatings in Figure 3.9(b), it is evident that the large activation barrier for the ORR at Au and Ag gave rise to a double semicircle in the Nyquist impedance curve at low and medium frequencies, which was not observed for the Pt coated system. The medium-frequency curve derived, most likely, from the charge transfer resistance of the ORR, which increased in accordance with the O_2 binding energy of these metals (Pt>Ag>Au). The low-frequency curve arose from limited diffusion of reactants to the catalytic site; the required water (H_2O) reactant may have been unable to readily access the ORR Pt catalyst, or the OH^- reactant was unable to access the HOR Pt catalyst, because of the high hydrophobicity of the Pt layer. Another possibility arises from a gas-phase, mass transfer barrier due to limited diffusivity of O_2 in water formed at cathode.

To further probe the electro catalytic activity of sputtered Pt-based Gortex electrodes, fuel cells with symmetrical arrangements of electrodes were tested; that is, the same electrode composition was used at the anode and cathode in each test. Figure 3.10(a) depicts polarisation (left axis) and power density (right axis) curves for fuel cells with Gortex electrodes incorporating sputter-coated Pt of nominal thickness 50 nm, 100 nm and 150 nm. Figure 3.10(b) shows the equivalent circuit that was used to model the electrochemical impedance spectra (EIS) of the cells. Figure 3.10(c)-(d) depict the two-electrode Nyqist and Bode plots of the above cells, measured under potentiostatic conditions at 0.8 V.[15]

As is evident from Figure 3.10(a), the 100 nm Pt-coated electrodes gave the best fuel cell performance over the full range of current densities measured, albeit achieving only small currents overall (e.g. 12 mA cm^{-2} at 0.4 V). The cells containing Gortex coated with Pt of 200 nm or 400 nm nominal thicknesses performed still more poorly.

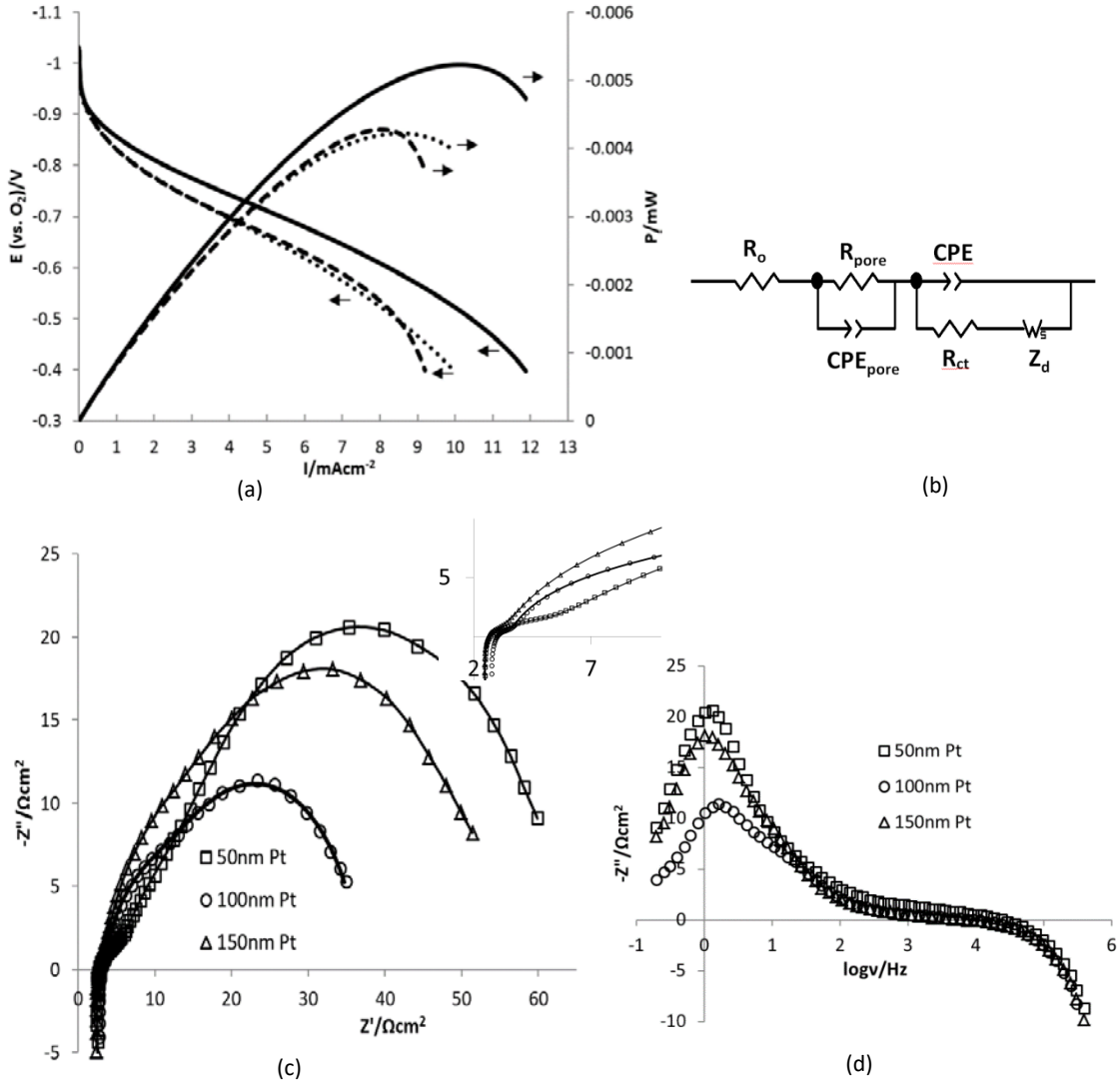

Figure 3.10. *(a) Polarization Curves (left axis) and Power Curves (right axis) at 20 °C for alkaline fuel cells containing Gortex electrodes sputter-coated with Pt having nominal thickness of (– – –) 50 nm, (—) 100 nm, and (•••) 150 nm. Electrolyte: 6 M KOH. (b) EIS Equivalent circuit. (c) Nyquist and (d) Bode plots showing measured data (individual data points) and modelled data (solid lines) (modelled using the equivalent circuit depicted in (b)) at 0.8V.*

While exhibiting low overall performance, the above fuel cells were, nevertheless, of interest because their properties were strongly influenced by both the Gortex substrate and the

current carrier Ni mesh that had been used. These influences provided insights in respect of optimizing Gortex-based gas diffusion electrodes.

Referring to the Nyquist plot in Figure 3.10(c), the charge transfer resistance at the cathode likely dominates over charge transfer resistance at the anode since, in alkaline fuel cells, the Hydrogen Oxidation Reaction (HOR) at the anode is kinetically favoured over the Oxygen Reduction Reaction (ORR) at the cathode. At higher frequencies, the kinetic impedance (which is indicative of activation processes) for the 50 nm sample was more than for the 100 nm and 150 nm sample, as demonstrated by the larger arc widths of these samples at ca. 7.5 Ω cm^2 (Figure 3.10(c) inset). At higher Z' values, mass transport impedance (indicative of diffusion processes) was greater in the 50 nm and 150 nm samples as compared to the 100 nm samples, as seen in the Bode Plot in Figure 3.10(d), which provides a comparison of the curve heights. It can be concluded that the 100 nm electrodes were best performing in terms of mass transport. It seems likely that the hydrophobicity of the platinized surface of the

Nominal Pt thickness	R_Ω (Ω cm^2)	R_{pore} (Ω cm^2)	$Q_{CPE,pore}$ ($\mu\Omega^{-1}$cm^{-2}s^n)	$n_{CPE,pore}$	C_{pore} (μFcm^{-2})	R_{ct} (Ω cm^2)	$Q_{CPE,ct}$ ($\mu\Omega^{-1}$cm^{-2}s^n)	$n_{CPE,ct}$	C_{ct} (μF cm^{-2})	Z_d (Ω cm^2)
50 nm	2.73	2.95	397	0.82	86.92	8.87	1500	0.88	679.1	47.9
100 nm	2.63	0.599	929	0.85	298.1	8.01	1299	0.94	893.7	25.3
150 nm	2.63	0.698	2598	0.83	907.2	16.13	2600	0.85	1068.7	35.01

Table 3.4. *Data from Electrochemical Impedance Spectroscopy (EIS) of alkaline fuel cells containing Gortex electrodes sputter-coated with Pt, modelled using the equivalent circuit in Figure 3.10(b) (ohmic resistance (R_Ω), pore resistance (R_{pore}), charge transfer resistance (R_{ct}), diffusional resistance (Z_d), and capacitance expressed in terms of constant phase element[17] (Pore: $Q_{CPE,pore}$, $n_{CPE,pore}$, and C_{pore}) (Charge transfer: $Q_{CPE,ct}$, $n_{CPE,ct}$, and C_{ct})). Electrolyte: 6 M KOH.*

Gortex-based gas diffusion electrodes was critical, with the 100 nm electrodes providing the best, albeit overall still very poor access to the catalyst layer by reactant OH^- ions and water molecules.

In order to model the EIS of the fuel cells, we noted that each Nyquist plot exhibited at least two arcs (Figure 3.10(c) and inset). This, combined with the highly porous surface structure evident in Figure 3.4, led us to use the equivalent circuit shown in Figure 3.10(b), which follows ones previously employed in similar systems.[16] This circuit accounted for the pore structure that was present (in terms of pore resistance, R_{pore}, and capacitance, expressed as a constant phase element, CPE_{pore}, involving $Q_{CPE,pore}$, $n_{CPE,pore}$, and C_{pore})[17] as well as catalytic charge transfer (in terms of charge transfer resistance, R_{ct}, and capacitance, expressed as a constant phase element, involving $Q_{CPE,ct}$, $n_{CPE,ct}$, and C_{ct}),[17] and diffusional resistance (Z_d). Table 3.4 provides the resulting data.

The solid lines in Figure 3.10(c) depict the modelled data, while the individual data points show the measured data. As can be seen, an excellent match was obtained between the modelled data and the measured results. The use of the constant phase elements produced a significantly better fit than C_{dl} elements, which is why they were used. The n_{CPE} values are also, in both cases, close to 1 ($n_{CPE,\ pore}$ =0.82-0.85; $n_{CPE,\ ct}$ = 0.85-0.94), supporting the use of constant phase elements.[17]

The data in Table 3.4 indicates that the electrodes sputter-coated with Pt of 100 nm nominal thickness performed the best because the combination of their pore resistance (R_{pore} 0.599 Ω cm^2), their charge transfer resistance (R_{ct} 8.01 Ω cm^2), and their diffusion resistance (Z_d 25.3 Ω cm^2) was the lowest of the samples tested (R_{total}= 33.909 Ω cm^2). By contrast, the 150 nm sample exhibited a pore resistance of R_{pore} 0.698 Ω cm^2, a charge transfer resistance of R_{ct} 16.13 Ω cm^2, and a diffusion resistance of Z_d 35.01 Ω cm^2, giving R_{total}= 51.838 Ω cm^2, which is well above that of the 100 nm sample. This was the case despite the 100 nm sample

having a lower pore capacitance (298.1 μF cm^{-2} vs 907.2 μF cm^{-2}) and charge transfer capacitance (893.7 μF cm^{-2} vs 1068.7 μF cm^{-2}) than the 150 nm electrodes. While the 150 nm electrodes appeared to have provided a greater active area, the lower diffusion resistance, as well as the catalytic charge transfer and pore resistance of the 100 nm sample overwhelmed that effect.

These results confirmed that diffusional access to the 3-phase zone played the major role in the poor performance of these electrodes, however the intrinsic charge transfer resistance was also substantial, even in the best performing system. The electrochemically active surface area of all of the above materials was large, as indirectly indicated by the capacitance values in Table 3.4.

The diffusion resistance likely arose from a general mismatch between the location of the gas-liquid interface and the location of the conductive, catalytic layer. One or more of the reactants likely had to diffuse from the gas-liquid interface to the catalytic coating, and this provided the main impediment to reaction. It is possible that the liquid electrolyte penetrated deeper than 0.85 μm into the Gortex, meaning that the gases would have had to diffuse through a layer of water between the gas-liquid interface and the Pt layer.

It can be concluded that the Pt-coatings in these electrodes were generally too thin and their hydrophobicities too mismatched to that required for the formation of a more substantial 3-phase zone. The minor variations observed in the fuel cell performance of the 50 nm, 100 nm, and 150 nm samples likely derived from complex interactions – involving their differing hydrophobicities, their different Pt layer thicknesses and their differing pore structures – that marginally moved the gas-liquid interface. These variations are irrelevant to the overarching fact that a large 3-phase zone does not appear to have been realized in these electrodes.

While the sputter-coated electrodes were not high performing, they, nevertheless, did demonstrate "leak-free" operation under conditions where the liquid electrolyte was overpressured relative to the gases.

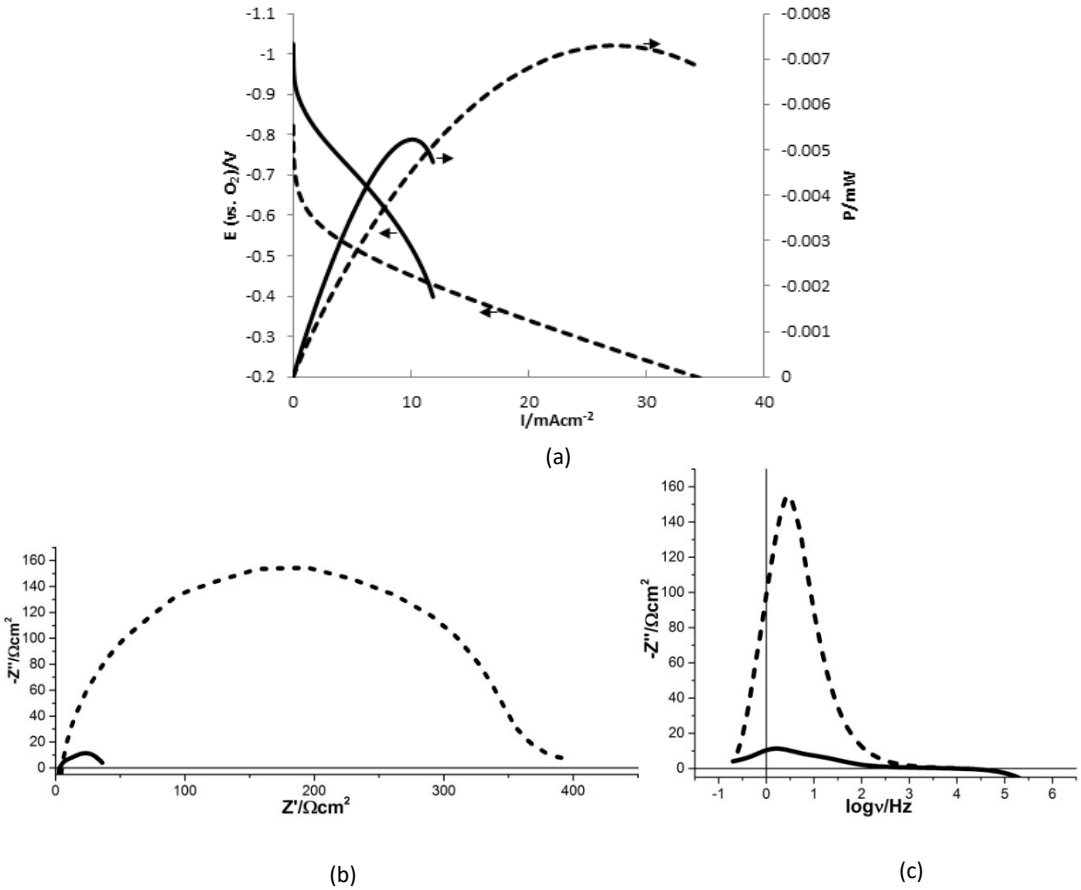

Figure 3.11. *(a) Polarization Curves (left axis) and Power Curves (right axis) at 20 °C for alkaline fuel cells containing Gortex electrodes sputter-coated with Pt having nominal thickness of 100 nm in (——) 6 M KOH and (– – –) 1 M H_2SO_4. (b) Nyquist and (c) Bode plots showing measured data at 0.8 V.*

Another feature of the data is the ohmic resistance (R_Ω) of the cells, which was higher than expected. As 6 M KOH has a conductance at 20 °C of 0.5697 S cm^{-1},[18] R_Ω has a theoretical minimum value of 0.5266 Ω cm^2 when a 3 mm inter-electrode gap is used. However, as can be seen in Table 3.4, the above fuel cells exhibited R_Ω's of 2.63-2.73 Ω cm^2. We initially

assumed that this property also derived from the very high hydrophobicity of the sputter-coated surface of the Gortex electrodes. However, it later came to our attention that the Ni mesh that had been used with the sputter-coated electrodes – a flat, non-woven, electroformed mesh provided by Precision eForming (Cortland, NY) that afforded the best contact with the sputter-coated Pt surface – was overall more resistive than equivalent, weaved Ni meshes of similar lines per inch, at least with the electrical connections of our setup. A comparison of fuel cells utilizing Gortex electrodes overcoated with precious metal catalysts supported on Vulcan XC72 incorporating carbon black, PTFE binder and a Ni mesh displayed a notably lower ohmic resistance when a weaved Ni mesh was used than when the electroformed Ni mesh was used (Chapter 2 Section 2.8.4). Weaved meshes could not be successfully used with the sputter-coated electrodes because they achieved poor contact with the deposited Pt.

Alkaline fuel cells have the inherent advantage of facilitating faster ORR kinetics than is the case in acidic media. In a recent study it was shown that HOR/HER kinetics are 100-fold lower in alkaline medium when compared to acidic medium.[19] To determine the influence of the pH of the electrolyte on fuel cells containing the metallized ePTFE electrodes, polarisation and power curves were measured using strongly alkaline (6 M KOH) and strongly acidic (1 M H_2SO_4) electrolytes. All fuel cell tests were conducted using symmetrical arrangements of electrodes; that is, a nominal thickness of 100 nm of Pt was coated on both anode and cathode in each test. Electroformed Ni mesh as current collector was replaced with weaved stainless steel mesh when the electrolyte medium was changed from alkaline to acidic. The results are shown in Figure 3.11.

As can be seen in Figure 3.11(a), below a current density of 10 mA cm^{-2} strong alkali provided the best electrolyte. Above that current density however, 1 M acidic media was more favourable. To examine the kinetics with these electrolytes, EIS spectra were measured. The wide arc in 1 M acid compared to the smaller arc obtained in alkaline

medium (Figure 3.11(b)) shows that charge transfer at the cathode due to the ORR dominates, becoming the rate determining step even where HOR kinetics were increased in the acidic medium. In respect of ohmic losses, Figure 3.11(b) shows that R_{Ω} was lower in the alkaline electrolyte than in the acidic medium ($R_{\Omega,alkaline}$ = 2.63 Ω cm^2 vs. $R_{\Omega,acidic}$ = 4.72 Ω cm^2). Figure 3.11(c) indicates that, at lower frequencies mass transport impedance was less in the alkaline medium than the acidic medium due to the higher conductivity.

3.2.12 Fuel Cells with Electro-coated Pt on Gortex Electrodes

Another catalyst attachment technique that was studied was electrodeposition (ED). Electrodeposition techniques offer better material utilization efficiency when compared to sputter-coating, and also offer superior structural and morphological control. Figure 3.12 shows SEM images of a 100 nm thick sputtered-coated Pt layer on ePTFE membranes before and after electrodeposition.

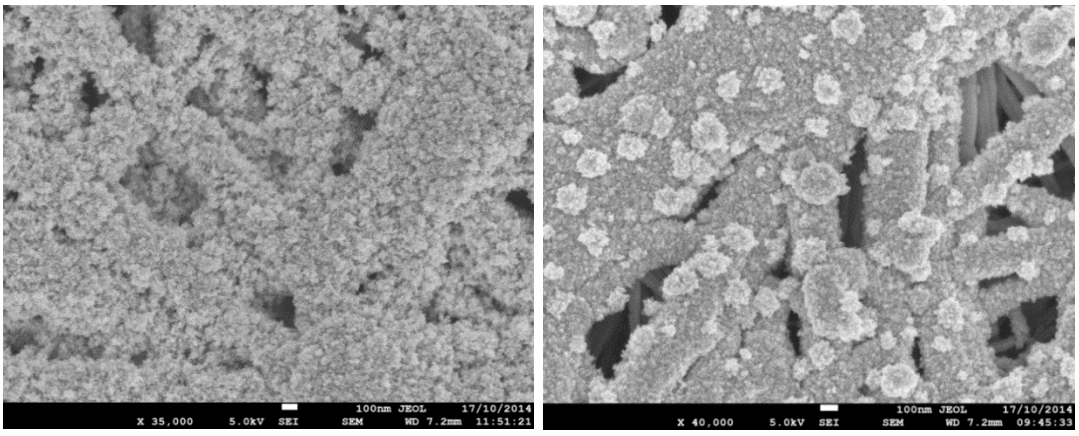

(a) (b)

Figure 3.12. *Scanning electron microscopy (SEM) images of Gortex electrodes electrodeposited with Pt on an underlying layer of sputtered Pt (a) before and (b) after electrodeposition of Pt (initial pulse of -1.0 V applied for 4 s followed by cyclic voltammetry from +0.2 V to -0.58 V up to a charge density of 5 C cm^{-2}).*

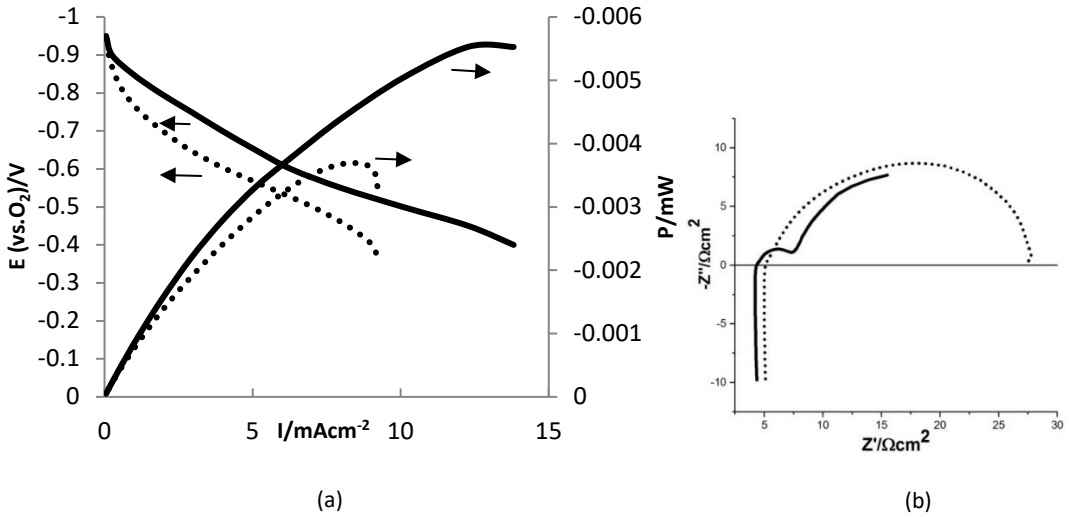

Figure 3.13. *(a) Polarization Curves (left axis) and Power Curves (right axis) at 20 °C for alkaline fuel cells containing Gortex electrodes electrodeposited with Pt on an underlying layer of sputtered Pt before and after electrodeposition of Pt. (• • •) Pt only (nominal thickness = 100 nm) before electrodeposition, (—) Pt electrodeposited on an underlying 100nm layer of Pt. Electrolyte: 6 M KOH. (b) Nyquist plots showing measured data at 0.8 V.*

For electrodeposition, an aqueous solution of 100 mM K_2PtCl_4 and 1 M Na_2SO_4 was used in a three electrode cell with sputtered Pt on Gortex as the working electrode, sputtered Pt on Gortex covered with Ni mesh as auxiliary electrode, and a Pt wire as pseudo reference electrode. An initial pulse of -1.0 V was applied for 4 s followed by cyclic voltammetry from +0.2 V to -0.58 V up to a charge density of 5 C cm^{-2}. As can be seen in Figure 3.13(a), at every measured voltage the current density was higher after ED of platinum. For example, at -0.5 V the current density increased from 5.57 mA cm^{-2} (before ED) to 7.86 mA cm^{-2} (after ED). This increase in current density value can be attributed to the fact that the active surface area of the catalysts increased after ED.

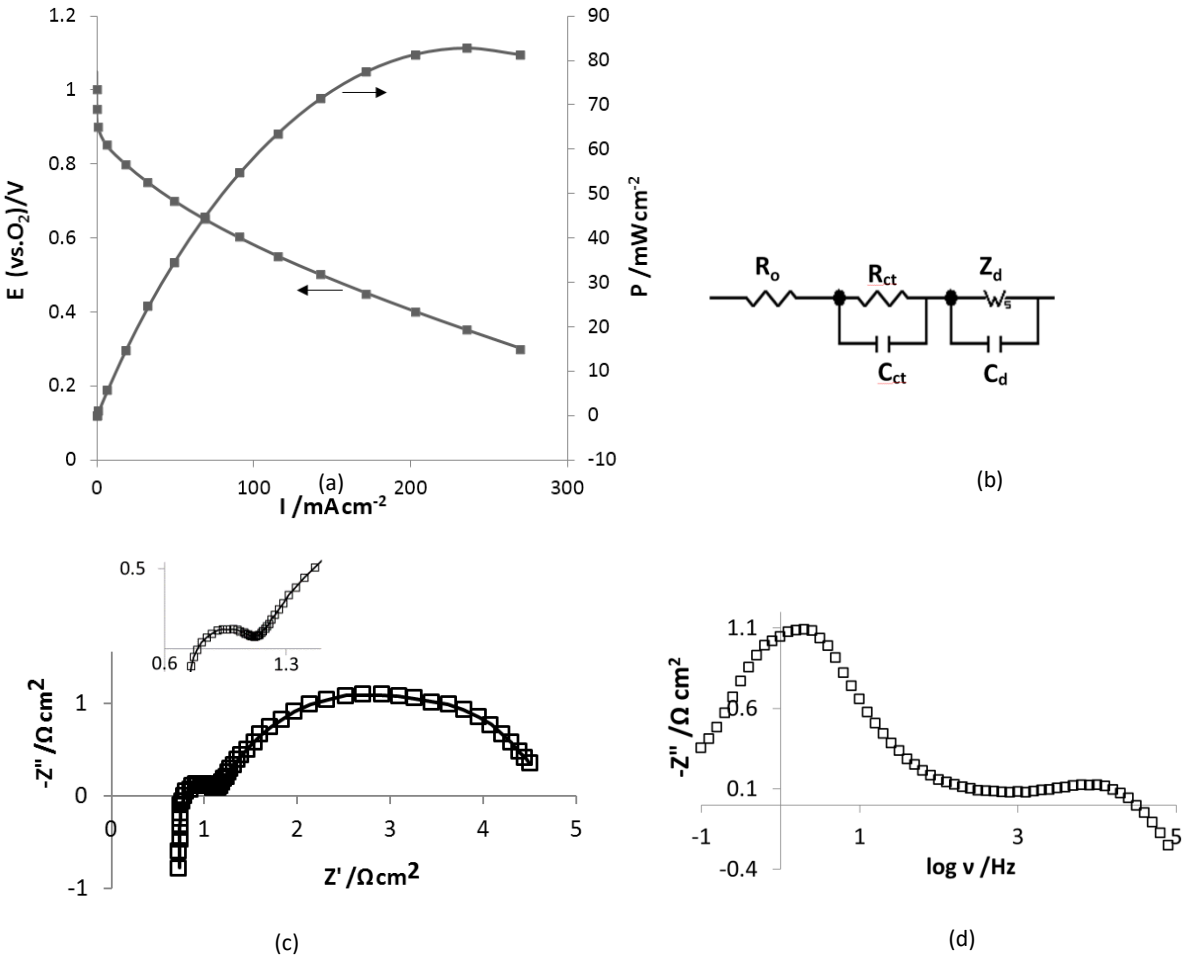

Figure 3.14. *(a) Polarization Curves (left axis) and Power Curves (right axis) at 10 mA cm^{-2} and 20 ^{o}C for alkaline fuel cells containing Gortex electrodes coated with 10% Pt on Vulcan XC72, carbon black, PTFE, and woven Ni mesh. Electrolyte: 6 M KOH. (b) EIS equivalent circuit. (c) Nyquist and (d) Bode plots showing measured data (individual data points) and modelled data (solid line) (modelled using the equivalent circuit depicted in (b)).*

This can be clearly seen in Figure 3.12, which depicts SEM images showing the formation of coarse electrodeposited Pt islands on a Pt sputtered membrane after ED.

Figure 3.13(b) shows the Nyquist spectrum of the ED Pt-coated electrodes. The R_{Ω} was 5.02 Ω cm^2 before ED of Pt which dropped to 4.31 Ω cm^2 after ED of Pt. Electro-coated Pt also

demonstrated a small arc at high frequency, indicative of facile reaction kinetics. The low frequency feature in the impedance spectra likely arises from a gas-phase, mass transfer barrier due to limited diffusivity of oxygen in water formed at cathode.

3.2.13 Fuel Cells with Gortex Electrodes Coated with 10% Pt on Vulcan XC72, Carbon Black, PTFE Binder and Ni Mesh

Gas diffusion electrodes comprising of Gortex membranes coated with 10% Pt on Vulcan XC72, carbon black, PTFE binder and a weaved Ni mesh (200 lines per inch), were then studied in comparable alkaline fuel cells (6 M KOH electrolyte), using symmetrical arrangements of electrodes. That is, the same electrode composition was used at the anode and cathode in each test. The composition of the electrodes was optimized by systematically increasing the weight of the catalyst layer per unit area and measuring: (i) the current at 0.4 V, and (ii) the voltage at 10 mA cm^{-2}. As already discussed in Chapter 2 Section 2.8.5, fuel cell performance improved consistently up to loadings of ca. 0.75 g Pt per m^2 and thereafter plateaued, with little further improvements. Accordingly, the optimum electrodes were fabricated with catalyst loadings of 0.75 g Pt per m^2. This equated to a Pt loading of 0.075 mg/cm^2, which was an order of magnitude lower than comparable PEM hydrogen – oxygen fuel cells, which typically employ Pt loadings of ~0.3 mg/cm^2.[19(a)]

Figure 3.14(a) depicts polarisation (left axis) and power density (right axis) curves for an alkaline fuel cell (6 M KOH electrolyte) incorporating the optimized electrodes. Figure 3.14(b) depicts the equivalent circuit used for modelling the corresponding two-electrode electrochemical impedance spectrum in the form of a Nyquist plot (Figure 3.14(c)) and Bode plot (Figure 3.14(d)), measured galvanostatically at 10 mA cm^{-2}.

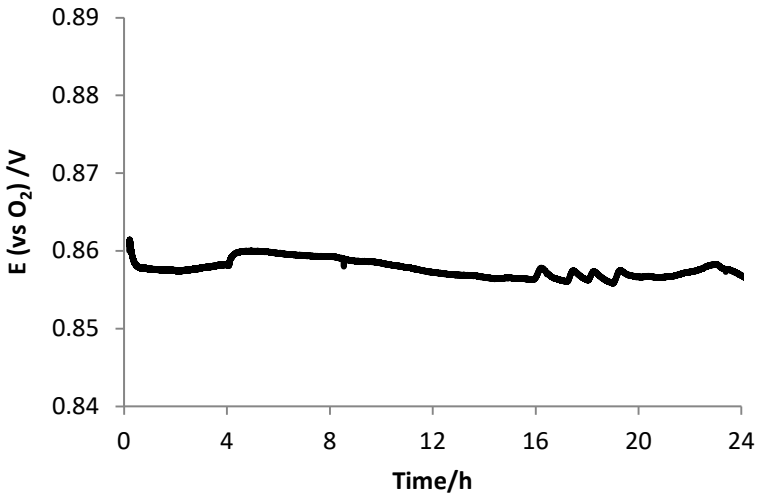

Figure 3.15. *Chronopotentiogram measured over 24 h at + 10 mA cm^{-2} for a symmetrical fuel cell utilizing Gortex electrodes incorporating 10% Pt on Vulcan XC 72 catalyst. The small variations observed in the measured voltage appear to coincide with small temperature variations in the environment, including due to the fume cupboard turning on and off. Carbon black used in the catalyst slurry was treated with ascorbic acid prior to use.*

As can be seen, the above gas diffusion electrodes performed very significantly better than their sputter-coated analogues, with the alkaline fuel cell generating 230 mA cm^{-2} and 84 mA cm^{-2} at 0.35 V and 20 ^{o}C. At a constant 0.7 V, the cell produced 75 mA cm^{-2}. At 10 mA cm^{-2}, the cell produced a constant 0.857-0.860 V over 2 d of continuous operation with the electrolyte headspace open to the air (Figure 3.15). The minor variations in the voltage observed over that period appeared to be periodic and associated with small temperature fluctuations in the external environment, including when the fume hood was opened and closed. The cell was clearly robustly tolerant of CO_2.

Catalyst Layer	Activation overpotential (V)	Voltage at 10 mA cm^{-2} (V)	R_Ω (Ω cm^2)	R_{ct} (Ω cm^2)	C_{ct} (F)	Z_d (Ω cm^2)
10%Pt on Vulcan, carbon black, PTFE, weaved Ni mesh	0.375	0.857-0.860	0.79	0.31	0.000098	3.4

Table 3.5. *Electrochemical Impedance Spectroscopy modelling data for ohmic resistance (R_Ω), charge transfer resistance (R_{ct}), charge transfer capacitance (C_{ct}) and diffusion resistance (Z_d) of the alkaline fuel cell containing Gortex electrodes coated with 10% Pt on Vulcan XC72, carbon black, PTFE, and Ni mesh. Electrolyte: 6 M KOH. The equivalent circuit in Figure 3.13(b) was used to model the EIS data.*

These results compare well with previously reported alkaline fuel cells. For example, Gouérec and co-workers at Eident Energy built alkaline fuel cells containing 0.6-0.7 mg Pt per cm^2 at both the anode and cathode, that yielded ca. 55 mA cm^{-2} at 0.7 V.[20(a)] Strasser and co-workers recently described a Pt-based reversible alkaline fuel cell – electrolyser that generated 60 mA cm^{-2} at 0.7 V in fuel cell mode and used 0.5 mg Pt/cm^2, which is about triple the Pt loading of the present study.[19(b)] Kiros and colleagues[20(b)] and Kordesch and colleagues[20(c)] have previously reported alkaline fuel cells that delivered 88-125 mA cm^{-2} and 125-160 mA cm^{-2}, respectively, at 0.7 V at elevated temperatures and pressures. The latter had been used in a vehicle application. Tomantschger et al. have previously shown that increases in temperature and pressure amplify current and power densities in alkaline fuel cells.[6(b)] PEM fuel cells generally produce higher current and power densities than alkaline fuel cells, albeit at higher cost, due, usually, to higher Pt loadings and smaller inter-electrode gaps. For example, the PEM fuel cells of Ioroi and co-workers[21] yielded ca. 500 mA cm^{-2} at 0.7 V and 80 ^oC thanks to Pt/Ir loadings that were around 50-times larger and an inter-electrode separation (0.127 mm) that was one-twentieth that used in this work.

The EIS data of the above fuel cell was modelled using the equivalent circuit depicted in Figure 3.13(b). The individual data points in Figure 3.13(c) show the data as measured, while the solid lines in Figure 3.13(c) show the modelled data. As can be seen, there was, for this fuel cell also, an outstanding fit of the modelled and the measured data. The modelling results are provided in Table 3.5.

As can be seen, all of the EIS data substantially improve upon their equivalents in the fuel cells utilizing the sputter-coated Gortex electrodes. The charge transfer resistance (R_{ct} 0.3 Ω cm^2) and diffusion resistance (Z_d 3.4 Ω cm^2) were both orders of magnitude lower. The ohmic resistance (R_Ω 0.79 Ω cm^2) was also close to the expected resistance of 0.5266 Ω cm^2 for a 6 M KOH solution at 20 ^oC over a 3 mm inter-electrode gap.[18] The activation overpotential, which corresponds to the hypothetical y-axis intercept of the ohmic region of the polarisation curve, was 0.375 V. The hydrophilicity of the particulate coating, which was confirmed by the absence of a contact angle, clearly drastically improved the performance of the Gortex electrodes.

3.2.14 The Significance of these Results: An Efficient Gas Diffusion Electrode that is Highly Flood-Resistant

The Gortex electrodes coated with 10% Pt on Vulcan XC72, carbon black, PTFE binder and a fine, weaved Ni mesh current carrier, were therefore efficient and highly active electrodes in the above alkaline fuel cell. This is significant because, as noted earlier, the half-reaction at the cathode of the above fuel cell is identical to the half-reaction at an oxygen-depolarised cathode in a chlor-alkali cell (equation (3)), which also operates under strongly basic conditions. It can be concluded that such Gortex-based electrodes may potentially have practical utility in efficiently depolarising counter electrodes in the chlor-alkali process and in other industrial electrochemical processes of similar ilk.[1(a)] Their prime advantage in this respect would, however, not only be their high electrochemical performance but also the fact

that they display a hitherto unprecedented resistance to flooding and leaking. Indeed, using pure water, they only leak when the excess of the water-side pressure over the gas side pressure is 5.7 bar (Table 3.1). This is more than an order of magnitude greater than any gas diffusion electrode developed to date and overcomes the key impediment that has prevented the use of gas depolarisation at the counter electrode in chlor-alkali cells.[1]

Given the ready availability, low cost, and narrow engineering specifications of Gortex membranes, Gortex-based gas diffusion electrodes of this type can potentially be reproducibly manufactured in volume. As such, these results may be important for the gas-depolarisation using gas diffusion electrodes in industrial electrochemistry.

3.3 Conclusions

This Chapter has sought to address the obstinate challenge of flooding and leaking that has, to date, made the widespread adoption of gas diffusion electrodes impossible in industrial electrochemical processes. A new approach has been developed in which the gas diffusion layer of such electrodes has been optimized in terms of water-repellence (for flood-resistance) and porosity (for gas transport) but not electrical conductance (for electron transport), which has, instead, been provided by other means.

Gortex membranes, also known as *expanded PTFE* (or *ePTFE)*, are well-known to be near-ideal in respect of water-repellence and porosity. In this Chapter, they have been used, in finely-pored form, as gas diffusion layers in novel gas diffusion electrodes. The Gortex membranes were coated with thinly-applied, sputter-coated Pt, or thickly-applied mixtures of particulate, supported Pt incorporating carbon black, and PTFE binder. Fine Ni meshes, either wedged tight against, or included within the catalyst layer, served as electron conductors and current carriers. The thinly-coated electrodes proved to be too hydrophobic and too thinly coated at their catalytic surfaces to afford efficient electrochemical operation

using an aqueous electrolyte. However, the catalyst layers in the particulate electrodes were well-wetted and produced high electrochemical performance. Accompanying that high performance, they also displayed hitherto unprecedented water-entry pressures for a gas diffusion electrode, demonstrating a remarkable resistance to flooding and leaking. Capillary flow porometry on the Gortex-based electrodes showed them to flood and leak only when the excess of pressure on their liquid-side over the gas-side was a remarkable 4.3-5.7 bar.

When deployed in a desktop alkaline fuel cell charged with aqueous 6 M KOH electrolyte, the particulate-coated Gortex electrodes generated current and power densities of 230 mA cm^{-2} and 84 mW cm^{-2}, respectively, at 0.35 V. This was achieved with extremely low Pt loadings (0.075 mg cm^{-2}) during room temperature operation. The alkaline fuel cells also functioned without need for an ion-permeable, gas-impermeable diaphragm between the electrodes and were robustly tolerant of CO_2 over extended periods.

In conventional gas diffusion electrodes, the entire electrode is generally conductive, with a variety of pore sizes of differing hydrophobicity causing the three-way solid-liquid-gas interface to be distributed within the catalyst layer. This interface is therefore relatively poorly controlled and ill-defined, making the electrode prone to flooding and leaking. By contrast, Gortex-based electrodes of the present study have smaller, more uniform, more hydrophobic pores that better confine the solid-liquid-gas interface to the catalyst layer. Whereas a conventional gas diffusion electrode relies upon the presence of larger pores on the gas side to provide for low-pressure ingress of gases to the interface, Gortex-based gas diffusion electrodes rely upon the Gortex membrane to provide for ready and unhindered ingress of gases. Such an electrode may be distinguished by the fact that it has a better-defined and narrower three-phase solid-liquid-gas interface, whose structure and character is quite different to that found in traditional gas diffusion electrodes.

References

1. (a) Moussallem, I.; Jörissen, J.; Kunz, U.; Pinnow, S.; Turek, T. *J. Appl. Electrochem.* **2008**, *38*, 1177 and references therein; (b) Gullá, A. F.; Krasovic, J. L. *International Patent application* ***WO2013037902***, and references therein.
2. (a) McLean, G. F.; Niet, T.; Prince-Richard, S.; Djilali, N. *Int. J. Hydrog. Energy* **2002**, *27*, 507; (b) Gülzow, E. *J. Power Sources* **1996**, *61*, 99; (c) Rolla, A.; Sadkowski, A.; Wild, J.; Zóltowski, P. *J. Power Sources* **1980**, *5*, 189, and references therein.
3. (a) Wagner, K.; Tiwari, P.; Swiegers, G. F.; Wallace, G. G. *Adv. Energy Mat.* accepted; (b) Wagner, K.; Tiwari, P.; Swiegers, G. F.; Wallace, G. G. *Energy. Environ. Sci.* accepted for publication.
4. (a) Goetz, M; Lefebvre, J.; Moers, F.; McDaniel Koch, A.; Graf, F.; Bajohr, S.; Reimert, R.; Kolb, T. *Renewable Energy* **2016**, *85*, 1371; (b) Melaina, M. W.; Antonia, O.; Penev, M. in "*Blending Hydrogen into Natural Gas Pipeline Networks: A Review of Key Issues*" Technical Report NREL/TP-5600-51995, National Renewable Energy Laboratory, March 2013, and references therein (https://energy.gov/eere/fuelcells /downloads/blending-hydrogen-natural-gas-pipeline-networks-review-key-issues); (c) "*Power-to-Gas: The Case for Hydrogen - White Paper*", California Hydrogen Business Council, Los Angeles, CA 90049, 2015 and references therein (https://californiahydrogen.org/sites/default/files/CHBC%20Hydrogen%20Energy%20Storage%20White%20Paper%20FINAL.pdf)
5. (Inventors not named) *British patents* ***985,063***; ***985,239***; ***1,014,335***; ***1,020,918***; ***1,032,935***; E. Guth, *US patent* ***3,238,069***; Plust, H.-G.; Telschow, C. G. *US patent* ***3,248,787***; Dieberg, R. *US patent* ***3,306,780***.
6. For alkaline fuel cell gas diffusion electrodes, see: (a) Liu, J.; Yang, C.; Liu, C.; Wang, F.; Song, Y. *Ind. Eng. Chem. Res.* **2014**, *53*, 5866, and references therein; (b) Tomantschger, K.; McClusky, F.; Oporto, L.; Reid, A.; Kordesch, K. *J. Power Sources*

1986, *18*, 317, and references therein; (c) Bidault, F.; Brett, D. J. L.; Middleton, P. H.; Brandon, N. P. *J. Power Sources* **2009**, *187*, 39, and references therein.

7. De Geeter, E.; Mangan, M.; Spaepen, S.; Stinissen, W.; Vennekens, G. *J. Power Sources* **1999**, *80*, 2017.
8. (a) Winther-Jensen, B.; Winther-Jensen, O.; Forsyth, M.; MacFarlane, D. R. *Science* **2008**, *321*, 671; (b) Winther-Jensen, B.; Fraser, K.; Ong, C.; Forsyth, M.; MacFarlane, D. R. *Adv. Mat.* **2010**, *22*, 1727; (c) Winther-Jensen, O.; Chatjaroenporn, K.; Winther-Jensen, B.; MacFarlane, D. R. *Int. J. Hydrog. Energy* **2012**, *37*, 8185; (d) Kolodziejczyk, B.; Winther-Jensen, O.; Pereira, B. A.; Nair, S. S.; Winther-Jensen, B. *J. Appl. Polymer Sci*. **2015**, *132*, 42359.
9. (a) Wikol, M.; Hartmann, B.; Brendle, J.; Crane, M.; Beuscher, U.; Brake, J.; Shickel, T. Chap 23 in *Filtration and Purification in the Biopharmaceutical Industry, Second Edition* (Eds. Jornitz, M. W.; Meltzer, T. H.), Taylor & Francis, 2007; (b) AlMarzooqi, F. A.; Bilad, M. R.; Mansoor, B.; Arafat, H. A. *J. Mater. Sci.* **2016**, *51*, 2017.
10. Tang, Y.; Yang, R.; Du, Z.; Zeng, F. *Transp Porous Med* **2015**, *107*, 205 (DOI 10.1007/s11242-014-0433-1)
11. See for example: Tomantschger, K.; Kordesch, K. V. *J. Power Sources* **1989**, *25*, 195, and references therein
12. (a) Rigby, S. P. *J. Colloid Interf. Sci.*, **2000**, *224*, 382; (b) Calvo, J. I.; Hernandez, A.; Pradanos, P.; Martinez, L.; Bowen, W. R. *J. Colloid Interf. Sci.* **1995**, *176*, 467; (c) Li, D. P.; Frey, M. W.; Joo, Y. L. *J. Membrane Sci.*, **2006**, *286*, 104-114; (d) Rigby, S. P.; Daut, S. *Adv. Colloid Interfac.* **2002**, *98*, 87.
13. O'Hayre, R.; Lee, Cha, S.-W.; Prinz, F. B. *J. Power Sources* **2002**, *109*, 483.
14. Rheinländer, P. J.; Herranz, J.; Durst, J.; Gasteiger, H. A. *J. Electrochem. Soc.* **2014**, *161*, F1448.
15. Yuan, X.-Z.; Song, C.; Wang, H.; Zhang, J. in *Electrochemical Impedance Spectroscopy in PEM Fuel Cells: Fundamentals and Applications*, eds. Yuan, X.-Z.; Song, C.; Wang,

H.; Zhang, J.; Springer London, London, 2010 (DOI: 10.1007/978-1-84882-846-9_5, pp. 193-262).

16. (a) Manazoglu, M.; Hapci, G.; Orhan, G. *J. Mater. Eng. Perform.* **2016**, *25*, 130 (DOI: 10.1007/s11665-015-1849-7); (b) Swierk, J. R.; Klaus, S.; Trotochaud, L.; Bell, A. T.; Tilley, T. D. *J. Phys. Chem. C* **2015**, *119*, 19022; (c) Doyle, R. L.; Lyons, M. E. G. *Phys. Chem. Chem. Phys.* **2013**, *15*, 5224; (d) Papaderakis, A.; Tsiplakides, D.; Balomenou, S.; Sotiropoulos, S. *J. Electroanal. Chem*. **2015**, *57*, 216.
17. Brug, G. J.; van den Eeden, A. L. G.; Sluyters-Rehbach, M.; Sluyters, J. H. *J. Electroanal. Chem.* **1984**, *176*, 275.
18. Gilliam, R. J.; Graydon, J. W.; Kirk, D. W.; Thorpe, S. J. *Int. J. Hydrogen Energy* **2007**, *32*, 359.
19. (a) Gasteiger, H. A.; Kocha, S. S.; Sompalli, B.; Wagner, F. T. *Appl. Catal., B* **2005**, 56, 9; (b) Oezaslan, M.; Hasche, F.; Strasser, P. *J. Electrochem. Soc.* **2012**, 159, B394.
20. (a) Gouérec, P.; Poletto, L.; Denizot, J.; Sanchez-Cortezon, E.; Miners, J. H. *J. Power Sources* **2004**, *129*, 193; (b) Kiros, Y.; Myren, C.; Schwartz, S.; Sampathrajan, A.; Ramanathan, M. *Int. J. Hydrogen Energy* **1999**, *24*, 549; (c) Kordesch, K.; Gsellmann, J.; Cifrain, M.; Voss, S.; Hacker, V.; Aronson, R. R.; Fabjan, C.; Hejze, T.; Daniel-Ivad, J. *J. Power Sources* **1999**, *80*, 190.
21. Ioroi, T.; Okub, T.; Yasuda, K.; Kumagai, N.; Miyazaki, Y. *J. Power Sources* **2003**, *124*, 385.

CHAPTER 4

Gortex Electrode Substrates May Drastically Diminish the Activation Overpotential for O_2 Formation from Water. Alkaline Electrolysers with Remarkably Low Activation Overpotentials

4.1 Introduction

As noted earlier, a water electrolyser splits water electrochemically into its component gases, hydrogen (H_2) and oxygen (O_2). When including the effects of electrical energy and heat, the reaction may be formulated as follows:[1]

$$2\,H_2O + electricity + heat \rightarrow O_2(g) + 2\,H_2(g) \qquad E^0_{cell} = -1.23\ V \qquad ...(4.1)$$

The negative sign for E_{cell} indicates that electrical energy must be applied to drive the reaction; that is, the overall reaction is not thermodynamically favoured. The minimum electrical voltage that must be applied in order for the reaction to occur is 1.23 V (vs NHE). As can also be seen in the above equation, water electrolysis is an *endothermic* reaction that requires heat. This heat derives from the heat energy component that is present in hydrogen. When operated above the *equilibrium voltage* (1.23 V at 25 ^oC; 1.18 V at 80 ^oC), that heat is

supplied by the resistance deriving from the electrical current. At the so-called *thermoneutral voltage* (1.48 V at 25-80 ºC) the heat generated by the electrical current equals the heat required by the reaction in equation 4.1. Above, the *thermoneutral voltage*, excess heat is generated. That is, the electrical current generates more heat than is needed by the reaction and this heat is radiated, making the overall process *exothermic*. Figure 4.1 depicts these voltage ranges as a function of the reaction temperature.

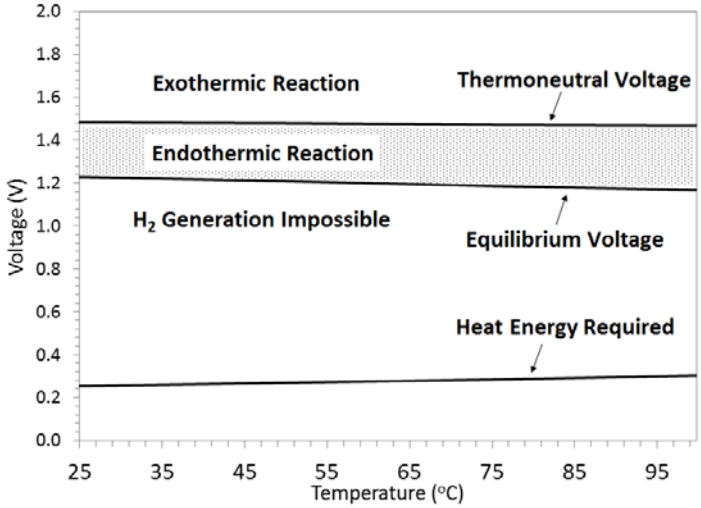

Figure 4.1. *Cell potentials for water electrolysis as a function of temperature.*[2(b)]

These voltage ranges arise, fundamentally, because hydrogen gas contains 33.33 kWh kg^{-1} of electrical energy and 6.08 kWh kg^{-1} of heat energy.[2(a)] The minimum theoretical potential needed to provide the 33.33 kWh kg^{-1} of electrical energy is the *equilibrium voltage*.[2(a)] A higher voltage – the *thermoneutral voltage* – is required to produce the additional 6.08 kWh kg^{-1} of heat energy (by the resistance to the electrical current).[2(a)] The former (33.33 kWh kg^{-1}) corresponds to the *Lower Heating Value* (or LHV) of hydrogen, while the sum of the two (33.33 + 6.08 = 39.41 kWh kg^{-1}) corresponds to the *Higher Heating Value* (or HHV) of hydrogen (as discussed in Chapter 1).[2(a)]

Figure 4.1 shows that, when a voltage is applied to an electrolyser in the range between the *equilibrium voltage* and the *thermoneutral voltage*, the electrolyser should, in theory,

produce insufficient heat, causing it to extract heat from its surroundings. That is, under these conditions, the electrolyser should "*run cold*". To the best of our knowledge however, endothermic operation of this type has never been demonstrated in actual practice in an operating electrolyser. When a voltage above 1.48 V is applied, excess heat should be produced, which the electrolyser radiates to its surroundings, causing it to "*run hot*". This is the standard operating condition of water electrolysers at the present time.

While the above quantities are well known, very few catalysts, in fact, have the capacity to facilitate water electrolysis below the thermoneutral voltage, at the thermoneutral voltage, or even above but near to the thermoneutral voltage. In the field of alkaline water electrolysis, Dai and co-workers reported in 2014, a two-electrode electrolyser that achieved 20 mA cm^{-2} at a voltage of 1.50 V at room temperature.[3] The electrolyser could be sustainably operated with a single-cell alkaline battery. The catalysts were nanoscale NiO and Ni heterostructures on carbon nanotube sidewalls (Ni-CNT) for the hydrogen evolution reaction (HER) and a NiFe-layered double hydroxide for the oxygen evolution reaction (OER); they displayed activities that were comparable to Pt/C.[3] Wang and colleagues later reported an alkaline electrolyser that approached 20 mA cm^{-2} at a voltage of 1.55 V using a bifunctional catalyst.[4] Cui and co-workers subsequently reported a two-electrode electrolyser utilizing non-noble metal catalysts that achieved a water-splitting current of 10 mA cm^{-2} at 1.51 V for >200 h.[5] This was better than the combination of Ir and Pt as benchmark catalysts in the 1 M KOH electrolyte used.[5]

It should be noted that catalysts for water-splitting are routinely compared to each other at low current densities (e.g. 10 mA cm^{-2})[6] in order to minimize differences arising from extraneous influences, such as electrical resistance in the driving circuits, ohmic resistance in the electrolyte, and mass transport effects.

To the best of our knowledge, the most active reported alkaline water electrolysers are those of Schiller,[7] Hug[8] and Villa.[9] Schiller and co-workers[7] used Raney-Ni (HER catalyst) and a Raney-Ni/Co_3O_4 composite (OER catalyst), both produced by vacuum plasma spraying (VPS), in an electrolyser having a "zero gap" configuration[10] (<0.5 mm inter-electrode distance). Their cell achieved 25 mA cm^{-2} at 1.44 V at 80 ^oC.[7] Hug and colleagues[8] used "galvanically-fixed" Raney-Ni (HER catalyst) and Raney-Ni : Fe-powder (OER catalyst), also in a "zero-gap" cell.[10] Their cell yielded 1.41 V at 10 mA/cm^2 at 80 ^oC. Villa and co-workers[9] used closely arrayed gas diffusion electrodes comprising Raney-Ni(Mo)+PTFE (HER catalyst) and Raney-Ni(Fe)+PTFE (OER catalyst) to also achieve 10 mA cm^{-2} at 1.41 V at 80 ^oC. All of the above cells employed 6 M KOH as electrolyte.

In the field of acid-based, *Proton Exchange Membrane* (PEM) electrolysers, which is presently considered to be the cutting edge of water electrolysis technology, Zhigang and colleagues reported a cell with Pt black (HER catalyst) and IrO_2 (OER catalyst) that consumed 50 mA cm^{-2} at 1.48 V at 80 ^oC in electrolysis mode during scanning.[11] Swette and colleagues achieved voltages as low as 1.45 V under similar circumstances with similar catalysts in a PEM cell.[12]

To the best of our knowledge, the record for the lowest published electrolyser cell potential at 10 mA cm^{-2} is held by Ioroi and colleagues,[13] who reported a unitized, regenerative PEM fuel cell–electrolyser utilizing Pt black (HER and OER; 3-4 mg Pt per cm^2), that, at 80 ^oC, yielded 10 mA cm^{-2} at 1.40 V in electrolyser mode. In fuel cell mode at 80 ^oC, the same cell generated 0.93 V at 10 mA cm^{-2} in the opposite direction, giving a round-trip energy efficiency at 10 mA cm^{-2} in each direction, of 66.4%.[13] This value assumes complete conservation of heat; i.e. that the heat generated during fuel cell operation was used to maintain the temperature of the cell during electrolyser operation. The cell utilized a Nafion 115 proton exchange membrane, meaning that its inter-electrode gap was 0.127 mm.

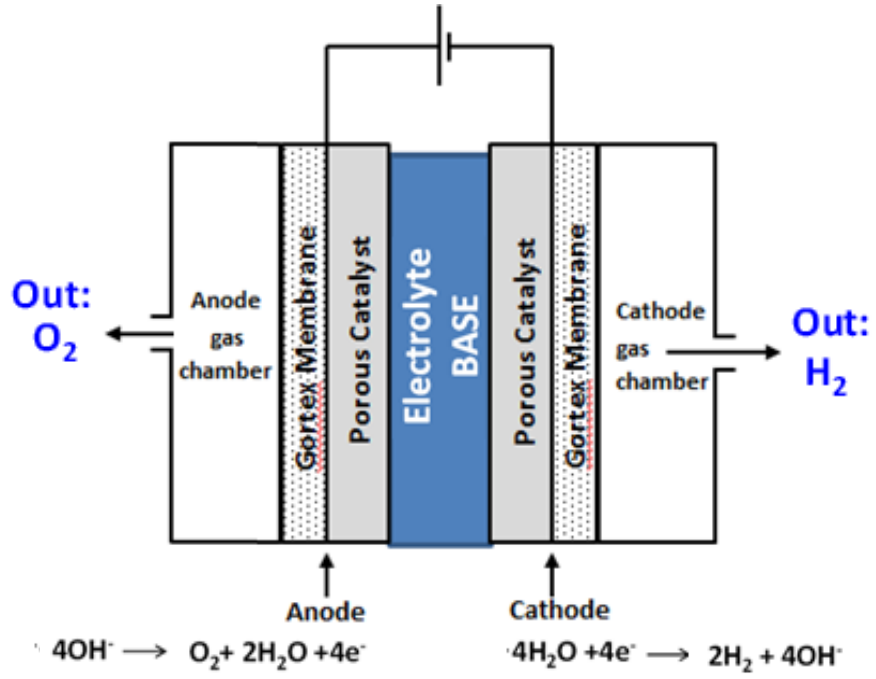

Figure 4.2. *Schematic depiction of an electrolyser cell used for the studies in this Chapter.*

In this chapter, we describe novel alkaline electrolysers of the type depicted in Figure 4.2, employing conventional catalysts and Ni meshes layered on Gortex membrane electrodes, with 10 mm inter-electrode gaps that sustainably achieved 10 mA cm^{-2} at voltages as low as 1.23 V after 1 h at 80 ^oC. The total cell activation overpotential, η_{Cell}, was as low as 0.09 V. These effects were further indicated to derive from the Gortex substrate, which appeared to facilitate "bubble-free" hydrogen and oxygen formation to thereby drastically decrease the activation overpotential for water-splitting as the temperature was increased to 80 ^oC and above. The Gortex appeared, specifically, to largely eliminate the bubble overpotential for oxygen formation, with an accompanying decrease to near-negligible proportions, in the activation overpotential for oxygen formation from water. Equivalent, high-performing fuel cell with Gortex-based electrodes generated 0.88-0.89 V at 10 mA cm^{-2} in the reverse direction after 1 h at 80 ^oC. The combination of the most efficient of the above electrolysers and the cells have a notional round-trip energy efficiency of 72.4%-73.5%, after 1 h at 10 mA cm^{-2} and 80 ^oC in each direction, assuming full conservation of heat.

4.2 Results & Discussion

4.2.1 Use of expanded PTFE (*ePTFE*) Membrane ('Gortex') as an Electrode Substrate

In several recent studies, a novel material, *Gortex*, has been employed as an electrode substrate.[14-18] The unique properties of Gortex[19] and its numerous applications[20], have been discussed in Chapter 3 Section 3.2.3.

As previously noted, the key utility of *Gortex* is that it combines high porosity with high hydrophobicity to thereby allow the passage of gases but not aqueous liquids. For example, in textile applications Gortex allows the water vapour from a wearer's body to pass through, but not liquid rain that may fall on the textile. A promising feature of Gortex is that it has a significantly more uniform and hydrophobic pore structure than is possible in present-day, conventional gas diffusion electrodes. Thus, finely-pored Gortex membranes may be used to fabricate gas diffusion electrodes that do not flood until the excess of the water-side pressure over the gas-side pressure is >4 bar.[14] This is more than an order of magnitude greater than conventional gas diffusion electrodes, which typically flood at overpressures of <0.1 bar.[21] It drastically supersedes the cutting edge in conventional gas diffusion electrode technology, which involves leak/flooding resistance up to 0.2 bar.[22] Highly flood/leak-resistant electrodes of this type potentially open up the possibility of substantially decreasing the energy consumption of several industrial electrochemical processes, by bathing their unproductive counter-electrodes in a depolarising gas.[21] This field has, to date, been blocked in practice by the low resistance of conventional gas diffusion electrodes to flooding/leaking.

Novel, active Gortex-based gas diffusion electrodes have also been successfully deployed in fuel cells and electrolysers.[15-18] The Gortex gas diffusion electrodes in the water electrolysers were found to split water into its constituent gases without generating gas bubbles in the aqueous electrolyte; that is they directly produced the gases in a "bubble-free" manner.[17]

However, these studies involved relatively poor and/or little-known catalytic materials. The use of conventional, high-performing water-splitting and fuel cell catalysts, deposited on Gortex, was not examined. The studies also did not consider the effect of bubble-free generation of hydrogen and oxygen from water using Gortex-based gas diffusion electrodes on the thermodynamics of the water electrolysis process.[17(a)] This is of interest since bubble formation is known to consume energy, but the quantity of energy required has not, to the best our knowledge, been firmly established. The mechanism of the bubble-free gas formation was also not studied.

To remedy these omissions, a set of gas diffusion electrodes were prepared comprising of Gortex membrane substrates layered with a range of well-known catalysts, utilizing dispersed, colloidal poly(tetrafluoroethylene) (PTFE) as a binder and a fine Ni mesh as a current carrier. Combinations of these were then studied as anodes and cathodes in a two-electrode, desktop water electrolyser, including the effect that they had on the thermodynamics of water electrolysis. While twenty-seven different catalysts were examined in all, this Chapter reports notable results involving only three of those catalysts; namely, Raney Ni, cubical $NiCo_2O_4$ spinel, and 10% Pt on carbon black. A full compilation of results for all of the catalysts studied are presented in Chapters 5-6 of this work. The present Chapter also describes an equivalent high-performing fuel cell, fabricated in the same desktop cell, and employing 20% Pd-Pt/CB as anode and cathode catalyst. Polypropylene-backed *Preveil*^{TM} expanded PTFE (ePTFE) ('Gortex') membranes, produced by General Electric Energy were used in all experiments. The membranes were resistant to flooding/leaking to liquid-side overpressures of >4 bar.

4.2.2 Catalyst Slurries and their incorporation as a Layer on Porous, ePTFE Membrane Electrodes

Chapter 2 provides a detailed description of the experimental techniques used in this Chapter. The text below summarizes how the study was carried out.

In the initial phase of the study, the adherence to the Gortex membranes, of various powdered catalysts, with and without carbon black powder, when mixed with aqueous-alcoholic solutions of dispersed PTFE as a binder was prepared and tested. The optimum recipe from an adherence and catalytic performance point of view, proved to contain 30-50% by weight of PTFE after drying, with the rest made up of the powdered catalytic and/or carbon black materials (details in Chapter 2).

Catalyst coated Gortex electrodes were prepared and mounted as described in Chapter 2 Section 2.4. The mounted electrodes could be interchangeably incorporated into a custom-built, desktop, stainless steel test cell (see Chapter 2 Section 2.5). The configuration of the stainless steel test cell during electrolyser operation is described in Section 2.7. The arrangement of the same cell when operated as a fuel cell is described in Section 2.6.

To maintain a constant temperature, the entire desktop test cell was submersed in a stirred, temperature-controlled, water bath containing de-ionized water. The water-bath was wrapped with thermal insulation during the experiments. A heater-controller maintained the water bath at the set temperature. The sealed nature of the test cell ensured that its gaseous and liquid contents did not contact or mix with the surrounding water in the water bath.

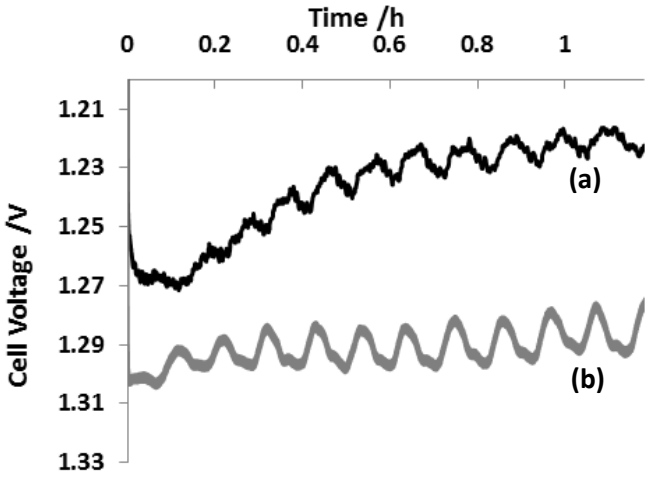

Figure 4.3. *Chronoamperograms at 10 mA cm^{-2} of electrolysers operating at 80 ^{o}C and comprising of: (a) Raney Ni+CB+PTFE+Ni-mesh/Gortex (cathode) and $NiCo_2O_4$+PTFE+Ni-mesh/Gortex (anode), and (b) 10% Pt/CB+PTFE+Ni-mesh/Gortex (cathode) and $NiCo_2O_4$+PTFE+Ni-mesh/Gortex (anode). The periodic fluctuations in the measured voltage appeared to derive from temperature swings (~±5 ^{o}C) that occurred in the water bath.*

4.2.3 Chronoamperometry of Electrolysers with Gortex-based Gas Diffusion Electrodes

Electrochemical testing as a water electrolyser was carried out using different combinations of catalyst+PTFE+Ni-mesh/Gortex electrodes in the above cell. To eliminate artefacts arising from transiently high or low activities (which is common in, particularly, Pt catalysts) and any possible sacrificial reactions, the catalytic electrodes were initially poised at a constant 10 mA cm^{-2} for >1 h at 80 ^{o}C and their performance monitored.

The most active combination of electrodes for water electrolysis using this approach involved a cathode comprising of a mixture of Raney Ni (388 g per m^2), carbon black (CB) (24 g per m^2) and PTFE (152 g per m^2) with a fine, woven Ni mesh current collector, deposited on Gortex ('Raney Ni+CB+PTFE+Ni-mesh/Gortex'). When combined with an

anode, containing cubical $NiCo_2O_4$ spinel (262 g per m^2) and PTFE (167 g per m^2) with a fine, woven Ni mesh current collector, deposited on Gortex ('$NiCo_2O_4$+PTFE+Ni-mesh/Gortex'), the resulting electrolyser required a remarkably low 1.23 – 1.27 V to generate 10 mA cm^{-2} over 1 h at 80±5 ^oC in 6 M KOH.

Figure 4.3(a) depicts the chronoamperogram of the electrolyser. As can be seen, the electrolyser initially required a cell voltage of 1.26±0.03 V to maintain the 10 mA cm^{-2} current, however over 1 h, its cell voltage declined steadily to eventually stabilize at around 1.23 V.

The periodic voltage fluctuations that can be seen in Figure 4.3(a) derived from notable temperature swings of ca. ±5 ^oC that occurred in the water bath as the heater-controller turned on and off during operation. The heater-controller struggled to maintain a fixed 80 ^oC temperature in the face of what was clearly a formidable cooling effect created by the cell, which was operating at a potential far below the thermoneutral voltage. As predicted by theory, the cell was strongly endothermic.

Another highly active combination involved the above anode combined with a cathode comprising of 10% Pt/CB (0.071 g Pt per m^2, which equates to a very low 0.071 mg/cm^2), carbon black (21 g per m^2) and PTFE (21 g per m^2), with a Ni mesh current collector, deposited on Gortex ('10% Pt/CB+PTFE+Ni-mesh/Gortex'). This combination required 1.28 – 1.30 V to generate 10 mA cm^{-2} over 1 h at 80±5 ^oC (Figure 4.3(b)).

In these experiments, carbon black was not included in the anode due to the risk of carbon corrosion in the strongly oxidising environment that exists at the anode. When incorporated in the cathode of alkaline water electrolysers, which has a strongly reducing environment, carbon black is not usually subject to corrosion. However, to confirm that the observed current did not include a component arising from carbon corrosion at the cathode, control

experiments were conducted under identical conditions, using cathodes in which the Raney Ni or 10% Pt/CB catalysts were replaced with an equivalent weight of carbon black. Reasonable voltages could not be obtained in these experiments, indicating that the carbon black was a passive conductor in the cathode and did not undergo an electrochemical reaction. We note that this comparison did not take account of the possibility of carbon corrosion due to reaction with the catalyst.

To further confirm that the current was due to water electrolysis therefore, the gases generated by the cathode in the cell after 1 h of operation, were collected in upturned measuring cylinders filled with water, within a second water bath. At 10 mA cm^{-2}, a water electrolysis cell should produce 3.04 mL of hydrogen gas (cathode) and 1.52 mL of oxygen (anode) over 40 min. In a an experiment conducted at 10.0 mA/cm^2, the volume of hydrogen gas collected from the cathode was found to be 98.4% of the amount expected to be produced. The gas was also confirmed to be hydrogen using an attached gas chromatograph (GC). To the limit of the detection capability of the Shimadzu GC used, oxygen (from the anode) could not be detected in the hydrogen collected. Measurements by AquaHydrex Pty Ltd using their more sophisticated GC system showed that the hydrogen was 99.952% - 99.989% pure (directly off the stack)[17(b)]; that is, it contained 0.011%-0.048% oxygen. By comparison, conventional alkaline and PEM electrolysers cannot safely operate at current densities of only 10 mA/cm^2 because gas crossover exceeds the 3.9% lower explosion limit of counter-electrode-derived impurities in the gas streams. Clearly, the “bubble-free” 6 M KOH electrolyte offered a truly outstanding barrier to the migration of dissolved gases between the anode and cathode electrodes.

4.2.4 Temperature-dependent Current-Voltage Polarization Plots of Electrolysers with Gortex-based Electrodes

Polarisation curves were measured for the above electrolysers at different temperatures.

Figure 4.4 depicts the curves obtained for the Raney Ni+CB+PTFE+Ni-mesh/Gortex (cathode) and $NiCo_2O_4$+PTFE+Ni-mesh/Gortex (anode) electrolyser at 40 °C, 60 °C, and 80 °C.

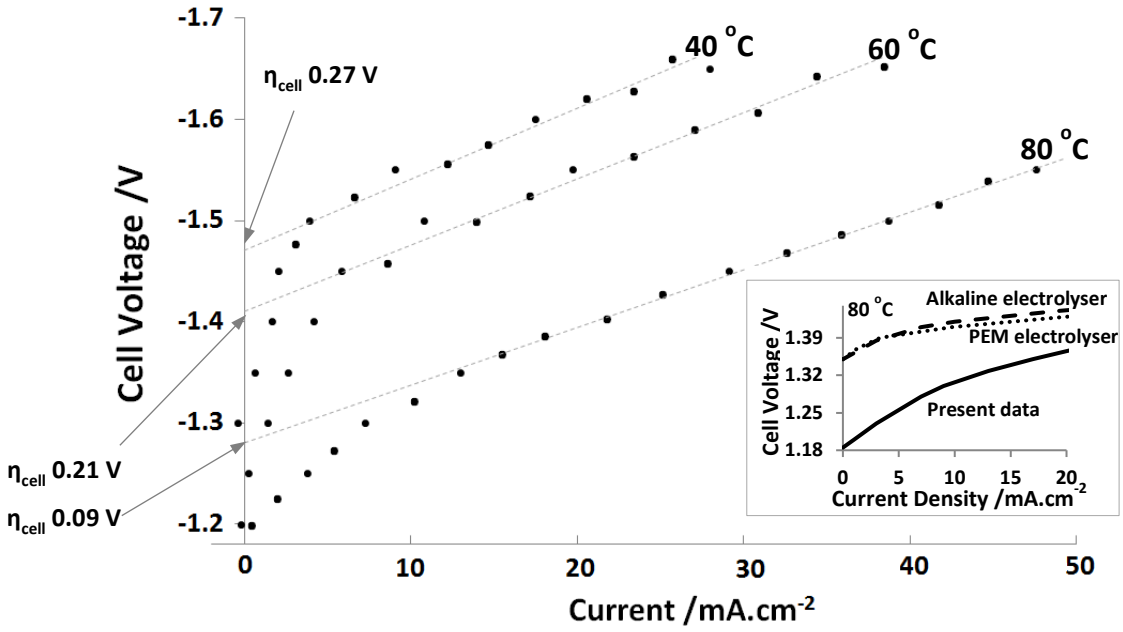

Figure 4.4. *Current-voltage curves for the Raney Ni+CB+PTFE+Ni-mesh/Gortex (cathode) and $NiCo_2O_4$+PTFE+Ni-mesh/Gortex (anode) electrolyser (6M KOH electrolyte) at different temperatures. The inset graph depicts the data at 80 °C (solid line) compared to interpolations of the most active reported alkaline[8] (dashed line) and PEM[13] (dotted line) electrolysers at the same temperature.*

As can be seen in Figure 4.4, the total activation overpotential of the electrolyser (η_{cell}), which incorporates the activation overpotentials at both the anode and the cathode, was found to drop remarkably precipitously as the temperature increased. Thus, at 40 °C, the activation voltage, which is the voltage at which a straight line passing through data in the linear (ohmic) region intercepts the y-axis, was 1.48 V. At 40 °C, the theoretical minimum voltage (E^o_{cell}) for water splitting is 1.21 V,[23] meaning that the activation overpotential of the cell, η_{cell}, was 1.48 – 1.21 = 0.27 V. At 60 °C however, the activation voltage was 1.41 V.

As the E^{o}_{cell} for water splitting is 1.20 V at that temperature,[23] the activation overpotential of the cell, η_{cell}, was 1.41 – 1.20 = 0.21 V.

At 80 ^{o}C, the theoretical minimum voltage (E^{o}_{cell}) for water splitting is 1.183 V.[23] To this may be added the ohmic losses deriving from the electrolyte and the resistance of the Ni mesh, both of which may become more substantial at the higher temperature. Given that the conductance of a 6 M KOH solution at 80 ^{o}C is 1.3499 S cm^{-1},[24] the expected voltage drop over a 10 mm (=1 cm) inter-electrode gap can be calculated to be 0.0074 V. The voltage drop due to the Ni mesh current collectors was similarly calculated to be $5.67x10^{-7}$ V. Accordingly, the minimum theoretical voltage for water-splitting by the cell at 80 ^{o}C, including the ohmic losses was: 1.183 (E^{o}) + 0.0074 + $5.67x10^{-7}$ = 1.19 V. The activation voltage at that temperature, according to Figure 4.4, was 1.28 V, indicating that the overall activation overpotential of the cell, η_{cell}, had declined to an extraordinarily low 0.09 V. To the best of our knowledge, this cell may constitute the most energy efficient water electrolyser yet reported.

Figure 4.4 also shows that the current-voltage curve becomes significantly flattened and closer to linear at 80 ^{o}C than at 60 ^{o}C and 40 ^{o}C. It further crosses the y-axis at near to the theoretical minimum potential for water electrolysis (E^{o} 1.18 V at 80 ^{o}C). The activation region of the curve can be clearly seen to flatten as the current increases from 40 ^{o}C to 60 ^{o}C to 80 ^{o}C. That is, an initially steeply rising voltage at low current densities at 40 ^{o}C gives way to a less steeply rising, linearly-increasing voltage, in low current densities at 80 ^{o}C. A steeply rising ‘activation dogleg’ is highly characteristic of water electrolysis polarisation curves.

Similar results were obtained with the electrolyser having 10% Pt/CB+PTFE+Ni-mesh/Gortex at the cathode and $NiCo_2O_4$+PTFE+Ni-mesh/Gortex at the anode. Full details of this electrolyser are discussed in Chapter 6.

To the best of our knowledge, these results are unprecedented in liquid-phase water electrolysis. It is not usual for the activation overpotential of an electrolyser cell to decline in this way and for its current-voltage curve to flatten out to near-linearity. It is also unusual for such a curve to intercept the y-axis at or near to the theoretical minimum (E^o) voltage. Indeed, as far as we are aware, only high-temperature steam electrolysers, for example solid-oxide electrolysers operating at 800-900 ^oC, display near-linear current-voltage curves that pass through or near to the theoretical minimum voltage.[25]

4.2.5 The Energy Penalty Due to Bubble Formation and Release

To illustrate the remarkable nature of this data, the inset graph in Figure 4.4 depicts the current-voltage curve at low current densities of the above, Gortex-based electrolyser at 80 ^oC (solid line), as it compares to one of the most active reported alkaline electrolysers at the same temperature; namely, the "zero-gap" electrolyser of Hug and colleagues[8] (dashed line). For completeness, the current-voltage curve at 80 ^oC of the most active recorded PEM electrolyser, namely that of Ioroi and co-workers[13] (dotted line), is also depicted. The PEM electrolyser had a 0.127 mm inter-electrode gap.

As can be seen in the inset graph in Figure 4.4, the activation overpotentials of the Hug[8] and Ioroi[13] electrolyzers (0.26 V and 0.25 V respectively), which were more than 0.16 V larger than the Gortex-based electrolyzer at 80 ^oC. This was despite the Gortex electrolyser having an order-of-magnitude larger inter-electrode gap. On approaching a current density of zero, the voltages in the Hug[8] and Ioroi[13] electrolyzers were $\geq$0.16 V greater than they would have been without the need for bubble formation and release. Bubbles in an electrolyser generally have the effect of increasing the electrical energy required to split water. This arises from effects due to bubble formation, bubble coverage/bubble curtain and bubble release (voidage). For formation of bubbles, an additional energy is required known as the bubble

overpotential, which can be substantial. Once formed, the very small initial bubbles spontaneously expand because of their large internal pressure. Bubble coverage at the electrode surface creates a bubble curtain between the liquid electrolyte and the active surface of the electrode. This bubble curtain typically impedes movement of the electrolyte to the electrode surface. To overcome this effect, continuous mechanical pumping to sweep the electrolyte over the surface of the electrodes to dislodge surface bubbles, which diminishes overall electrical efficiency of electrolyser. Even after bubbles release from an electrode surface into the electrolyte, they still impede electrical efficiency because the bubbles form a non-conducting void within the conduction pathway that comprises of liquid electrolyte between the two electrodes.

Energy efficiency in endothermic electrolyzers may be calculated in terms of the lower heating value (LHV) of hydrogen, relative to E^o (1.18 V at 80 ^oC).[1(a)] This comparison therefore suggests that, bubble formation and release decreases the maximum available energy efficiency in the most intrinsically efficient, impedance-optimized "bubbled" electrolyzers to $\leq 1.18/(0.16+1.18) \times 100 = \leq 88.1\%$ LHV. That is, the minimum decrease in energy efficiency due to bubble formation and release is 11.9%, which is massive. This minimum is observed only as the current density approaches zero, when very few bubbles are formed. The penalty to energy efficiency would likely be larger – possibly much larger – at higher current densities. It must also be larger in less intrinsically efficient electrolyzers. This may include many apparently high-performing "bubbled" electrolyzers whose polarisation curves only become ohmic (i.e. overcome activation) above 300-500 mA cm^{-2}.[1(b)-(d)] Until now it has not been possible to experimentally measure in any way, the minimum decrease in the energy efficiency of water electrolyzers deriving from the need for bubble formation and release.

(a)

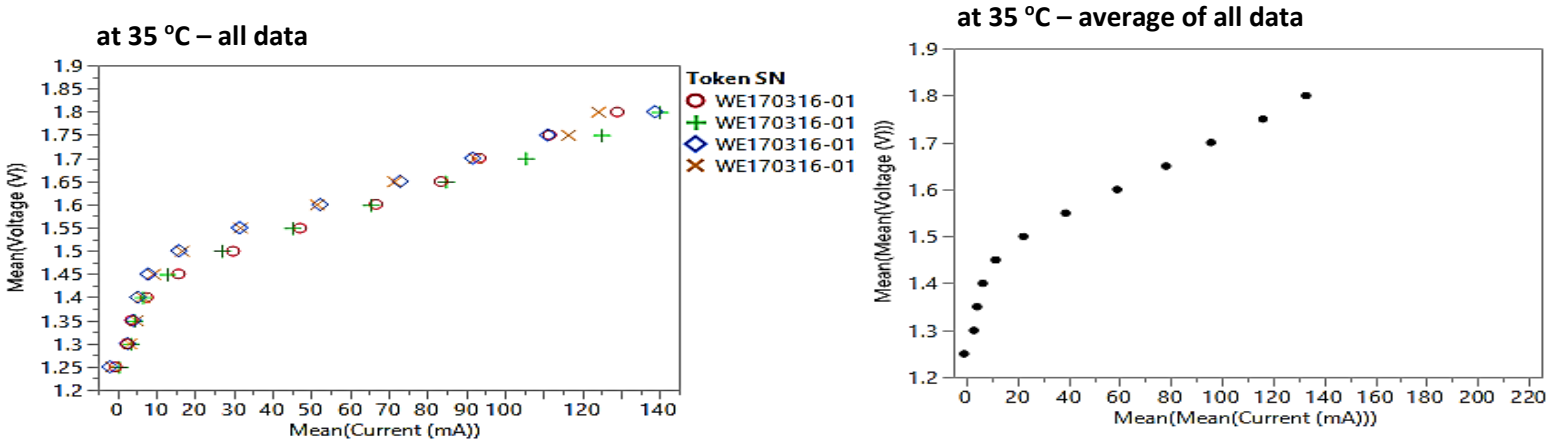

(b)

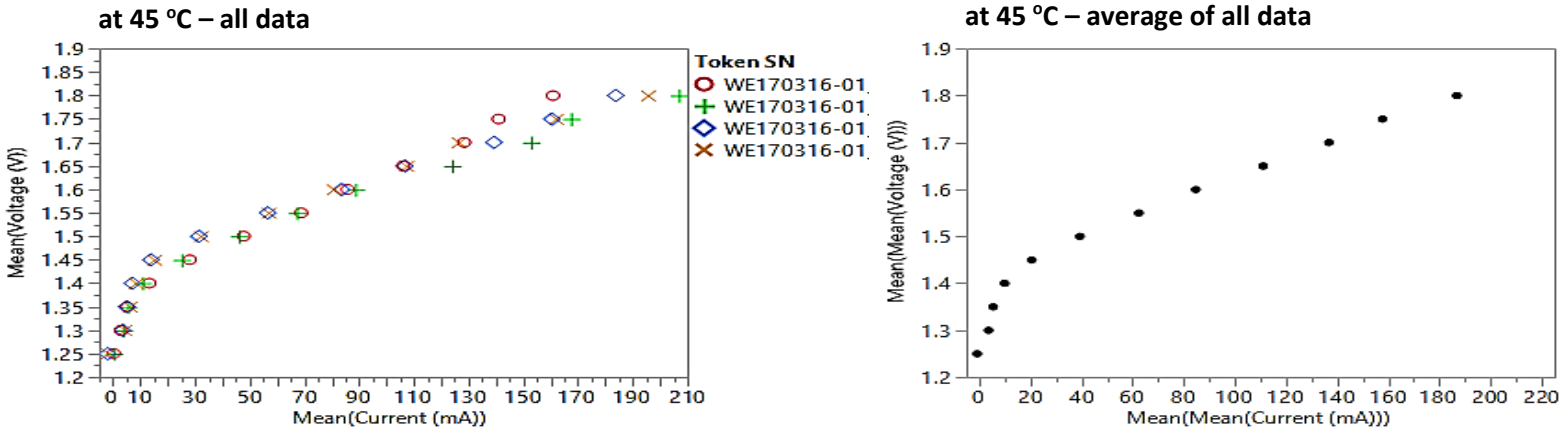

Figure 4.5(A). *Current-voltage curves for a test water electrolyser that was independently fabricated by AquaHydrex Pty Ltd, and that contained Plasma-nano-Ni+CB+PTFE+Ni-mesh/Gortex (cathode) and Plasma-nano-Ni+PTFE+Ni-mesh/Gortex (anode) electrolyser (6 M KOH electrolyte) at 35°C and 45°C.*

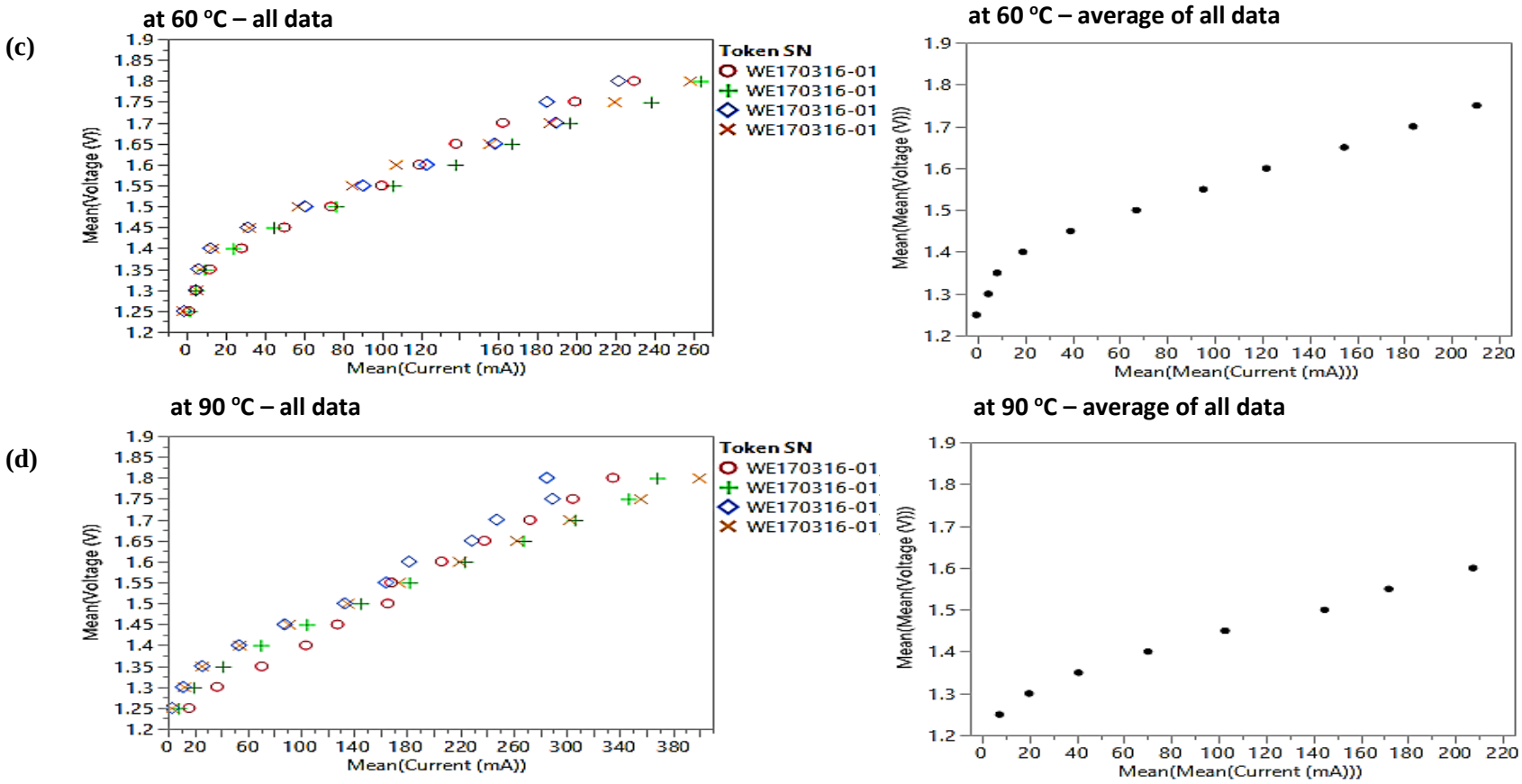

Figure 4.5 (B). *Current-voltage curves for a test water electrolyser that was independently fabricated by AquaHydrex Pty Ltd, and that contained Plasma-nano-Ni+CB+PTFE+Ni-mesh/Gortex (cathode) and Plasma-nano-Ni+PTFE+Ni-mesh/Gortex (anode) electrolyser (6 M KOH electrolyte) at 60°C and 90°C.*

4.2.6 Independent Verification and Similar Effects in other Electrolysers

To independently confirm that the observed trends were not due to an artefact in our test set-up or in our catalysts, we asked AquaHydrex Pty Ltd to perform comparable tests using a plasma-generated nanoparticulate Ni catalyst (‘*plasma-nano-Ni’*) catalyst that they had developed. Their polarisation data at different temperatures (35 ^{o}C, 45 ^{o}C, 60 ^{o}C, and 90 ^{o}C), which was repeated in quadruplicate, is shown on the left-hand side of Figure 4.5(A) and (B). The average of their data at each temperature is shown on the right-hand side of Figure 4.5(A) and (B). As can be seen, the AquaHydrex data shows all of the same elements present in the polarisation curves in Figure 4.4, namely: (i) dramatically declining activation overpotentials as the temperature increased (achieving an η_{cell} of 0.10 V at 90 ^{o}C), (ii) a systematic diminution in the gradient of the curve in the activation region, (iii) a flattening to near-linearity of the overall polarisation curve, and (iv) a y-axis intercept near to the thermodynamic minimum potential at >80 ^{o}C.

It can be concluded that the above effects are real and not due to an artefact of any type. Moreover, given that: (a) all of the best-performing conventional alkaline electrolysers with polarisation curves depicted in the inset graph in Figure 4.4,[7-9] employed Raney Ni and/or cubical spinel catalysts, with an electrolyte of 6 M KOH, and (b) the Plasma-nano-Ni/Gortex equipped electrolyser produced almost identical effects to the Raney-Ni and spinel/Gortex equipped electrolysers, it seemed that the lower activation overpotential of the Gortex-based electrolysers could not have originated in the catalytic materials used. Instead, the decrease in cell overpotential and the near-linear nature of the current-voltage curve at elevated temperature must have been caused by the Gortex substrates used in the gas diffusion electrodes.

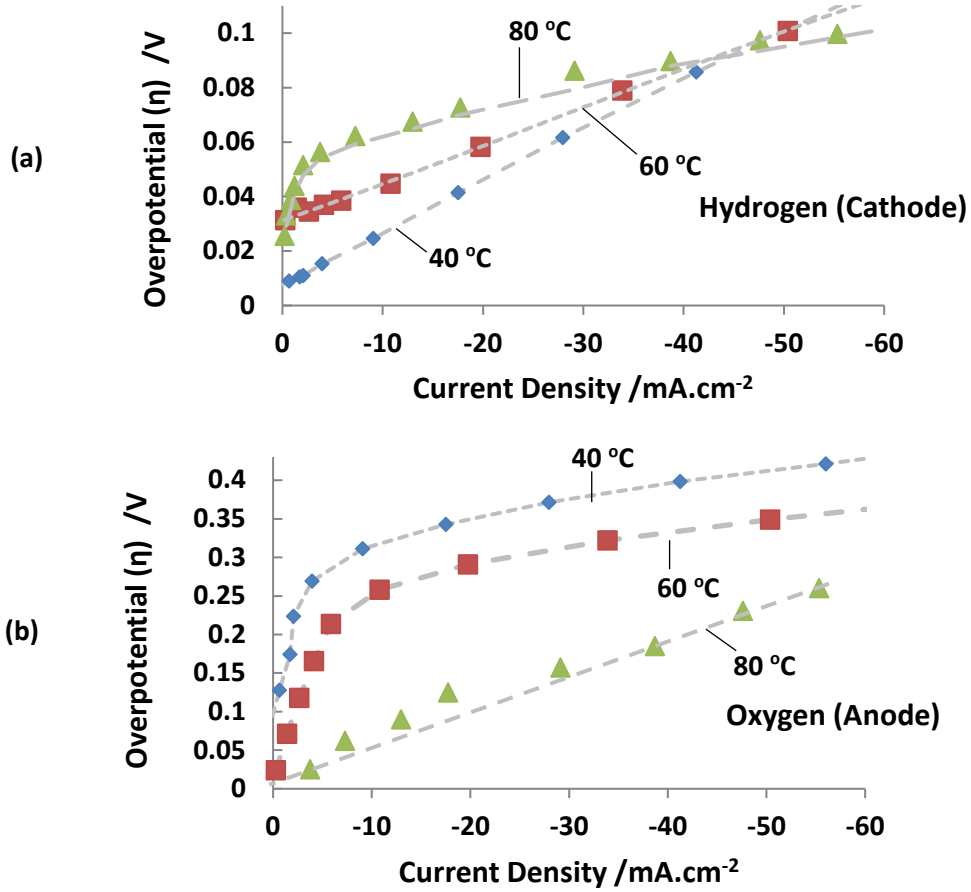

Figure 4.6. *Overpotential as a function of current density and temperature for Raney Ni+CB+PTFE+Ni-mesh/Gortex (cathode) and $NiCo_2O_4$+PTFE+Ni-mesh/Gortex (anode) electrolyser (6M KOH electrolyte; 80 °C) at: (a) the hydrogen-generating cathode, and (b) the oxygen-generating anode.*

4.2.7 The Nature of the Decline in Overpotential – the Activation Overpotential for O_2 Formation is Almost Eliminated

To try to understand the origin and nature of the lowered overpotential, we studied the Raney-Ni/spinel Gortex-based electrolyser in a 3-electrode system. A miniature Ag/AgCl reference electrode was introduced into the inter-electrode space of the electrolyser. Two potentiostats were then used to simultaneously monitor the voltage at each of the electrolyser

cathode and anode relative to the reference electrode, during sweeps to measure current-voltage polarization curves. As the theoretical minimum voltage at each of the anode and cathode may be calculated based on the electrolyte pH and temperature,[23] one may then determine the overpotential at each of the cathode and anode as a function of the current density during the current-voltage sweep.

Figure 4.6 depicts the cathode and anode overpotentials measured in this way at 40 ^{o}C, 60 ^{o}C, and 80 ^{o}C. As can be seen in Figure 4.6(a), the overpotential for hydrogen formation from the alkaline electrolyte is relatively small, being below 0.10 V at all current densities studied. Its activation overpotential is 0.01 V at 40 ^{o}C, rising to 0.06 V at 80 ^{o}C. The overpotential for hydrogen formation also shows relatively little temperature dependence. To the extent that there is a temperature dependence however, the overpotential for hydrogen formation is lowest at the lower temperatures (40 ^{o}C); it increases as the temperature increases. Indeed, it is notable that the overpotential-current curve for hydrogen at the lower temperature, namely 40 ^{o}C, is linear and passes close to the point of zero overpotential. At 10 mA/cm^2, the hydrogen overpotential in Figure 4.6(a) can be seen to be ca. 0.027 V. This result is itself astonishing as, to the best of our knowledge, the lowest overpotential ever reported for a hydrogen-generating electrode in alkaline media at 10 mA cm^{-2} was 0.07 V.[26]

By contrast, the overpotential for oxygen formation from the aqueous electrolyte is substantially larger than that of hydrogen. At 40 ^{o}C, it is 0.3 V at 10 mA cm^{-2} and 0.4 V at 40 mA cm^{-2}. However, as shown in Figure 4.6(b), when the temperature is increased to 80 ^{o}C, the oxygen overpotential falls precipitously. Its curve also flattens. Thus, the activation overpotential for oxygen formation is a mere 0.025 V at 80 ^{o}C, with the overpotential-current density curve linear.

These trends are also seen in the activation overpotential for the electrolyser. It can be concluded that the cell overpotential is dominated by the overpotential for oxygen formation from the alkaline 6 M KOH electrolyte.

The dramatic decline in the O_2 overpotential and activation overpotential observed at elevated temperatures must clearly be due to the Gortex substrate, which appears to drastically diminish the overpotential for O_2 formation from the water electrolyte.

It should also be noted that the above data indicates that the lowest cumulative overpotential and therefore the maximum performance, in a Gortex-based electrolyser may be achieved by selectively heating the O_2-generating anode but cooling the H_2-generating cathode. Thus, the oxygen overpotential-current curve is linear and passes near to zero at higher temperatures, whilst the hydrogen one does so at lower temperatures. Further investigations of this effect will form part of future research.

4.2.8 The Origin of the Lowered Activation Overpotential for O_2-formation from Water

In order to study how the Gortex at the anode largely eliminated the O_2 bubble overpotential, the physical interaction of gas bubbles with an uncoated Gortex membrane was examined. For this experiment, the contact angle of air bubbles on the surface of the Gortex was measured, when that surface was immersed in water. The so-called “Captive Bubble” technique of contact angle measurement was used. Figure 4.7 shows the sequence of events observed.

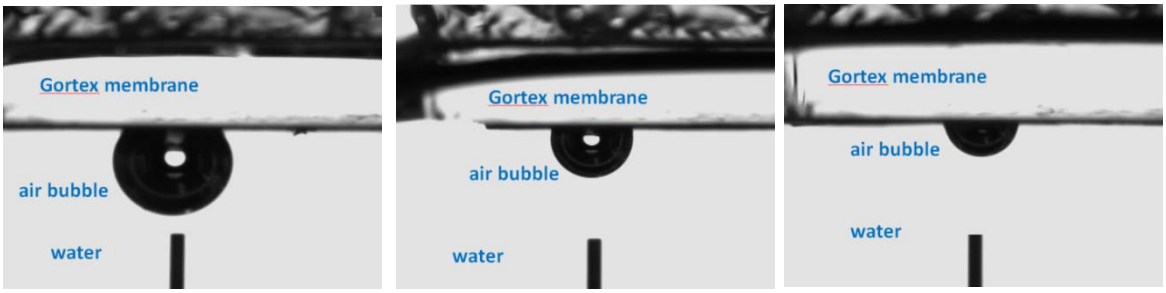

Figure 4.7. *Sequence of events in an attempt to measure the contact angle, using the "Captive Bubble" technique, of an air bubble on a Gortex surface immersed in water. The Gortex was tight up against a glass backing plate (shown at the very top of each photograph). In (a), an air bubble is carefully placed on the Gortex surface. Before a contact angle can be measured however, the Gortex draws the air bubble into it, as shown in (b) and then in (c). Within a matter of seconds, the air bubble is almost totally taken up by the Gortex.*

As can be seen in Figure 4.7, it proved impossible to determine a contact angle because air bubbles placed on the Gortex surface were, over a few seconds, drawn into the Gortex itself. This occurred despite the Gortex being placed tight up against a solid glass backing plate (shown at the very top of the images in Figure 4.7). When the glass backing plate was removed, any air bubbles that contacted the Gortex were rapidly and immediately drawn into it, within a fraction of a second. The same effect was observed when the Gortex was placed vertically in the water and a bubble released near to its surface, so that it would come into contact with the surface. Upon contact, the bubble was drawn into the Gortex membrane, perpendicular to the direction it would have followed had its buoyancy determined its direction of motion.

These experiments demonstrated that the Gortex surface was highly "bubble-philic". Gas bubbles are, of course, strongly hydrophobic and are therefore attracted to the surface of

Gortex, which is also hydrophobic. But, it was not clear why they were so aggressively drawn into the Gortex?

4.2.9 A Possible Explanation: the Gortex Substrate has a Strong Capillary Action that Repels Water but Attracts Gas Bubbles

The results above can potentially be explained by considering capillary effects deriving from the hydrophobic pores of the Gortex. Capillary pressures in porous materials can be calculated using the Young-Laplace equation:

$$P_c = \frac{2\gamma}{r}\cos\varphi \qquad \ldots (4.2)$$

where, P_C = the capillary pressure, r = the pore radius, γ = the surface tension of the liquid, and φ = the contact angle of the material from which the porous structure is composed.

The Gortex used in the above experiments had hydrophobic pores of 0.1 μm average radius. The contact angle of the Gortex with the 6 M KOH electrolyte was measured using the sessile drop technique to be ca. 115°. The surface tension of 6 M KOH at 80 °C is 0.078409 N m^{-1}.[27] Using this data, the capillary pressure exerted by the pores can be calculated using equation (4.2) to be -662,742 N m^{-2}, which equates to -6.6 bar. The negative sign indicates only the direction of the capillary action; that is, it indicates that this is a "repulsive" capillary action in which water is repelled by the Gortex pores. A hydrophobic element, like a gas bubble would, by contrast, be attracted and drawn into the pores by such a capillary action.

The pressure needed inside a gas bubble, to support it, is inversely proportional to the diameter of the gas bubble, with the excess internal pressure ΔP, known as the Laplace pressure, given by the equation:

$$\Delta P = \gamma \frac{2}{R} \qquad \ldots (4.3)$$

where γ is the surface tension and R is the radius of the bubble.

Consider now a newly-formed gas bubble of radius 0.1 μm. In open, solution at 80 °C, equation (4.3) indicates that the bubble would have to have an excess internal pressure of 1,496,000 N m^{-2} (15.0 bar) above the ambient 1 bar pressure of the liquid. That is, the total internal pressure of the bubble would be 15.0 + 1 = 16.0 bar.

If, however, the bubble was instead formed inside or at a *hydrophilic* porous structure, into which liquid electrolyte was drawn by an "attractive" (positive) capillary action, then such a bubble would need extra internal pressure in order to push the water out of the pores as the bubble expanded. That extra pressure required would equal the positive capillary pressure that was exerted on the water molecules in the pore.

In the same way, if the bubble instead formed inside or at a *hydrophobic* pore, such the Gortex pores, where there is a "repulsive" (negative) capillary pressure, then the pressure needed inside the bubble would be decreased. It would be decreased because the liquid electrolyte is already partially displaced from the Gortex pores by their repulsive capillary action. That decrease would equal the negative capillary pressure exerted by the pores, namely, 6.6 bar. That is, an internal pressure of only 16.0 – 6.6 = 9.4 bar would be needed in a bubble of radius 0.1 μm.

The limiting situation would arise when the bubble in or at the hydrophobic pore grew larger than ca. 0.2 μm in radius. At ca. 0.2 μm radius, the internal pressure of the bubble would equal the capillary pressure exerted by the Gortex (i.e. 6.6 bar). If the bubble grew larger than 0.2 μm, its internal pressure would necessarily fall below the external capillary pressure. Under these circumstances, the gas inside the bubble would be spontaneously

extracted from the bubble and drawn into the Gortex. That is, the bubble would cease to exist. In effect, the Gortex would thereby cap the maximum size of gas bubbles that could be present to microscopically small radii. In this way, O_2 bubbles could conceivably be largely eliminated at the Gortex surface, thereby explaining the negligible activation overpotential for oxygen formation.

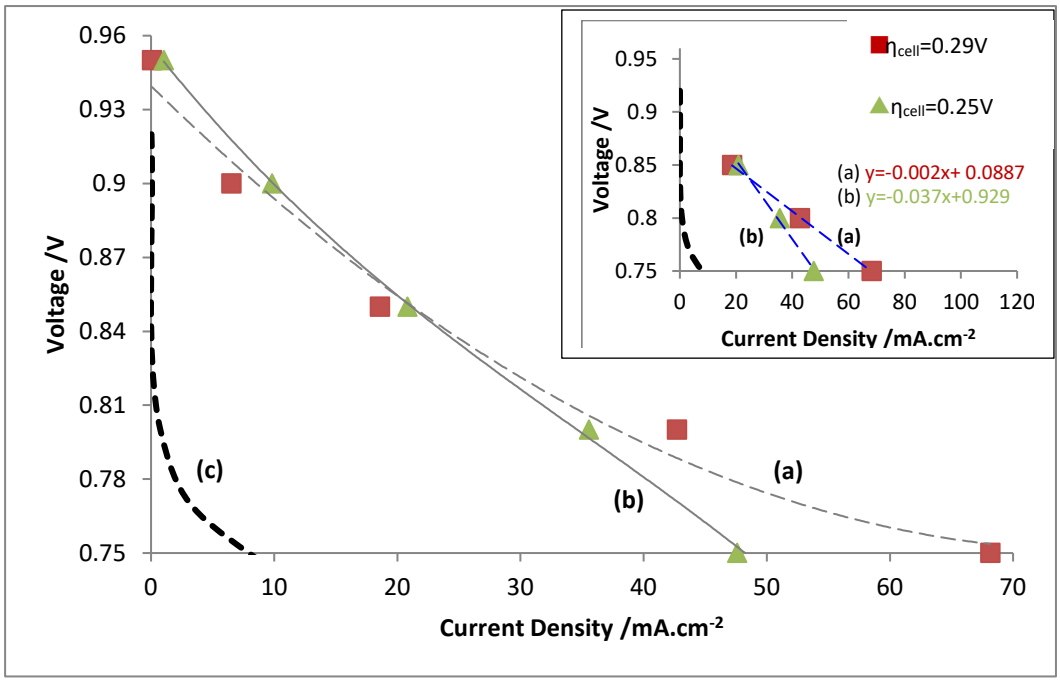

Figure 4.8. *Polarisation curve after 1 h of cells in fuel cell mode at 80 °C (6 M KOH electrolyte; 10 mm inter-electrode gap) having: (a) Fuel cell 1 containing 20% Pd-Pt/CB+PTFE+Ni-mesh/Gortex at both the H_2 and O_2 electrodes; (b) Fuel cell 2 containing 20% Pd-Pt/CB+PTFE+Ni-mesh/Gortex at the H_2 electrode and $La_{0.8}Sr_{0.2}MnO_3$/CB+PTFE+Ni-mesh/Gortex at the O_2 electrode; and (c) Fuel cell 3 containing 20% Pd-Pt/CB+PTFE+Ni-mesh/Gortex at the H_2 electrode and carbon black+Ni-mesh/Gortex at the O_2 electrode. Inset shows fitted straight lines of the ohmic regions, which have the general formula y=mx+c, where the value of c accords with the onset potential of the fuel cell. The activation overpotential (η_{cell}) is difference between the onset potential and 1.18 V, which is the E^o of the cell at 80 °C.*

While the above provides a possible explanation for the lowered overpotentials for oxygen formation from water, it should be noted that no experimental evidence is as yet available to unambiguously demonstrate that the low voltage arises from the capillary effect of the Gortex.

4.2.10 Efficient H_2/O_2 Fuel Cells Employing Gortex-based Electrodes

Studies also examined the utility of Gortex-based electrodes layered with catalysts in fuel cell mode, utilizing reaction (4.4):

$$O_2 + 2H_2 \rightarrow 2H_2O + electricity + heat \quad E^0_{cell} = 1.23 \text{ V vs SHE} \quad ...(4.4)$$

The catalyst-coated Gortex membranes were prepared using the same slurry technique employed to make the various electrolyser electrodes. This technique had been optimized for the electrolyser work. Nevertheless, the catalyst-layered Gortex electrodes that were tested did yield H_2/O_2 fuel cells. The same desktop cell and physical conditions were used for the fuel cell work, however, instead of collecting H_2 and O_2 generated at the electrodes, high purity H_2 and O_2 at atmospheric pressure was slowly fed into and through the respective gas chambers during these experiments.

One of the best performing fuel cells, *fuel cell 1* employed a mixture of 20% Pd-Pt/CB (2.3 g Pt-Pd per m^2), carbon black (37 g per m^2) and PTFE (47 g per m^2), with a Ni mesh current collector, deposited on Gortex ('*20% Pd-Pt/CB+PTFE+Ni-mesh/Gortex*'), at both the anode and cathode. The polarization curve after 1 h (80 ^oC) at 10 mA cm^{-2} in the reverse direction (fuel cell mode), is shown in Figure 4.8(a). As can be seen, the cell generated a voltage of 0.88 V at 10 mA cm^{-2}.

Another of the best performing fuel cells, *fuel cell 2* employed a non-precious metal catalyst as cathode. The cathode used in *fuel cell 2* contained a mixture of $La_{0.8}Sr_{0.2}MnO_3$ (232 g $La_{0.8}Sr_{0.2}MnO_3$ per m^2), carbon black (41 g per m^2) and PTFE (62 g per m^2), with a Ni mesh current collector, deposited on Gortex (‘*$La_{0.8}Sr_{0.2}MnO_3$/CB+PTFE+Ni-mesh/Gortex*’), as the cathode; and a mixture of 10%Pt/CB (0.55 g Pt per m^2), carbon black (17 g per m^2) and PTFE (17 g per m^2), with a Ni mesh collector, deposited on Gortex (‘*20% Pd-Pt/CB+PTFE+Ni-mesh/Gortex*’) as the anode. The polarization curve after 1 h (80 ^oC) at 10 mA cm^{-2} in the reverse direction (fuel cell mode), is shown in Figure 4.8(b). As can be seen, the cell generated a voltage of 0.89 V at 10 mA cm^{-2}.

To assess whether carbon corrosion in the strongly oxidizing environment of the O_2 electrode may have contributed to the current and voltage, we also prepared and tested under identical conditions, a control *fuel cell 3* with the same H_2 electrode but with an O_2 electrode in which the catalyst had been replaced with only carbon black; that is, with a carbon black+Ni-mesh/Gortex electrode. *Fuel cell 3* produced a current only below voltages in the low 0.8 V region (Figure 4.8(c)). It could thereby be unequivocally concluded that carbon corrosion at the O_2 electrode did not contribute in any way to the performance of fuel cell having either 20% Pd-Pt or $La_{0.8}Sr_{0.2}MnO_3$ at O_2 electrodes at 10 mA cm^{-2}.

To estimate the performance of both of the high performing fuel cells (*fuel cell 1 and fuel cell 2*), particularly below 20 mA cm^{-2} (see Figure 4.8), activation overpotentials were calculated. As in the electrolysers, the total activation overpotential of the fuel cell (η_{cell}), incorporated the activation overpotentials at both the anode and the cathode. As can be seen in the inset graph in Figure 4.8, the activation overpotential was 0.29 V for *fuel cell 1* and even lower for *fuel cell 2* (η_{cell} 0.25 V). To investigate the source of the lowered cell overpotential (incorporating both the cathode and anode overpotentials), the same technique was employed as described in Section 4.2.5.

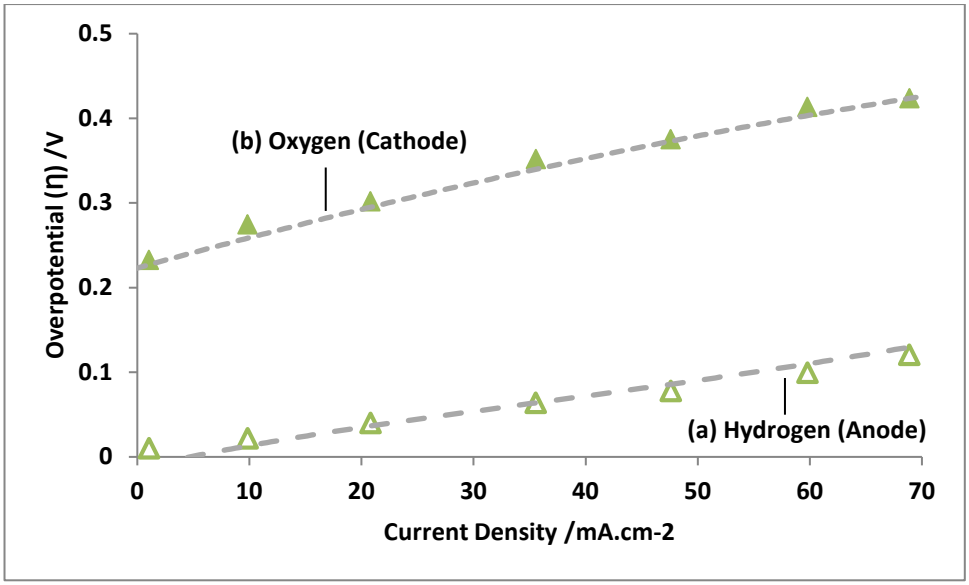

Figure 4.9. *Overpotential (hydrogen (a) and oxygen (b)) as a function of current density for 20% Pd-Pt/CB+PTFE+Ni-mesh/Gortex at the H_2 electrode and $La_{0.8}Sr_{0.2}MnO_3$/CB+PTFE+Ni-mesh/Gortex at the O_2 electrode in fuel cell 2(6M KOH electrolyte) at 80 °C.*

Figure 4.9 depicts the oxygen-side and hydrogen-side overpotentials measured at 80 °C. As can be seen in Figure 4.9(a), the hydrogen-side overpotential for dissociation of hydrogen, according to equation 4.5, is negligible, being below 0.10 V at all current densities studied. The hydrogen-side overpotential-current curve passes close to the point of zero overpotential on the y-axis, with a negligible activation overpotential. At 10 mA cm^{-2} the overpotential is only 0.02 V.

$$H_2 + 2OH^- \rightarrow 2H_2O + 2e^- \qquad E^0_{oxidation} = 0.83 \text{ V vs SHE} \qquad \text{... (4.5)}$$

These results stand in contrast to the data in Figure 4.6(a) at 80 °C.

By contrast, the oxygen overpotential for water formation by the reduction of oxygen is substantially larger than that of hydrogen.

$O_2 + 2H_2O + 4e^- \rightarrow 4OH^-$ $E^0_{reduction}$ = 0.40 V vs SHE ... (4.6)

At 80 °C, the cathode overpotential is an order of magnitude higher than the anode overpotential at 10 mA cm^{-2} and a similar correlation between cathode and anode overpotentials is observed at all current densities studied.

It can be concluded that the cathode overpotential (i.e. the oxygen overpotential) governs the overall cell overpotential. However, as seen in the case of the electrolysers, where the oxygen overpotential drops to near negligible values at 10 mA cm^{-2} when the temperature is increased to 80 °C, in case of fuel cell, such a significant difference in oxygen overpotential is not observed, in other words, an increase in temperature had little to no effects on the behavior of the cathode overpotential (- this topic is discussed in detail in Chapters 5 and 6).

When the electrolyser having Raney Ni+CB+PTFE+Ni-mesh/Gortex (cathode) and $NiCo_2O_4$+PTFE+Ni-mesh/Gortex (anode) is combined with either of the above fuel cells ((20%Pt-Pd/CB+PTFE+Ni-mesh/Gortex at both electrodes) or ($La_{0.8}Sr_{0.2}MnO_3$/CB+PTFE+Ni-mesh/Gortex (cathode) and 20%Pt-Pd/CB+PTFE+Ni-mesh/Gortex (anode)), then the system has a notional round-trip energy efficiency after 1 h at 10 mA cm^{-2} and 80 °C in each direction, of 72.6% and 73.5% respectively (assuming full conservation of heat). This exceeds that achieved by the regenerative PEM fuel cell–electrolyser of Ioroi and colleagues,[13] which yielded a round-trip energy efficiency at 80 °C and 10 mA cm^{-2} in each direction, of 66.4%.[13]

4.3 Conclusions

In this Chapter, the utility in alkaline water electrolysis of gas diffusion electrodes comprising of Gortex substrates layered with several well-known, conventional water-

splitting catalysts was examined. The best-performing electrolyser employed a cathode comprising of a mixture of Raney Ni, carbon black and poly(tetrafluoroethylene) (PTFE), with a Ni mesh current collector, deposited on Gortex. When combined with an anode containing a mixture of $NiCo_2O_4$, PTFE, and a Ni-mesh, deposited on Gortex, in 6 M KOH with a 10 mm inter-electrode gap, the resulting electrolyser required only 1.23 V to achieve 10 mA cm^{-2} after 1 h at 80 ^oC. The combined cathode and anode activation overpotential (η_{Cell}) comprised a mere 0.09 V. Current-voltage polarisation curves indicated that the Gortex substrate had a notable effect in diminishing the cumulative overpotential of the catalysts during electrolysis at temperatures of 80 ^oC and above. Specifically, the Gortex decreased the activation overpotential for oxygen formation from water to near negligible proportions. It appears to have had less effect on the overpotential for hydrogen formation. Studies show the Gortex surface to be highly "bubble-philic", rapidly drawing gas out of contacting bubbles and into the Gortex itself. Application of the Young-Laplace and related equations suggest that the porous Gortex surface exerted a considerable capillary action for uptake of oxygen. The associated capillary pressure may cap the maximum size of bubbles formed on the Gortex surface to submicron radii. When the above electrolyser is combined with a best, equivalent fuel cell having 20%Pt-Pd/CB, CB, PTFE, and a Ni-mesh, deposited on Gortex as anode and $La_{0.8}Sr_{0.2}MnO_3$, CB, PTFE, and a Ni-mesh, deposited on Gortex as cathode, then the system has a notional round-trip energy efficiency after 1 h at 10 mA cm^{-2} and 80 ^oC in each direction, of 73.5% (assuming complete conservation of heat). The fuel cell generated 0.89 V at 10 mA cm^{-2} in the reverse direction after 1 h at 80 ^oC.

The development of water-splitting catalysts with substantially lowered overpotentials has, for decades, constituted a key objective in science. While that field is now truly mature, with few improved new catalysts being discovered annually, the present Chapter describes a new approach that may be used to amplify the energy efficiency of existing catalysts. The new

approach utilizes a porous, hydrophobic substrate, Gortex, upon which catalysts are deposited, to thereby decrease their overpotentials.

References

1. (a) M. Gabbasa, K. Sopian, A. Fudholi, N. Asim *Int. J. Hydrog. Energy* **2014**, *39*, 17765-17778. (b) J. Pettersson, B. Ramsey, D. Harrison *J. Power Sources* **2006**, *157*, 28–34. (c) D. Shapiro, J. Duffy, M. Kimble, M. Pien *Solar Energy* **2005**, *79*, 544–550. (d) S. Markgrafa, M. Hörenza, T. Schmiela, W. Jehleb, J. Lucasb, N. Hennc *J. Power Sources* **2012**, *201*, 236– 242. (e) A. Züttel, A. Remhof, A. Borgschulte, O. Friedrichs *Phil. Trans. R. Soc. A* **2010**, *368*, 3329–3342.
2. (a) J. O. Jensen, V. Bandur, N. J. Bjerrun, S. H. Jensen, S. Ebbesen, M. Mogensen, N. Trophoj, L. Yde, "*Pre-Investigation of Water Electrolysis*", Publication PSO-F&U 2006-1-6287, RISO and the Danish Technical University, 2008. (c) K. Zeng, D. Zhang *Prog. Energy Combust. Sci.***2010**, *36*, 307-326.
3. M. Gong, W. Zhou, M.-C. Tsai, J. Zhou, M. Guan, M.-C. Lin, B. Zhang,Y. Hu, D.-Y. Wang, J. Yang, S. J. Pennycook, B.-J. Hwang, H. Dai *Nature Commun*. **2014**, *5*, article number 4695.
4. H. Jin, J. Wang, D. Su, Z. Wei, Z. Pang, Y. Wang *J. Am. Chem. Soc.* **2015**, *137*, 2688−2694.
5. H. Wang, H.-W. Lee, Y. Deng, Z. Lu, P.-C. Hsu, Y. Liu, D. Lin, Y. Cui *Nature Commun.* **2015**, *6*, article number 7261.
6. C. C. L. McCrory, S. Jung, I. M. Ferrer, S. M. Chatman, J. C. Peters, T. F. Jaramillo *J. Am. Chem. Soc.* **2015**, *137*, 4347−4357.
7. G. Schiller, R. Henne, P. Mohr, V. Peinecke *Int. J. Hydrogen Energy* **1998**, *23*, 761-765.
8. W. Hug, J. Divisek, J. Mergel, W. Seeger, H. Steeb *Int. J. Hydrogen Energy* **1992**, *17*, 699-705

9. S. Marini, P. Salvi, P. Nelli, R. Pesenti, M. Villa, M. Berrettoni, G. Zangari, Y. Kiros Electrochim. Acta **2012**, *82*, 384-391.
10. R. Phillips, C. W. Dunill, *RSC Advances* **2016**, *6*, 100643-100651.
11. S. Zhigang, Y. Baolian, H. Ming *J. Power Sources* **1999**, *79*, 82–85.
12. L. L. Swette, A. B. LaConti, S. A. McCatty *J. Power Sources* **1994**, *47*, 343-351.
13. T. Ioroi, T. Okub, K. Yasuda, N. Kumagai, Y. Miyazaki *J. Power Sources* **2003**, *124*, 385–389. The data in this paper appears to supercede that made publicly available by electrolyser companies (see, for example: M. Hamdan, Presentation PD030, 2013 Hydrogen Program Annual Merit Review Meeting, US Department of Energy).
14. P. Tiwari, G. Tsekouras, G. F. Swiegers, G. G. Wallace, submitted for publication.
15. B. Winther-Jensen, O. Winther-Jensen, M. Forsyth and D. R. MacFarlane *Science* 2008, **321**, 671-674.
16. B. Winther-Jensen, K. Fraser, C. Ong, M. Forsyth, D. R. MacFarlane *Adv. Mater*. 2010, **22**, 1727–1730.
17. (a) O. Winther-Jensen, K. Chatjaroenporn, B. Winther-Jensen and D. R. MacFarlane *Int. J. Hydrog. Energy* 2012, **37**, 8185-8189. (b) "Methods of Improving the Efficiency of Gas-Liquid Electrochemical Cells. Swiegers, G. F.; Tiwari, P. et al PCT International Patent Application ***WO2017100840*** and family.
18. B. Kolodziejczyk, O. Winther-Jensen, B. A. Pereira, S. S. Nair and B. Winther-Jensen *J. Appl. Polymer Sci*. 2015, **132**, 42359
19. (i) M. Wikol, B. Hartmann, J. Brendle, M. Crane, U. Beuscher, J. Brake, T. Shickel, Chap 23 in *Filtration and Purification in the Biopharmaceutical Industry, Second Edition* (Eds. Maik W. Jornitz and Theodore H. Meltzer), Taylor & Francis, 2007; (ii) F. A. AlMarzooqi, M. R. Bilad, B. Mansoor, H. A. Arafat *J. Mater. Sci.* 2016, **51**, 2017
20. See, for example: Z. Radivojeviz, J. Saunamaeki *International Patent Application* **WO2009074160A1**.
21. I. Moussallem, J. Jorissen, U. Kunz, S. Pinnow, T. Turek *J. Appl. Electrochem.* 2008, ***38***, 1177–1194 and references therein.

22. A. F. Gulla, J. L. Krasovic *International Patent application* **WO2013037902**, and references therein.
23. S. G. Bratsch *J. Phys. Chem. Ref. Data* **1989**, 18, 1-21.
24. R. J. Gilliam, J.W. Graydon, D. W. Kirk, S. J. Thorpe *Int. J Hydrogen Energy*, **2007**, *32*, 359.
25. M. A. Laguna-Bercero *J. Power Sources* **2012**, 203, 4-16.
26. L. Yang, H. Qi, C. Zhang, X. Sun *Nanotechnology* **2016**, 27, 23.
27. A. Brockmeier, F. J. Santos Rodriguez, M. Harrison, U. Hilleringmann *J. Micromech. Microeng.* **2012,** 22, 125012**.**

CHAPTER 5

Other Efficient Alkaline Fuel Cells, Electrolysers, and Discrete Regenerative Fuel Cells Utilizing Gortex-based Precious Metal Catalysts

5.1 Introduction

With ever-increasing requirements for energy, renewable power sources, including solar, wind and geothermal, are receiving considerable attention and investment in recent years. However, the irregular and sporadic nature of these power sources has limited their widespread application. To balance their irregularity in energy production, increased attention has been placed on batteries or regenerative fuel cell (RFC) systems as auxiliary energy storage.

RFCs may seem to be an attractive option for energy storage during off-peak periods and energy production during peak periods. However, the major problem associated with RFCs is: (i) their relatively low roundtrip efficiency when compared with pumped hydro and batteries; and, (ii) their high capital costs for electrolyser and fuel cell units.

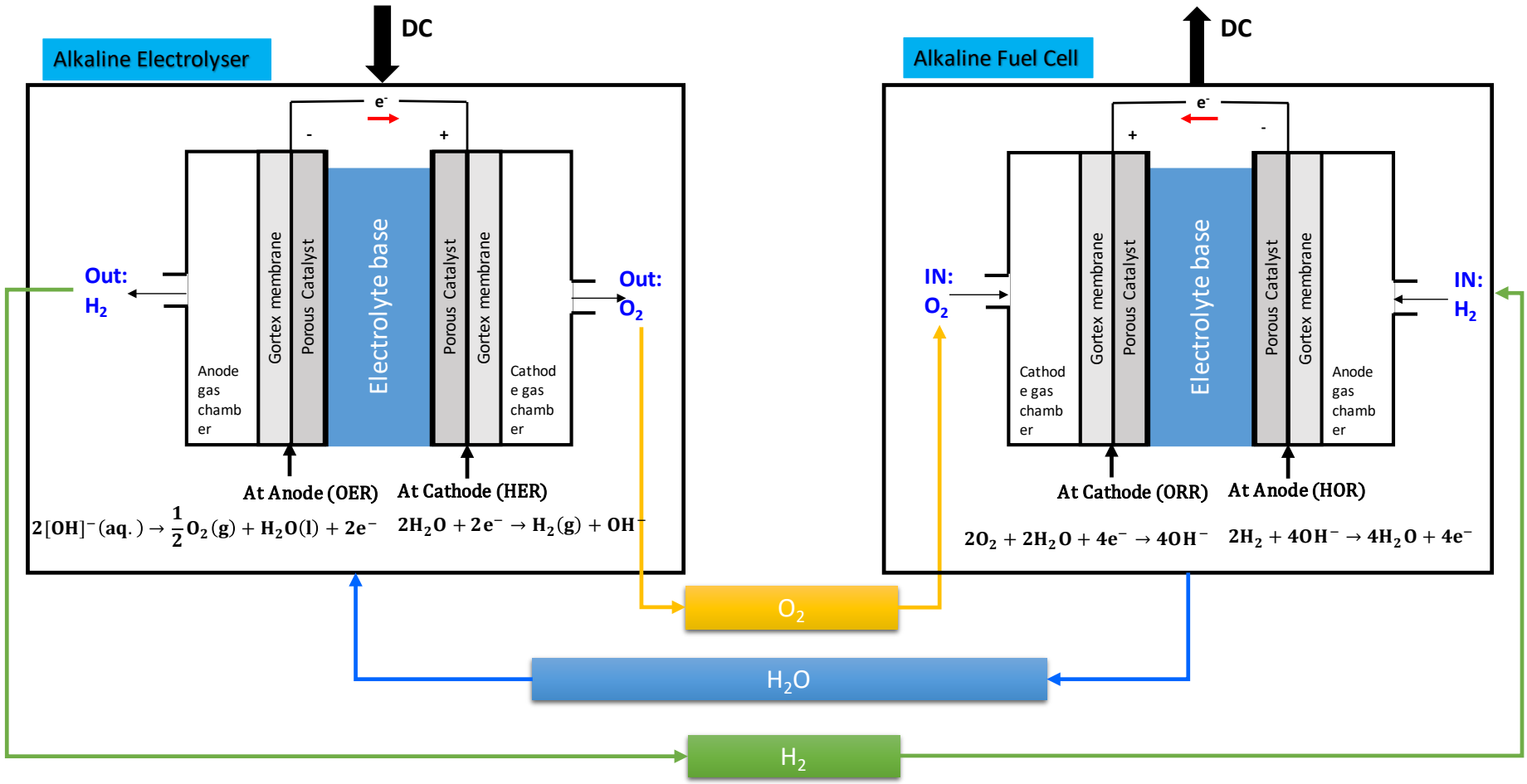

Figure 5.1. *Schematic diagram for discrete regenerative fuel cell (DRFC)*

Two types of RFC approaches have been developed, namely: unitized regenerative fuel cell (URFC) systems and discrete regenerative fuel cell (DRFC) systems. In the case of URFCs,[1] only one compact system is present wherein a fuel cell unit and an electrolyzer unit is combined in a single electrochemical device, which can alternately function as a fuel cell or an electrolyzer. For DRFCs,[2] two different electrochemical devices are used: one as an electrolyzer and another as a fuel cell (see Figure 5.1). There are several advantages of DRFCs over their unitized counterpart:[3] (1) There are fewer design restrictions if the device is used in only one mode; (2) The balance of plant can be decreased as oxygen storage can be excluded; (3) In a DRFC, a separate electrolyzer operates at higher output pressure than a URFC, so that the cost of the separate components can be justified by the savings associated with reduced tank volume; (4) URFCs cannot operate in situations where there is a large difference between the charging and discharging power, whereas DRFCs can handle these conditions since separate devices can be better optimized for respective charge and discharge powers; (5) The roundtrip efficiency of a DRFC can be maximized by utilizing the best available designs for the electrolyser and fuel cell electrodes – that is, the electrode design in the electrolyser system can be substantially different to the design of the electrodes in the fuel cell system; and (6) Finally, one can take advantage of mature technologies developed in each mode in the case of DRFCs, thereby increasing the roundtrip efficiency.

Power and energy ratings for several commercial DRFC options have been compared and reviewed by Gahleitner.[4,5]

Alkaline electrolysers typically operate at 70 °C - 140 °C, at pressures of 1 bar - 30 bar, whilst achieving efficiencies of 60% - 71% (HHV).[4,6] Also, alkaline electrolysers are the most mature and cheapest technology available.[6] Therefore, alkaline-based electrolysers are popularly used in many DRFC applications for electrolysis. However, the case for alkaline fuel cells (AFCs) is different to that of alkaline electrolyzers. Although, AFCs may have an electrical efficiency of up to ca. 70%[7] and use simpler structures, they are easily

contaminated by CO_2, also referred as the CO_2 poisoning problem.[8] This problem along with other challenges, as discussed in Chapter 3 Section 3.1, limits its applicability in DRFC for fuel cell mode.

For this thesis we studied a wide range of precious metals and their alloys as catalysts in electrolysers and fuel cells fitted with Gortex-based gas diffusion electrodes. The study aimed to examine alkaline-based DRFCs and the performance of various combinations of precious metals and their alloys as catalysts in electrolysers and fuel cells. Gortex based gas diffusion electrodes coated with commercially available precious metals and their alloys were prepared and tested.

The studies were generally carried out in custom-built, 2-electrode prototype cells with closely-spaced, equally-sized electrodes. The cells were designed to predict, as accurately as possible, the performance of larger-scale commercial devices utilizing the same catalysts and the same 2-electrode cell arrangement. Studies in 3-electrode format, using a reference electrode, were carried out in some, limited cases, but not generally pursued. In our experience, the engineering compromises that must be made in fabricating 3-electrode test cells undermine the reliability of their data in respect of extrapolating it to commercial 2-electrode cells. For example, the data generated by a closely-spaced arrangement of two, large-area electrodes may be affected by the precise location of the reference electrode when operated in 3-electrode format.

Chapter 4 reported the most significant findings of this thesis in this respect. In the present chapter, we report further findings, deriving from an examination of precious metals and their alloys as Gortex-based catalyst systems. These findings and the main features of the work can be summarized as follows:

(1) The highest performing anode in the fuel cells tested was 10% Pt/CB+PTFE+Ni-mesh/Gortex. This anode was used a standard against which the PGM-based ORR catalysts were evaluated.

(2) Temperatures above 25 ^{o}C had an insignificant effect on the ORR activity of precious metals and their alloys at lower current densities (relative to the standard anode), but substantially amplified ORR activities at higher current densities. By contrast, as noted in Chapter 4, the OER activity and consequently, the electrical efficiency of electrocatalytic water-splitting, drastically increased at temperatures of 80 ^{o}C and above. Therefore, all of the electrolyzers were tested at 80 ^{o}C in order to realize the maximum possible electrical efficiencies.

(3) Because carbon black is not preferred in OER electrodes for water electrolysis (due to its corrosion in the highly oxidizing electrolysis environment), we made comparisons of Gortex-based precious metal/alloy catalysts using only IrO_2 as the catalyst in electrolyser anodes (relative to the standard anode), since all other available Pt-based catalysts were carbon supported.

(4) The study demonstrated a correlation in the ORR performance of precious metals and their alloys to their "*Volcano plots*". Electrochemical impedance spectroscopy was employed to elucidate the order of ORR electroactivity as projected in Volcano plots.

(5) The best fuel cell cathode comprised 20% Pd-Pt/CB+PTFE+Ni-mesh/Gortex, which, at 10 mA cm^{-2}, with a counter electrode of 10% Pt/CB+PTFE+Ni-mesh/Gortex, yielded a voltage of ca. 0.88 V at 20 ^{o}C. The use of 10% Pt/CB+PTFE+Ni-mesh/Gortex at both electrodes produced a constant 0.857-0.860 V at 10 mA cm^{-2}, at 20 ^{o}C, over 2 d of continuous operation. The best-performing electrolyser with IrO_2

at the anode and 10% Pt/CB+PTFE+Ni-mesh/Gortex at the cathode required 1.4 V to achieve 10 mA cm^{-2} after 1 h at 80 ^{o}C.

(6) The highest performing alkaline DRFC studied in this Chapter displayed a notional round-trip energy efficiency after 1 h at 80 ^{o}C and 10 mA cm^{-2} in each direction, of 64.3%, assuming full conservation of heat. It involved a fuel cell composed of 20% Pd-Pt/CB+PTFE+Ni-mesh/Gortex (cathode) / 10% Pt/CB+PTFE+Ni-mesh/Gortex (anode) with an electrolyzer containing Gortex-based IrO_2 as the anode and 10% Pt/CB+PTFE+Ni-mesh/Gortex as the cathode.

5.2 Experimental

5.2.1 Materials

The following materials were employed (Supplier): Carbon black (AkzoNobel), 20% Pt-Pd on Vulcan XC-72 (Premetek Co. # P13A200), 10% Pt on Vulcan XC-72 (Premetek Co. # P10A100), 20% Pt-Ru on Vulcan XC-72 (Premetek Co. # P12A200), 20% Pt-Ir on Vulcan XC-72 (Premetek Co. # P14A200), 20% Pt-Co on Vulcan XC-72 (Premetek Co. # P1CA200), 20% Pt-Ni on Vulcan XC-72 (Premetek Co. # P1DA200), Pt Black (Premetek Co. # P10V010), IrO_2 (Premetek Co. # P40V030), Poly(tetrafluoroethylene) (PTFE) (60 wt.% dispersion in alcohols/H_2O; Sigma-Aldrich #665800), KOH 90%, flakes (Sigma-Aldrich #484016), Ni mesh (woven), 200 LPI (Precision EForming LLC of Cortland NY) (cleaned using isopropyl alcohol prior to use), and copper tape 6.35 mm width (3M). Polypropylene-backed Preveil^{TM} expanded PTFE (ePTFE) membranes with 0.2 μm pore size, produced by General Electric Energy were used in all experiments.

5.2.2 Preparation of Catalyst-coated Gortex

See Chapter 2 Section 2.4.

5.2.3 Cell Construction

See Chapter 2 Section 2.5.

5.2.4 Reactant Gases and Electrochemical Testing

The hydrogen and oxygen used in the test fuel cells were piped in from high-pressure cylinders connected via suitable polymer tubing. The anode compartment of the cell was fed with high purity hydrogen, while high purity oxygen was supplied to the cathode.

Electrochemical testing was carried out using a Biologic VSP potentiostat. The fuel cells were characterised by steady-state current-voltage (*I-V*) curves, chronoamperometry, and chronopotentiometry. The electrolyte was 6 M KOH. The H_2 electrode (anode) was connected as the working electrode and the O_2 electrode was connected as a combined auxiliary/reference electrode. Thus, all reported voltages are *vs.* O_2. The electrolysers were characterized in a similar manner to that described above for fuel cells.

Electrochemical impedance spectroscopy (EIS) measurements were recorded at open circuit or at the constant current density of 10 mA cm^{-2} between 0.1 Hz and 200 kHz with an AC amplitude of ± 1 mA cm^{-2}. Spectra were analysed and fitted using ZView version 3.4.

5.3 Results and discussion

5.3.1 The Use of *Expanded PTFE* (*ePTFE*) Membranes ('*Gortex*') as Electrode Substrates

For this Chapter, we fabricated and studied alkaline fuel cells and electrolysers containing two Gortex-based gas diffusion electrodes, facing each other, separated by a defined distance of either 3 mm or 10 mm. An aqueous electrolyte of 6 M KOH filled the gap between the electrodes. In each of the fuel cells and electrolysers, the electrodes were prepared by coating the Gortex substrate with a slurry that contained catalysts, carbon black (CB) (that had been pre-treated with ascorbic acid to remove Fe impurities), dispersed poly(tetrafluoroethylene) (PTFE) as a binder, and a fine Ni mesh as a current carrier (as described in the Experimental section). Carbon black (CB) was not used in electrodes employed as the anode in the electrolysers in order to avoid carbon corrosion, which is known to be favoured in the highly oxidising environment of electrolyser anodes.[9] After drying and compacting by rolling in a two-roll mill (as described in the Experimental Section), the Gortex-based gas diffusion electrodes were ready for use. The following catalysts ('catalysts'), all of which were obtained from commercial vendors, were studied in this work:

- 20% Pt-Pd on Vulcan XC-72 (hereafter referred to as: '20% Pt-Pd')
- 10% Pt on Vulcan XC-72 ('10% Pt')
- 20% Pt-Ru on Vulcan XC-72 ('20% Pt-Ru')
- 20% Pt-Ir on Vulcan XC-72 ('20% Pt-Ir')
- 20% Pt-Co on Vulcan XC-72 ('20% Pt-Co')
- 20% Pt-Ni on Vulcan XC-72 ('20% Pt-Ni'), and
- IrO_2

When referred to in the text below as being incorporated in a Gortex-based electrode, this means that, unless stated otherwise, the electrode had the formulation 'Catalyst+CB+PTFE+Ni-mesh/Gortex'.

5.3.2 Polarisation Curves

To characterize the overall fuel cell-electrolyser performance, polarization curves were measured. These curves plot voltage against current; an example is provided in Figure 5.2.

Curves of this type have three different regions: (a) *a kinetic*, (b) *an ohmic*, and (c) a *mass transport* which have been discussed in great detail under Section 1.2.2.4 in Chapter 1.

Cell potentials were measured between the cathode and anode, meaning that the polarization curves represent the combination of the polarizations of these two electrodes. Power curves were obtained by multiplying the applied cell potential with the current density it generated.

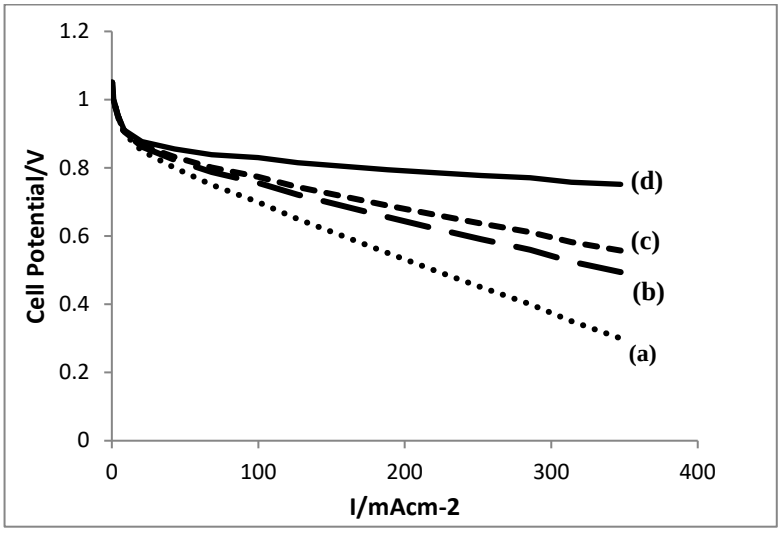

Figure 5.2. *Typical polarization curves during fuel cell operation, showing: (a) uncorrected data (….), and data corrected by taking into account: (b) the resistance due to the electrical contacts (- - -- --), (c) the resistance due to the electrolyte (- - -), and (d) the total resistance, as measured using EIS (——).*

The ohmic resistance of the supporting electrolyte (E_{el}) depends on the anode-to-cathode spacing or the charge-transport length (d), cross-sectional area of charge transport (A) and the ionic conductivity (σ) according to the equation:

$$E_{el} = \frac{d}{\sigma A} \qquad \ldots(5.1)$$

The E_{el} of the 6 M KOH electrolyte was calculated to be 0.5266 Ω for 20 °C experiments (d = 1 cm, σ = 1.35 S/cm,[10] and A=1 cm^2) and 0.741 Ω for 80 °C experiments (d = 0.3 cm, σ =

0.57 S/cm,[10] and A= 1 cm^2). Polarization curves reported below were iR-corrected to account for the electrolyte resistance. Figure 5.2(a) shows an uncorrected polarization curve, while Figure 5.2(c) depicts the equivalent polarisation curve corrected for the solution resistance. The polarization curves have also been corrected for ohmic resistance R_Ω from EIS (for example, as shown in Figure 5.2(d)) (obtained after subtraction of E_{el} from R_Ω) and for resistance due to the electrical contacts (for example, as shown in Figure 5.2(b)). The latter was done in order to better isolate the kinetic losses. The resulting iR-corrected polarization curves were later used for the generation of Tafel plots.

5.3.3 Tafel Plots

At low current densities, reaction kinetics are commonly modelled by the Tafel equation, given as:

$$\eta = A\ln\left(\frac{i}{i_o}\right) \qquad \ldots(5.2)$$

where η defines the overpotential, which is the difference between the electrode potential E and the standard potential E_0 ($\eta = E - E_0$), i denotes the current density, i_o is the exchange current density, and A is the Tafel slope. The Tafel slope provides insight into the reaction kinetics and also the mechanism, to thereby elucidate the elementary steps and the rate determining steps. The Tafel slope indicates how the current density changes with increasing overpotential. A is higher for an electrochemical reaction that is slow, since a slow reaction leads to a higher overvoltage.

The exchange current density (i_o), in case of highly irreversible reactions like the OER and ORR, cannot be used to accurately compare catalytic activity. Therefore, the potential at a defined steady-state current or the current at a defined steady-state potential, together with the value of the Tafel slope, can be used to measure or understand catalytic activity. In this

work, we have used the Tafel slope together with the measured potential at a fixed current density of 10 mA cm^{-2} to compare catalytic capacity.[11]

5.3.4 Electrochemical Impedance Spectroscopy

To break down the total cell resistance into individual polarization contributions, electrochemical impedance spectroscopy (EIS) was applied. EIS has proved to be very useful in distinguishing processes with different time constants. Preliminary EIS measurements were taken with hydrogen gas (H_2/H_2) and oxygen gas (O_2/O_2), supplied symmetrically to each of the facing Gortex electrodes in the cells, to determine the anode and cathode transfer functions at the open circuit voltage (E^0) and compare these with cells operated with either H_2 or O_2 at the same conditions.[24]

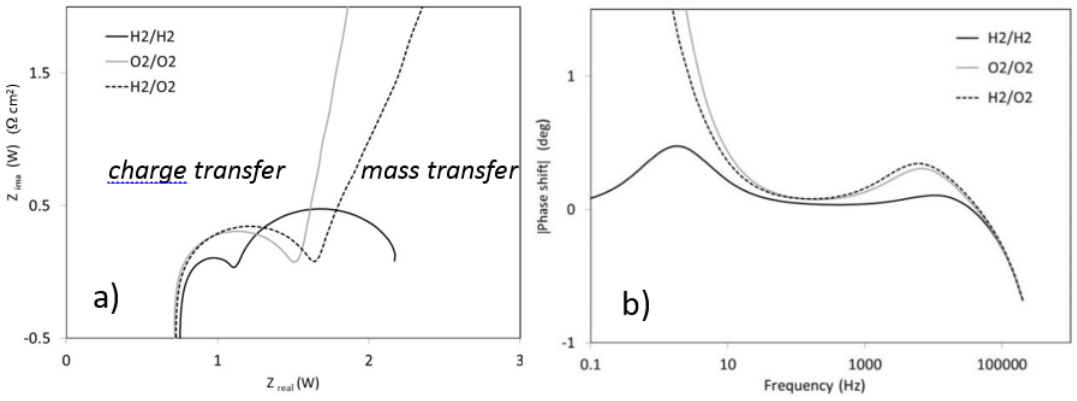

c)

H_2 %	$R_{(ct)}$ Ω	$C_{(ct)}$ F
H2/H2	0.23	8.0E-05
O2/O2	0.67	4.0E-05
H2/O2	0.76	3.7E-05

d)

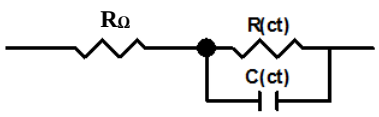

Figure 5.3. *(a) Nyquist and (b) Bode plots of symmetrically supplied hydrogen (H_2/H_2, black line), oxygen (O_2/O_2, grey line) and (H_2/O_2, dotted line), at the two electrodes of a fuel cell having two 20% Pd-Pt on Vulcan XC32+CB+PTFE+Ni mesh/Gortex gas diffusion electrodes, at open circuit potential (OCV); (c) table with charge transfer resistance (R_{ct}), double layer capacitance (C_{ct}); (d) equivalent electrical circuit*

For example, Figure 5.3(a) shows EIS data for cells containing two Gortex-based electrodes coated with 20% Pt–Pd on Vulcan XC-72, carbon black, PTFE binder and Ni mesh current carriers. The manifestation of two semi-circles in the Nyquist plots can be explained as a combination of two time constants or two characteristic processes i.e., *kinetic* and *diffusion* processes. The *kinetic* part dominates at higher frequencies and includes ohmic resistance (R_Ω), a charge transfer (R_{ct}) associated with the processes at the electrodes and a double layer capacitance within the catalyst layer (C_{ct}), wherein, the *first time constant* consists of C_{ct} in parallel with R_{ct}. The *diffusion* process dominates overall impedance at lower frequencies and the *second time constant* comprises of Warburg impedance (Z_d) in parallel with another double layer capacitance (C_d).

The impedance spectra in the higher frequency range (i.e. only kinetic process) were simulated with the equivalent circuit (corresponding to the first time constant) in Figure 5.3(d) and the inductance of the wires was not considered. The Nyquist plots were fitted using Zview software® according to the equivalent circuit diagram. The charge transfer arc for H_2/H_2 shows, as expected, a lower R_{ct} and higher C_{ct} when compared to cells operated with O_2/O_2 and H_2/O_2. Additionally, from the Bode plot (Figure 5.3(b)), which provides a clearer description of the electrochemical processes in the frequency domain, it can be see that charge transfer for the H_2/H_2 cell occurs at a higher frequency (≈16 kHz) compared to O_2/O_2 and H_2/O_2 (≈10 kHz) indicating slower kinetics for O_2/O_2 and H_2/O_2. Thus we can reasonably assume that the impedance measured in a 2-electrode cell will be dominated by the slower kinetics of the O_2-electrode, which would be the cathode in a fuel cell and the anode in an electrolyser.

5.3.5 Bifunctional Hydrogen Catalysts (BHC)

At the start of the present study we sought to identify catalysts that worked well for both the HOR and the HER and could therefore be employed on the H_2-electrode in fuel cells and electrolysers. Catalysts of this type may be said to be bifunctional hydrogen catalysts (BHCs).

Pt is considered to be the most efficient and stable BHC for fuel cells and electrolysers.[12] Due to its scarcity and high cost, efforts have been made to reduce its loading in fuel cells to <0.5 mg/cm^2.[13] In our cells with Gortex-based electrodes, the Pt loading could be decreased to 0.05 mg/cm^2 and it not only exhibited low overvoltage in HER but also exhibited high efficiency for HOR (discussed in detail in Chapter 4).

5.3.6 Bifunctional Oxygen Catalysts (BOC)

For the same reason we sought to identify catalysts that worked well for both the OER and the ORR and could therefore be employed on the O_2-electrode in fuel cells and electrolysers. Catalysts of this type may be said to be bifunctional oxygen catalysts (BOCs).

In this case also, Pt offers the best-available BOC. Other noble metals such as Ag show high performance for the ORR but are not suitable for the OER due to dissolution during electrolysis. Several literature studies[14,15,16,17] have proposed the use of alternate catalysts primarily based on Ir, Ru and their oxides, and their combinations. For instance, $CoIrO_3$ and $NiIrO_3$ show reasonable activity for the OER in a high surface area form; RhO_2 and IrO_2 have higher surface area, imparting them with higher activity for oxygen evolution[18]; and $PbPdO_2$ [19] and their combinations also exhibit good activity and stability.

In this work, we aimed to, first; examine a range of precious metals as ORR catalysts in fuel cell mode at room temperature (20 ^oC). In a second step, we then studied the effect of temperature on the best ORR performing catalysts. The effect of temperature was examined

by comparing these catalysts at 20 °C versus 80 °C. Finally, the best performing ORR catalyst at 80 °C was tested in electrolyser mode at same temperature to analyze the bi-functionality and efficiency of that catalyst in a DRFC running at 80 °C.

5.3.7 Fuel Cell Performance at Room Temperature (20 °C)

The high cost of Pt hinders the large-scale application of alkaline fuel cells where Pt amounts to around 55 % of the total cost. To address these issues, recent significant advances on the reported new chemical synthesis of Pt-based nanostructures provide new opportunities for achieving high ORR activities. Combining Pt with other relatively low cost noble metals and with low-cost transition metals not only increases surface sites but also helps in tuning the binding strength of adsorbed species with Pt.[20] In this study we therefore examined the performance, in fuel cells, of Gortex-based gas diffusion electrodes incorporating commercially available Pt catalysts (10% Pt and Pt black), Pt-based bimetallic catalysts (20%Pt-Pd, 20%Pt-Ir, 20%Pt-Ru, 20%Pt-Ni, 20%Pt-Co) and precious metal oxide catalysts (IrO_2).

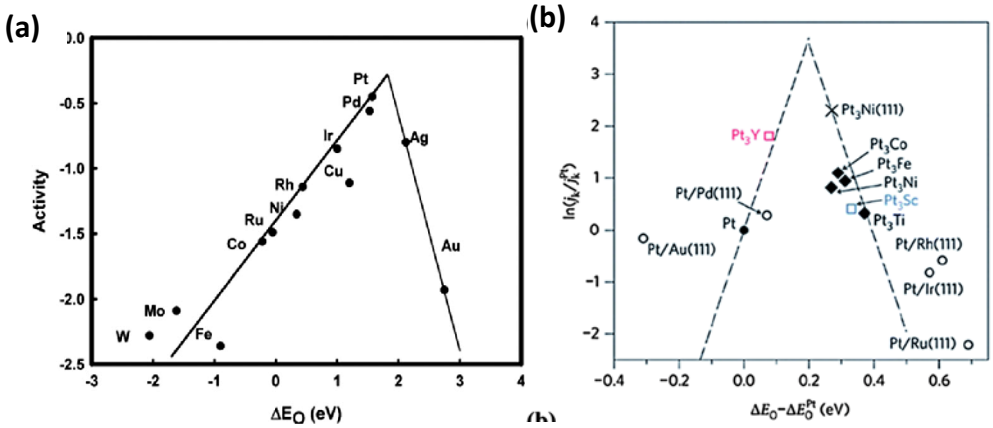

Figure 5.4. *(a) Volcano plot for oxygen reduction reaction (ORR) activity as a function of oxygen binding energy on metals,[21] (b) Volcano plot for oxygen reduction reaction (ORR) activity as a function of oxygen binding energy on Pt-based transition metal alloys.[22] Reproduced with permission from references 21 and 22.*

Cathode Catalyst	η_{act} (V)	$V_{@10mAcm-2}$ (V)	R_Ω (Ω cm^2)[a]	R_{ct} (Ω cm^2)	C_{ct} (μF)	Z_d (Ω cm^2)	b_1 (mV dec^{-1})	b_2 (mV dec^{-1})	Loading (mg_{metal} cm^{-2})
20%Pt-Pd	0.376	0.86	0.71	0.29	58.1	2.7	43	125	0.101
10%Pt	0.430	0.854	0.79	0.31	113.2	3.4	52	134	0.052
20%Pt-Ru	0.454	0.838	0.69	0.35	53.0	4.68	45	150	0.097
Pt black	0.387	0.835	0.73	0.2	6461.6	4.99	-	-	1.62
20%Pt-Co	0.540	0.828	0.71	1.78/1.93*	56/22*	5.8/6.1*	-	-	0.097
20%Pt-Ni	0.434	0.818	0.68	1.72/1.88*	57/30*	5.8/6.2*	-	-	0.101
20%Pt-Ir	0.465	0.816	0.76	0.37	52.7	3.75	44	145	0.12
IrO_2	0.530	0.778	0.91	0.47	9218.8	3.3	51	115	5.42

*values after 10 minutes of operation; [a] 3 mm inter-electrode gap;

Table 5.1. *Comparison, at 20 ^oC, of alkaline fuel cells containing Gortex anode electrodes coated with different precious metal catalysts. Gortex coated with 10% Pt served as the anode (H_2 catalyst) in all cases. Symbols: activation overpotential (η_{act}), Voltage at 10 mA cm^{-2} ($V_{@10mAcm-2}$), Tafel slope (b_1) (at lower current density (LCD)), Tafel slope (b_2) (at higher current density (HCD)); from electrochemical impedance, ohmic resistance (R_Ω), charge transfer resistance $R_{(ct)}$, double-layer capacitance within the catalyst layer $C_{(ct)}$, diffusional resistance $Z_{(d)}$.*

The above-mentioned catalysts were layered on Gortex electrodes that were then tested in a fuel cell configuration. All of the fuel cell cathodes comprised of a mixture of one of the above catalysts, carbon black (CB) and PTFE with a Ni mesh current collector, deposited on Gortex ('Catalyst+CB+PTFE+Ni-mesh/Gortex'). The anode was kept the same for all the different cathodes, and comprised of 10% Pt on Vulcan XC72, carbon black (CB) and PTFE with a Ni mesh current collector, deposited on Gortex ('10%Pt+CB+PTFE+Ni-mesh/Gortex'). Table 5.1 lists the specific metal loadings used for each electrode studied. Cathodes involving carbon supported Pt-based catalysts had an average metal loading of 0.1 mg cm^{-2}, along with carbon black and PTFE, each having an average loading of 1.54 mg cm^{-2}. The cathodes containing unsupported Pt black and IrO_2 had catalyst loadings of 0.16 mg cm^{-2} and 0.54 mg cm^{-2} respectively, mixed with carbon black and PTFE, each having an average loading of 5.4 mg cm^{-2}. The anodes contained an average of 0.05 mg cm^{-2} of Pt, with average carbon black and PTFE loadings of 1.5 mg cm^{-2}. The carbon black used was pretreated using ascorbic acid in order to remove Fe impurities and enhance its corrosion resistance.[23]

Alloying Pt with lower-cost transition metals can lead to significant improvements in atomic and electronic structure as well as the available surface sites (known as an 'ensemble effect'), benefiting for tuning the binding strength of adsorbed species (reactants, products, spectator ions) with Pt.[24] Figure 5.4(a) and (b) shows the measured activities of pure Pt and various metals (precious as well as transition metals) along with Pt alloys as a function of oxygen adsorption energy (also known as volcano plot). For metals that bind oxygen too strongly, the rate is limited by the removal of adsorbed O and OH species. For metal surface that bind oxygen too weakly, the rate is limited by the dissociation of O_2, or more likely, the transfer of electrons and proton to adsorbed O_2.[21]

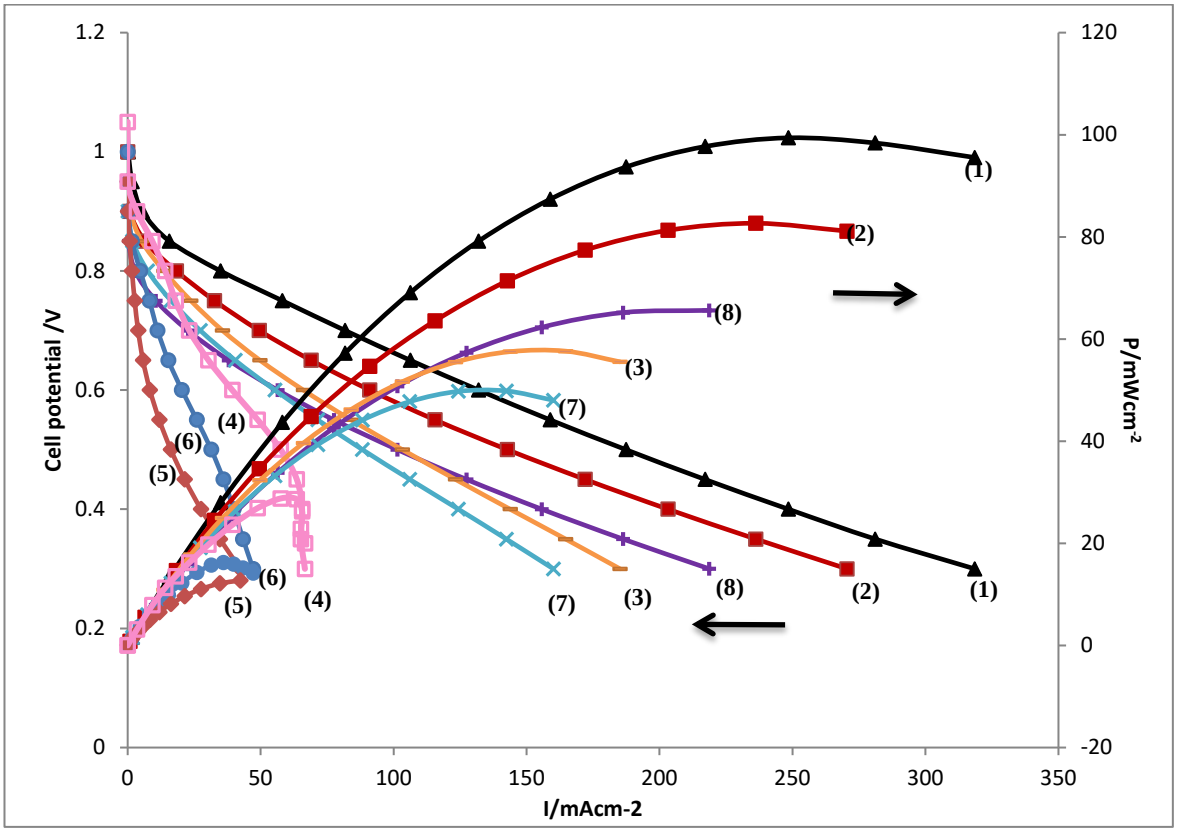

Figure 5.5. *Polarization curves (left axis) and power density curves (right axis) at 20 °C for alkaline fuel cells containing Gortex electrodes coated with (1) ▲-20% Pt-Pd (2) ■-10% Pt (3) —-20% Pt-Ru (4) □-Pt black (5) ♦ -20% Pt-Co (6) ●-20% Pt-Ni (7) X -20% Pt-Ir (8) +-IrO_2 as cathode (O_2 catalyst). Gortex coated with 10% Pt served as the anode (H_2 catalyst) in all cases. Electrolyte: 6 M KOH.*

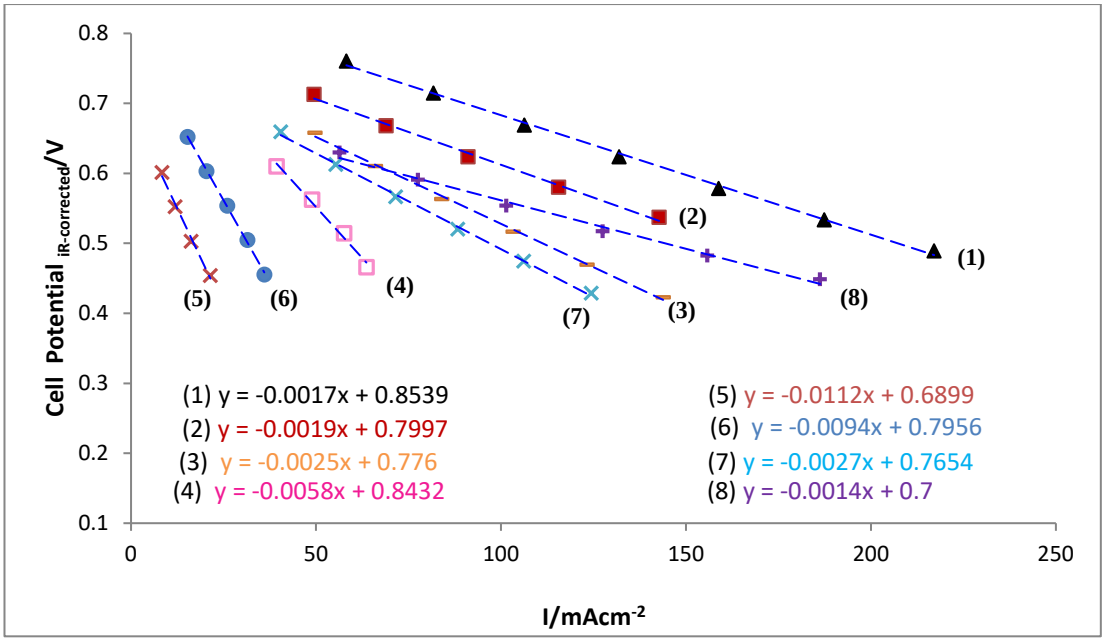

Figure 5.6. *Straight line fits of the ohmic regions (iR-corrected) for the alkaline fuel cells, at 20 °C, containing Gortex electrodes coated with (1) ▲-20% Pt-Pd (2) ■-10% Pt (3) ▬-20% Pt-Ru (4) □-Pt black (5) ♦ -20% Pt-Co (6) ●-20% Pt-Ni (7) X -20% Pt-Ir (8) +-IrO_2 as cathode (O_2 catalyst). Gortex coated with 10% Pt served as the anode (H_2 catalyst) in all cases. The fitted straight lines have the general formula y=mx+c, where the value of c accords with the onset potential of the fuel cell. The activation overpotential is the difference between the onset potential and 1.23 V, which is the E^o of the cell at 20 °C. Electrolyte: 6 M KOH. The cell potential was iR-corrected for resistance due to electrical contacts*

A trend similar to the volcano plot is visible in the fuel cell polarisation curves of the various Pt-based bimetallics shown in Figure 5.5. As can be seen, 20% Pt-Pd is the best catalyst for oxygen reduction. The alkaline fuel cell using '20%Pt-Pd+CB+PTFE+Ni-mesh/Gortex' as a cathode generated 281 mA cm^{-2} and 98 mW cm^{-2} at 0.35 V and 20 °C. At a constant 0.7 V, the cell produced 82 mA cm^{-2}. It delivered a stable current of 10 mA cm^{-2} for 1 h at a constant voltage of 0.860 V (see Figure 5.6). Its activation overpotential was 376 mV (Table 5.1 and Figure 5.6).

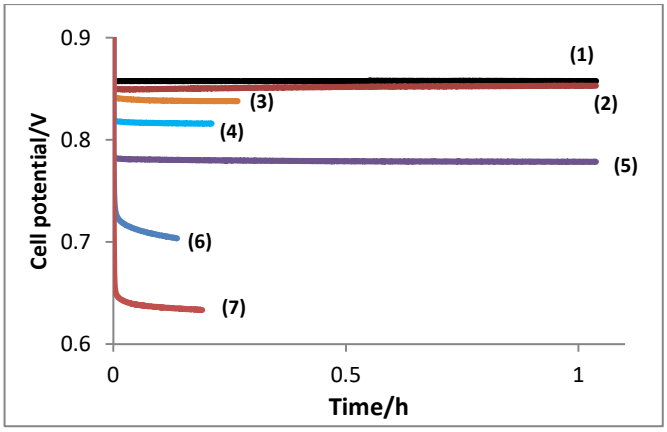

Figure 5.7. *Chronopotentiograms (CP) at 10 mA cm^{-2} for alkaline fuel cells, at 20 °C, containing Gortex electrodes coated with (1) —20% Pt-Pd (2) —10% Pt (3) —20% Pt-Ru (4) —20% Pt-Ir (5) — IrO_2 (6) —20% Pt-Ni (7) — 20% Pt-Ir, as cathode (O_2 catalyst). Gortex coated with 10% Pt served as the anode (H_2 catalyst) in all cases. Electrolyte: 6 M KOH.*

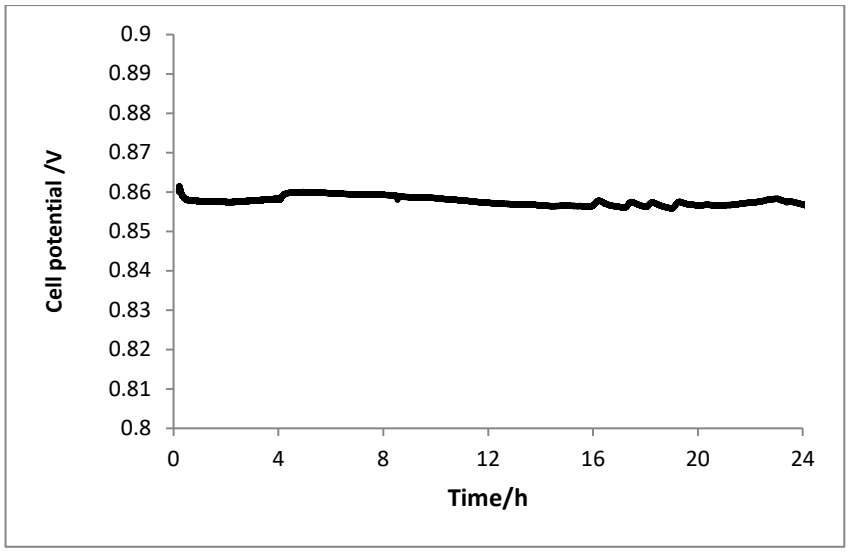

Figure 5.8. *Chronopotentiogram (CP) at 10 mA cm^{-2} for a fuel cell with 10% Pt/CB+PTFE+Ni-mesh/Gortex at both the anode and cathode, at 20 °C. Electrolyte: 6 M KOH*

The catalytic performance of 20% Pt-Pd may be attributed to the modified surface electrochemical properties caused by charge redistribution upon forming the Pt-Pd bond.[24] Arenz et al. also reported that Pd/Pt (111) has a higher ORR activity than Pt (111) in alkaline solution,[25] as also indicated in the volcano plot.

The fuel cell with a cathode comprising of '10%Pt+CB+PTFE+Ni-mesh/Gortex' recorded an activation overpotential of 430 mV. As previously noted, this may be attributed to the formation of Pt-OH on the catalyst surface, leading to a loss of active sites for the ORR,[27,28] although carbon supported Pt has also been reported to be subject to mild corrosion in alkaline media.[26] The latter explanation seems unlikely given that, as depicted in Figure 5.8, the '10%Pt+CB+PTFE+Ni-mesh/Gortex' cathode produced a stable current density of 10 mA cm^{-2} for more than 24 h. The ascorbic acid pretreatment of the carbon black clearly helped improve catalyst stability.

By contrast, degradation of alkaline fuel cell performance over time is common when using conventional gas diffusion electrodes. It is often attributed to flooding of the cathode by the aqueous electrolyte. This typically involves the solid-liquid-gas interface progressively re-locating itself from the catalytic layer of the gas diffusion electrode into the gas diffusion layer, thereby reducing the accessibility of oxygen to the catalytic sites by blocking the gas pores.[29] Another study explained that flooding may arise due to the role of 'electrocapillarity', in which the contact angle between the electrode surface and the electrolyte is potential dependent.[30] It was shown that the contact angle decreased with a decrease in potential from the OCV, resulting in greater wetting of the electrode. An increase in pH and temperature also led to flooding of the electrode, especially at 90 °C, when vapour condensed in the gas pores. The hydrophobicity of traditional GDEs, in any case, degrade over time, resulting in pore flooding, which thereby limits gas transport.[31]

Replacing conventional gas diffusion electrodes with Gortex-based electrodes addresses all the above issues. The hydrophobic nature of the Gortex gas diffusion layer prevents any flooding of the electrode over time and maintains a well-defined three phase interface for oxygen/catalyst/electrolyte.

The highest activation overpotential was produced by the fuel cell which used 'IrO_2+CB+PTFE+Ni-mesh/Gortex' as cathode. The commercially supplied batches of Pt black and IrO_2 that were studied were, unfortunately, characterized by relatively low surface areas and poor catalyst utilization, likely due to sintering and agglomeration.[32]

In order to compare the catalytic activity of other Pt-based bimetallic cathodes, Table 5.1 lists the voltage required to produce a current of 10 mA cm^{-2}. The values show that overall fuel cell performance was influenced by the kinetics of the ORR as facilitated by the catalysts used at the cathodes. This was, in turn, dependent on the nature of the alloying component, with Pt-Pd > Pt > Pt-Ru > Pt-Co > Pt-Ni > Pt-Ir. Cathodes containing the Pt bimetallics Pt-Ru, Pt-Ir, Pt-Co, and Pt-Ni, yielded activation overpotentials of 454 mV, 465 mV, 540 mV and 434 mV respectively, which was higher than the Pt-Pd bimetallic. They, likewise, produced 10 mA cm^{-2} at lower potentials than Pt-Pd.

However, as seen in Figure 5.7, only fuel cells with either '20%Pt-Ir+CB+PTFE+Ni-mesh/Gortex' or '20%Pt-Ru+CB+PTFE+Ni-mesh/Gortex' as cathodes, could be considered to be truly stable over the first hour at 10 mA cm^{-2} (with degradation rates as low as 5±0.3 mV hr^{-1}). The fuel cell cathodes comprising '20%Pt-Co+CB+PTFE+Ni-mesh/Gortex' or '20%Pt-Ni+CB+PTFE+Ni-mesh/Gortex' catalysts, rapidly deteriorated at a rate of approximately ~90 mV hr^{-1} and ~180 mV hr^{-1} respectively, in less than 10 min of operation. For Pt-Co and Pt-Ni catalyst, the degradation in performance indicates segregation of Ni and Co on the surface.[33]

The long-term stability of fuel cells comprising '20%Pt-Pd+CB+PTFE+Ni-mesh/Gortex', '10%Pt+CB+PTFE+Ni-mesh/Gortex' or 'IrO_2+CB+PTFE+Ni-mesh/Gortex' as cathodes indicates that these Gortex-based fuel cells were clearly robust to CO_2 poisoning, which otherwise causes carbonate precipitation in electrode pores and eventually electrode degradation over time in conventional gas diffusion electrodes.[34]

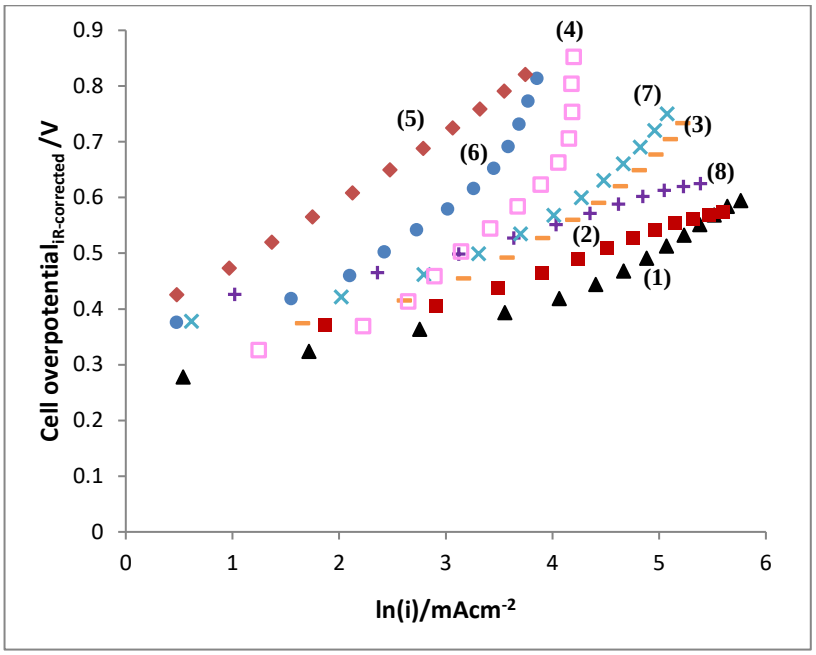

Figure 5.9. *iR-corrected Tafel plots for the alkaline fuel cells, at 20 °C, containing Gortex electrodes coated with (1) ▲-20%Pt-Pd (2) ■-10%Pt (3) —-20%Pt-Ru (4) □-Pt black (5) ♦ -20%Pt-Co (6) ●-20%Pt-Ni (7) X -20%Pt-Ir (8) +-IrO_2 as cathode (O_2 catalysts). Gortex coated with 10% Pt served as the anode (H_2 catalyst). Electrolyte: 6 M KOH.*

To further compare electrocatalytic activity of the fuel cells, a Tafel plot analysis was undertaken, involving determination of potential-dependent (i.e. coverage dependent) changes in the Tafel slope.[35] The Tafel slopes evaluated are descriptive of ORR at cathode and therefore governed by the oxygen overpotential.

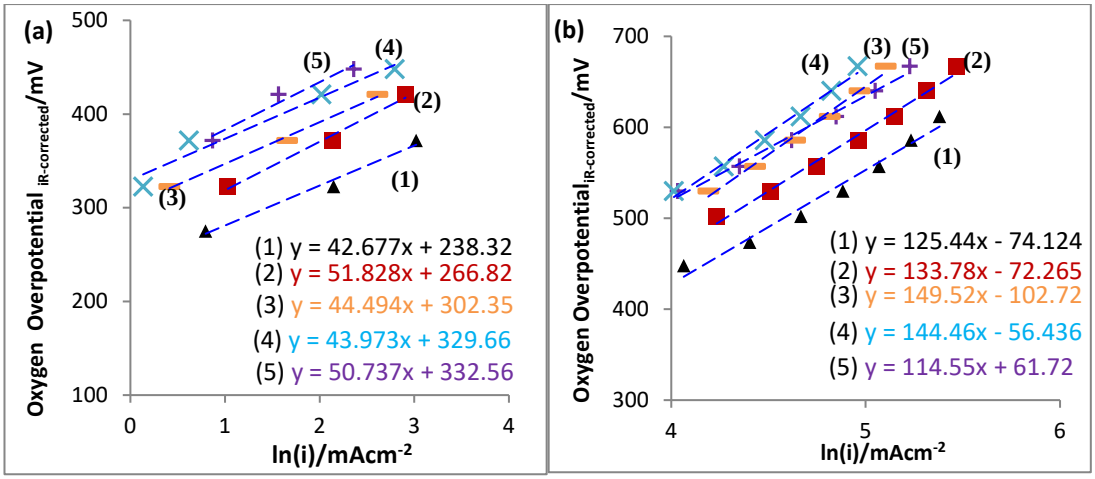

Figure 5.10. *iR-corrected Tafel plots at (a) Low Current density (LCD) (b) High Current Density (HCD) for the alkaline fuel cells, at 20 °C, containing Gortex electrodes coated with (1) ▲-20%Pt-Pd (2) ■-10%Pt (3) ▬-20%Pt-Ru (4) X -20%Pt-Ir (5) +-IrO_2 as cathode (O_2 catalysts). Gortex coated with 10% Pt served as the anode (H_2 catalyst). The fitted straight lines have the general formula y=mx+c, where m is the Tafel slope and c is the imputed exchange ciurrent density, i_o. Electrolyte: 6 M KOH.*

Two Tafel slopes were evaluated. Tafel slope b_1 and Tafel slope b_2 were calculated at lower current densities (LCD) and higher current densities (HCD) respectively. The two Tafel slopes and their calculation are shown in Figure 5.9 and Figure 5.10(a)-(b).

As noted in Table 5.1, the fuel cell with a '20%Pt-Pd+CB+PTFE+Ni-mesh/Gortex' cathode, exhibited two Tafel slopes: 43 mV dec^{-1} (b_1) and 125 mV dec^{-1} (b_2). The fuel cell with a '10%Pt+CB+PTFE+Ni-mesh/Gortex' cathode followed closely behind, with b_1 starting from 52 mV dec^{-1}, and b_2, increasing to >100 mV dec^{-1}; these are less than Pt-based catalysts that have been reported previously.[36]

Noticeably, amongst the Pt and Pt-based bimetallic cathodes tested, cathodes made up of '20%Pt-Pd+CB+PTFE+Ni-mesh/Gortex' exhibited the lowest Tafel slopes at both lower and higher overpotentials. Generally, a lower Tafel slope indicates a faster electrochemical

reaction. The Tafel slope usually increases with higher current densities. In addition, a smaller Tafel slope is preferred since a small change in electrode overpotential results in a large increase in current. When IrO_2 was employed as a cathode catalyst, the resulting fuel cell produced a Tafel slope of 51 mV dec^{-1} at lower overpotentials, which increased to 115 mV dec^{-1} at higher overpotentials.

To further investigate the electrocatalytic activity, electrochemical impedance measurements of each of the fuel cells were undertaken. Figure 5.11(a) and (b) depict the two-electrode Nyquist and Bode plots of the above cells, measured under galvanostatic conditions at 10 mA cm^{-2}. The Nyquist plots, showing experimental as well as model fitting data, are provided in Figure 5.11(a). All of the fuel cells with Pt-based catalysts as cathodes (loading = 0.1 mg cm^{-2}) recorded very similar ohmic resistances (as indicated by the intercept of the Nyquist plot with the x-axis) whereas the ohmic resistance recorded for the fuel cell containing IrO_2 as cathode (loading = 5.4 mg cm^{-2}), was a bit higher in value, indicating a better contact resistance and lower internal resistance in the Pt-based cathodes. Figure 5.11(c) shows the equivalent circuit incorporating the time constants mentioned earlier (see Section 5.3.4).

The Bode plots (Figure 5.11(b)) show the frequencies of the different arcs in the Nyquist plots (Figure 5.11(a)). Lower frequencies (<ca. 100 Hz) are characteristic of diffusion processes, whereas the higher frequencies (>ca. 100 Hz) indicate charge transfer (catalytic processes).

From Figure 5.11(a) it can be seen that the Nyqist plots generally contain two semicircular arcs, with the left-hand arc being smaller than the right-hand one. The Bode plots (Figure 5.11(b)) indicate that the smaller, left-hand arc corresponds to a charge transfer process, while the right-hand arc is due to a diffusion-related process.

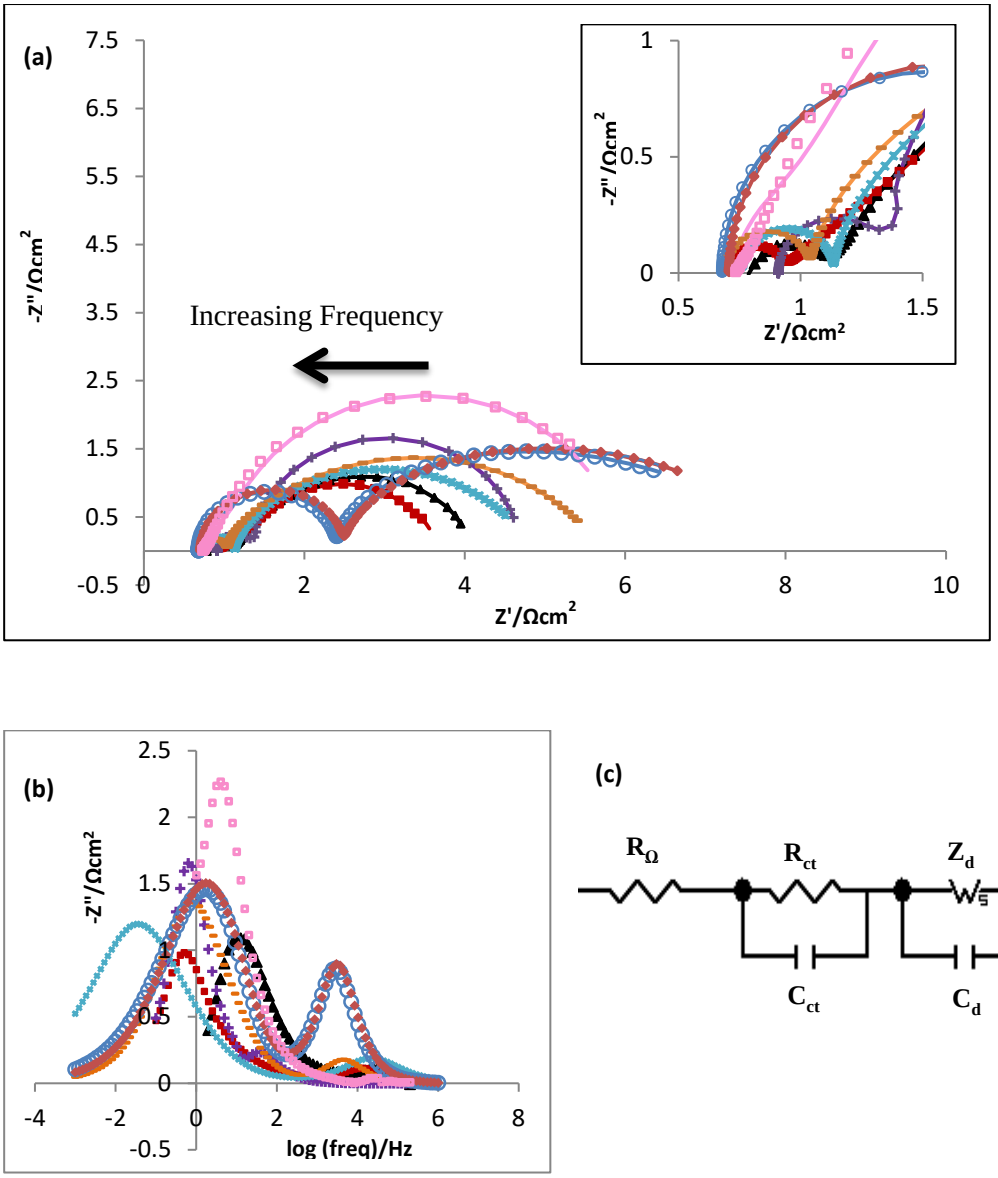

Figure 5.11. *(a) Nyquist plot and inset showing an enlargement of the high frequency impedance region, (b) Bode plots; at 10 mA cm^{-2}, showing measured data (individual data points) and modelled data (solid line). The modelled data used the equivalent circuit shown in (c). Alkaline fuel cells, at 20 ^{o}C, containing Gortex electrodes coated with (1) ▲-20%Pt-Pd (2) ■ -10%Pt (3) — -20%Pt-Ru (4) □ -Pt black (5) ♦ -20%Pt-Co (6) ○ -20%Pt-Ni (7) X -20%Pt-Ir (8) + -IrO$_2$ as cathode (O$_2$ catalysts). Gortex coated with 10% Pt served as the anode (H$_2$ catalyst). Electrolyte: 6 M KOH.*

The left-hand arc is smallest for the fuel cell containing Pt black as the cathode catalyst. This is followed by 20% Pt-Pd > 10% Pt > 20% Pt-Ru > 20% Pt-Ir > 20% Pt-Ni > 20% Pt-Co, as cathode catalysts respectively. As the first semicircle in the Nyquist plot is descriptive of charge transfer kinetics, this means that R_{ct} follows the same trend.

The right-hand semi-circle in the Nyquist plot in Figure 5.11(a), which measures the diffusional resistance Z_d, is relatively large for the fuel cell with Pt black as the cathode catalyst. This is followed by the fuel cells with 20%Pt-Ni and 20%Pt-Co as cathode catalysts, demonstrating an equally higher Z_d for these three fuel cells. A similar trend to what was observed for R_{ct} in the Nyquist plots at higher frequencies, is therefore observed, with cathodes having Pt black producing the lowest impedance while the highest is produced by cathodes with 10% Pt-Co. At lower frequencies, the Bode plots indicate that the cathodes with Pt black, 20% Pt-Ni or 20% Pt-Co display much higher impedance when compared with cathodes containing other catalysts.

Both R_{ct} and Z_d can be used to establish a correlation between impedance and volcano plots. As mentioned earlier, the stronger/weaker the binding energy of a catalyst, the more the resistance faced by catalyst to transfer charge during ORR, and thus the higher the R_{ct} exhibited in the electrochemical impedance spectrum. In addition, when an intermediate species binds strongly to a catalyst site, the number of active sites available for reaction decreases. As a result, mass transport resistance increases which may be related to Z_d from the electrochemical impedance analysis (see Table 5.1). Stated another way: Z_d may be used to evaluate the robustness of a catalyst; a more robust and durable catalyst should produce a lower Z_d value.

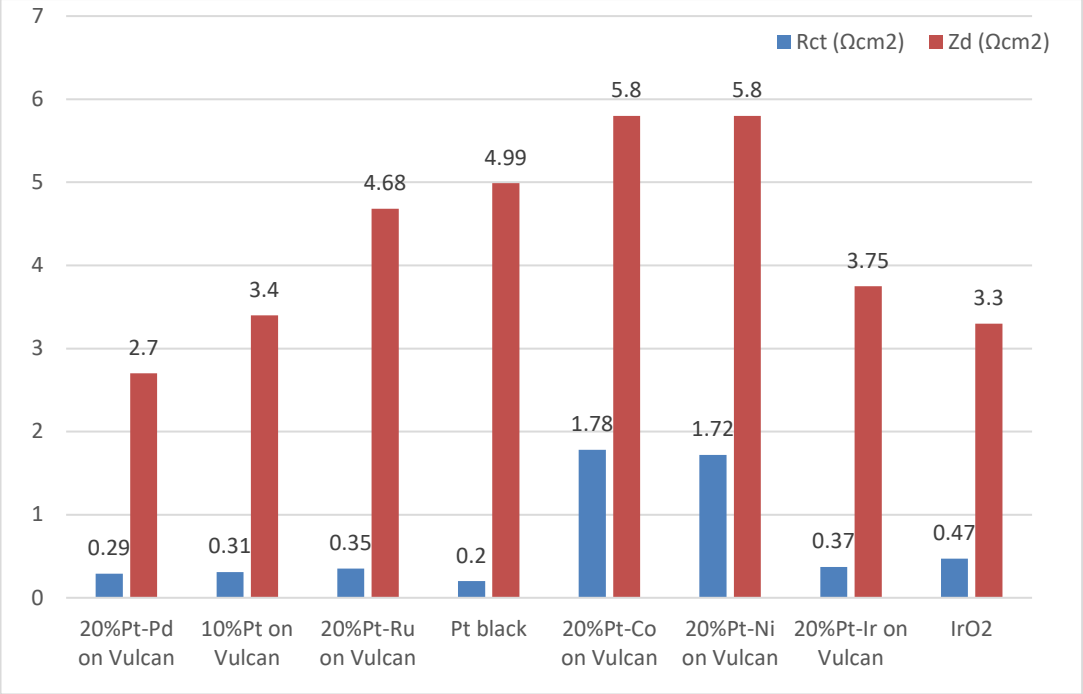

Figure 5.12. *Parameters obtained from equivalent electric circuit fitted to electrochemical impedance of different precious catalyst: charge transfer resistance $R_{(ct)}$, diffusional resistance $Z_{(d)}$.*

As is evident from the volcano plot, 20% Pt-Pd displayed the highest oxygen reduction activity, which manifested in the fuel cell with the '20%Pt-Pd+CB+PTFE+Ni-mesh/Gortex' cathode, as the lowest combination of R_{ct} (0.29 Ω cm^2) and Z_d (2.7 Ω cm^2) values (see Table 5.1 and Figure 5.12). A small R_{ct} and Z_d indicates fast electron transfer and easy accessibility of oxygen ions to the active sites. The fuel cell with the '10%Pt+CB+PTFE+Ni-mesh/Gortex' cathode exhibited a comparable R_{ct} but a slightly higher Z_d, indicating slightly more constrained access to the active sites. Owing to the low Z_d, both of the fuel cells containing 20%Pt-Pd and 10%Pt as cathode catalysts respectively, recorded a stable current density value of 10 mA cm^{-2} for more than 1 h with a negligible degradation rate.

Figure 5.12 also shows that the fuel cell containing unsupported Pt black as the cathode catalyst exhibited the lowest R_{ct} (that is, it was catalytically the most active) but due to its

much higher Z_d, its performance rapidly degraded. In effect, the highly active catalytic sites were progressively starved, resulting in an overall declining performance.

The fuel cell with unsupported IrO_2 as cathode catalyst, produced a higher R_{ct} but a lower Z_d than its unsupported Pt black analogue, giving it an overall lower total resistance ($R_{ct} + Z_d$ = 3.77 Ω cm^2). It was therefore stable enough to sustain a constant current density of 10 mA cm^{-2} for more than 1 h. Similarly, fuel cells with cathodes employing 20% Pt-Ir and 20% Pt-Ru as catalysts, also exhibited stable current values owing to low mass transport resistances (Z_d).

Co and Ni are known to exhibit lower oxygen reduction activity (as per the volcano plot), so when the fuel cell cathode comprised of Pt-Co or Pt-Ni catalysts, a much higher charge transfer resistance of roughly ~1.75 Ω cm^{-2} and an equally high mass transport resistance of 5.8 Ω cm^{-2}, was observed (see Figure 5.12). It can be concluded that, when Pt is combined with an earth-abundant transition metal like Ni and Co, it is prone to segregation at the surface, especially at higher current densities. Consequently, there is an increase in R_{ct} and Z_d values for Pt-Ni and Pt-Co over time as indicated in Table 5.1. Though, the environment of oxide-covered Ni or Co atoms inhibits the formation of hydroxide on Pt and thereby enhances the kinetics of the bimetallic catalysts,[24] coverage of the active Ni and Co sites with oxides impedes their access to charge, thereby decreasing the capacitance of the bimetallic catalysts by roughly a factor of 2 when compared to cathodes containing pure Pt/Vulcan as catalyst (as seen in Table 5.1). When equivalent electric circuits were fitted to impedance data from fuel cells comprising of Pt-Ni or Pt-Co as cathode catalysts, a capacitance element (C_{dl}) gave the best fit in the first 10 min of operation, but thereafter a constant phase element (CPE) produced a better fit. Noticeably, for these catalysts, capacitance decreased by half over its initial value in less than 10 min, which is indicative of reduced electrochemical active area and therefore declining performance.

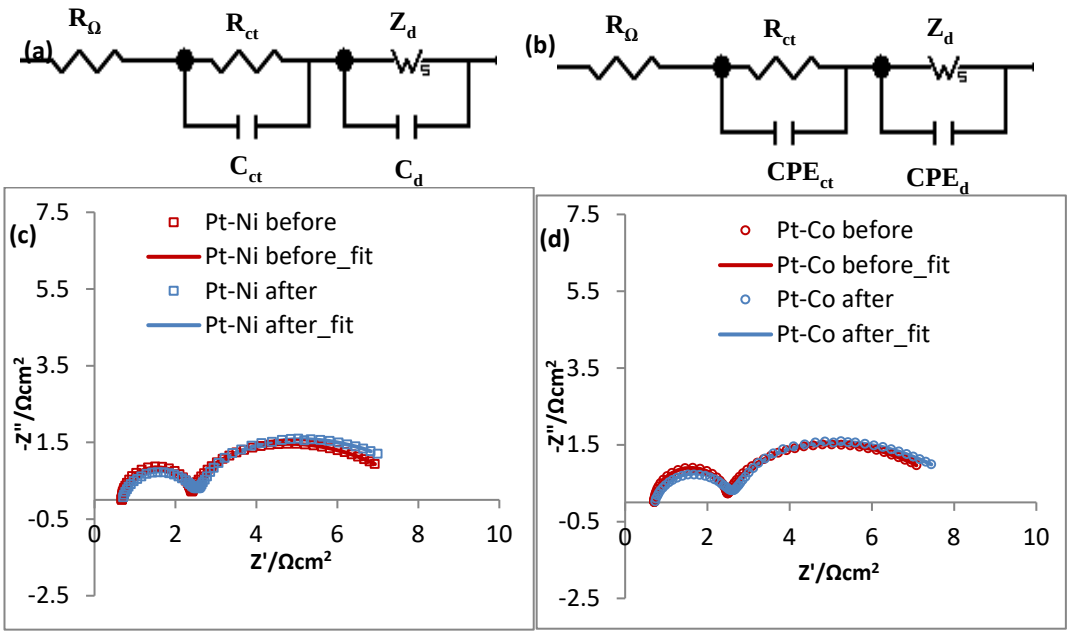

Figure 5.13. *(a) Equivalent circuit before chronopotentiometry (CP) at 10 mA/cm^2 for10 min, (b) Equivalent circuit after chronopotentiometry (CP) at 10 mA/cm^2 for10 min, (c) Nyquist and (d) Bode plots at 10 mA cm^{-2}, showing measured data (individual data points) and modelled data (solid line). The modelled data used the equivalent circuit shown in (a) for before chronopotentiometry (CP) at 10 mA/cm^2 for10 min, and (b) for after chronopotentiometry (CP) at 10 mA/cm^2 for10 min. Alkaline fuel cells, at 20 ^{o}C, containing Gortex electrodes coated with (1) □-20%Pt-Ni before (2) □-20%Pt-Ni after (3) ○-20%Pt-Co before (4) ○-20%Pt-Co after, as the cathode (O_2 catalysts). Gortex coated with 10% Pt served as the anode (H_2 catalyst). Electrolyte: 6 M KOH.*

5.3.8 Fuel Cell Performance at 80 ^{o}C

We then used 20% Pt-Pd, 10% Pt and IrO_2 as cathode catalysts to study the effect of temperature on their respective electrocatalytic performances in fuel cell mode. As at 20 ^{o}C, the fuel cells utilized the same anode ('10%Pt+CB+PTFE+Ni-mesh/Gortex'). Loadings of each catalyst, carbon black and PTFE on cathode and anode were similar to the 20 ^{o}C values. Their polarization/power curves and performance at 80 ^{o}C before and after chronopotentiometry at 10 mA/cm^2 for 10 min was also evaluated.

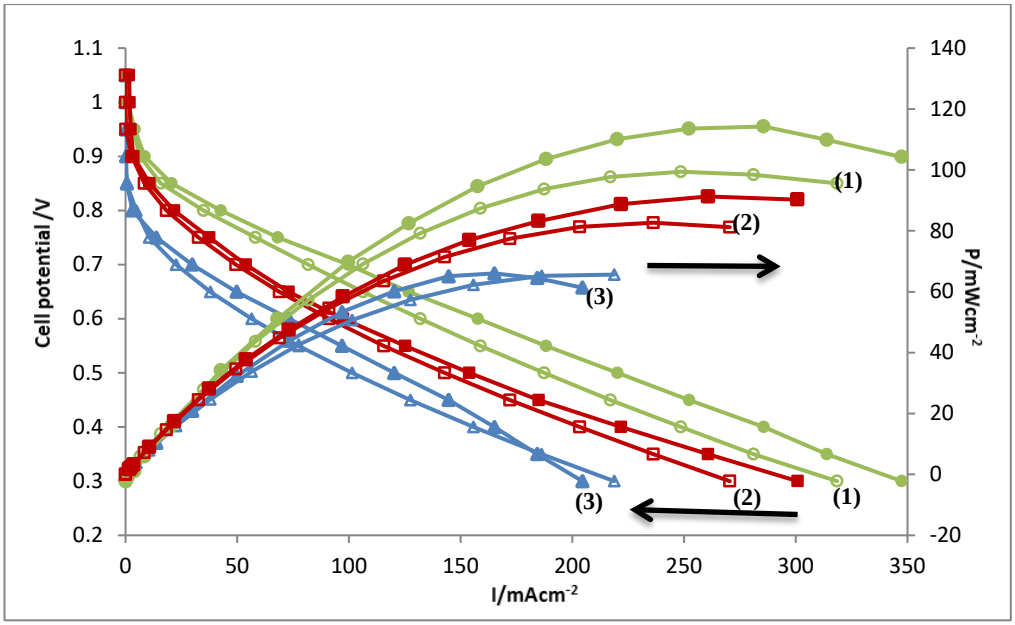

Figure 5.14. *Polarization curves (left axis) and power density curves (right axis) for alkaline fuel cells containing Gortex electrodes coated with (1)○● -20%Pt-Pd; (2)□■ -10%Pt and (3) △▲ - IrO_2 as the cathode (O_2 catalysts). Gortex coated with 10% Pt served as the anode (H_2 catalyst). Empty and filled markers denote 20 °C and 80 °C data respectively. Electrolyte: 6 M KOH.*

Cathode Catalyst	η_{act}(V)		$V_{@10mAcm-2}$ (V)		R_Ω (Ω cm²)		R_{ct} (Ω cm²)		C_{ct} (μF)		Z_d (Ω cm²)		b_1 (mV dec^{-1})	
	20°C	80°C	20°C	80°C	20°C [a]	80°C [b]	20°C	80°C	20°C	80°C	20°C	80° C	20° C	80° C
20%Pt-Pd on Vulcan	0.376	0.325	0.86	0.87	0.71	1.3	0.29	0.21	58	26	2.7	2.7	43	42
10%Pt on Vulcan	0.430	0.365	0.85	0.85	0.79	1.39	0.31	0.82	113	23	3.4	2.9	52	50
IrO_2	0.530	0.418	0.78	0.79	0.91	1.40	0.47	0.31	9219	802	3.3	2.3	51	47

[a] 3 mm inter-electrode gap; [b] 10 mm inter-electrode gap

Table 5.2: *Data from Tafel plots and modelling of EIS data for alkaline fuel cells containing Gortex electrodes coated with different precious metal catalysts at 20 °C vs 80 °C. Gortex coated with 10% Pt served as the anode (H_2 catalyst) in all cases. Showing: (from Tafel plots) activation overpotential (η_{act}), voltage at 10 mA cm^{-2} ($V_{@10mAcm-2}$), Tafel slope (b_1) (at lower current density (LCD)); (from EIS) ohmic resistance (R_Ω), charge transfer resistance $R_{(ct)}$, double-layer capacitance within the catalyst layer $C_{(ct)}$, diffusional resistance $Z_{(d)}$.*

As seen from the polarization curves in Figure 5.14, an increase in temperature improved the current densities generated by these fuel cells at any given overpotential. Both 20% Pt-Pd and 10% Pt produced roughly a 30 mA cm^{-2} increase in current values at 0.3 V when operated at 80 ^{o}C relative to 20 ^{o}C (Figure 5.14). The fuel cell with '20%Pt-Pd+CB+PTFE+Ni-mesh/Gortex' as cathode, generated a maximum power of 114 mW cm^{-2} at a much lower overpotential of 780 mV (1.18 V-0.4 V) when compared to the fuel cell with '10%Pt+CB+PTFE+Ni-mesh/Gortex' as cathode. That fuel cell produced a maximum power of 91 mW cm^{-2} at the slightly higher overpotential of 830 mV (1.18 V-0.35 V). At 0.7 V, the fuel cell with a '20%Pt-Pd+CB+PTFE+Ni-mesh/Gortex' cathode produced 18 mA cm^{-2} more at 80 ^{o}C than that at 20 ^{o}C. No significant increase in performance was observed under the same circumstances in the fuel cell with a '10%Pt+CB+PTFE+Ni-mesh/Gortex' cathode. The fuel cell with an 'IrO_2+CB+PTFE+Ni-mesh/Gortex' cathode did not exhibit a significant change in maximum power (65 mW cm^{-2}) with an increase in operating temperature.

Table 5.2 lists data obtained from Tafel plot and modelling of the measured EIS data on the above fuel cells. As can be seen, both at 20 ^{o}C and 80 ^{o}C, the voltage at 10 mA cm^{-2} ($V_{@10mAcm-2}$) of the fuel cells with cathodes containing 20% Pt-Pd and 10% Pt fell close to each other (~0.85-0.87 V), while that with the IrO_2 cathode lagged behind by ~70-80 mV. Increasing the temperature had little to no effect on all of the above fuel cell in terms of voltages recorded at lower current densities. Nonetheless, at higher current densities (> 10 mA cm^{-2}) (Figure 5.14), the fuel cell containing '20%Pt-Pd+CB+PTFE+Ni-mesh/Gortex' as cathode surpassed those involving the two other catalysts, both at 20 ^{o}C and 80 ^{o}C. From Table 5.2, it is evident that increasing the operating temperature of fuel cells employing Gortex based cathodes and anodes decreased their activation overpotential by 14% for cathodes containing 20% Pt-Pd, 15% for cathodes containing 10% Pt, and 21% for cathodes containing IrO_2.

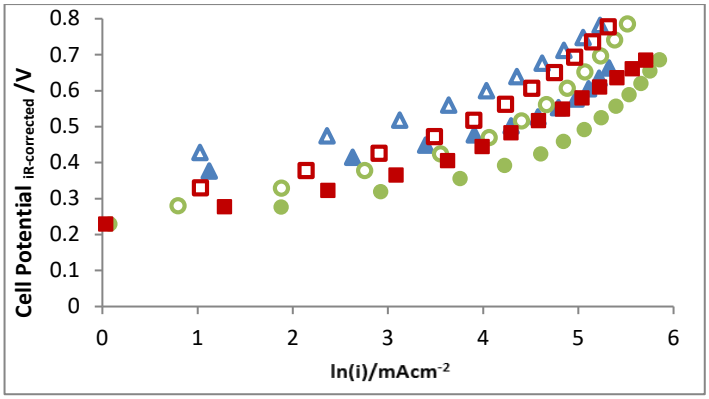

Figure 5.15. *iR-corrected Tafel plots for alkaline fuel cells containing Gortex electrodes coated with (1) ○● -20%Pt-Pd; (2) □■ -10%Pt and (3) Δ▲ -IrO_2 as cathode (ORR catalysts). Gortex coated with 10% Pt served as the anode (HOR catalyst) in all cases. Empty and filled markers denote 20 °C and 80 °C data respectively. Electrolyte: 6 M KOH.*

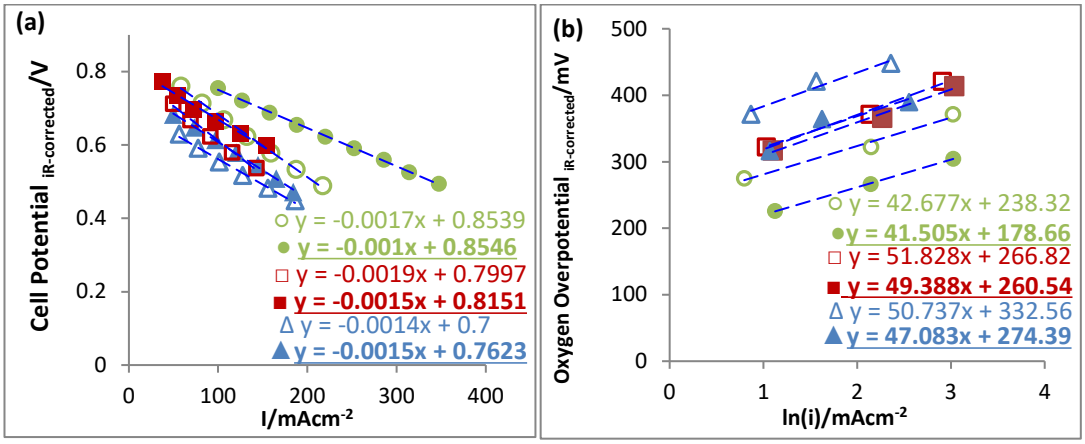

Figure 5.16. *(a) Plots of cell potential vs current density (iR-corrected) showing straight line fits of the ohmic region (with formula y=mx+c, where the intercept of that line with the y-axis, c, is the onset potential. The activation overpotential is the difference between the onset potential and E_{cell}^{o} (E_{cell}^{o} =1.23 V at 20 °C, E_{cell}^{o} =1.18 V at 80 °C); (b) Tafel plots (iR-corrected), at Low Current density (LCD), showing straight-line fits (with formula y=mx+c, where m is the Tafel slope and c is the exchange current density, i_o); for the alkaline fuel cells containing Gortex electrodes coated with (1) ○● -20%Pt-Pd; (2) □■ -10%Pt and (3)Δ▲ -IrO_2 as cathode (ORR catalysts). Gortex coated with 10% Pt served as the anode (H_2 catalyst) in all cases. Empty and filled markers denote 20 °C and 80 °C data respectively. Electrolyte: 6 M KOH.*

However, the Tafel slopes (b_1) displayed little to no change at 80 °C when compared to 20 °C for the fuel cells with 20% Pt-Pd and 10% Pt cathodes (Table 5.2). Although, the Tafel slope of the kinetic current was down by 4 mV dec^{-1} for the cathode loaded with IrO_2 at 80 °C (Figure 5.16(b)). It was also 23% lower than reported for a previously-reported fuel cell comprising of the same catalyst couple and electrolyte at 80 °C.[37] Tafel slopes were not calculated for the higher overpotential regime as we suspect that the above catalysts might not be stable at such high current densities due to corrosion of the carbon support as well as the catalysts.

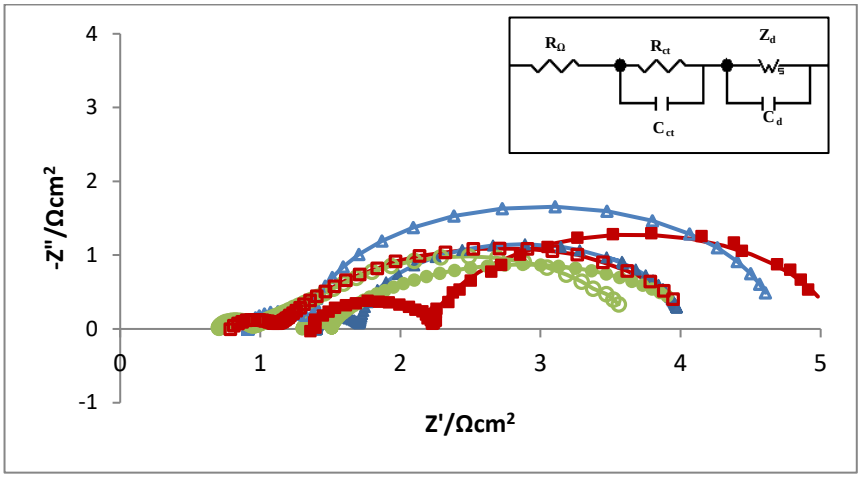

Figure 5.17. *Nyquist plot at 10 mA cm^{-2}, (inset: equivalent electrical circuit) showing measured data (individual data points) and modelled data (solid line). The modelled data used the equivalent circuit shown in (a). Alkaline fuel cells containing Gortex electrodes coated with (1) ○● -20%Pt-Pd; (2) □■ -10%Pt and (3) △▲ -IrO_2 as cathode (ORR catalysts). Gortex coated with 10% Pt served as the anode (HOR catalyst) in all cases. Empty and filled markers denote 20 °C and 80 °C data respectively. Electrolyte: 6 M KOH.*

The EIS data of the above gas diffusion electrodes at 80 °C was modelled using the equivalent circuit depicted in the inset of Figure 5.17. The individual data points in Figure 5.17 show the data as measured, while the solid lines show the modelled data. The modelling results are provided in Table 5.2. As can be seen, the ohmic resistance (0.71 Ω cm^2 and 0.79

Ω cm^2) for fuel cells with cathodes containing 20% Pt-Pd and 10% Pt respectively, was close to the expected resistance of 0.5266 Ω cm^2 for a 6 M KOH solution at 20 °C over a 3 mm inter-electrode gap. However, all experiments at 80 °C were performed using a custom-built stainless steel cell with a 10 mm inter-electrode gap, which means that the expected resistance for a 6 M KOH solution is 0.741 Ω cm^2. Thus, the fuel cells operated at 80 °C produced a relatively higher ohmic resistance R_Ω (for example, 45% increase for fuel cell containing '20%Pt-Pd+CB+PTFE+Ni-mesh/Gortex' as cathode). The fuel cell with an IrO_2 cathode produced a higher R_Ω both at 20 °C and 80 °C, which may be due to the lower electrical conductivity of such oxides when compared to the supported metals.

As can be seen, the fuel cell with a '20%Pt-Pd+CB+PTFE+Ni-mesh/Gortex' cathode, performed the best overall because the combination of ohmic resistance (R_Ω), charge transfer resistance (R_{ct}) and diffusion resistance (Z_d) was the lowest (3.7 Ω cm^2 at 20 °C and 4.21 Ω cm^2 at 80 °C). Although, the cell with the 10% Pt cathode had a capacitance (C_{ct}) that was double that of the cell with the 20% Pt-Pd cathode, it still showed a higher overall combined resistance ($R_\Omega + R_{ct} + Z_d$ = 4.5 Ω cm^2 at 20 °C and 5.11 Ω cm^2 at 80 °C). As noted earlier, the inhibition effect of the formation of hydroxide on Pt due to an environment of oxide covered Pd atoms enhances the kinetics of the bimetallic catalysts[24] but coverage of the active Pd sites with oxides impedes the access of charge to them, thereby decreasing the capacitance of 20% Pt-Pd by about half. For the cell with the IrO_2 cathode, the C_{ct} is fairly high due to the higher loading of IrO_2 (100-times that of Pt) which, in turn, provides more catalytic sites for charge interaction. As seen in Figure 5.17 and Table 5.2, cathode laden with IrO_2 exhibits the smallest mass transport limitation with the lowest Z_d value at 80 °C (30% decrease compared to 20 °C). This feature contributed to the observed stability of the fuel cell containing the IrO_2 cathode at 10 mA cm^{-2} at 80 °C (Figure 5.18(b)).

5.3.9 Some Discrete Regenerative Fuel Cells (DRFC) at 80 ºC

In the final portion of this work, we were interested to see what sort of round-trip energy efficiencies could be achieved by fuel cells and electrolysers utilizing Gortex-based gas diffusion electrodes that had been coated with precious metal type catalysts. These would have to be separate combinations of electrolysers and fuel cells because carbon black is, generally an essential ingredient for high performance in both electrodes of the fuel cells and in the cathodes of the electrolysers. However, it could not be included at the O_2-generating anode of the electrolysers, because the strongly oxidative environment aggressively corrodes carbon black. Thus, the fuels cell could not have the same Gortex-based gas diffusion electrodes as the electrolyser, meaning that the fuel cell and electrolyser would have to be separate cells within a Discrete Regenerative Fuel Cell (DRFC).

A previous report has described alkaline based DRFCs using IrO_2 (loading of 16 mg cm^{-2}) as both ORR and OER catalysts, operating at 80 ºC in 30% KOH, that generated round-trip electrical efficiencies of 65% at 10 mA cm^{-2}.[38] PEM-based DRFCs with multi-walled carbon nanotube-supported IrO_2 as ORR catalyst and Pt/C as HOR catalyst, also exhibited high electrocatalytic activity and durability at 80 ºC.[39]

In this study, therefore, we avoided a carbon black supported precious metal catalyst at the electrolyzer anode. Instead, we tested an electrolyser having unsupported IrO_2-coated Gortex (loading of 15.1 mg cm^{-2}) at the anode and 10% Pt/CB+PTFE+Ni-mesh/Gortex at the cathode at 80 ºC.

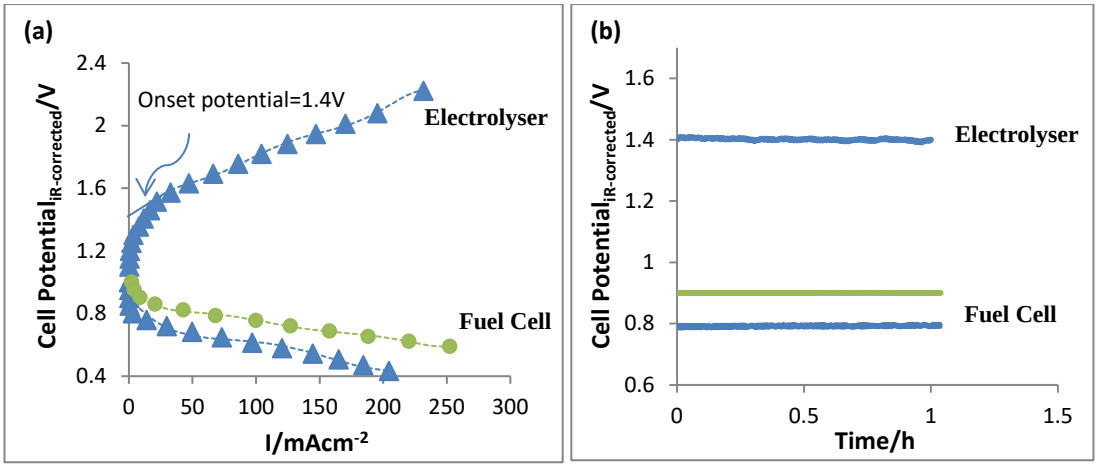

Figure 5.18. *(a) Polarization curves (iR-corrected) and (b) chronopotentiograms (iR-corrected) for alkaline fuel cells containing Gortex electrodes coated with (1) ●-20%Pt-Pd (2) ▲- IrO_2 at 80 ^oC, as O_2-catalysts and alkaline water electrolyzers containing Goretex electrodes coated with ▲- IrO_2 as O_2-catalysts at 80 ^oC. Alkaline fuel cell cathodes contained either of 20%Pt-Pd or IrO_2 as O_2-catalyst along with carbon black. Alkaline water electrolysers contained only IrO_2 as O_2 catalyst, without any addition of carbon black. 20%Pt-Pd was not chosen as O_2 catalyst for electrolyser as it contained carbon black as a support. The H_2-catalysts in all cells were 10% Pt/CB+PTFE+Ni-mesh on Gortex. Electrolyte: 6 M KOH.*

The abovementioned cell catalyzed water electrolysis with an onset potential of 1.4 V, which is 70 mV lower than a similar Pt/IrO_2 couple, which had an onset potential of ~1.47 V at room temperature.[40] As can be seen in Figure 5.18(b) ('electrolyser'), the cell generated a stable current of 10 mA cm^{-2} over 1 h at a very low overpotential of 0.22 V (1.4 $V_{iR\ corrected}$ - 1.18 $V_E{}^o{}_{at\ 80\ ^oC}$). This is 30 mV lower than reported for the same combination of catalysts in solid state form (i.e. Pt (cathode)/IrO_2 (anode), at 80 ^{o}C in ~6 M KOH).[37] The tremendous improvement in efficiency is undoubtedly due to the Gortex substrate, which induces a dramatic decrease in the cumulative overpotential of the catalysts during electrolysis at temperatures of 80 ^{o}C and above. The Gortex clearly decreased the activation overpotential for oxygen formation from water as discussed in detail in Chapter 4.

Combining the above electrolyzer with a fuel cell having IrO_2/CB+PTFE+Ni-mesh/Gortex as cathode and 10% Pt/CB+PTFE+Ni-mesh/Gortex as the anode, yields a notional round trip electrical efficiency at 80 ^oC and 10 mA/cm^2 in each direction of 55.7% (0.78 $V_{iR\ corrected}$ in fuel cell mode at 80 ^oC, as shown in Figure 5.18(a)).

Alternatively, combining the above electrolyzer with a fuel cell containing 20% Pt-Pd/CB+PTFE+Ni-mesh/Gortex as cathode and 10% Pt/CB+PTFE+Ni-mesh/Gortex as the anode, gives a notional round trip electrical efficiency at 80 ^oC and 10 mA/cm^2 in each direction of 64.3% (0.9 $V_{iR\ corrected}$ in fuel cell mode at 80 ^oC, as shown in Figure 5.18 (a)).

5.4 Conclusion

In this Chapter, the function of gas diffusion electrodes comprising of Gortex substrates layered with several well-known, conventional, precious metal catalysts, in alkaline-based DRFCs, was examined. When deployed in a desktop alkaline fuel cell charged with aqueous 6 M KOH electrolyte, Gortex electrodes coated with '20% Pt-Pd/CB+PTFE+Ni-mesh/Gortex', generated current and power densities of 230 mA cm^{-2} and 84 mW cm^{-2}, respectively, at 0.35 V, at 20 ^oC. When operating the same fuel cell at 80 ^oC, the current density and power density increased by 27% and 24% respectively at 0.35 V. This was achieved with extremely low Pt-Pd loadings of an average of 0.075 mg cm^{-2}, both at 20 ^oC as well as at 80 ^oC. In addition, the energy efficiency (LHV) of this Gortex-based alkaline fuel cell was 76% (=0.9/1.18 X 100) at 80 ^oC and 10 $mAcm^{-2}$. At a current density of 170 mA cm^{-2}, the energy efficiency generated by Gortex-based fuel cell was 57% which is 11% more than alkaline fuel cells for spacecraft applications at 80 ^oC.[41] The alkaline fuel cells also recorded very low tafel slopes at low current densities indicating the faster electrochemical kinetics due to the better three phase interaction obtained by using Gortex as GDEs. The alkaline fuel cells also functioned without need for an ion-permeable, gas-impermeable diaphragm between the electrodes and were robustly tolerant of CO_2. They were further

flood resistant over extended periods. An important correlation was established between the electrochemical activity of the catalysts as predicted by volcano plots and the electrochemical activity predicted by electrochemical impedance spectroscopy. The parameters derived from fitting an equivalent electrical circuit to experimentally obtained impedance data correlated with the positions of the different catalysts on the volcano plot. The most important parameters were charge transfer resistance (R_{ct}) and diffusional resistance (Z_d) which could be used as a guide for selecting appropriate catalysts for cathodes in fuel cells.

As mentioned earlier in this chapter, alkaline electrolyzer is a mature technology with lifetimes of 100 000 h and energy efficiencies ranging from 61% to 71%.[5] However, if we replace traditional gas diffusion electrodes with Gortex-based gas diffusion electrodes and employ conventional precious catalysts (like IrO_2), major inefficiencies associated with the overpotentials for hydrogen and oxygen formation are reduced. This enables Gortex-based alkaline electrolysers to achieve higher energy efficiencies.

Previous studies utilizing exceedingly high loadings of IrO_2 yielded an alkaline DRFC with a round-trip energy efficiency of 65% at 80 ^oC and 10 mA cm^{-2} in each direction.[38] Similar efficiencies can be achieved at vastly lower catalysts loadings if we combine our alkaline Gortex-based electrolyser, utilizing IrO_2 with our best performing alkaline Gortex-based fuel cell, utilizing 20%Pt-Pd. The resulting alkaline-based DRFC achieved a round-trip energy efficiency of 64.3%, at 80 ^oC and 10 mA cm^{-2} in each direction.

References:

1. Wang, Y.; Leung, D. Y. C.; Xuan, J.; Wang, H., *Renew Sust Energ Rev* **2016,** *65* (Supplement C), 961-977.
2. Park, K.; Lee, J.; Kim, H.-M.; Choi, K.-S.; Hwang, G., **2014,** *4*, 4592.

3. Barbir, F.; Molter, T.; Dalton, L., *Int. J. Hydrogen Energy* **2005,** *30* (4), 351-357.
4. Gahleitner, G., *Int. J. Hydrogen Energy* **2013,** *38* (5), 2039-2061.
5. Pellow, M. A.; Emmott, C. J. M.; Barnhart, C. J.; Benson, S. M., *Energy Environ. Sci* **2015,** *8* (7), 1938-1952.
6. Holladay, J. D.; Hu, J.; King, D. L.; Wang, Y., *Catal. Today* **2009,** *139* (4), 244-260.
7. Merle, G.; Wessling, M.; Nijmeijer, K., *Journal of Membrane Science* **2011,** *377* (1–2), 1-35.
8. Mekhilef, S.; Saidur, R.; Safari, A., *Renew Sust Energ Rev* **2012,** *16* (1), 981-989.
9. Gabbasa, M.; Sopian, K.; Fudholi, A.; Asim, N., *Int. J. Hydrogen Energy* **2014,** *39* (31), 17765-17778.
10. Gilliam, R. J.; Graydon, J. W.; Kirk, D. W.; Thorpe, S. J., *Int. J. Hydrogen Energy* **2007,** *32* (3), 359-364.
11. Fabbri, E.; Habereder, A.; Waltar, K.; Kotz, R.; Schmidt, T. J., *Catal. Sci. Technol.* **2014,** *4* (11), 3800-3821.
12. Tian, J.; Liu, Q.; Asiri, A. M.; Sun, X., *J. Am. Chem. Soc.* **2014,** *136* (21), 7587-7590.
13. Gasteiger, H. A.; Kocha, S. S.; Sompalli, B.; Wagner, F. T., *Appl. Catal., B* **2005,** *56* (1–2), 9-35.
14. Ioroi, T.; Kitazawa, N.; Yasuda, K.; Yamamoto, Y.; Takenaka, H., *J. Appl. Electrochem.* **2001,** *31* (11), 1179-1183.
15. Wittstadt, U.; Wagner, E.; Jungmann, T., *J. Power Sources* **2005,** *145* (2), 555-562.
16. Huang, S.-Y.; Ganesan, P.; Jung, H.-Y.; Popov, B. N., *J. Power Sources* **2012,** *198*, 23-29.
17. Ledjeff, K.; Mahlendorf, F.; Peinecke, V.; Heinzel, A., *Electrochim. Acta* **1995,** *40* (3), 315-319.
18. Chamberland, B. L.; Silverman, S., *Journal of the Less Common Metals* **1979,** *65* (2), 41-48.
19. Swette, L.; Kackley, N., *J. Power Sources* **1990,** *29* (3-4), 423-436.

20. Stamenkovic, V. R.; Strmcnik, D.; Lopes, P. P.; Markovic, N. M., *Nat Mater* **2017,** *16* (1), 57-69.
21. Nørskov, J. K.; Rossmeisl, J.; Logadottir, A.; Lindqvist, L.; Kitchin, J. R.; Bligaard, T.; Jónsson, H., *J. Phys. Chem. B* **2004,** *108* (46), 17886-17892.
22. GreeleyJ; Stephens, I. E. L.; Bondarenko, A. S.; Johansson, T. P.; Hansen, H. A.; Jaramillo, T. F.; RossmeislJ; ChorkendorffI; Nørskov, J. K., *Nat Chem* **2009,** *1* (7), 552-556.
23. Inomata, K.; Unagami, R.; Adachi, T.; Ito, A., Google Patents: 2012.
24. Marković, N. M.; Schmidt, T. J.; Stamenković, V.; Ross, P. N., *Fuel Cells* **2001,** *1* (2), 105-116.
25. Arenz, M.; Schmidt, T. J.; Wandelt, K.; Ross, P. N.; Markovic, N. M., *J. Phys. Chem. B* **2003,** *107* (36), 9813-9819.
26. Tomantschger, K.; Kordesch, K. V., *J. Power Sources* **1989,** *25* (3), 195-214.
27. Jin, W.; Du, H.; Zheng, S.; Xu, H.; Zhang, Y., *The Journal of Physical Chemistry B* **2010,** *114* (19), 6542-6548.
28. Sun, W.; Hsu, A.; Chen, R., 2011; Vol. 196, p 627-635.
29. Gouérec, P.; Poletto, L.; Denizot, J.; Sanchez-Cortezon, E.; Miners, J., *J. Power Sources* **2004,** *129* (2), 193-204.
30. Burchardt, T., *Journal of Power Sources* **2004,** *135* (1), 192-197.
31. Maja, M.; Orecchia, C.; Strano, M.; Tosco, P.; Vanni, M., *Electrochimica Acta* **2000,** *46* (2), 423-432.
32. Marshall, A.; Børresen, B.; Hagen, G.; Tsypkin, M.; Tunold, R., *Energy* **2007,** *32* (4), 431-436.
33. Paulus, U. A.; Wokaun, A.; Scherer, G. G.; Schmidt, T. J.; Stamenkovic, V.; Radmilovic, V.; Markovic, N. M.; Ross, P. N., *J. Phys. Chem. B* **2002,** *106* (16), 4181-4191.
34. Rolla, A.; Sadkowski, A.; Wild, J.; Zóltowski, P., *J. Power Sources* **1980,** *5* (2), 189-196.

35. Shinagawa, T.; Garcia-Esparza, A. T.; Takanabe, K., **2015,** *5*, 13801.

36. Geniès, L.; Faure, R.; Durand, R., *Electrochim. Acta* **1998,** *44* (8), 1317-1327.

37. Miles, M. H.; Huang, Y. H.; Srinivasan, S., *Journal of The Electrochemical Society* **1978,** *125* (12), 1931-1934.

38. Swette, L.; Kackley, N.; McCatty, S. A., *J. Power Sources* **1991,** *36* (3), 323-339.

39. Fujigaya, T.; Shi, Y.; Yang, J.; Li, H.; Ito, K.; Nakashima, N., *J. Mater. Chem. A* **2017,** *5* (21), 10584-10590.

40. You, B.; Jiang, N.; Sheng, M.; Gul, S.; Yano, J.; Sun, Y., *Chem. Mater.* **2015,** *27* (22), 7636-7642.

41. Markgraf, S.; Hörenz, M.; Schmiel, T.; Jehle, W.; Lucas, J.; Henn, N., *J. Power Sources* **2012,** *201*, 236-242.

CHAPTER 6

Other Efficient Alkaline Fuel Cells, Electrolysers, and Discrete Regenerative Fuel Cells Utilizing Gortex-based Spinel and Perovskite Catalysts

6.1 Introduction

As discussed in Chapter 5, the development of Regenerative Fuel Cell (RFC) systems for auxiliary energy storage is an attractive alternative to balance the irregularity in energy production by renewable energy sources. Alkaline-based Discrete Regenerative Fuel Cell (DRFC) operation is mainly dependant on the performance of ORR and OER reactions. The schematic of DRFC is shown in Figure 6.1. The most commonly used catalysts in these reactions involve platinum group metals (PGM) with Pt-based catalysts for the ORR and iridium or ruthenium oxides for the OER performing best. These catalysts have been described in the scientific literature[1-4] and were subjected to examination in Chapter 5. There are two main limitations to using PGMs in alkaline-based DRFCs. Firstly, two separate PGM catalysts are required for the OER and the ORR, with neither being effective for the

opposite reaction.[5] This limits their use in bifunctional applications. Secondly, the cost of using these PGM catalysts in alkaline-DRFCs is significant and their scarcity potentially restricts their use in large scale commercial applications. The ORR and OER require very different conditions especially with respect to the electrical potentials applied during the reaction. For this reason, only a few materials are capable of catalyzing both reactions. One of the most common methods to identify a good bifunctional catalyst for the ORR and the OER is to record its potential difference for reaction in one direction relative to the opposite direction. This difference is then, effectively, the electrical potential required to transition between the two reactions. A good bifunctional catalyst would have a small potential difference in this respect. Considerable research has recently focussed on the development of bifunctional catalysts employing materials that are Earth-abundant and that can perform both the ORR and OER.

Metal oxides of perovskite and spinel structures are seen as viable alternative to replace PGMs for DRFC applications. This is due their low-cost and abundance in nature, making them appropriate for commercial use. Also, metal oxides often operate synergistically when mixed, which can be useful when seeking to combine good ORR and OER performance into one material. Furthermore, metal oxides can easily shift between oxidation states, which can improve stability during bifunctional operation.

This Chapter aimed to examine the performance and operation of efficient, Earth-abundant bifunctional catalysts for alkaline-based DRFCs layered onto Gortex-based gas diffusion electrodes. The following commercially available metal oxide perovskites and spinels ('catalysts') were studied in this research were examined: $LaMnO_3$, $La_{0.8}Sr_{0.2}MnO_3$, $La_{0.7}Ca_{0.3}CoO_3$, $LaNi_{0.6}Fe_{0.4}O_3$ and $Ba_{0.5}Sr_{0.5}Co_{0.2}Fe_{0.8}O_3$; $NiCo_2O_4$, $Mn_{1.5}Co_{1.5}O_4$, $NiFe_2O_4$, $Co_{0.5}Ni_{0.5}Fe_2O_4$ and Co_3O_4. When referred to in the text below as being incorporated in a Gortex-based gas diffusion electrode, this means that, unless stated otherwise, the electrode had the formulation 'Catalyst+CB+PTFE+Ni-mesh/Gortex'.

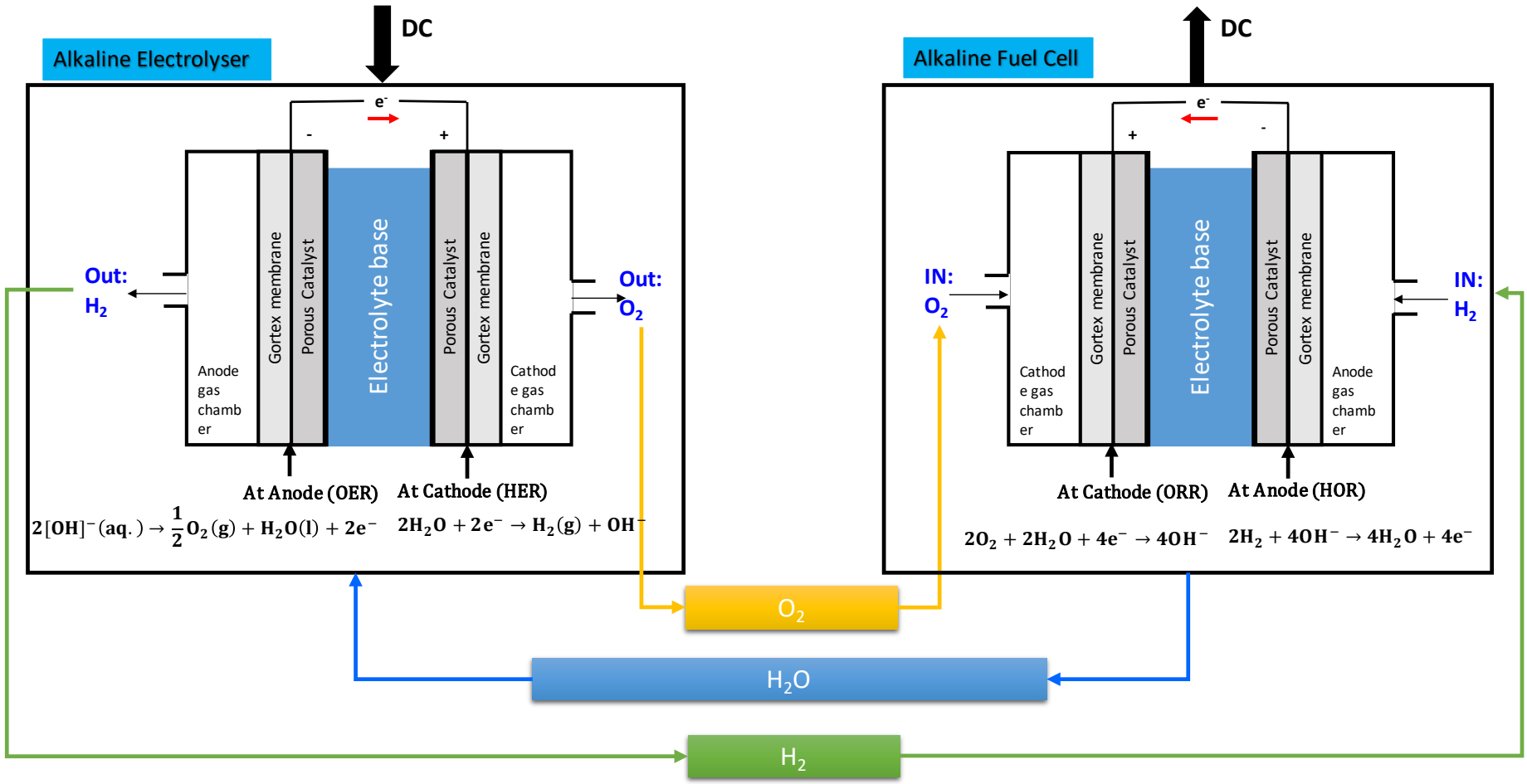

Figure 6.1. *Schematic diagram for discrete regenerative fuel cell (DRFC)*

As in Chapter 5, unless stated otherwise, H_2-handling counter electrodes of 10% Pt/CB+PTFE+Ni-mesh/Gortex were used as a standard for comparison in all cases. Studies were carried out using custom-built, 2-electrode prototype cells having closely-spaced, equally-sized electrodes. The cells were designed to accurately replicate the performance of larger-scale commercial devices utilizing the same catalysts in the same 2-electrode cell arrangement. As noted in Chapter 5, studies in 3-electrode format, using a reference electrode, were generally unreliable in respect of accurately predicting 2-electrode cell performance.

The layout of the Chapter is as follows. In the initial sections, a range of commercially available metal oxide perovskites and spinels were examined as Gortex-based ORR catalysts in fuel cell mode at room temperature (20 ^oC). Thereafter, the effect of temperature on the best performing of the Gortex-based ORR catalysts was studied by comparing their performance at room temperature (20 ^oC) and at 80 ^oC. Finally, the best performing ORR catalyst at 80 ^oC was tested in electrolyser mode at the same temperature in order to determine its OER activity and thus, bi-functional efficiency in a DRFC operating at 80 ^oC. An attempt was also made to correlate electrochemical impedance of the metal oxides to ORR electroactivity as projected in Volcano plots.

When employed in a fuel cell cathode, the best-performing perovskite, $La_{0.8}Sr_{0.2}MnO_3$, layered on Gortex ('$La_{0.8}Sr_{0.2}MnO_3$+CB+PTFE+Ni-mesh/Gortex'), exhibited a voltage of 0.85 V at 20 ^oC and 10 mA cm^{-2} (relative to the standard 10% Pt/CB+PTFE+Ni-mesh/Gortex anode). When the same fuel cell was operated at 80 ^oC, with a similar catalyst loading on both cathode and anode, it delivered a stable current of 10 mA cm^{-2} at 0.9 V for over 1 h, which is 50 mV higher than at 20 ^oC. Thus, a temperature increase led to an improvement in ORR activity, which is also expected theoretically.[6] Experimental data demonstrating such

performance improvements in perovskite catalysts as a function of temperature in alkaline fuel cells, has not been available until now.

The best-performing spinel was $NiCo_2O_4$ which, when tested in a fuel cell cathode in the form of '$NiCo_2O_4$+CB+PTFE+Ni-mesh/Gortex', delivered currents of 10 mA cm^{-2} at almost same voltage (0.85 V; relative to the standard 10% Pt/CB+PTFE+Ni-mesh/Gortex anode) both at room temperature and 80 ^oC. Temperature appeared to have little to no influence on its ORR performance, at least at the low current density of 10 mA cm^{-2}.

As observed in Chapter 4, the oxygen evolution activity and consequently, the electrical efficiency of electrocatalytic water-splitting drastically increases with temperature. Therefore, all of the electrolysers employing metal oxides as anode catalysts were tested at 80 ^oC. Carbon black was not incorporated in these anodes due to its ready corrosion in the highly oxidizing environment.

The highest performing alkaline DRFC studied in this Chapter displayed a notional round-trip energy efficiency after 1 h at 80 ^oC and 10 mA cm^{-2} in each direction, of 70.9%, assuming full conservation of heat. It involved combining a fuel cell composed of $La_{0.8}Sr_{0.2}MnO_3$+CB+PTFE+Ni-mesh/Gortex (cathode) / 10% Pt/CB+PTFE+Ni-mesh/Gortex (anode) with an electrolyzer containing $NiCo_2O_4$+PTFE+Ni-mesh/Gortex as the anode and 10% Pt/CB+PTFE+Ni-mesh/Gortex as the cathode.

6.2 Experimental

6.2.1 Materials Used

Perovskites and spinels studied in this research were sourced from American Elements. The following materials were employed (Supplier): Carbon black (AkzoNobel), Poly (tetrafluoroethylene) (PTFE) (60 wt. % dispersion in alcohols/H_2O; Sigma-Aldrich #665800), KOH 90%, flakes (Sigma-Aldrich #484016), Ni mesh (woven), 200 LPI (Precision EForming LLC of Cortland NY) (cleaned using isopropyl alcohol prior to use), and copper tape 6.35 mm width (3M). Polypropylene-backed Preveil™ expanded PTFE (ePTFE) membranes with 0.2 μm pore size, produced by General Electric Energy were used in all experiments.

6.2.2 Preparation of Catalyst-coated Gortex

See Chapter 2 section 2.4.

6.2.3 Cell Construction

See Chapter 2 section 2.5.

6.2.4 Reactant Gases and Electrochemical Testing

See Chapter 5 section 5.2.4.

6.3 Results and Discussion

Prior to discussing the studies carried out, we will briefly review metal oxide spinels and perovskites as bifunctional catalysts.

6.3.1 Perovskites as Bifunctional ORR-OER Catalysts

Perovskites are oxides that have the general formula ABO_3, where A and B are metal ions in the so-called A site and B site respectively. The A sites are occupied by rare earth metal ions and B sites are transition-metal ions. Perovskites typically have a variety of structural variants, which allows researchers to study range of different composition for ORR and OER activity.

Numerous researchers have examined O_2 reduction on perovskites,[7-11] since its first discovery by Meadowcroft.[12] Bockris and Otagawa were the first to report the activity of perovskites for the OER in 1984;[13] they related it to the weak bond of OH^- on the surface of the catalyst. Since then, a number of perovskites have been tested for OER and ORR catalysis in alkaline media, mainly as bifunctional catalysts.

Perovskite based oxides such as ABO_3 (where A = La, Ca, or Sr, and B = Co, Fe, or Mn) display high electrocatalytic acitivity for oxygen reduction, but were unstable in concentrated alkaline solutions.[14] On the other hand, ferrites (B = Fe) were more stable but less catalytically active.[15]

The ORR activity of range of perovskites can be enhanced by substituting B-sites. It was revealed that the ORR activity is mainly due to the σ^* antibonding orbital (e_g) occupation of transition metal ions.[16] The antibonding orbital occupation also represents the bond strength between B-site metal and oxygen. The degree of B-site transition metal oxygen covalence is used as a secondary factor to explain activity. The hybridization of bonding between the B site metal and oxygen has been shown to increase ORR activity. Maximum activity is obtained for perovskite with an e_g-filling of ~1. Perovskites such as $LaMnO_3$ and $LaNiO_3$ having e_g ~1 (representing moderate bond strength between catalyst and reactant) exhibit highest intrinsic ORR activity that is comparable to that of Pt/C.[16] A recent study involving La-based perovskite oxide ($LaMO_3$, M = Cr, Mn, Fe, Co and Ni) in alkaline solution showed

that the ORR activity is dependent on the B-site cations.[17] The effect of two transition metals in the B-site on the ORR activity was also studied.[18] The ORR activity improved in the order: $LaNi_{0.5}Fe_{0.5}O_3$ > $LaNi_{0.5}Co_{0.5}O_3$ > $LaNi_{0.5}Cr_{0.5}O_3$ > $LaNi_{0.5}Mn_{0.5}O_3$ when transition metals were incorporated in a ratio of 0.5 into the Ni site of $LaNiO_3$. Improved ORR activity was observed for Mn ions when compared with Fe ions in the $La_{0.4}Ca_{0.6}Mn_{1-y}Fe_yO_3$ oxides. Overall, these results indicated that two transition-metal ions worked positively towards improving the ORR catalytic activity. Apart from the impact of transition metal ions, the formation of certain oxidation states for cations also affect ORR activities. Studies confirmed that ORR activity was improved when Mg or Fe was substituted into the B-site of $LaNiO_3$ to form $LaNi_{0.85}Mg_{0.15}O_3$ and $LaNi_{0.8}Fe_{0.2}O_3$.[18,19] An increase in the OER activity of $LaNiO_3$ was seen with iron doping in $LaNi_{1-x}Fe_xO_3$ ($x = 0$, 0.1, 0.2 and 0.6). This was attributed to the reduced formation of Ni^{2+} on the perovskite surface thereby creating a stronger surface Ni–O bond.[19]

Apart from B-site cations, the A-site cations have also been found to have a strong effect on the electrocatalytic activity of perovskite oxides. A study involving a series of $LnMnO_3$ oxides where Ln = La or Y with similar specific surface areas, showed that the ORR activity in alkaline solution varied with the nature of the A-site cations with :La > Pr > Nd > Sm > Gd > Y > Dy > Yb. [20] A-site partial cation replacement can also affect the activities of parent perovskite oxides. Several perovskite compounds such as $La_{1-x}Sr_xMnO_3$ [21] [22], $La_{1-x}Ca_xCoO_3$ [11], and $La_{1-x}Ca_xMnO_3$[17] showed higher electrocatalytic ORR activities. $La_{1-x}Sr_xMnO_3$ perovskite oxides and specifically $La_{0.4}Sr_{0.6}MnO_3$ showed the best ORR performance in 1 M KOH.[21] A series of A-site cation-deficient $La_{1-x}FeO_{3-\delta}$ were developed for OER catalysis in a study by Zhu et al.[23] Among these, $La_{0.95}FeO_{3-\delta}$ exhibited the highest OER activity.

Perovskite oxides usually show low surface areas of less than 10 $m^2 g^{-1}$ due to their calcination in at high-temperature (greater than 800 °C) and longer annealing processes

during synthesis, which results in low mass catalytic activity. ORR performance may be improved by increasing the number of active sites through increasing the surface area of perovskite-type catalysts. Several studies developed nanostructured perovskite oxides to improve ORR catalytic performance. Different Mn-based nanostructured perovskites were reported to show enhanced ORR performance compared to oxides prepared using standard methods, including urchin-like $La_{0.8}Sr_{0.2}MnO_3$ perovskite, hollow spherical $La_{0.8}Sr_{0.2}MnO_3$ perovskite, and microporous $La_{0.8}Sr_{0.2}MnO_3$ nanorods.[24,25,26]

$Ba_{0.5}Sr_{0.5}Co_{0.8}Fe_{0.2}O_{3-\sigma}$ (BSCF) was found to be a promising bifunctional perovskite oxide for the ORR and OER due to its fast oxygen exchange kinetics and good ionic conductivity. In one study, it was shown that the disordered oxygen vacancies in BSCF can facilitate the mobility of oxygen anions resulting in a lower operating temperature for solid oxide fuel cells (SOFC).[27] Another study found that when BSCF was deposited onto thin-film $La_{0.8}Sr_{0.2}MnO_{3-\sigma}$ by pulsed laser deposition, the combined overpotential for both the ORR and OER achieved was 0.7 V.[28] This was believed to be due to the improved surface stability by BSCF.[28] In the case of perovskites where the B-site is completely substituted by Co ions the ORR follows exclusively the 4-electron route. However, when Co is partially substituted by Fe cations, poorer ORR activity was obtained due to competition with the 2-electron process.[29] BSCF has also been reported to show activity for the OER that is greater than that of IrO_2.[30] Along similar lines, several other catalysts were successfully developed to enhance OER activity such as $La_{0.7}(Ba_{0.5}Sr_{0.5})_{0.3}Co_{0.8}Fe_{0.2}O_{3-\delta}$,[31] $La_{0.6}Ca_{0.4}Mn_xCo_{1-x}O_{3-\delta}$,[32] $Ca_2Mn_2O_5$, [33] and $CaCu_3Fe_4O_{12}$.[34]

6.3.2 Spinels as Bifunctional ORR-OER Catalysts

Transition metals with spinel structure (spinel oxides) have attracted significant interest recently due to their controllable catalytic activity and stability in an alkaline environment.[35] Spinels are ternary oxides with an AB_2O_4 structure. The nature of the B cations have been

found to offer a potentially useful (and crucial) element for creating (and amplifying) an ability to act as useful catalysts.[36-37] Spinels can exist in two forms: normal spinel M^{2+} $[M_2^{3+}]$ O_4 and inverse spinels M^{3+} $[M^{2+}$ $M^{3+}]$ O_4. The distribution of cations among the A and B sites can significantly affect the catalytic properties as well as the morphology of the resulting electrode. A previous study revealed that the ORR activity can be improved by the substituting the B sites of cobaltite. This was due to the enhanced chemisorption of oxygen by the B site cations via their d-orbitals.[38] A wide range of spinel catalysts have been reported.

The normal spinel of Co_3O_4 has been the subject of significant interest since the 1980s.[35] Co_3O_4 has been widely studied to reveal its electrocatalysis properties in alkaline media. Co_3O_4 shows good activity and high stability together with being low cost and having simple preparation process. However, bulk Co_3O_4 exhibits relatively low electrical conductivity and diminished catalytic activity.

A study in 2011 found that Co_3O_4 nanoparticles on N-doped rGO (NrGO) achieved significantly higher electrocatalytic ORR and OER activity than available from either Co_3O_4 or their physical mixture.[39] Another study investigated ORR activities using the carbon supported Co_3O_4 electrocatalysts, with nanorods and spherical structures[40]. It was revealed that the ORR performance of Co_3O_4 was sensitive to the activity and number of surface-exposed Co^{3+} ions. Nanorods of Co_3O_4 electrocatalyst exhibited a higher current density that exceeded that of a costly palladium-based catalyst, in the low potential region. These results inspired other studies to use Co_3O_4 and its variants as efficient ORR/OER electrocatalysts. In particular, substitution of a Co in Co_3O_4 with Ni, Cu and Mn have demonstrated high activity and stability as electrocatalysts for ORR.[35] The OER activity activity follows the order: $Co_3O_4 < Ni_xCo_{3-x}O_4 < Cu_xCo_{3-x}O_4 < Li_xCo_{3-x}O_4$.[35]

Other electrocatalysts such as $NiCo_2O_4$, $Mn_xCo_{3-x}O_4$, and $NiFe_2O_4$ typically have inverse spinel structures. The inverse spinel structures offers good electrical conductivities[41] and desirable electrochemical activity.[35] Electrical conductivity arises from electron hopping between valence states of cations at octahedral sites, which occurs at comparatively low activation energy between cations of different valences. High electrochemical activities were due to their surface redox active centres. In order to modify the magnetic, electrical and catalytic properties of inverse spinel oxides, they have been frequently been substituted with different doping ions.[42,43]

$NiCo_2O_4$ has intensively studied due to its intrinsic high activity, resistance to corrosion, and easy availability.[44] $NiCo_2O_4$-related electrocatalysts for the ORR include: urchin-shaped $NiCo_2O_4$ spheres,[45] 3D macroporous $NiCo_2O_4$ sheets,[46] and hierarchical flower-like porous $NiCo_2O_4$ nanosheets,[47] the latter of which have shown excellent long term stability. $NiCo_2O_4$ has also received lot of attention as an efficient and low-potential electrode for the OER. Various $NiCo_2O_4$ nanostructures were developed in this respect, such as nanowire arrays,[48] core-ring nanoplatelets,[49] hexagonal nanosheets,[50] nanorods,[51] and various $NiCo_2O_4$ nanocomposites with aerogels,[52] and grapheme.[53,54] A study involving mesoporous $NiCo_2O_4$ nanoplatelets and graphene sheets ($NiCo_2O_4$–G) showed it to be an excellent bifunctional catalyst for both ORR and OER.[55]

Another inverse spinel for ORR is $Mn_xCo_{3-x}O_4$, where a Co has been substituted with Mn[38] Cubic $MnCo_2O_4$ displayed better catalytic performance for the OER when compared against tetragonal $CoMn_2O_4$ in alkaline medium. However, tetragonal $CoMn_2O_4$ exhibited better electrochemical ORR, in alkaline medium, at least in some reports.[56,57] A spinel-type $Mn_xCo_{3-x}O_{4-\delta}$ was synthesised by Ma et al.,[58] which showed ultra-active OER catalysis and strong durability in alkaline medium. These materials delivered a current density of 10 mA cm^{-2} at 1.58 V in 0.1 M KOH solution. High OER activity was also reported for a

nanocrystalline spinel $Co_xMn_{3-x}O_4$ synthesised under ambient conditions.[59] A cubic manganese cobalt spinel $MnCo_2O_4$ / graphene hybrid has been shown to have higher performance for the ORR in alkaline media.[60]

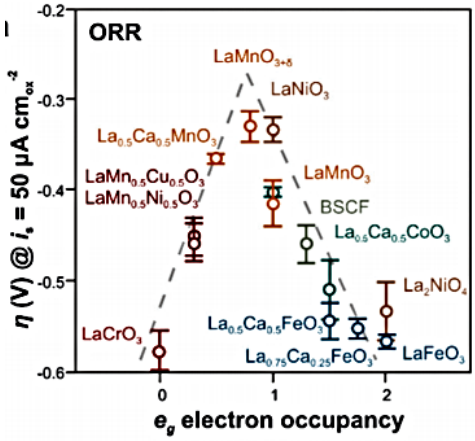

Figure 6.2. *Volcano plot for Oxygen Reduction activity as a function of oxygen binding energy on perovskites.*[61] *Reproduced with permission from reference 61.*

6.3.3 Mechanistic Pathways for Perovskites/Spinels as ORR-OER Catalysts

The ORR reaction pathways follows a different rationale compared to precious metal surfaces where the first electron transfer steps to adsorbed oxygen species determines the rate of the reaction. The ORR process for pervoskites/spinels follows a four step process; namely: (i) surface hydroxide displacement, (ii) surface peroxide formation, (iii) surface oxide formation and (iv) surface hydroxide regeneration.[16] In the first step (surface hydroxide displacement), the surface cations of transition metal oxides coordinate with the oxygen (of H_2O) to fulfil their full oxygen coordination and the hydrogen atoms (of H_2O) get distributed over the catalyst surface. To create OH^- species, the protonation of the surface oxygen ligand is charge-compensated by the reduction of a surface transition metal cation (M). In the second step (surface peroxide formation), the $M{-}OH^-$ species further interacts with O_2 which adsorbs on oxide surfaces in either end-on or side-on configurations. The ORR pathways on oxide surfaces are as follows:

$$2M^{m+} - O^{2-} + 2H_2O + 2e^- \rightleftharpoons 2M^{(m-1)+} - OH^- + 2OH^- \quad \ldots (6.1)$$

$$O_2 + e^- \rightleftharpoons O_{2,ads}^- \quad \ldots (6.2)$$

$$2M^{(m-1)+} - OH^- + O_{2,ads}^- + e^- \rightleftharpoons 2M^{m+} - O^{2-} + 2OH^- \quad \ldots (6.3)$$

Or possibly,

$$M^{m+} - O^{2-} + H_2O + 2e^- \rightleftharpoons M^{(m-1)+} - OH^- + OH^- \quad \ldots (6.4)$$

$$O_2 + e^- \rightleftharpoons O_{2,ads}^- \quad \ldots (6.5)$$

$$M^{(m-1)+} - OH^- + O_{2,ads}^- \rightleftharpoons M^{m+} - O - O^{2-} + OH^- \quad \ldots (6.6)$$

$$M^{m+} - O - O^{2-} + H_2O + e^- \rightleftharpoons M^{(m-1)+} - O - OH^- + OH^- \quad \ldots (6.7)$$

$$M^{(m-1)+} - O - OH^- + e^- \rightleftharpoons M^{m+} - O^{2-} + OH^- \quad \ldots (6.8)$$

$$M^{m+} - O - O^{2-} + H_2O + e^- \rightleftharpoons M^{(m-1)+} - OH^- + HO_2^- \quad \ldots (6.9)$$

Equations 6.3 and 6.9 are rate determining steps and these are also called surface hydroxide regeneration.[16]

In the case of OER in alkaline solution, the mechanism starts with the adsorption and discharge of the OH^- anion at the catalyst surface of a metal site (M). Then, OH^- reacts with the adsorbed OH species to produce H_2O and adsorbed atomic O* with an electron released. Afterwards, an OH^- reacts with an adsorbed O* atom to form adsorbed OOH species. Further reaction with additional OH^- results in adsorbed O_2 and H_2O. The adsorbed O_2 produced then desorbs in the last step as described below,[62]

$$M + OH^- \rightleftharpoons M - OH + e^- \quad \ldots (6.10)$$

$$M - OH + OH^- \rightleftharpoons M - O^\star + e^- + H_2O \quad \ldots (6.11)$$

$$M - O^\star + OH^- \rightleftharpoons M - OOH + e^- \quad \ldots (6.12)$$

$$M - OOH + OH^- \rightleftharpoons M - O_2 + e^- + H_2O \quad \ldots (6.13)$$

$$M - O_2 \rightleftharpoons M + O_2 \quad \ldots (6.14)$$

The rate determining step for transition metal oxides is theorized to be equation 6.12.[62]

6.3.4 Fuel Cell Performance at Room Temperature (20 ºC), using Perovskites as ORR Catalysts

The intrinsic ORR activity of perovskites exhibit a volcano shape as a function of e_g electron occupancy of B-site metal ions and a molecular orbital of surface oxygen, as shown in Figure 6.2.[16] According to the volcano plot, the highest electroactivity is exhibited by $LaMnO_3$ and $LaNiO_3$. This is due to the fact that both $LaMnO_3$ and $LaNiO_3$ have e_g electron occupancies close to unity. When $e_g < 1$ or $e_g > 1$, interactions with oxygenated species occur that are either too strong or too weak. Figure 6.2 shows that $LaMnO_3$ is the best catalyst for oxygen reduction, followed by $LaNiO_3 > LaCoO_3 >$ BSCF $> LaFeO_3 > LaCrO_3$.

A study of La-based perovskite oxide ($LaMO_3$, M = Cr, Mn, Fe, Co and Ni), demonstrated that the diffusion-limited current density increased in the following order $LaCrO_3 < LaFeO_3 < LaNiO_3 < LaMnO_3 < LaCoO_3$ in an alkaline solution.[17] This trend was different to that predicted by the volcano plot shown in Figure 6.2.

For the present study we examined $LaMnO_3$ and $La_{0.8}Sr_{0.2}MnO_3$, $LaCoO_3$ type; $La_{0.7}Ca_{0.3}CoO_3$ (A site substituted by Ca), $LaNiO_3$ type; $LaNi_{0.6}Fe_{0.4}O_3$ (B site substituted by Fe), and $Ba_{0.5}Sr_{0.5}Co_{0.2}Fe_{0.8}O_3$ (BSCF).

The above mentioned catalysts were individually incorporated on Gortex electrodes that served as the cathode in a fuel cell configuration as described in chapter 2 section. All the fuel cell cathodes comprised of a mixture of the perovskite catalyst, carbon black (CB) and PTFE with a Ni mesh current collector, deposited on Gortex ('Catalyst+CB+PTFE+Ni-mesh/Gortex') while the anode was kept same for all the different cathodes, and comprised of 10% Pt, carbon black (CB) and PTFE with a Ni mesh current collector, deposited on

Gortex ('10%Pt+CB+PTFE+Ni-mesh/Gortex'). Cathodes involving perovskites had an average metal loading of 14.5 mg cm^{-2} (individual loadings of each of the catalysts are reported in Table 6.1), along with carbon black and PTFE, each having an average loading of 3.8 mg cm^{-2}. Anodes prepared contained an average of 0.05 mg cm^{-2} of Pt, with carbon black and PTFE, each having an average loading of 1.5 mg cm^{-2}. The carbon black used was pre-treated using ascorbic acid in order to remove Fe impurities and enhance its corrosion resistance.[63]

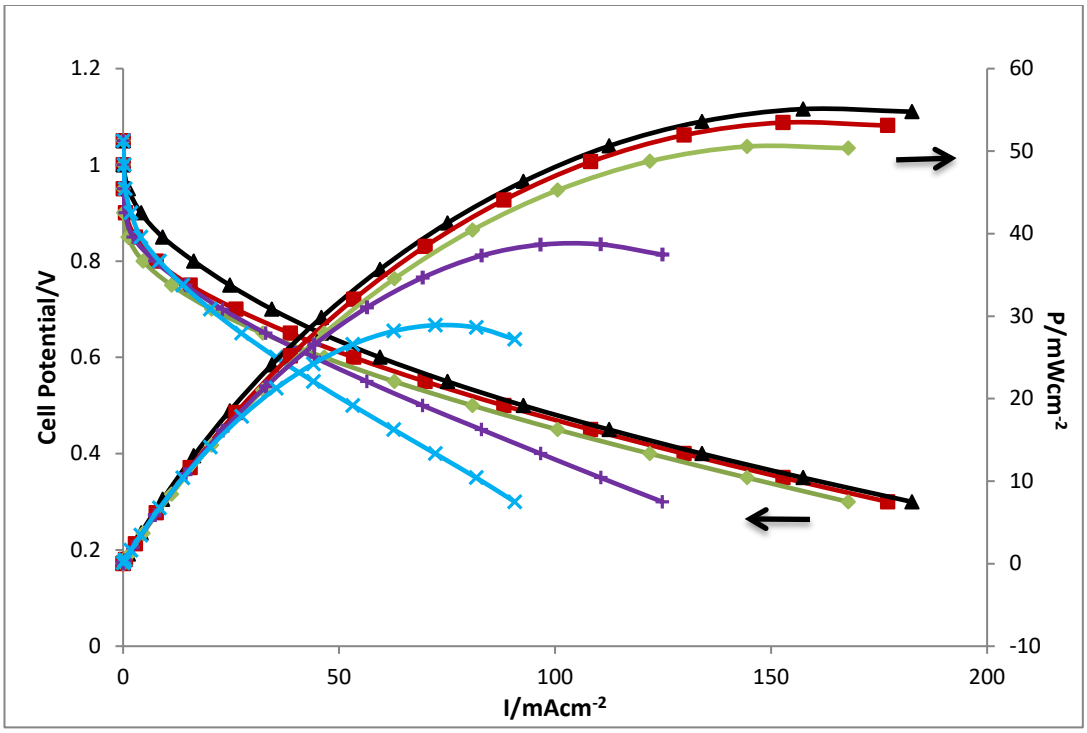

Figure 6.3. *Polarization curves (left axis) and power density curves (right axis) at 20 °C for alkaline fuel cells containing Gortex electrodes coated with (1) ▲-$La_{0.8}Sr_{0.2}MnO_3$ (2) ■-$LaMnO_3$ (3) ♦- $La_{0.7}Ca_{0.3}CoO_3$ (4) +-$LaNi_{0.6}Fe_{0.4}O_3$ (5) X –$Ba_{0.5}Sr_{0.5}Co_{0.2}Fe_{0.8}O_3$ as cathode (O_2 catalyst). Gortex coated with 10% Pt served as the anode (H_2 catalyst) in all cases. Electrolyte: 6 M KOH.*

Conductive carbon has generally been added to electrodes in order to enhance conductivity and catalyse the ORR when using perovskite type oxides.[64] Several recent studies reported

the fact that carbons in composite perovskite-based electrodes support the ORR mechanistic pathway.[65-68] In the case of BSCF perovskite, the ORR activity exhibited volcano-like behaviour for composition of BSCF/acetylene black (AB).[66] In composite electrodes, carbon appears to act not only as a conductive additive, but also as an ORR catalyst. This is because the peroxide production reaction occurs mainly on carbon as the first reduction step (i.e. primary catalyst[29]), with subsequent peroxide decomposition catalyzed by the perovskite in the following step (i.e. the carbon acts as a co-catalyst[29]).

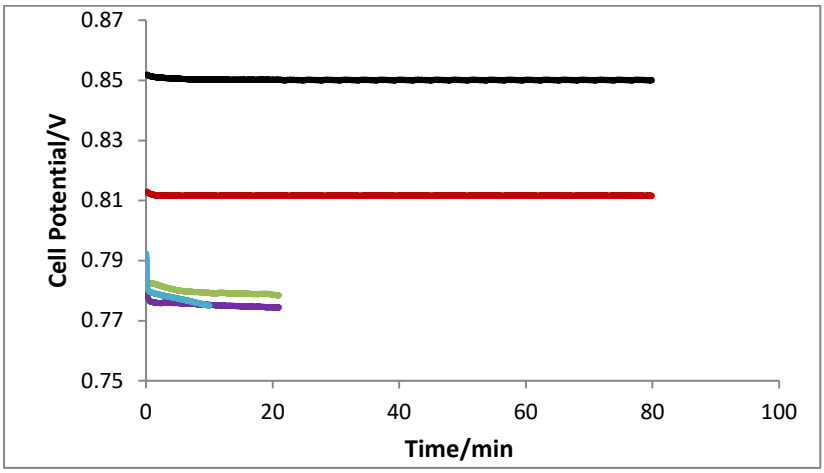

Figure 6.4. *Chronopotentiograms (CP) at 10 mA cm^{-2} for alkaline fuel cells, at 20 °C, containing Gortex electrodes coated with (1)* $La_{0.8}Sr_{0.2}MnO_3$ *(2)* $LaMnO_3$ *(3)* $La_{0.7}Ca_{0.3}CoO_3$ *(4)* $LaNi_{0.6}Fe_{0.4}O_3$ *(5)* $Ba_{0.5}Sr_{0.5}Co_{0.2}Fe_{0.8}O_3$ *as cathode (O_2 catalyst). Gortex coated with 10% Pt served as the anode (H_2 catalyst) in all cases. Electrolyte: 6 M KOH.*

The selected perovskites ($LaMnO_3$, $La_{0.8}Sr_{0.2}MnO_3$, $La_{0.7}Ca_{0.3}CoO_3$, $LaNi_{0.6}Fe_{0.4}O_3$ and $Ba_{0.5}Sr_{0.5}Co_{0.2}Fe_{0.8}O_3$ were incorporated into Gortex-based cathodes in our desktop alkaline fuel cells. A trend similar to the volcano plot was observed in the polarisation (IV) curves of the various perovskite-based cathodes tested (Figure 6.3). The activation overpotentials (η_{act}) were extracted from the polarization curves. The apparent electrochemical activity for the

ORR was also evaluated by extracting the overpotential values at a fixed current density of 10 mA cm^{-2}. The results were as follows.

Alkaline fuel cells using '$LaMnO_3$+CB+PTFE+Ni-mesh/Gortex' as cathode at 20 ^oC generated 153 mA cm^{-2} and 53 mW cm^{-2} at a cell voltage of 0.35 V (vs. the standard anode, '10% Pt+CB+PTFE+Ni-mesh/Gortex'). Comparative studies using a cathode containing $La_{0.8}Sr_{0.2}MnO_3$ as catalyst generated 4% more power at 0.35 V (Figure 6.3). Table 6.1 and Figure 6.5, show that it produces a stable current of 10 mA cm^{-2} at the lowest η_{act} of 421 mV.

$La_{0.8}Sr_{0.2}MnO_3$, having partial substitution of La with Sr at A-site, has previously been reported to be a catalyst for the ORR in alkaline medium.[21-22] The higher catalytic performance of $La_{0.8}Sr_{0.2}MnO_3$ has been attributed to an improved oxygen mobility[69] resulting from partial substitution of La with Sr. Substituting Ni by Fe in $LaNiO_3$ ($LaNi_{0.6}Fe_{0.4}O_3$) suppresses the formation of Ni^{II} on the perovskite surface and creates a stronger surface Ni-O bond resulting in better performance than $LaNiO_3$.[19] In another study, ORR activity was improved when the B-site of $LaNiO_3$ was substituted by Fe to form $LaNi_{0.8}Fe_{0.2}O_3$.[19] This revealed that the two transition-metal ions worked synergistically together, improving the ORR catalytic activity. Similarly, Co-based perovskite (e.g. $La_{0.7}Ca_{0.3}CoO_3$) performed better than $LaCoO_3$.[16]

Cathodes containing the following catalysts ('catalysts') in gas diffusion electrodes of the type 'Catalyst+CB+PTFE+Ni-mesh/Gortex', were studied: (Figure 6.5 and Table 6.1)

	Voltage at 10 mA/cm^{2} *
- $La_{0.8}Sr_{0.2}MnO_3$ (loading = 11 mg cm^{-2})	0.849 V
- $LaMnO_3$ (loading = 17 mg cm^{-2})	0.812 V
- $La_{0.7}Ca_{0.3}CoO_3$ (loading = 18 mg cm^{-2})	0.776 V
- $LaNi_{0.6}Fe_{0.4}O_3$ (loading = 11 mg cm^{-2})	0.774 V

- $Ba_{0.5}Sr_{0.5}Co_{0.2}Fe_{0.8}O_3$ (loading = 14 mg cm^{-2}) 0.775 V

(* vs 10%Pt+CB+PTFE+Ni-mesh/Gortex).

Thus, $La_{0.8}Sr_{0.2}MnO_3$, $LaMnO_3$, $La_{0.7}Ca_{0.3}CoO_3$, $LaNi_{0.6}Fe_{0.4}O_3$ and $Ba_{0.5}Sr_{0.5}Co_{0.2}Fe_{0.8}O_3$ exhibit ~99%, ~95%, ~91%, ~91% and ~91% electrochemical activity for the ORR compared to that of 10% Pt/C (0.075 mg cm^{-2}; which generates 0.854 V at 10 mA cm^{-2}), respectively.

In our studies, alkaline fuel cell cathodes containing Ni-based ('$LaNi_{0.6}Fe_{0.4}O_3$+CB+PTFE+ Ni-mesh/Gortex'), or Co-based ('$La_{0.7}Ca_{0.3}CoO_3$+CB+PTFE+Ni-mesh/Gortex') perovskites as catalyst, displayed an increase of 9% and 22% in activation overpotentials, when compared to cathodes containing Mn-based ($La_{0.8}Sr_{0.2}MnO_3$) perovskite. A similar trend in the oxygen reduction currents was also observed for Mn-based ($La_{0.8}Sr_{0.2}MnO_3$) perovskite, which performs better than Co-based ($LaCoO_3$) perovskite.[70] A minimal loss in current density was observed over 1 h for the alkaline fuel cells containing $La_{0.8}Sr_{0.2}MnO_3$ or $LaMnO_3$ (Figure 6.4). By contrast, alkaline fuel cells with cathodes containing either $La_{0.7}Ca_{0.3}CoO_3$, $LaNi_{0.6}Fe_{0.4}O_3$, or $Ba_{0.5}Sr_{0.5}Co_{0.2}Fe_{0.8}O_3$ showed clear rates of decay of 70 mV h^{-1}, 93 mV h^{-1} and 104 mV h^{-1} respectively, over just 10 min. Thus, cathodes containing Mn-based perovskites as catalysts were the most active and stable for the ORR while cathodes containing Co-based and Ni-based perovskites lacked activity and stability. This followed the report of Karlsson.[8]

Figure 6. 3 also shows that, among the Gortex cathodes containing either $La_{0.8}Sr_{0.2}MnO_3$, $LaMnO_3$, $La_{0.7}Ca_{0.3}CoO_3$, $LaNi_{0.6}Fe_{0.4}O_3$ and $Ba_{0.5}Sr_{0.5}Co_{0.2}Fe_{0.8}O_3$, the $Ba_{0.5}Sr_{0.5}Co_{0.2}Fe_{0.8}O_3$ cathode demonstrated the smallest diffusion-/mass-transport limited ORR current density, which generally comes into play at higher current densities. This was followed by $LaNi_{0.6}Fe_{0.4}O_3$, $La_{0.7}Ca_{0.3}CoO_3$, $LaMnO_3$, and $La_{0.8}Sr_{0.2}MnO_3$, in decreasing order. Lowest lowest η_{act} (assuming that a lower η_{act} equals higher overall catalytic activity) was also

observed for the $La_{0.8}Sr_{0.2}MnO_3$+CB+PTFE+Ni-mesh/Gortex cathode which recorded the largest diffusion-limited current density. The only noticeable exception to this was the $LaMnO_3$+CB+PTFE+Ni-mesh/Gortex cathode, which started catalysing the ORR at a high η_{act} whilst also showing a higher diffusion limited ORR current. Partially substituting Mn with other metals, for example, Sr, Co, Fe, Mn, and Cr, caused η_{act} to decrease.[17]

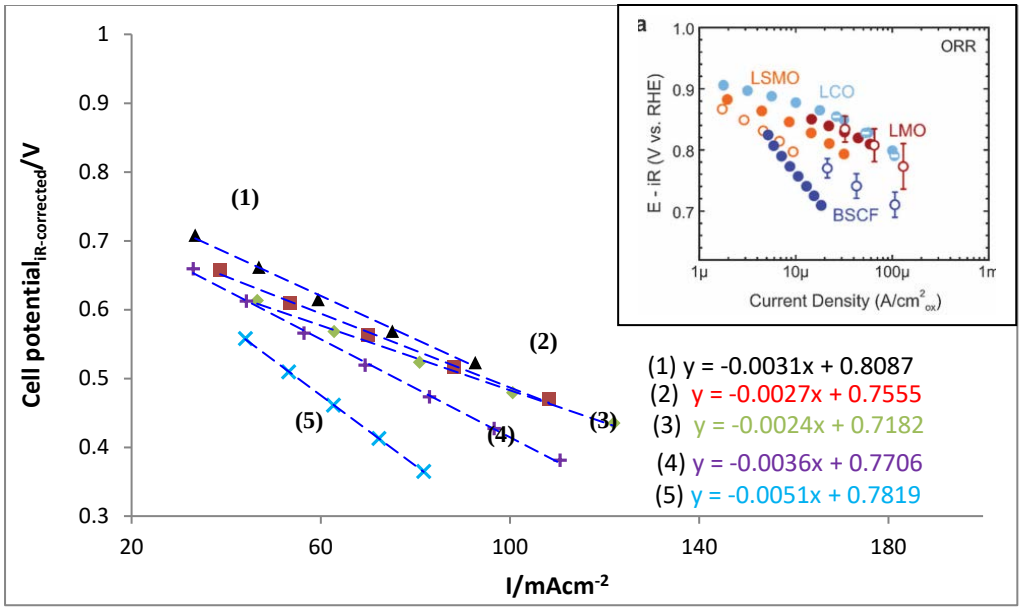

Figure 6.5. *Straight line fits of the ohmic regions (iR-corrected) for the alkaline fuel cells containing Gortex electrodes coated with (1) ▲-$La_{0.8}Sr_{0.2}MnO_3$ (2) ■-$LaMnO_3$ (3) ♦-$La_{0.7}Ca_{0.3}CoO_3$ (4) +-$LaNi_{0.6}Fe_{0.4}O_3$ (5) X –$Ba_{0.5}Sr_{0.5}Co_{0.2}Fe_{0.8}O_3$ as cathode (O_2 catalyst). Gortex coated with 10% Pt served as the anode (H_2 catalyst) in all cases. The fitted straight lines have the general formula y=mx+c, where the value of c accords with the onset potential of the fuel cell. The activation overpotential (η_{act}) is the difference between the onset potential and 1.23 V, which is the E^o of the cell at 20 °C. Inset: Tafel plots for Oxygen Reduction activity on perovskites; reproduced with permission from reference 61. Solid and open symbols represent activities of perovskites (LSMO- $La_{0.8}Sr_{0.2}MnO_{3-\delta}$, LMO- $LaMnO_{3\pm\delta}$, LCO- $LaCoO_3$, and BSCF- $Ba_{0.5}Sr_{0.5}Co_{0.8}Fe_{0.2}O_{3-\delta}$) tested in the form of thin films and powders respectively. Electrolyte: 6 M KOH.*

Catalyst	η_{act} (V)	$V_{@10mAcm-2}$ (V)	R_Ω (Ω cm^2) [a]	R_{ct} (Ω cm^2)	C_{ct} (μF)	Z_d (Ω cm^2)	b_1 (mV dec^{-1})	b_2 (mV dec^{-1})	Loading (mg_{metal} cm^{-2})
$La_{0.8}Sr_{0.2}MnO_3$	0.421	0.851	0.78	0.63	34	5.1	52	146	10.9
$LaMnO_3$	0.475	0.812	0.71	0.92	77	5.34	53	147	17.5
$LaNi_{0.6}Fe_{0.4}O_3$	0.459	0.774	0.81	0.73	85	6.8	48	172	11.6
$La_{0.7}Ca_{0.3}CoO_3$	0.512	0.776	0.82	0.72	34	6.45	55	148	18.0
$Ba_{0.5}Sr_{0.5}Co_{0.2}Fe_{0.8}O_3$	0.448	0.775	0.71	1.5	39	7.2	63	222	14.4

[a] *3 mm inter-electrode gap*

Table 6.1. *Comparison, at 20 ^oC, of alkaline fuel cells containing Gortex cathode electrodes coated with perovskite catalysts. Gortex coated with 10% Pt served as the anode (H_2 catalyst) in all cases. Symbols: activation overpotential (η_{act}), Voltage at 10 mA cm^{-2} ($V_{@10mAcm-2}$), Tafel slope (b_1) (at lower current density (LCD)), Tafel slope (b_2) (at higher current density (HCD)); from electrochemical impedance, ohmic resistance (R_Ω), charge transfer resistance (R_{ct}), double-layer capacitance within the catalyst layer (C_{ct}), diffusional resistance (Z_d).*

Catalyst	η_{act} (V)	$V_{@10mAcm-2}$ (V)	R_Ω (Ω cm^2) [a]	R_{ct} (Ω cm^2)	C_{ct} (μF)	Z_d (Ωcm^2)	b_1 (mV dec^{-1})	b_2 (mV dec^{-1})	Loading (mg_{metal} cm^{-2})
$NiCo_2O_4$	0.429	0.851	0.73	0.60	83	5.3	57	152	11.1
$Mn_{1.5}Co_{1.5}O_4$	0.473	0.784	0.73	0.68	44	5.78	62	162	14.8
Co_3O_4	0.492	0.770	0.83	0.85	36	5.8	61	155	17.8
$NiFe_2O_4$	0.492	0.767	0.69	1.78	44	6.8	64	159	17.8
$Co_{0.5}Ni_{0.5}Fe_2O_4$	0.491	0.767	0.76	1.9	35	7.1	65	163	10.0

[a] *3 mm inter-electrode gap*

Table 6.2. *Comparison, at 20 ^oC, for alkaline fuel cells containing Gortex cathode electrodes coated with spinel catalysts. Gortex coated with 10% Pt served as the anode (H_2 catalyst) in all cases. Symbols: activation overpotential (η_{act}), Voltage at 10 mA cm^{-2} ($V_{@10mAcm-2}$), Tafel slope (b_1) (at lower current density (LCD)), Tafel slope (b_2) (at higher current density (HCD)); from electrochemical impedance, ohmic resistance (R_Ω), charge transfer resistance (R_{ct}), double-layer capacitance within the catalyst layer (C_{ct}), diffusional resistance(Z_d).*

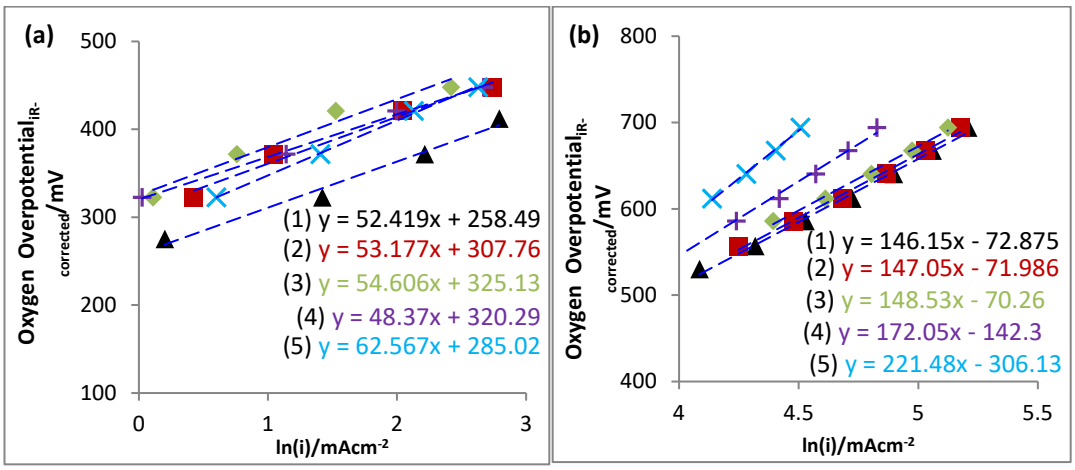

Figure 6.6. *iR-corrected Tafel plots at 20 °C of: (a) b_1 at Low Current density (LCD), (b) b_2 at High Current Density (HCD) for alkaline fuel cells containing Gortex electrodes coated with (1) ▲-$La_{0.8}Sr_{0.2}MnO_3$ (2) ■-$LaMnO_3$ (3) ♦- $La_{0.7}Ca_{0.3}CoO_3$ (4) +-$LaNi_{0.6}Fe_{0.4}O_3$ (5) X – $Ba_{0.5}Sr_{0.5}Co_{0.2}Fe_{0.8}O_3$, as cathode ($O_2$ catalyst). Gortex coated with 10% Pt served as the anode (H_2 catalyst) in all cases. The fitted straight lines have the general formula $y= b_{(1 \text{ or } 2)} x+c$, where $b_{(1 \text{ or } 2)}$ is the Tafel slope and c is the imputed exchange current density, i_o. Electrolyte: 6 M KOH.*

To compare the electrocatalytic activities of the fuel cells containing perovskites as catalysts, their Tafel slopes were calculated from their polarization curves. The curves were iR-corrected by subtracting the electrolyte resistance (R_{el}) from their ohmic resistance (R_Ω), as described in Chapter 5. The Tafel slopes evaluated are descriptive of ORR at cathode and therefore governed by the oxygen overpotential. Two Tafel slopes were evaluated for all the catalysts: Tafel slope b_1 and Tafel slope b_2 were calculated at lower current densities (LCD) and higher current densities (HCD) respectively, as tabulated in Table 6.1. The two Tafel slopes differ in respect of the role played by the mass transport of oxygen. The slope at low current density is, effectively, a measure of the intrinsic activity of the catalysts since it is not limited by the mass transport of oxygen, whereas that at high current density is controlled by the mass transport of oxygen.

Figure 6. 6 shows that b1 for the alkaline fuel cells containing $La_{0.8}Sr_{0.2}MnO_3$ or $LaMnO_3$ cathodes, extracted from low overpotentials where the influence of oxygen transport is minimal, were 52 mV dec^{-1} and 53 mV dec^{-1} respectively. These values are lower than earlier-reported Tafel slopes for these catalysts in the absence of the Gortex substrate, which were 77 mV dec^{-1} and 77.8 mV dec^{-1} for $La_{0.8}Sr_{0.2}MnO_3$[71] and $LaMnO_3$[72] respectively (as shown in the inset of Figure 6. 5). However, b_1 for the fuel cell with a $Ba_{0.5}Sr_{0.5}Co_{0.2}Fe_{0.8}O_3$ cathode was 63 mV dec^{-1}, whereas earlier literature reported it to be ~77.5 mV dec^{-1}.[72] In our study, we found that the fuel cell with a $La_{0.8}Sr_{0.2}MnO_3$+CB+PTFE+Ni-mesh/Gortex cathode, exhibited the lowest b_1, indicating a faster electrochemical reaction, whereas, that with the $Ba_{0.5}Sr_{0.5}Co_{0.2}Fe_{0.8}O_3$+CB+PTFE+Ni-mesh/Gortex cathode, displayed the highest b_1 among all the perovskites tested, indicating a poor electrochemical reaction. The fuel cells containing $LaMnO_3$+CB+PTFE+Ni-mesh/Gortex or $La_{0.7}Ca_{0.3}CoO_3$+CB+PTFE+Ni-mesh/Gortex cathodes, had b_1 of 53 mV dec^{-1} and 55 mV dec^{-1} respectively, which was less than the values reported by Yang et al.[16]

Partial substitution of La with Sr in $La_{0.8}Sr_{0.2}MnO$ leads to a lower Tafel slope than that of $LaMnO_3$ due to improved oxygen mobility,[69] making $La_{0.8}Sr_{0.2}MnO_3$ a promising candidate for catalysing the ORR in alkaline medium. Thus, the fuel cell with a $La_{0.8}Sr_{0.2}MnO_3$+CB+PTFE+Ni-mesh/Gortex cathode showed very similar ORR activity (due to improved kinetics) to that with a 10%Pt/CB+PTFE+Ni-mesh/Gortex cathode at low current density (Chapter 5).

However, if we consider b_2 from Table 6.1 (i.e. electrocatalytic activity for the ORR at high current densities), the fuel cell cathode catalysts display activities in the order: $La_{0.8}Sr_{0.2}MnO_3$ > $LaMnO_3$ > $La_{0.7}Ca_{0.3}CoO_3$ > $LaNi_{0.6}Fe_{0.4}O_3$ > $Ba_{0.5}Sr_{0.5}Co_{0.2}Fe_{0.8}O_3$, which indicates that fuel cell cathodes with $La_{0.8}Sr_{0.2}MnO_3$ as catalysts, facilitate a faster electrochemical reaction at high current densities as well. Clearly, oxygen mass transport is less hindered with this cathode than with the other cathodes.

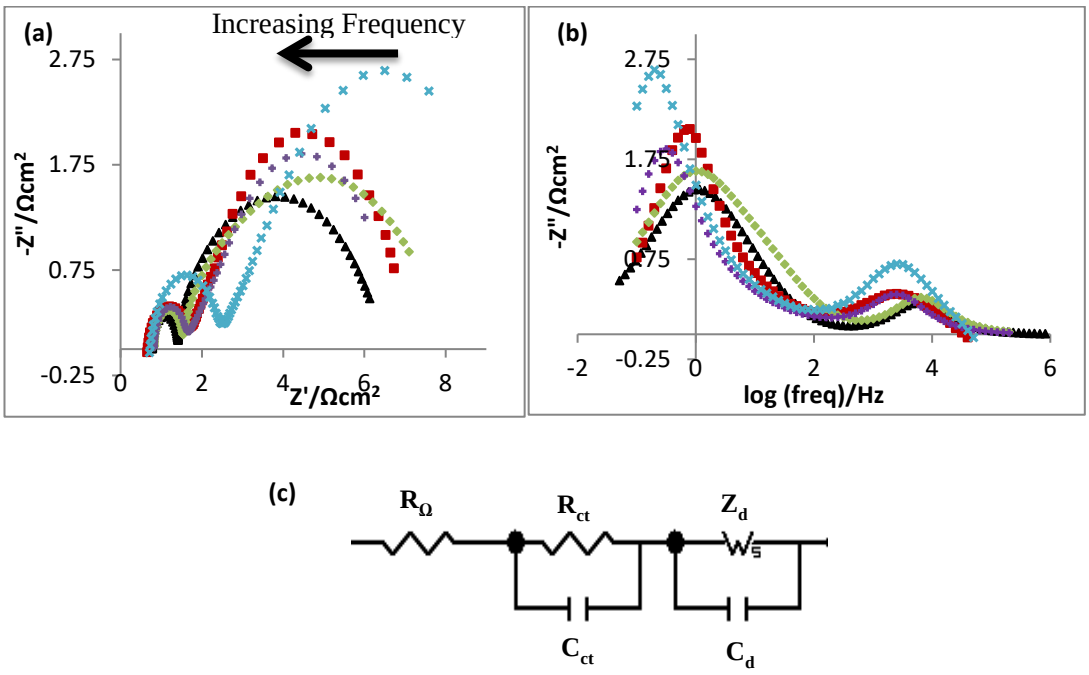

Figure 6.7. *(a) Nyquist and (b) Bode plots at 10 mA cm^{-2}, (c) Equivalent electric circuit used to model Nyquist impedance data, for alkaline fuel cells, at 20 ^{o}C, containing Gortex electrodes coated with (1) ▲-$La_{0.8}Sr_{0.2}MnO_3$ (2) ■-$LaMnO_3$ (3) ♦- $La_{0.7}Ca_{0.3}CoO_3$ (4) +-$LaNi_{0.6}Fe_{0.4}O_3$ (5) X –$Ba_{0.5}Sr_{0.5}Co_{0.2}Fe_{0.8}O_3$ as cathode (O_2 catalyst). Gortex coated with 10% Pt served as the anode (H_2 catalyst) in all cases. Electrolyte: 6 M KOH.*

Further insights into the electrochemical behaviour of the fuel cells having gas diffusion electrodes comprising Gortex incorporating perovskites may be obtained from galvanostatic electrochemical impedance spectroscopy (GEIS). Figure 6.7(a)-(b) depict the two-electrode Nyquist and Bode plots of the above cells respectively, measured under galvanostatic conditions at 10 mA cm^{-2}. The Nyquist plots display experimental data points in Figure 6.7(a). All of the perovskites displayed ohmic resistances similar to the Pt-based catalysts, which was confirmed by the ohmic resitance (R_Ω) from electrochemical impedance spectroscopy.

The Nyquist spectra were fitted with an equivalent electrical circuit shown in Figure 6.7 (c). The Nyquist plots of these electrodes displayed two semicircles representing two processes, one for each semi-circle. The low frequency arc indicates diffusion (Z_d) and the high frequency arc represents charge transfer (R_{ct}). The Nyquist plots of these electrodes (Figure 6.7(a)) clearly displayed two semicircles, which are due to the different time constants of these two processes in the electrodes. It can be seen that the low frequency semi-circle increased in arc depending on the catalysts used in cathodes. This can be explained by correlation with Z_d which can be assumed to be an inherent feature of the catalyst.

Table 6.1 shows that the fuel cell containing $La_{0.8}Sr_{0.2}MnO_3$+CB+PTFE+Ni-mesh/Gortex as cathode produced the lowest value of Z_d, indicating faster diffusion, and the lowest value of R_{ct}, indicating faster charge transfer, when compared to the other fuel cell cathodes. To extract information about the frequency at which each of the above-mentioned processes of diffusion and charge transfer resistance occur, we also obtained Bode plots (Figure 6.7(b)). As can be seen, the impedance of the fuel cell with a cathode containing $La_{0.8}Sr_{0.2}MnO_3$ is lowest at high frequency of ~ 6 kHz (indicative of a combination of charge transfer, R_{ct} and capacitance, C_{ct} within the catalyst layer) and at low frequency of ~ 1.4 Hz (indicative of diffusion). By contrast, the fuel cell with a cathode comprising of $Ba_{0.5}Sr_{0.5}Co_{0.2}Fe_{0.8}O_3$, produced the highest impedance at much lower frequencies (charge transfer at ~3 kHz and diffusion at ~0.2 Hz). The ORR electrochemical activity therefore, increases upon substitution of La by Sr in $LaMnO_3$ primarily due to a reduction in the value of R_{ct}. The substitution of La by Sr in $LaMnO_3$ increases the electrical conductivity and thereby the charge transfer and ORR rate.[73, 74] $La_{0.8}Sr_{0.2}MnO_3$, which has mixed $Mn^{3+/4+}$ ions, readily donate and accept electrons due to the ease of charge-transfer kinetics due to the Sr content. This phenomenon is consistent with the observed high activity exhibited by $La_{0.8}Sr_{0.2}MnO_3$ for the ORR.[22]

Both R_{ct} and Z_d could be used to establish a correlation between impedance and volcano plots as previously also observed in Chapter 5, section 5.3.7. As is evident from the volcano plot, $LaMnO_3$-type perovskites display the highest oxygen reduction activity, which is manifested in the fuel cell with either $La_{0.8}Sr_{0.2}MnO_3$+CB+PTFE+Ni-mesh/Gortex or $LaMnO_3$+CB+PTFE+Ni-mesh/Gortex as cathode, which registered the lowest combinations of R_{ct} and Z_d values (5.73 Ω cm^2 for $La_{0.8}Sr_{0.2}MnO_3$ and 6.26 Ω cm^2 for $LaMnO_3$) (Table 6.1). A low R_{ct} and Z_d indicate faster electron transfer and ready accessibility of active sites to oxygen ions. Owing to such low Z_d values, both the fuel cells containing $La_{0.8}Sr_{0.2}MnO_3$ and $LaMnO_3$ as cathode catalysts respectively, produced a stable current density of 10 mA cm^{-2} for more than 1 h, with a negligible degradation rate. However, fuel cells employing cathodes with $La_{0.7}Ca_{0.3}CoO_3$, $LaNi_{0.6}Fe_{0.4}O_3$ or $Ba_{0.5}Sr_{0.5}Co_{0.2}Fe_{0.8}O_3$ as catalysts, exhibited unstable current values which degraded rapidly owing to high mass transport resistance (Z_d).

6.3.5 Fuel Cell Performance at Room Temperature (20 ºC), using Spinels as ORR Catalyst

As discussed earlier, researchers have incorporated inexpensive transition metals like Ni, Mn, Cu and Fe atoms into the spinel structure, which enhanced the electrical conductivity of the metal oxide and increased the number of catalytically active sites.[5,75,76] Among these, we have examined Co_3O_4, $NiCo_2O_4$, $Mn_{1.5}Co_{1.5}O_4$, $NiFe_2O_4$ and $Co_{0.5}Ni_{0.5}Fe_2O_4$ as ORR catalysts. These catalysts were tested individually on Gortex cathodes in fuel cells having a standard, invariant 10% Pt+CB+PTFE+Ni mesh/Gortex anode. All the fuel cell cathodes comprised of a mixture of catalyst, carbon black (CB) (which was pre-treated with ascorbic acid)[63] and PTFE with a Ni mesh current collector, deposited on Gortex (‘Catalyst+CB+PTFE+Ni-mesh/Gortex’). The anode was, in all cases, 10%Pt, carbon black (CB) and PTFE with a Ni mesh current collector, deposited on Gortex (‘10%Pt+CB+PTFE+Ni-mesh/Gortex’). Cathodes involving spinels had an average metal

loading of 14.3 mg cm^{-2} (individual loadings of each of the catalysts is provided in Table 6.2), along with carbon black and PTFE, each of an average loading of 4.1 mg cm^{-2}. Significantly, spinel oxides as compared to Pt based catalyst exhibit lower mass activity; therefore, spinels require higher loadings. For instance, a $MnCo_2O_4$-carbon black catalyst at 14 mg/cm^2 loading in 6 M KOH at ~0.2 V produced a current density of 300 mA/cm^2 at 60 ^oC. However, Pt/CNT/C at 0.1 mg/cm^2 loading offered current density of 125 mA/cm^2 at 25 ^oC.[77] Although the spinel oxides are of low cost, there is a maximum acceptable electrode loading of the catalyst due to the resistivity of oxygen and electrolyte transport.[77] Anodes used in the fuel cells contained an average of 0.05 mg cm^{-2} of Pt, and carbon black and PTFE, each with an average loading of 1.5 mg cm^{-2}.

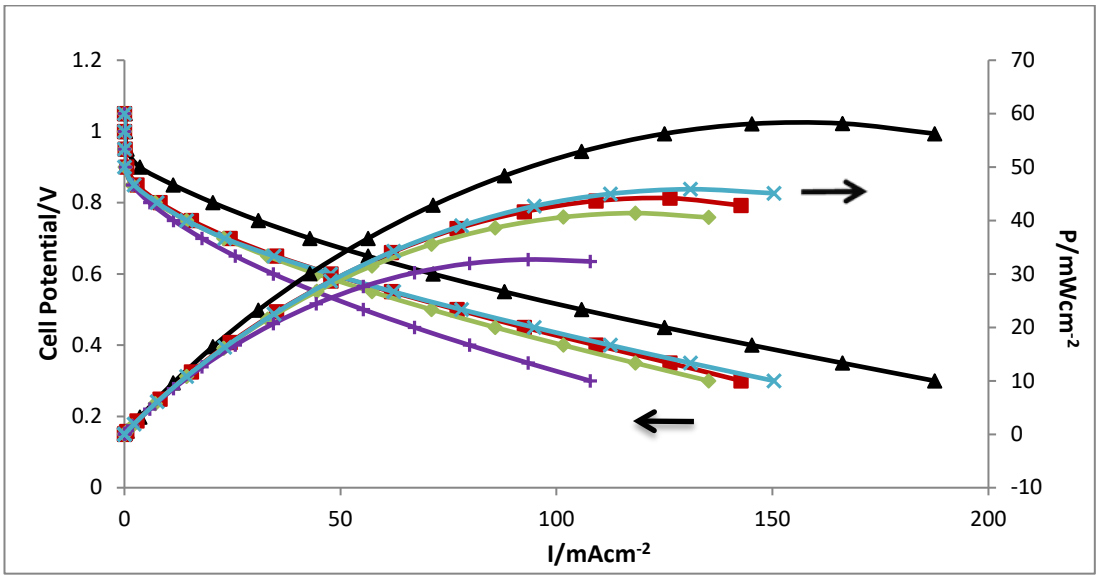

Figure 6.8. *Polarization curves (left axis) and power density curves (right axis) at 20 ^oC of alkaline fuel cells containing Gortex electrodes coated with (1) ▲-$NiCo_2O_4$ (2) ■-$Mn_{1.5}Co_{1.5}O_4$ (3) ♦- $NiFe_2O_4$ (4) +-$Co_{0.5}Ni_{0.5}Fe_2O_4$ (5) X –Co_3O_4, as cathode (O_2 catalyst). Gortex coated with 10% Pt served as the anode (H_2 catalyst) in all cases. Electrolyte: 6 M KOH.*

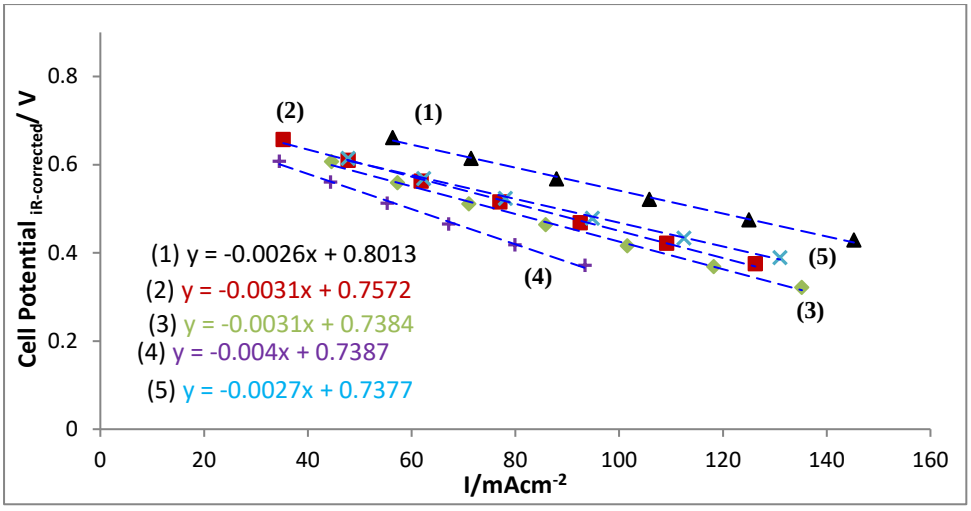

Figure 6.9. *Straight line fits of the ohmic regions (iR-corrected) at 20 °C for the alkaline fuel cells containing Gortex electrodes coated with: (1) ▲-$NiCo_2O_4$ (2) ■-$Mn_{1.5}Co_{1.5}O_4$ (3) ♦- $NiFe_2O_4$ (4) +-$Co_{0.5}Ni_{0.5}Fe_2O_4$ (5) X –Co_3O_4 as cathode (O_2 catalyst). Gortex coated with 10% Pt served as the anode (H_2 catalyst) in all cases. The fitted straight lines have the general formula y=mx+c, where the value of c is the onset potential of the fuel cell. The activation overpotential (η_{act}) is the difference between the onset potential and 1.23 V, which is the E^o of the cell at 20 °C. Electrolyte: 6 M KOH.*

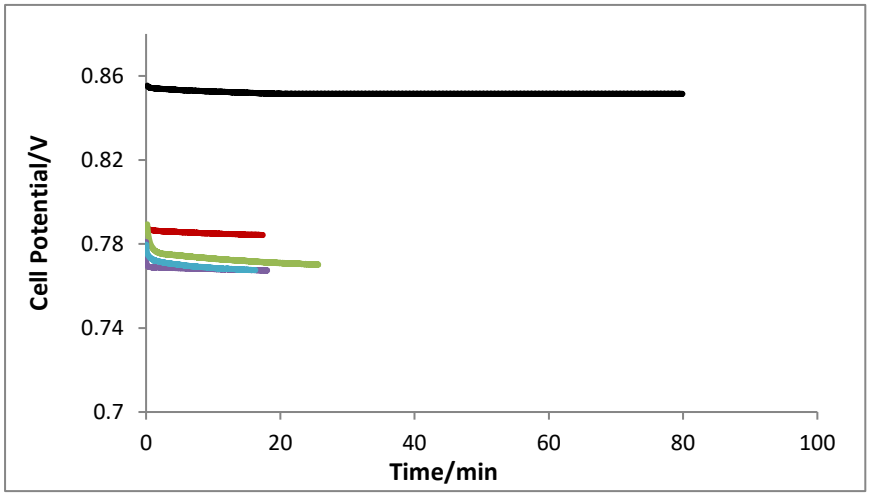

Figure 6.10. *Chronopotentiograms (CP) at 10 mA cm^{-2} for alkaline fuel cells, at 20 °C , containing Gortex electrodes coated with (1) — $NiCo_2O_4$ (2) — $Mn_{1.5}Co_{1.5}O_4$ (3) — $NiFe_2O_4$ (4) — $Co_{0.5}Ni_{0.5}Fe_2O_4$ (5) — Co_3O_4, as cathode (O_2 catalyst). Gortex coated with 10% Pt served as the anode (H_2 catalyst) in all cases. Electrolyte: 6 M KOH.*

As mentioned, the activation overpotential (η_{act}) and the overpotential at a fixed current density of 10 mA cm^{-2}, were calculated from the polarization curves in order to evaluate their apparent activity towards ORR catalysis. The best performing of the spinels were Co_3O_4 and $NiCo_2O_4$. Alkaline fuel cells using Co_3O_4+CB+PTFE+Ni-mesh/Gortex as cathode generated 131 mA cm^{-2} and 46 mW cm^{-2} at 0.35 V and 20 ^oC (Figure 6.8). Under the same conditions, the use of $NiCo_2O_4$+CB+PTFE+Ni-mesh/Gortex as cathode generated 166 mA cm^{-2} and 58 mW cm^{-2} at 0.35 V and 20 ^oC. Partial substitution of Co with another transition element Ni in Co_3O_4, therefore reduced the activation overpotential η_{act} of the fuel cell by 13% when the cathode comprised of $NiCo_2O_4$+CB+PTFE+Ni-mesh/Gortex (Table 6.2). This makes $NiCo_2O_4$ a promising candidate for catalysing the ORR in alkaline media. The catalytic improvement has been attributed to the fact that $NiCo_2O_4$ reduces oxygen predominantly by a 4 e^- reaction, leading to water without the intermediate formation of hydrogen peroxide, as compared to Co_3O_4.[78] Based on η_{act}, the spinel based fuel cell cathodes displayed activities in the order: $NiCo_2O_4$ > $Mn_{1.5}Co_{1.5}O_4$ > $Co_{0.5}Ni_{0.5}Fe_2O_4$ > $Co_3O_4 \approx NiFe_2O_4$. As is evident from the trend in η_{act}, cathodes containing $Mn_{1.5}Co_{1.5}O_4$ as catalyst showed superior activity for O_2 reduction than Co_3O_4. In this case, it is believed that the partial substitution of Co sites by Mn increased the ORR activity of the catalytic sites when compared to Co_3O_4 in alkaline solutions.[60]

Cathodes containing the following catalysts ('catalysts') in gas diffusion electrodes of the type 'Catalyst+CB+PTFE+Ni-mesh/Gortex', were studied:

	Voltage at 10 mA/cm^{2} *
- $NiCo_2O_4$ (loading = 11 mg cm^{-2})	0.851 V
- $Mn_{1.5}Co_{1.5}O_4$ (loading = 15 mg cm^{-2})	0.784 V
- Co_3O_4 (loading = 18 mg cm^{-2})	0.770 V
- $NiFe_2O_4$ (loading = 18 mg cm^{-2})	0.767 V

- $Co_{0.5}Ni_{0.5}Fe_2O_4$ (loading = 10 mg cm^{-2}) 0.767 V

(* vs 10%Pt+CB+PTFE+Ni-mesh/Gortex).

Thus, the fuel cells with $NiCo_2O_4$, $Mn_{1.5}Co_{1.5}O_4$, Co_3O_4, $NiFe_2O_4$ or $Co_{0.5}Ni_{0.5}Fe_2O_4$ as cathode catalysts, exhibited ~99%, ~92%, ~91%, ~90% or ~90% of the electrochemical activity for the ORR respectively, compared to fuel cell with cathodes containing 10%Pt/CB (0.854 V at 10 mA cm^{-2}) (Chapter 5).

The voltage at a steady current of 10 mA cm^{-2} for fuel cells with cathodes containing $NiCo_2O_4$ was also close to those with cathodes containing 10% Pt on Vulcan XC72 (Figure 6.10). A minimal loss in voltage over 1 h for the fuel cell containing $NiCo_2O_4$ as cathode catalyst was observed (Figure 6.10); most of the voltage loss occurred in the initial few minutes. By contrast, alkaline fuel cells with cathodes containing Co_3O_4, $Mn_{1.5}Co_{1.5}O_4$, $NiFe_2O_4$ or $Co_{0.5}Ni_{0.5}Fe_2O_4$ displayed decay rates of 67 mV h^{-1}, 21 mV h^{-1}, 101 mV h^{-1} and 77 mV h^{-1} respectively over just 10 min.

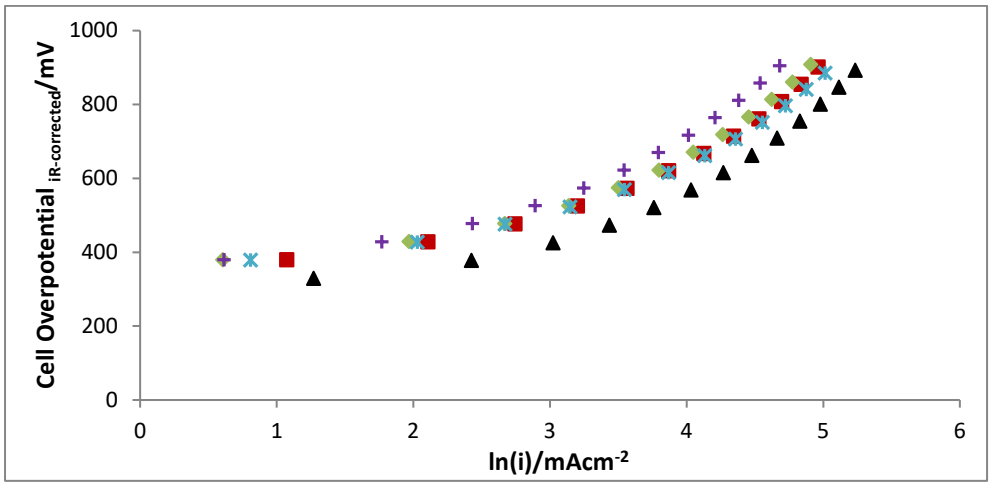

Figure 6.11. *iR-corrected Tafel plots for alkaline fuel cells, at 20 °C, containing Gortex electrodes coated with (1) ▲-$NiCo_2O_4$ (2) ■-$Mn_{1.5}Co_{1.5}O_4$ (3) ♦- $NiFe_2O_4$ (4) +-$Co_{0.5}Ni_{0.5}Fe_2O_4$ (5) X – Co_3O_4, as cathode (O_2 catalyst). Gortex coated with 10% Pt served as the anode (H_2 catalyst) in all cases. Electrolyte: 6 M KOH.*

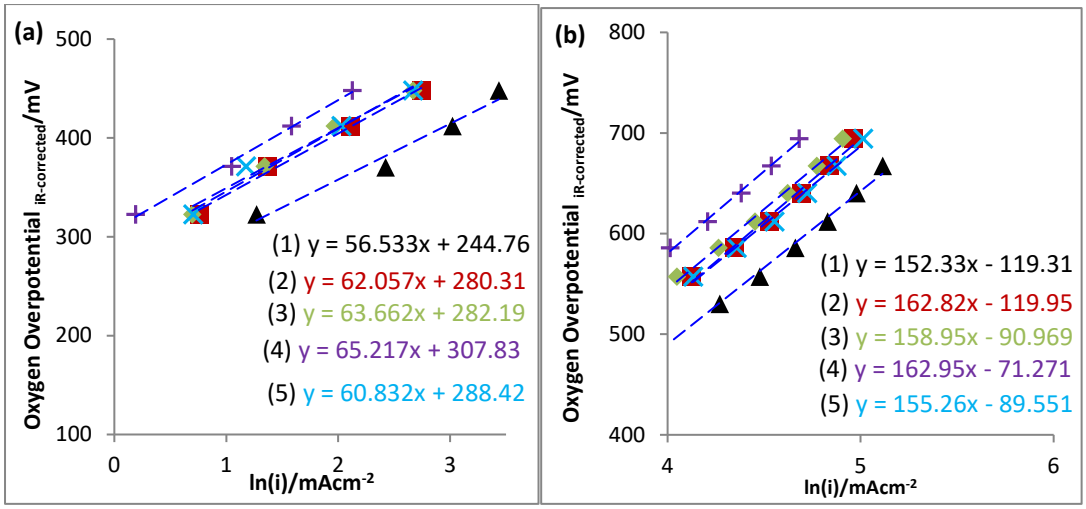

Figure 6.12. *iR-corrected Tafel plots at: (a) Low Current density (LCD), and (b) High Current Density (HCD) for alkaline fuel cells, at 20 °C, containing Gortex electrodes coated with (1) ▲-$NiCo_2O_4$ (2) ■-$Mn_{1.5}Co_{1.5}O_4$ (3) ♦- $NiFe_2O_4$ (4) +-$Co_{0.5}Ni_{0.5}Fe_2O_4$ (5) X –Co_3O_4, as cathode (O_2 catalyst). Gortex coated with 10% Pt served as the anode (H_2 catalyst) in all cases. The fitted straight lines have the general formula $y=b_{1/2}x+c$, where $b_{1/2}$ is the Tafel slope. Electrolyte: 6 M KOH.*

To compare the electrocatalytic activities of the fuel cells containing spinels as catalysts, Tafel slopes were also extracted from the polarization curves. Figure 6.11 shows the Tafel curves of the fuel cells. The curves were iR-corrected, following the method described for the perovskites. As with the perovskites, two Tafel slopes were calculated, b_1 at low current densities and b_2 at high current densities. Figure 6.12 shows that b_1 for the alkaline fuel cell with a $NiCo_2O_4$ catalyst on Gortex, was 57 mV dec^{-1}, which is low when compared to the use of Co_3O_4 as catalyst. This Tafel slope is in fair agreement with those obtained by Iwakura et al[79] but lower than reported in another work.[80]

Fuel cells with $NiFe_2O_4$ on Gortex cathodes gave lower b_1 values than previously reported $NiFe_2O_4$/graphene nanohybrid,[81,82] that were said to display enhanced three phase interfaces. Furthermore, the b_1 of the fuel cell with a $Mn_{1.5}Co_{1.5}O_4$ cathode was higher than the fuel cell

with a Co_3O_4 cathode, which might be due to low ORR activity of tetragonal structure of $Mn_{1.5}Co_{1.5}O_4$.[60]

Considering now b_2 from Table 6.2, i.e. the electrocatalytic activity for the ORR at high current densities, the fuel cells displayed the following order of activity deriving from their cathode catalysts: $NiCo_2O_4$ > Co_3O_4 > $NiFe_2O_4$ > $Mn_{1.5}Co_{1.5}O_4$ > $Co_{0.5}Ni_{0.5}Fe_2O_4$. This indicates that fuel cells with $NiCo_2O_4$ cathodes facilitated a faster electrochemical reaction at high current densities as well. The fuel cell with $Co_{0.5}Ni_{0.5}Fe_2O_4$ as cathode catalyst displayed the highest b_1 and b_2 values, and was therefore the least active catalyst for oxygen reduction; some literature sources[43] claim it to be a good ORR catalyst.

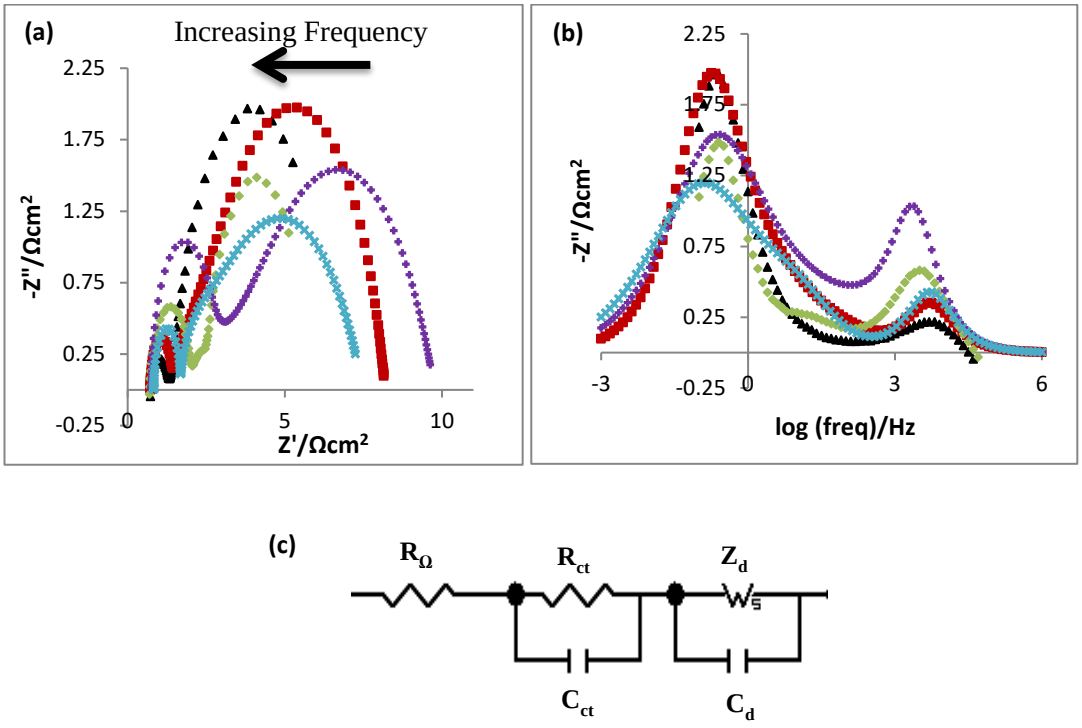

Figure 6.13. *(a) Nyquist and (b) Bode plots at 10 mA cm^{-2}, (c) Equivalent electric circuit used to model the Nyquist impedance data, for alkaline fuel cells, at 20 °C, containing Gortex electrodes coated with (1) ▲-$NiCo_2O_4$ (2) ■-$Mn_{1.5}Co_{1.5}O_4$ (3) ♦- $NiFe_2O_4$ (4) +-$Co_{0.5}Ni_{0.5}Fe_2O_4$ (5) X – Co_3O_4, as cathode (O_2 catalyst). Gortex coated with 10% Pt served as the anode (H_2 catalyst) in all cases. Electrolyte: 6 M KOH.*

Figure 6.13(a) and (b) depict the two-electrode Nyquist and Bode plots of the above cells, measured under galvanostatic conditions at 10 mA cm^{-2}. The Nyquist plots of experimental data are shown in Figure 6.13 (a). Figure 6.13 (c) shows the equivalent electrical circuit used to model the Nyquist spectra.

As was the case with fuel cells having perovskite ORR catalysts, Nyquist plots for fuel cells with spinel ORR catalysts also displayed two semicircular traces: a large, low frequency diffusion (Z_d) arc and a small, high frequency charge transfer arc (R_{ct}) (Figure 6.13 (a)).

Analysis of the galvanostatic electrochemical impedance spectra (GEIS) indicated (Table 6.4) that the fuel cell with $NiCo_2O_4$+CB+PTFE+Ni-mesh/Gortex as cathode, produced the lowest combination of R_{ct} (0.60 Ω cm^2) and Z_d (5.1 Ω cm^2). Substituting B sites by Ni/Mn in Co_3O_4, clearly diminishes the value of R_{ct} (from 0.85 Ω cm^2 to 0.60-0.68 Ω cm^2). It also lowers Z_d in the case of Ni substitution. Such low resistance values, deriving from efficient charge transfer during the ORR process, $NiCo_2O_4$ was the only spinel that delivered steady currents of 10 mA cm^{-2} for more than 1 h (Figure 6.10). The other spinels displayed much higher $R_{ct,}$ thereby exhibiting higher activation overpotentials of ~417 - 455 mV (Table 6.2).

The Bode plots in Figure 6.13(b) indicate that the impedance at high frequencies was the least for the fuel cell with the $NiCo_2O_4$ cathode and the greatest when the cathode contained $Co_{0.5}Ni_{0.5}Fe_2O_4$ as catalyst. Similarly, at low frequencies, the impedance was highest with $NiCo_2O_4$ or of $Mn_{1.5}Co_{1.5}O_4$ cathodes and lowest for the Co_3O_4 containing cathode. In addition, all the spinels displayed ohmic resistances similar to the Pt-based catalysts, as confirmed by the x-axis intercept, R_Ω, in the electrochemical impedance spectrum.

6.3.6 Fuel Cell Performance at 80 °C using the Best Performing Perovskite and Spinel as ORR Catalyst

Following the above work, we selected the best of the perovskite and spinels catalysts – namely, $La_{0.8}Sr_{0.2}MnO_3$ and $NiCo_2O_4$ – and studied the effect of temperature (80 °C) on their performance as Gortex-based ORR catalysts in fuel cells having the standard 10% Pt+CB+PTFE+Ni mesh/Gortex electrode as the anode.

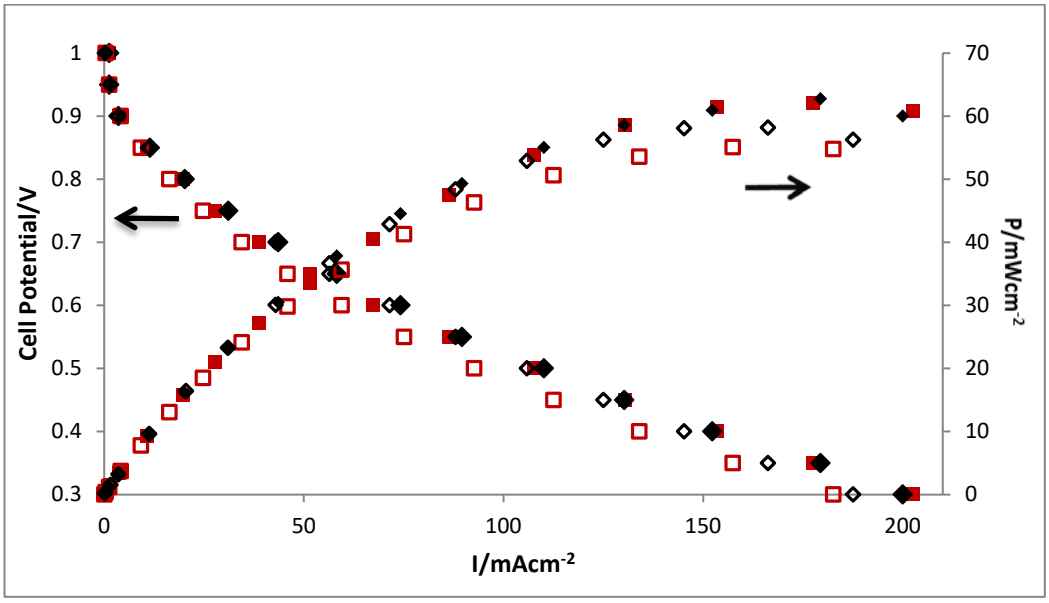

Figure 6.14. *Polarization curves (left axis) and power density curves (right axis) for alkaline fuel cells containing Gortex electrodes coated with: (1) □■ - $La_{0.8}Sr_{0.2}MnO_3$ and (2) ◊♦ - $NiCo_2O_4$ as cathode (O_2 catalyst). Gortex coated with 10% Pt served as the anode (H_2 catalyst) in all cases. Empty and filled markers denote 20 °C and 80 °C data respectively. Electrolyte: 6 M KOH.*

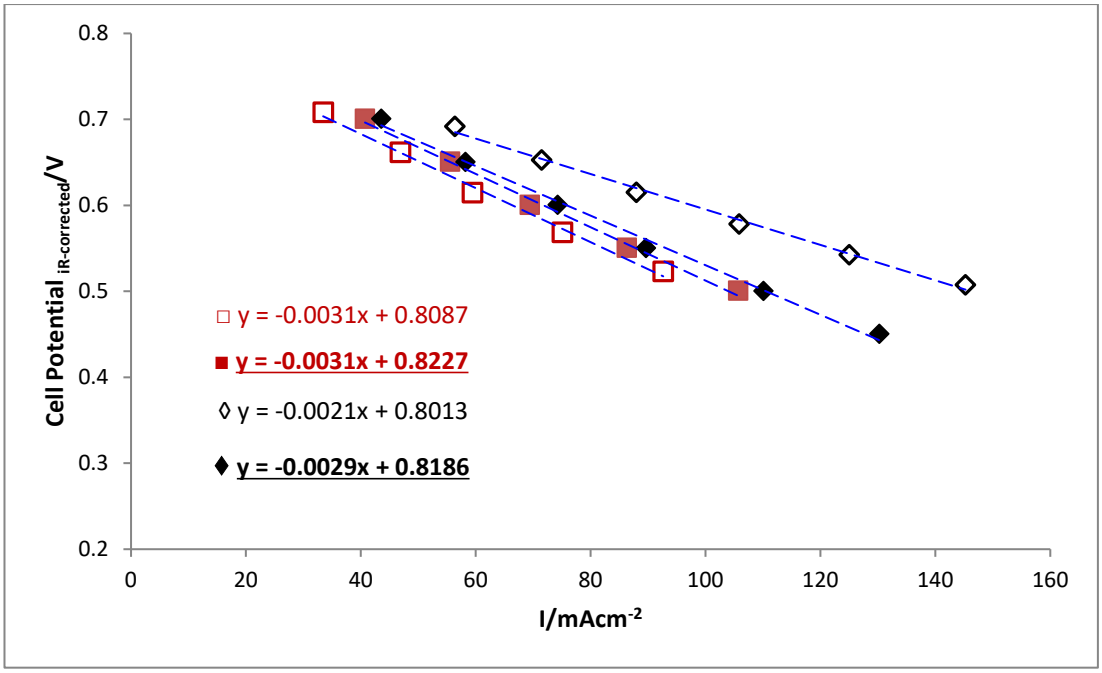

Figure 6.15. *Plots of cell potential vs current density (iR-corrected) showing straight line fits of the ohmic region for the alkaline fuel cells containing Gortex electrodes coated with (1) □■ - $La_{0.8}Sr_{0.2}MnO_3$ and (2) ◊♦ - $NiCo_2O_4$ as cathode (O_2 catalyst). Gortex coated with 10% Pt served as the anode (H_2 catalyst) in all cases. Empty and filled markers denote 20 °C and 80 °C data respectively. The straight lines fits have formula y=mx+c, where the intercept of the straight line with the y-axis, c, is the onset potential. The activation overpotentials (η_{act}) provided on the graph are the difference between the onset potential and E_{cell}^o (E_{cell}^o =1.23 V at 20 °C, E_{cell}^o =1.18 V at 80 °C). Electrolyte: 6 M KOH.*

Catalyst	η_{act} (V)		$V_{@10mAcm-2}$ (V)		R_Ω (Ω cm²)		R_{ct} (Ω cm²)		C_{ct} (μF)		Z_d (Ω cm²)		b_1 (mV dec^{-1})	
	20 ºC	80 ºC	20 ºC	80 ºC	20 ºC [a]	80 ºC [b]	20 ºC	80 ºC	20 ºC	80 ºC	20 ºC	80 ºC	20 ºC	80 ºC
$La_{0.8}Sr_{0.2}MnO_3$	0.421	0.357	0.851	0.89	0.78	1.38	0.63	0.24	34	78	5.1	1.5	60	43
$NiCo_2O_4$	0.429	0.361	0.851	0.86	0.73	0.967	0.6	0.29	83	148	5.3	1.81	57	51

[a] *3 mm inter-electrode gap* [b] *10 mm inter-electrode gap*

Table 6.3. *Parameters for a comparison of electrochemical activity for alkaline fuel cells containing Gortex electrodes coated with $La_{0.8}Sr_{0.2}MnO_3$ and $NiCo_2O_4$ as cathode (O_2 catalyst) at 20 ºC and 80 ºC. Gortex coated with 10% Pt served as the anode (H_2 catalyst) in all cases. Column titles: activation overpotential (η_{act}), Voltage at 10 mA cm^{-2} ($V_{@10mAcm-2}$), Tafel slope (b_1) (at lower current density (LCD)); from electrochemical impedance, ohmic resistance (R_Ω), charge transfer resistance (R_{ct}), double-layer capacitance within the catalyst layer (C_{ct}), diffusional resistance (Z_d).*

Catalyst	η_{act} (V)		$V_{@10mAcm-2}$ (V)		R_Ω (Ω cm²)		R_p (Ω cm²)		C_p (mF)		R_{ct} (Ω cm²)		$C_{CPE,ct}$ (mF)		b (mV dec^{-1})	
	20 ºC	80 ºC	20 ºC	80 ºC	20 ºC [a]	80 ºC [b]	20 ºC	80 ºC	20 ºC	80 ºC	20 ºC	80 ºC	20 ºC	80 ºC	20 ºC	80 ºC
IrO_2	0.358	0.331	1.52	1.43	1.01	1.03	0.26	0.30	8.36	1.0	4.34	3.68	28.7	13.9	139	125
$La_{0.8}Sr_{0.2}MnO_3$	0.395	0.301	1.60	1.38	0.90	1.19	0.36	0.22	0.14	1.45	6.84	2.82	27.1	17.5	93	97
$NiCo_2O_4$	0.348	0.245	1.58	1.28	0.73	0.97	0.55	0.20	0.08	2.0	5.65	2.34	25.8	21.2	124	70

[a] *3 mm inter-electrode gap* [b] *10 mm inter-electrode gap*

Table 6.4. *Parameters for a comparison of electrochemical activity for alkaline electrolysers containing Gortex electrodes coated with IrO_2, $La_{0.8}Sr_{0.2}MnO_3$ and $NiCo_2O_4$ as anode (O_2 catalyst) at 20 ºC and 80 ºC. Gortex coated with 10% Pt served as the cathode (H_2 catalyst) in all cases. Column titles: activation overpotential (η_{act}), Voltage at 10 mA cm^{-2} ($V_{@10mAcm-2}$), Tafel slope b; from electrochemical impedance, ohmic resistance (R_Ω), polarisation resistance of the catalysts (R_p), double-layer capacitance (C_p), charge transfer resistance (R_{ct}), and constant phase element of the catalysts layer ($C_{CPE,ct}$).*

The polarization curve of fuel cells fabricated with $La_{0.8}Sr_{0.2}MnO_3$ or $NiCo_2O_4$ (total loading = 11 mg cm^{-2} each) as cathode catalyst and 10% Pt as the anode catalyst (Pt loading = 0.05 mg of Pt per cm^2), produced, at 20 °C, a maximum power density of 55 mW cm^{-2} ($La_{0.8}Sr_{0.2}MnO_3$ as cathode catalyst) / 58 mW cm^{-2} ($NiCo_2O_4$ as cathode catalyst) at 0.35 V (Figure 6.14). This is ~56-59% of that generated by the best performing fuel cell of this thesis, which used 20% Pt-Pd (Pt loading = 0.1 mg of Pt-Pd per cm^2) as the cathode catalyst (~98 mW cm^{-2} as reported in Chapter 5).

Moreover, our Gortex-based fuel cell anodes had a tiny loading of 0.05 mg of Pt / cm^2 which is 60% less than the DOE target for precious metal loadings of less than or equal to 0.125 mg of Pt / cm^2.[83] The power density of the above fuel cell with $La_{0.8}Sr_{0.2}MnO_3$ as cathode catalyst, further, produced a 15% increase at 80 °C, when compared to 20 °C.

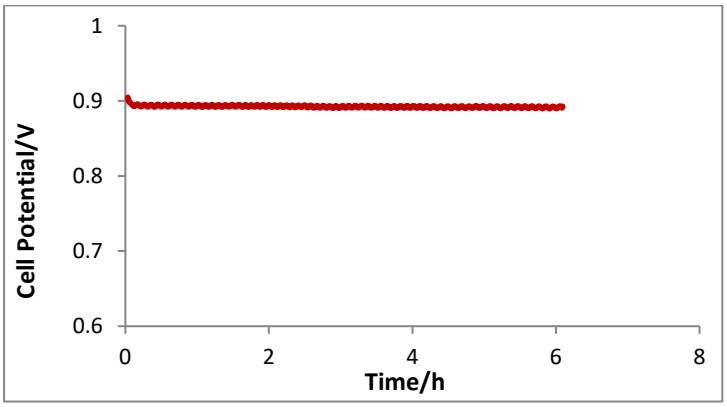

Figure 6.16. *Chronopotentiogram (CP) at 10 mA cm^{-2} and 80 °C for alkaline fuel cell containing Gortex electrode coated with — $La_{0.8}Sr_{0.2}MnO_3$, as cathode (O_2 catalyst). Gortex coated with 10% Pt served as the anode (H_2 catalyst). Electrolyte: 6 M KOH.*

As seen in Figure 6.14, the polarisation curves of the fuel cells containing $La_{0.8}Sr_{0.2}MnO_3$ or $NiCo_2O_4$ as cathode catalysts almost coincide with each other at current densities less than equal to 10 mA cm^{-2}, at 20 °C. However, when the temperature is increased to 80 °C, the cell with $La_{0.8}Sr_{0.2}MnO_3$ ORR catalyst recorded a positive shift in η_{act}, roughly by 15% of its

value at 20 °C. Consequently, it delivered a current of 10 mA cm^{-2} at close to 0.89 V, which is roughly a 5% increase from its value at 20 °C (Table 6.3).

To the best of our knowledge, this is a record high for any non-precious catalyst reported to date; it matches the performance of the 10% Pt on Vulcan XC72 catalyst as an anode. This fuel cell also exhibited a 20 mA cm^{-2} increase in current densities at 0.35 V from 20 °C to 80 °C.

By contrast, increasing the temperature to 80 °C had little to no effect on the comparable $NiCo_2O_4$ system, in terms of η_{act} and voltages recorded at lower current densities. However, at 80 °C and higher overpotentials (0.35 V), $NiCo_2O_4$ recorded an 8% increase in current density from 20 °C. The improvement in current densities with temperature for the above fuel cells can be attributed to faster kinetics and diffusion of reactants.[84-85]

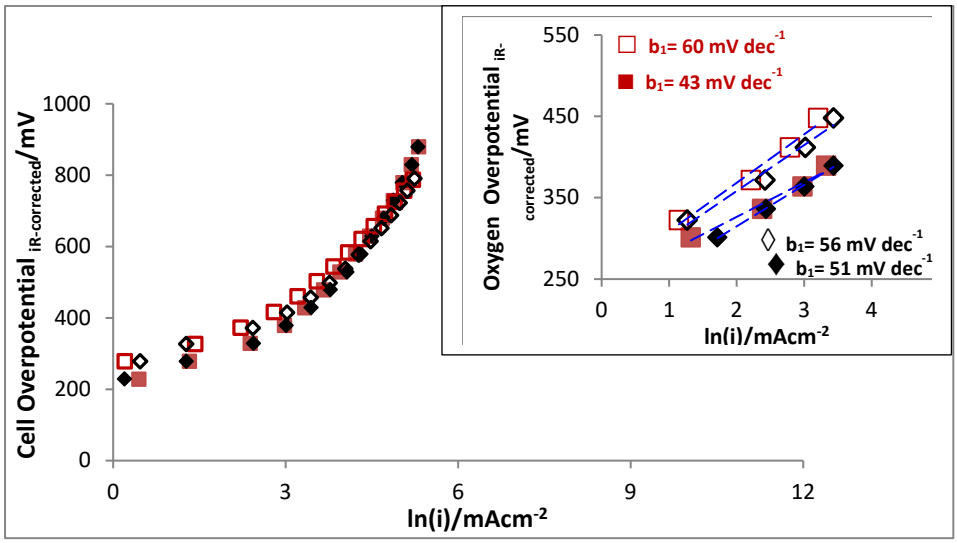

Figure 6.17. *iR-corrected Tafel plots and inset showing Tafel slopes calculated at low current density (LCD) for the alkaline fuel cells containing Gortex electrodes coated with (1) □■ - $La_{0.8}Sr_{0.2}MnO_3$ and (2) ◊♦ - $NiCo_2O_4$ as cathode (O_2 catalyst). Gortex coated with 10% Pt served as the anode (H_2 catalyst) in all cases. Empty and filled markers denote 20 °C and 80 °C data respectively. The straight line fits of the ohmic region shown in the inset have the formula $y=b_1x+c$, where m is Tafel slope. Electrolyte: 6 M KOH.*

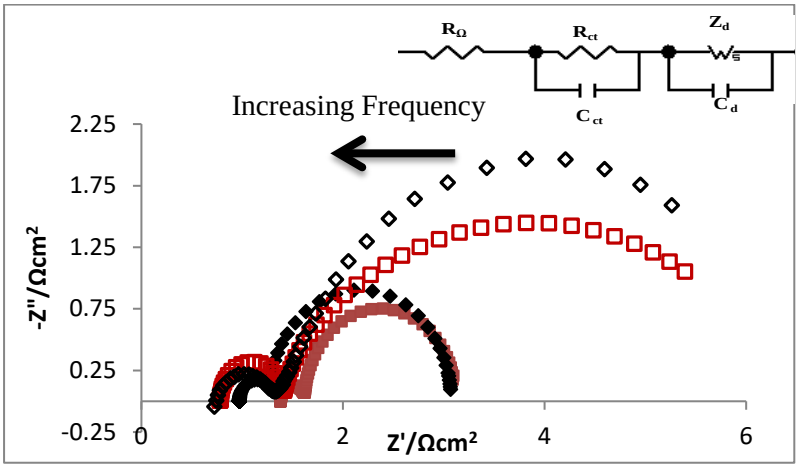

Figure 6.18. *Nyquist plot and inset showing the equivalent circuit used to model the data, for alkaline fuel cells containing Gortex electrodes coated with (1) □■ - $La_{0.8}Sr_{0.2}MnO_3$ and (2) ◊♦ - $NiCo_2O_4$ as cathode (O_2 catalyst). Gortex coated with 10% Pt served as the anode (H_2 catalyst) in all cases. Empty and filled markers denote 20 °C and 80 °C data respectively. Electrolyte: 6 M KOH.*

It is also worth noting that, as shown in Figure 6.17, b_1 exhibited a decline of 17 mV dec^{-1} for fuel cell with cathodes having $La_{0.8}Sr_{0.2}MnO_3$ as catalysts, when the temperature was increased to 80 °C. Fuel cell with $NiCo_2O_4$ as cathode catalyst also demonstrated a lower b_1 (51 mV dec^{-1}) at 80 °C, when compared to 20 °C. By contrast, fuel cell with a 20%Pt-Pd cathode catalyst (see Chapter 5), showed little change in b_1 on changing the operating temperature from 20 °C to 80 °C.

Tafel slopes were not calculated for the high overpotential regime as it appeared that these catalysts ($La_{0.8}Sr_{0.2}MnO_3$ and $NiCo_2O_4$) were not particularly stable at high current densities.

The galvanostatic electrochemical impedance spectroscopy data of the above gas diffusion electrodes at 80 °C was modelled using the equivalent circuit depicted in the inset of Figure 6.18. The individual data points in the Figure show the data as measured. The modelling

results are provided in Table 6.3. The ohmic resitance (R_Ω) from EIS increases when the fuel cell is tested at 80 °C, because the inter-electrode distance was changed from 3 mm to 10 mm when switching from 20 °C to 80 °C.

At 80 °C, the charge transfer resistance (R_{ct}) of the fuel cell containing $La_{0.8}Sr_{0.2}MnO_3$+CB+PTFE+Ni-mesh/Gortex as the cathode was 0.24 Ω cm^2 i.e., a decrease of 62% from the 20 °C value (Table 6.3). By contrast, the fuel cell containing 20wt% Pt-Pd +CB+PTFE+Ni-mesh/Gortex as cathode, produced only a 28% decrease from the 20 °C value when operated at 80 °C (see Chapter 5). Similarly, when operated at 80 °C, there was a 52% decrease in R_{ct}, from the 20 °C value when $NiCo_2O_4$+CB+PTFE+Ni-mesh/Gortex was used as cathode. Thus, temperature has a significant effect on the R_{ct} of both $La_{0.8}Sr_{0.2}MnO_3$ and $NiCo_2O_4$. Likewise, the mass transport diffusion resistance (Z_d) also decreased from 5.1 Ω cm^2 (at 20 °C) to 1.5 Ω cm^2 (at 80 °C), thus imparting the fuel cell with $La_{0.8}Sr_{0.2}MnO_3$ as ORR catalyst, a high and stable current density of 10 mA cm^{-2} for >6 h. In addition, the capacitance (C_{ct}) increased for both of the catalysts, confirming a better charge interaction with temperature increase.

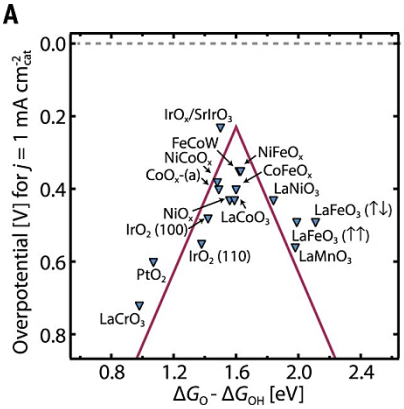

Figure 6.19. *Volcano plot for Oxygen Evolution activity as a function of oxygen binding energy on metal oxides.*[86] *Reproduced with permission from reference 85.*

6.3.7 Electrolyser Performance at Room Temperature (20 ºC) and 80 ºC, using Perovskites and Spinels as OER catalysts

Catalyst materials for the OER are generally metal oxides, so, volcano plots for the OER have been constructed for a wide variety of metal oxide surfaces (including rutile, perovskite and spinel). As can be seen from the volcano plot in Figure 6.19, $NiCo_2O_4$ turns out to be a better OER catalyst when compared to $LaMnO_3$ and IrO_2. Accordingly, it was decided to test $NiCo_2O_4$ as a Gortex based OER catalyst.

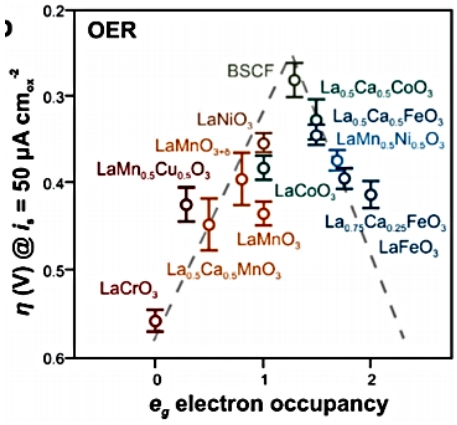

Figure 6.20. *Volcano plot for oxygen evolution activity as a function of oxygen binding energy on perovskites. BSCF stands for* $Ba_{0.5}Sr_{0.5}Co_{0.8}Fe_{0.2}O_{3-\delta}$ *.*[61] *Reproduced with permission from reference 61.*

A volcano-shaped dependency of the intrinsic OER activity on the e_g electron occupancy was previously also observed for 10 transition metal perovskite oxides (Figure 6.20).[30] Oxides having e_g occupancy of near unity exhibited maximum OER activity. As such, the high activity of $Ba_{0.5}Sr_{0.5}Co_{0.8}Fe_{0.2}O_{3-x}$ (BSCF) was predicted to be at least one order of magnitude higher than the IrO_2.[16] Accordingly, we selected $Ba_{0.5}Sr_{0.5}Co_{0.2}Fe_{0.8}O_3$ from amongst the available perovskites for OER electrolyser operation because according to the volcano plot shown in Figure 6.20, it was predicted to be the most active OER catalyst.

Accordingly, it was decided to test $Ba_{0.5}Sr_{0.5}Co_{0.2}Fe_{0.8}O_3$ and $La_{0.8}Sr_{0.2}MnO_3$ as Gortex based OER catalysts.

In the case of the OER, apart from the Tafel slope and exchange current density, there is no common parameter with which to compare the activities of different catalysts. Different kinetic parameters can be used in combination with the Tafel slope to define the activity of oxygen evolution catalysts.[87] In this work, we have used the Tafel slope (b), together with the voltage at 10 mA cm^{-2} to compare activity.

As already mentioned, in this research, we avoided any carbon black in the anode of electrolysers because of the likelihood of carbon corrosion under the strongly oxidising conditions present. In our studies of alkaline electrolysers utilizing perovskites and spinels, we therefore examined the following anodes:

- $La_{0.8}Sr_{0.2}MnO_3$+PTFE+Ni-mesh/Gortex,
- $Ba_{0.5}Sr_{0.5}Co_{0.2}Fe_{0.8}O_3$+PTFE+Ni-mesh/Gortex and
- $NiCo_2O_4$+PTFE+Ni-mesh/Gortex.

Note that none of these contained carbon black (CB). Each anode was coupled to a 10% Pt/CB+PTFE+Ni-mesh/Gortex cathode and the resulting cell characterised as an electrolyser.

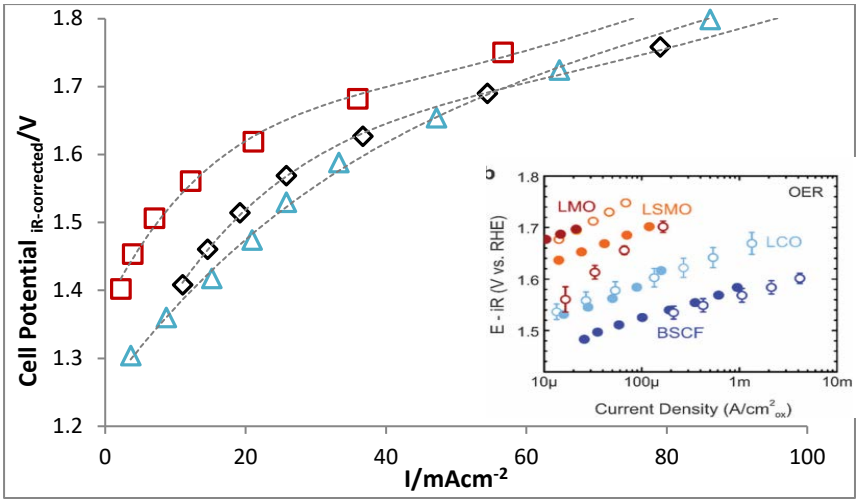

Figure 6.21. *iR-corrected current-voltage curves at 20 °C for alkaline electrolysers containing Gortex anodes (O_2 catalysts) coated with (1) □ - $La_{0.8}Sr_{0.2}MnO_3$ (2) ◊ - $NiCo_2O_4$ and (3) Δ - $Ba_{0.5}Sr_{0.5}Co_{0.2}Fe_{0.8}O_3$. Gortex coated with 10% Pt served as the cathode (H_2 catalyst) in all cases. Inset shows Tafel plots for oxygen evolution activity on perovskites; reproduced with permission from reference 61. Solid and open symbols represent activities of perovskites (LSMO- $La_{0.8}Sr_{0.2}MnO_{3-\delta}$, LMO- $LaMnO_{3\pm\delta}$, LCO- $LaCoO_3$, and BSCF- $Ba_{0.5}Sr_{0.5}Co_{0.8}Fe_{0.2}O_{3-\delta}$) tested in the form of thin films and powders respectively. Electrolyte: 6 M KOH.*

The current-voltage curves were obtained for the above mentioned electrolysers at 20 °C as well as at 80 °C (Figure 6. 22). At 20 °C, the minimum theoretical voltage (E^0_{cell}) for water splitting is 1.23 V whereas it is 1.183 V at 80 °C.[88] Ohmic losses from the electrolyte and the resistance of the Ni mesh are slightly more at the higher temperature, so that the iR-corrected minimum theoretical voltage for water-splitting by the cell at 80 °C, including the ohmic losses was 1.19 V.

Electrolysers with an anode containing $Ba_{0.5}Sr_{0.5}Co_{0.2}Fe_{0.8}O_3$ as catalyst exhibited a remarkably low cell activation overpotential (η_{act}) of only 260 mV at 20 °C (=1.49 $V_{iR\ corrected}$-1.23 V). The cell also recorded a b value of around 78 mV dec^{-1} at 20 °C as shown in the inset of Figure 6.21. But when the operating temperature of the same electrolyser was

increased to 80 °C, the value of b increased to 82 mV dec^{-1} and η_{act} increased to 352 mV (=1.53 $V_{iR\ corrected}$ – 1.19 V), indicating that $Ba_{0.5}Sr_{0.5}Co_{0.2}Fe_{0.8}O_3$ tends to degrade and perform poorly at 80 °C.

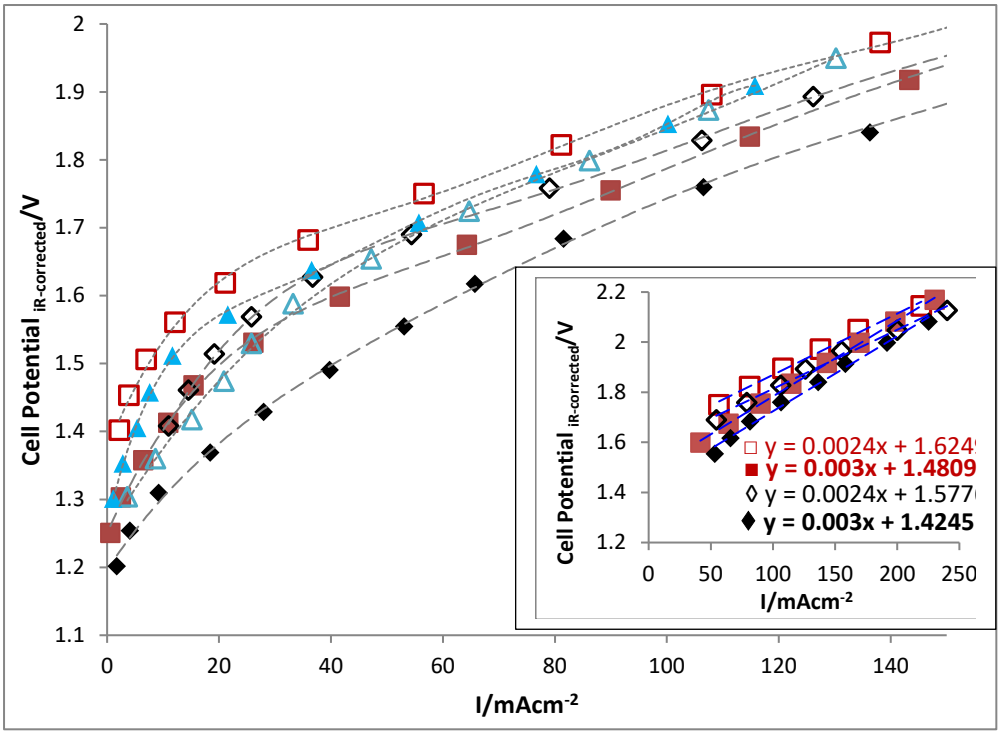

Figure 6.22. *iR-corrected current-voltage curves for alkaline electrolysers containing Gortex anodes coated with (1) □■ - $La_{0.8}Sr_{0.2}MnO_3$ (2) ◊♦ - $NiCo_2O_4$ and (3) △▲- $Ba_{0.5}Sr_{0.5}Co_{0.2}Fe_{0.8}O_3$. Gortex coated with 10% Pt served as the cathode (H_2 catalyst) in all cases. Empty and filled markers denote 20 °C and 80 °C data respectively. Inset shows straight line fits of the ohmic region, with formula y=mx+c, where the intercept of that line with the y-axis, c, is the onset potential. The activation overpotential (η_{act}) is the difference between the onset potential and E_{cell}^o (E_{cell}^o =1.23 V at 20 °C, E_{cell}^o =1.18 V at 80 °C). Electrolyte: 6 M KOH.*

The electrolyser operated at 20 °C with $La_{0.8}Sr_{0.2}MnO_3$+PTFE+Ni-mesh/Gortex as anode recorded a Tafel slope of 93 mV dec^{-1}, close to value[61] shown in the inset of Figure 6.21 with a η_{act} of 395 mV. In contrast to the electrolyser with the $Ba_{0.5}Sr_{0.5}Co_{0.2}Fe_{0.8}O_3$ anode, that with the $La_{0.8}Sr_{0.2}MnO_3$ anode at 80 °C, displayed a diminished η_{act} and a significantly

lower potential of 1.38 V at a steady current of 10 mA cm^{-2} (see Table 6.4 and Figure 6.23). As noted in Chapter 4, the regular oscillations observed in Figure 6.23 derived from the strongly endothermic nature of the electrolyser cell when operated at 10 mA/cm^2. The cell fought a constant battle with the heater-controller in the surrounding temperature-controlled water bath, and this resulted in temperature oscillations of ca. ±5 °C, which created the voltage swings.

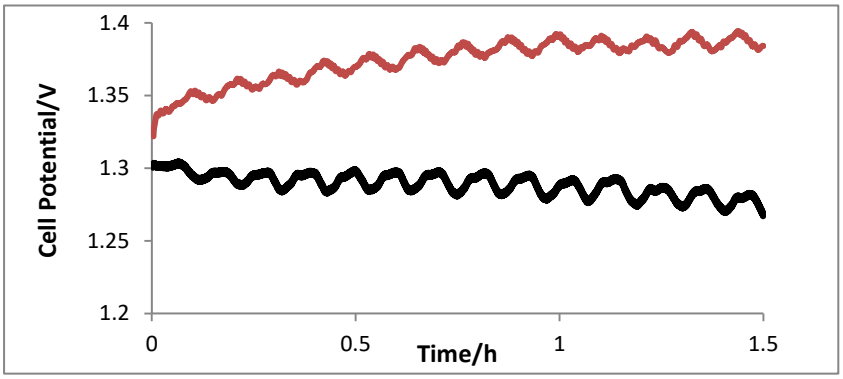

Figure 6.23. *Chronopotentiogram (CP) at 10 mA cm^{-2} and 80 °C for alkaline electrolysers containing Gortex anodes coated with* — *$La_{0.8}Sr_{0.2}MnO_3$ and* — *$NiCo_2O_4$. Gortex coated with 10% Pt served as the cathode (H_2 catalyst) in all cases. Electrolyte: 6 M KOH.*

When $NiCo_2O_4$ was tested as an anode catalyst at 20 °C, it exhibited an even lower η_{act} of 348 mV. The overpotential for $NiCo_2O_4$ for OER at 10 mA cm^{-2} was found earlier to be 360 mV and the Tafel slope to be 70 mV dec^{-1}.[89] Upon operating the electrolyser with $NiCo_2O_4$ at 80 °C, the η_{act} dropped to a low value of 245 mV. The electrolyser also exhibited a remarkably low potential of 1.28±1 V at a steady current of 10 mA cm^{-2} (see Table 6.4 and Figure 6.23).

Further tests were conducted to confirm that the currents of 10 mA cm^{-2} in Figure 6.23 were due to water electrolysis. The gases generated by the cathode (after 1 h of operation), were collected in upturned measuring cylinders filled with water, within a second water bath. As

noted in Chapter 4, at 10 mA cm^{-2}, a water electrolysis cell should produce 3.04 mL of hydrogen gas (at cathode) and 1.52 mL of oxygen (at anode) over 40 min. With this view, experiments were conducted at 9.5 and 13.0 mA cm^{-2} on electrolysers containing $La_{0.8}Sr_{0.2}MnO_3$ and $NiCo_2O_4$ as anode catalysts. The volume of hydrogen gas collected from the cathode was found to be 82.6% and 91.1% of the amount expected. An attached gas chromatograph (GC) confirmed that the sole gas produced was hydrogen.

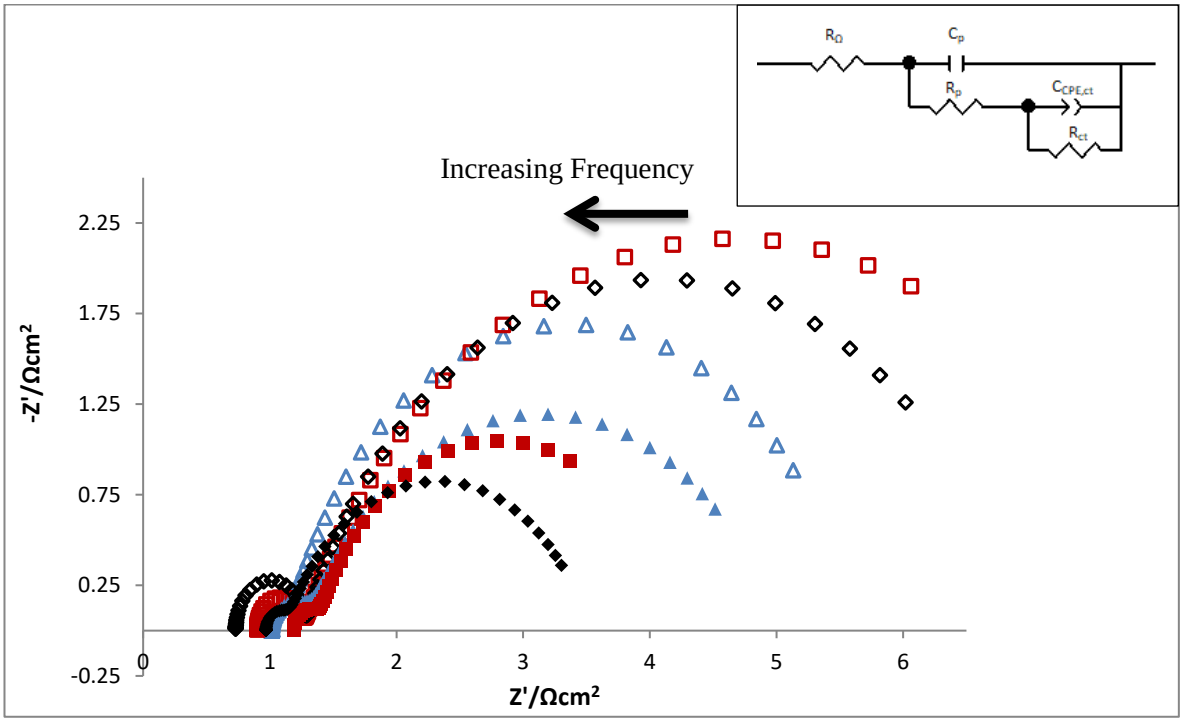

Figure 6.24. *Nyquist plot and inset showing the equivalent circuit used to model the data for alkaline electrolysers containing Gortex anodes coated with (1) □■ - $La_{0.8}Sr_{0.2}MnO_3$, (2) ◊♦ - $NiCo_2O_4$ and (3) ⊿▲ -IrO_2. Gortex coated with 10% Pt served as the cathode (H_2 catalyst) in all cases. Empty and filled markers denote 20 °C and 80 °C data respectively. Electrolyte: 6 M KOH.*

From Table 6.4, it is clear that, at 80 °C, the electrolysers with $La_{0.8}Sr_{0.2}MnO_3$+PTFE+Ni-mesh/Gortex and $NiCo_2O_4$+PTFE+Ni-mesh/Gortex anodes outperformed the comparable electrolyser with an IrO_2+PTFE+Ni-mesh/Gortex anode (total loading = 15.1 mg cm^{-2}) both in terms of η_{act} as well as stability of the voltage required to deliver 10 mA cm^{-2}. The

overpotential required to obtain a current density of 10 mA cm^{-2} for the electrolyser with an IrO_2 anode catalyst was 210 mV (=1.4 $V_{iR\ corrected}$ − 1.19 V) (See Chapter 5). The electrolysers having, as anode catalysts, $La_{0.8}Sr_{0.2}MnO_3$ (catalyst loading = 20 mg cm^{-2}) and $NiCo_2O_4$ (catalyst loading = 26 mg cm^{-2}), displayed excellent catalytic activity for the OER with overpotentials of 200 mV and 100 mV at a fixed current density of 10 mA cm^{-2}, respectively. Thus, $La_{0.8}Sr_{0.2}MnO_3$ and $NiCo_2O_4$ show remarkable OER electrochemical activity, which is about 9% and 26% less in η_{act} than that of IrO_2. This clearly indicates an improvement in the reaction kinetics (decrease in activation polarization) for $La_{0.8}Sr_{0.2}MnO_3$ and, in particular, $NiCo_2O_4$.

The GEIS data of the above electrolysers at 20 ºC and 80 ºC is shown in the Nyquist plots in Figure 6.24. The experimental data in the Nyquist plots for the electrolysers with $La_{0.8}Sr_{0.2}MnO_3$+PTFE+Ni-mesh/Gortex and $NiCo_2O_4$+PTFE+Ni-mesh/Gortex anodes was modelled using the equivalent circuit shown in inset of inset of Figure 6.24. In equivalent circuits, C_p elements model the double layer capacitance, while R_Ω represents the ohmic resistance. The resistive elements R_p (polarisation resistance) and R_{ct} (charge transfer resistance) are related to the kinetics of the interfacial charge transfer reaction. $Q_{CPE,ct}$ is the constant phase element of the catalysts layer, which in parallel with the resistance, R_{ct}, correctly models the relaxation of the charge associated with the adsorbed intermediate.[90,91] As discussed in Chapter 2, $Q_{CPE,ct}$ is then used to estimate the double layer capacitance $C_{CPE,ct}$. The values of the above parameters are shown in in Table 6.4.

It is interesting to see that, upon increasing the operating temperature to 80 ºC, the electrolysers with the $NiCo_2O_4$+PTFE+Ni-mesh/Gortex or $La_{0.8}Sr_{0.2}MnO_3$+PTFE+Ni-mesh/Gortex anodes, recorded ~59% decrease in the charge transfer resistance, R_{ct}, from the 20 ºC values. The electrolyser with $NiCo_2O_4$ displayed a significantly lower R_{ct} of 2.34 Ω cm^2 when compared to other metal oxides based anodes. This indicated that a faster charge transfer occurred after increasing the temperature of electrolyser to 80 ºC. As already seen in

Figure 6.22, at 1.4 V, the current generated for the electrolyer with the $NiCo_2O_4$+PTFE+Ni-mesh/Gortex anode at 80 ^oC was almost 3-times that at 20 ^oC, thereby increasing the volume of oxygen bubbles generated. For this reason, $C_{CPE,ct}$, which correlates with the accessible surface area, saw a decrease and this can be attributed to the formation of more bubbles blocking active sites.[92] This was true for other two (containing $La_{0.8}Sr_{0.2}MnO_3$ and IrO_2 as anode catalyst) electrolysers as well. The $NiCo_2O_4$+PTFE+Ni-mesh/Gortex electrolyser also recorded the lowest combination of interfacial charge transfer (R_p + R_{ct}). A possible explanation of the extraordinary OER activities at 80 ^oC of these electrolysers with Gortex-based gas diffusion electrodes is described in detail in Chapter 4.

6.3.8 Efficient Alkaline-based Discrete Regenerative Fuel Cell

As previously noted, an increase in temperature decreases the overpotentials for both oxygen reduction and evolution reactions.[93] Therefore, operating both alkaline fuel cells and alkaline water electrolysers at 80 ^oC will lower the potential difference between the oxygen reduction and evolution processes, thereby increasing the round trip efficiency of an alkaline-based DRFC.

The best performing combination of electrolyser and fuel cell at 80 ^oC, involves the alkaline water electrolyser with $NiCo_2O_4$+PTFE+Ni-mesh/Gortex as anode and 10% Pt/CB+PTFE+Ni-mesh/Gortex as cathode, and the alkaline fuel cell with $La_{0.8}Sr_{0.2}MnO_3$+CB+PTFE+Ni-mesh/Gortex as cathode and 10% Pt/CB+PTFE+Ni-mesh/Gortex as anode. The anode in the electrolyser contained 26 mg cm^{-2} of $NiCo_2O_4$ as catalyst whereas, the cathode in the fuel cell contained 11 mg cm^{-2} of $La_{0.8}Sr_{0.2}MnO_3$ as catalyst.

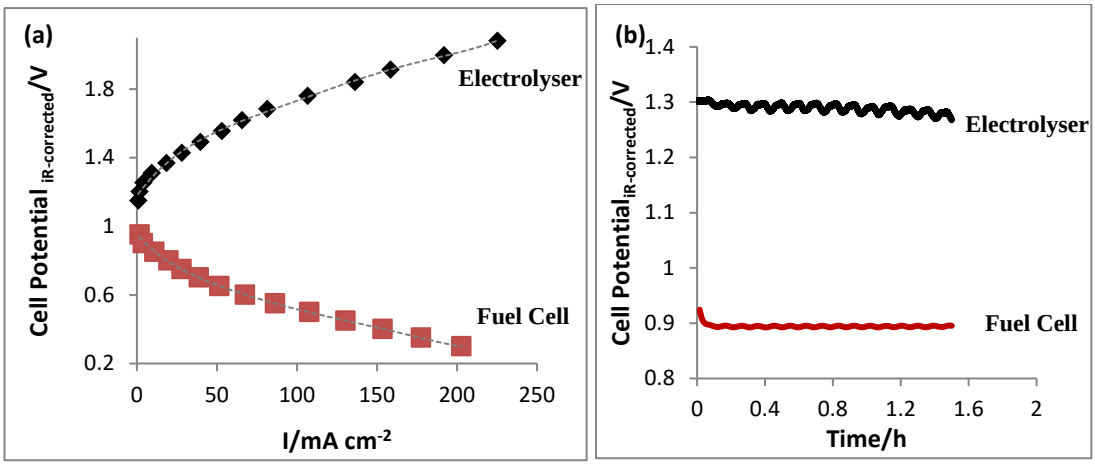

Figure 6.25. *(a) Current-voltage curves (iR-corrected) and (b) chronopotentiograms (iR-corrected) at 80 °C for alkaline fuel cells containing Gortex electrodes coated with* ■ *- $La_{0.8}Sr_{0.2}MnO_3$ at 80 °C, as cathode (O_2 catalyst) and alkaline water electrolysers containing Goretx electrodes coated with* ♦ *- $NiCo_2O_4$ as anode (O_2 catalyst). Gortex coated with 10% Pt served as the H_2 catalyst in both cases. Electrolyte: 6 M KOH.*

The electrolyser had an iR-uncorrect onset potential of 1.31 V and generated a stable current of 10 mA cm^{-2} after 1 h at a very low overpotential of 0.08 V ($1.27V_{iR\ corrected}$ -1.19V). This compares well with the hitherto most active reported alkaline (water electrolyser, which employed a Raney-Ni(Mo)+PTFE cathode and a Raney-Ni(Fe)+PTFE anode[94] to achieve an overall overpotential of 0.21 V at 10 mA cm^{-2} at 80 °C ($1.41V_{iR\ corrected}$ -1.19V)..

The energy efficiency (LHV) of the above electrolyser operating at 10 mA cm^{-2}, was 94%, which is 11% more than the electrolysers employing Gortex-based IrO_2 as anode catalyst, and roughly 34% more the 70% efficiencies achieved by typical conventional AFCs.[95-96] The Tafel slope also decreased to 70 mV dec^{-1}, which is the lowest recorded for $NiCo_2O_4$.[80] This improvement in efficiency is likely due to the Gortex substrate, which, as discussed in Chapter 4, appears to diminish the overpotential for oxygen formation during electrolysis at temperatures of 80 °C and above.

Combining the above electrolyser with the above, similarly efficient alkaline fuel cell, utilizing $La_{0.8}Sr_{0.2}MnO_3$+CB+PTFE+Ni-mesh/Gortex as cathode, provides for a DRFC with a notional round trip electrical efficiency after 1 h at 10 mA/cm^2 in each direction, of 70.9%, assuming complete conservation of heat (given the 0.9 $V_{iR\ corrected}$ in fuel cell mode at 80 ^oC, from Figure 6.25 (b)). This performance exceeds the performance achieved by the regenerative PEM fuel cell–electrolyser of Ioroi and colleagues,[97] which yielded a round-trip energy efficiency at 80 ^oC and 10 mA cm^{-2} in each direction, of 66.4%.

6.4 Conclusion

In this chapter, the operation of Gortex-based gas diffusion electrodes layered with well-known, conventional metal oxides as catalysts, in alkaline-based fuel cells, electrolysers, and DRFCs, was examined. It was found that metal oxides (both perovskites and spinels) display promising bifunctional activity for both OER and ORR. However, the highest ORR activity was seen for perovskites and the highest OER activity was seen for spinels. A desktop alkaline fuel cell with aqueous 6 M KOH electrolyte, having a $La_{0.8}Sr_{0.2}MnO_3$+CB+PTFE+Ni-mesh/Gortex cathode and a 10% Pt+CB+PTFE+Ni mesh/Gortex anode, generated current and power densities of 157 mA cm^{-2} and 55 mW cm^{-2}, respectively, at 0.35 V, at 20 ^oC. At 80 ^oC, the same fuel cell displayed a current density and power density that was 14% and 15% higher, respectively, at 0.35V. The energy efficiency (LHV) of this alkaline fuel cell, utilizing Gortex-based non precious $La_{0.8}Sr_{0.2}MnO_3$ as cathode catalyst, was 76% (=0.9/1.18 x 100) at 10 mA cm^{-2} and 80 ^oC. This efficiency is similar to that obtained from a similar alkaline fuel cell utilizing Gortex-based 20% Pt-Pd as cathode catalyst. The alkaline fuel cells also recorded very low tafel slopes at low current densities indicating the faster electrochemical kinetics due to the better three phase interaction obtained by using Gortex as GDEs. The electrochemical activity, for both the ORR and OER, of metal oxides, as predicted by volcano plots, correlated with the

electrochemical activity determined using electrochemical impedance spectroscopy. The parameters obtained by modelling an equivalent electrical circuit to experimental impedance data could be used to explain the location of the different catalysts on the volcano plots. The most important parameters were the charge transfer resistance (R_{ct}) and diffusional resistance (Z_d) in the case of the ORR catalysts and the charge transfer resistance (R_{ct}) and polarisation resistance (R_p) in the case of the OER catalyst. These could be used as a guideline for selecting appropriate catalysts for cathodes in fuel cells and anodes in electrolysers.

As discussed previously, alkaline electrolyser is a well-developed technology with lifetimes of 100 000 h and energy efficiencies ranging from 61% to 71%.[96] However, if we replace traditional gas diffusion electrodes with Gortex-based ones and employ conventional metal oxides as catalysts (like $NiCo_2O_4$), major inefficiencies associated with the overpotentials for hydrogen and oxygen formation are notably reduced. This enables Gortex-based alkaline electrolysers to achieve higher energy efficiencies, close to 94% relative to LHV, at 10 mA cm^{-2}. This is around 12% more than electrolysers employing Gortex-based IrO_2 as anode catalyst.

To the best of our knowledge, the lowest published RFC potential at 10 mA cm^{-2} is held by Ioroi and colleagues,[98] who reported a unitized, regenerative PEM fuel cell–electrolyser utilizing Pt black, that, at 80 ^oC, yielded 10 mA cm^{-2} at 1.40 V in electrolyser mode. In fuel cell mode at 80 ^oC, the same cell generated 0.93 V at 10 mA cm^{-2} in the opposite direction, giving it a round-trip energy efficiency at 10 mA cm^{-2} in each direction, of 66.4%.[98]

Higher efficiencies could, however, be achieved by combining the best performing alkaline Gortex-based fuel cell of this Chapter, utilizing $La_{0.8}Sr_{0.2}MnO_3$ as ORR catalyst, with the best performing alkaline Gortex-based electrolyser of this Chapter, utilizing $NiCo_2O_4$ as OER catalyst, with 10% Pt on Vulcan XC72 as HOR and HER catalysts in each of the fuel

cell and electrolyser. The resulting, alkaline-based DRFC achieved round-trip energy efficiencies of 70.9%, at 80 ºC and10 mA cm^{-2} in each direction, assuming complete conservation of heat. The present Chapter describes a new approach which employs the unique properties of Gortex as electrode substrates and Earth-abundant metal oxides as oxygen reducing and evolving catalysts, to amplify the efficiency of mature technologies like alkaline fuel cells and alkaline water electrolysers.

References

1. Sunarso, J.; Glushenkov, A. M.; Torriero, A. A. J.; Howlett, P. C.; Chen, Y.; MacFarlane, D. R.; Forsyth, M., *Journal of the Electrochemical Society* **2013,** *160* (1), H74-H79.
2. Lu, Y.-C.; Xu, Z.; Gasteiger, H. A.; Chen, S.; Hamad-Schifferli, K.; Shao-Horn, Y., *J. Am. Chem. Soc.* **2010,** *132* (35), 12170-12171.
3. Han, X.; Cheng, F.; Zhang, T.; Yang, J.; Hu, Y.; Chen, J., *Adv. Mater.* **2014,** *26* (13), 2047-2051.
4. Sasikala, N.; Ramya, K.; Dhathathreyan, K. S., *Energy Conversion and Management* **2014,** *77*, 545-549.
5. Jörissen, L., *J. Power Sources* **2006,** *155* (1), 23-32.
6. O'Hayre, R.; Cha, S.-W.; Colella, W.; Prinz, F. B., John Wiley & Sons, Inc: 2016; pp 77-116.
7. van Buren, F. R.; Broers, G. H. J.; Boesveld, C.; Bouman, A. J., *Journal of Electroanalytical Chemistry* **1978,** *87* (3), 381-388.
8. Karlsson, G., *Electrochim. Acta* **1985,** *30* (11), 1555-1561.
9. Kahoul, A.; Hammouche, A.; Nâamoune, F.; Chartier, P.; Poillerat, G.; Koenig, J. F., *Mater. Res. Bull.* **2000,** *35* (12), 1955-1966.

10. El Baydi, M.; Tiwari, S. K.; Singh, R. N.; Rehspringer, J.-L.; Chartier, P.; Koenig, J. F.; Poillerat, G., *Journal of Solid State Chemistry* **1995,** *116* (1), 157-169.
11. Hammouche, A.; Kahoul, A.; Sauer, D. U.; De Doncker, R. W., *J. Power Sources* **2006,** *153* (2), 239-244.
12. Meadowcroft, D. B., *Nature* **1970,** *226* (5248), 847-848.
13. Bockris, J. O.; Otagawa, T., *The Journal of Physical Chemistry* **1983,** *87* (15), 2960-2971.
14. Hyodo, T.; Shimizu, Y.; Miura, N.; Yamazoe, N., *Electrochemistry (Tokyo, Japan)* **1994,** *62*, 158.
15. Hyodo, T.; Miura, N.; Yamazoe, N. 1995; pp 79-84.
16. Suntivich, J.; Gasteiger, H. A.; Yabuuchi, N.; Nakanishi, H.; Goodenough, J. B.; Shao-Horn, Y., *Nat Chem* **2011,** *3* (7), 546-550.
17. Sunarso, J.; Torriero, A. A. J.; Zhou, W.; Howlett, P. C.; Forsyth, M., *The Journal of Physical Chemistry C* **2012,** *116* (9), 5827-5834.
18. Du, Z.; Yang, P.; Wang, L.; Lu, Y.; Goodenough, J. B.; Zhang, J.; Zhang, D., *J. Power Sources* **2014,** *265*, 91-96.
19. Zhang, D.; Song, Y.; Du, Z.; Wang, L.; Li, Y.; Goodenough, J. B., *J. Mater. Chem. A* **2015,** *3* (18), 9421-9426.
20. Hyodo, T.; Hayashi, M.; Miura, N.; Yamazoe, N., *Journal of the Electrochemical Society* **1996,** *143* (11), L266-L267.
21. Tulloch, J.; Donne, S. W., *J. Power Sources* **2009,** *188* (2), 359-366.
22. Stoerzinger, K. A.; Lü, W.; Li, C.; Ariando; Venkatesan, T.; Shao-Horn, Y., *The Journal of Physical Chemistry Letters* **2015,** *6* (8), 1435-1440.
23. Zhu, Y.; Zhou, W.; Yu, J.; Chen, Y.; Liu, M.; Shao, Z., *Chem. Mater.* **2016,** *28* (6), 1691-1697.
24. Jin, C.; Cao, X.; Zhang, L.; Zhang, C.; Yang, R., *Journal of Power Sources* **2013,** *241* (Supplement C), 225-230.
25. Lu, F.; Sui, J.; Su, J.; Jin, C.; Shen, M.; Yang, R., *J. Power Sources* **2014,** *271*, 55-59.

26. Lu, F.; Wang, Y.; Jin, C.; Li, F.; Yang, R.; Chen, F., *J. Power Sources* **2015,** *293*, 726-733.
27. Bucher, E.; Egger, A.; Ried, P.; Sitte, W.; Holtappels, P., *Solid State Ionics* **2008,** *179* (21), 1032-1035.
28. Jung, J.-I.; Edwards, D., 2012; Vol. 32, p 3733–3743.
29. Malkhandi, S.; Trinh, P.; Manohar, A. K.; Jayachandrababu, K. C.; Kindler, A.; Surya Prakash, G. K.; Narayanan, S. R., *Journal of The Electrochemical Society* **2013,** *160* (9), F943-F952.
30. Suntivich, J.; May, K. J.; Gasteiger, H. A.; Goodenough, J. B.; Shao-Horn, Y., *Science* **2011,** *334* (6061), 1383-1385.
31. Jung, J.-I.; Risch, M.; Park, S.; Kim, M. G.; Nam, G.; Jeong, H.-Y.; Shao-Horn, Y.; Cho, J., *Energy Environ. Sci* **2016,** *9* (1), 176-183.
32. Malkhandi, S.; Trinh, P.; Manohar, A. K.; Manivannan, A.; Balasubramanian, M.; Prakash, G. K. S.; Narayanan, S. R., *The Journal of Physical Chemistry C* **2015,** *119* (15), 8004-8013.
33. Kim, J.; Yin, X.; Tsao, K.-C.; Fang, S.; Yang, H., *J. Am. Chem. Soc.* **2014,** *136* (42), 14646-14649.
34. Yagi, S.; Yamada, I.; Tsukasaki, H.; Seno, A.; Murakami, M.; Fujii, H.; Chen, H.; Umezawa, N.; Abe, H.; Nishiyama, N.; Mori, S., **2015,** *6*, 8249.
35. Hamdani, M.; Singh, R. N.; Chartier, P., *Int. J. Electrochem. Sci.* **2010,** *5*, 556.
36. Ortiz, J.; Gautier, J. L., *Journal of Electroanalytical Chemistry* **1995,** *391* (1-2), 111-118.
37. Ríos, E.; Reyes, H.; Ortiz, J.; Gautier, J. L., *Electrochim. Acta* **2005,** *50* (13), 2705-2711.
38. Restovic, A.; Ríos, E.; Barbato, S.; Ortiz, J.; Gautier, J. L., *Journal of Electroanalytical Chemistry* **2002,** *522* (2), 141-151.
39. Liang, Y.; Li, Y.; Wang, H.; Zhou, J.; Wang, J.; Regier, T.; Dai, H., *Nat Mater* **2011,** *10* (10), 780-786.

40. Xu, J.; Gao, P.; Zhao, T. S., *Energy & Environmental Science* **2012,** *5* (1), 5333-5339.
41. Neburchilov, V.; Wang, H.; Martin, J. J.; Qu, W., *J. Power Sources* **2010,** *195* (5), 1271-1291.
42. Rios, E.; Gautier, J. L.; Poillerat, G.; Chartier, P., *Electrochimica Acta* **1998,** *44* (8), 1491-1497.
43. Zhao, X.; Fu, Y.; Wang, J.; Xu, Y.; Tian, J.-H.; Yang, R., *Electrochimica Acta* **2016,** *201* (Supplement C), 172-178.
44. Li, Y.; Hasin, P.; Wu, Y., *Advanced Materials* **2010,** *22* (17), 1926-1929.
45. Liu, Z.-Q.; Xu, Q.-Z.; Wang, J.-Y.; Li, N.; Guo, S.-H.; Su, Y.-Z.; Wang, H.-J.; Zhang, J.-H.; Chen, S., *Int. J. Hydrogen Energy* **2013,** *38* (16), 6657-6662.
46. Xiao, Y.; Hu, C.; Qu, L.; Hu, C.; Cao, M., *Chem. Eur. J.* **2013,** *19* (42), 14271-14278.
47. Liu, Z.-Q.; Xiao, K.; Xu, Q.-Z.; Li, N.; Su, Y.-Z.; Wang, H.-J.; Chen, S., *RSC Advances* **2013,** *3* (13), 4372-4380.
48. Lu, B.; Cao, D.; Wang, P.; Wang, G.; Gao, Y., *Int. J. Hydrogen Energy* **2011,** *36* (1), 72-78.
49. Cui, B.; Lin, H.; Li, J.-B.; Li, X.; Yang, J.; Tao, J., *Adv. Funct. Mater.* **2008,** *18* (9), 1440-1447.
50. Yang, J.; Li, J.; Lin, H.; Yang, X.; Tong, X.; Guo, G., *J. Appl. Electrochem.* **2006,** *36* (8), 945-950.
51. Garg, N.; Basu, M.; Upadhyaya, K.; Shivaprasad, S. M.; Ganguli, A. K., *RSC Advances* **2013,** *3* (46), 24328-24336.
52. Chien, H.-C.; Cheng, W.-Y.; Wang, Y.-H.; Wei, T.-Y.; Lu, S.-Y., *Journal of Materials Chemistry* **2011,** *21* (45), 18180-18182.
53. Srivastava, M.; Elias Uddin, M.; Singh, J.; Kim, N. H.; Lee, J. H., *Journal of Alloys and Compounds* **2014,** *590*, 266-276.
54. Chen, S.; Qiao, S.-Z., *ACS Nano* **2013,** *7* (11), 10190-10196.
55. Lee, D. U.; Kim, B. J.; Chen, Z., *J. Mater. Chem. A* **2013,** *1* (15), 4754-4762.

56. Menezes, P. W.; Indra, A.; Sahraie, N. R.; Bergmann, A.; Strasser, P.; Driess, M., *ChemSusChem* **2015,** *8* (1), 164-171.

57. Lee, E.; Jang, J.-H.; Kwon, Y.-U., *Journal of Power Sources* **2015,** *273* (Supplement C), 735-741.

58. Ma, T. Y.; Dai, S.; Jaroniec, M.; Qiao, S. Z., *Chem. Eur. J.* **2014,** *20* (39), 12669-12676.

59. Cheng, F.; Shen, J.; Peng, B.; Pan, Y.; Tao, Z.; Chen, J., *Nat Chem* **2011,** *3* (1), 79-84.

60. Liang, Y.; Wang, H.; Zhou, J.; Li, Y.; Wang, J.; Regier, T.; Dai, H., *J. Am. Chem. Soc.* **2012,** *134* (7), 3517-3523.

61. Hong, W. T.; Risch, M.; Stoerzinger, K. A.; Grimaud, A.; Suntivich, J.; Shao-Horn, Y., *Energy Environ. Sci* **2015,** *8* (5), 1404-1427.

62. Zhao, Q.; Yan, Z.; Chen, C.; Chen, J., *Chem. Rev.* **2017,** *117* (15), 10121-10211.

63. Inomata, K.; Unagami, R.; Adachi, T.; Ito, A., Google Patents: 2012.

64. Suntivich, J.; Gasteiger, H. A.; Yabuuchi, N.; Shao-Horn, Y., *Journal of The Electrochemical Society* **2010,** *157* (8), B1263-B1268.

65. Poux, T.; Napolskiy, F. S.; Dintzer, T.; Kéranguéven, G.; Istomin, S. Y.; Tsirlina, G. A.; Antipov, E. V.; Savinova, E. R., *Catal. Today* **2012,** *189* (1), 83-92.

66. Fabbri, E.; Mohamed, R.; Levecque, P.; Conrad, O.; Kötz, R.; Schmidt, T. J., *ACS Catalysis* **2014,** *4* (4), 1061-1070.

67. Fabbri, E.; Nachtegaal, M.; Cheng, X.; Schmidt, T. J., *Advanced Energy Materials* **2015,** *5* (17), 1402033-n/a.

68. Lee, D.-G.; Gwon, O.; Park, H.-S.; Kim, S. H.; Yang, J.; Kwak, S. K.; Kim, G.; Song, H.-K., *Angew. Chem. Int. Ed.* **2015,** *54* (52), 15730-15733.

69. Yuan, X.-Z.; Li, X.; Qu, W.; Ivey, D. G.; Wang, H., *ECS Transactions* **2011,** *35* (33), 11-20.

70. Miyahara, Y.; Miyazaki, K.; Fukutsuka, T.; Abe, T., *Journal of The Electrochemical Society* **2014,** *161* (6), F694-F697.

71. Risch, M.; Stoerzinger, K. A.; Maruyama, S.; Hong, W. T.; Takeuchi, I.; Shao-Horn, Y., *J. Am. Chem. Soc.* **2014,** *136* (14), 5229-5232.

72. Suntivich, J.; Perry, E.; Gasteiger, H.; Shao-Horn, Y., *Electrocatalysis* **2013,** *4* (1), 49-55.

73. Ju, H. L.; Sohn, H. C.; Krishnan, K. M., *Physical Review Letters* **1997,** *79* (17), 3230-3233.

74. Zhong, Z.; Hansmann, P., *Physical Review X* **2017,** *7* (1), 011023.

75. Jasem, S. M.; Tseung, A. C. C., *Journal of The Electrochemical Society* **1979,** *126* (8), 1353-1360.

76. Singh, N. K.; Tiwari, S. K.; Anitha, K. L.; Singh, R. N., *Journal of the Chemical Society, Faraday Transactions* **1996,** *92* (13), 2397-2400.

77. Bidault, F.; Brett, D. J. L.; Middleton, P. H.; Brandon, N. P., *J. Power Sources* **2009,** *187* (1), 39-48.

78. Sönmez, T.; Thompson, S. J.; Price, S. W. T.; Pletcher, D.; Russell, A. E., *Journal of The Electrochemical Society* **2016,** *163* (10), H884-H890.

79. Morita, M.; Iwakura, C.; Tamura, H., *Electrochim. Acta* **1979,** *24*, 357.

80. Prabu, M.; Ketpang, K.; Shanmugam, S., *Nanoscale* **2014,** *6* (6), 3173-3181.

81. Li, P.; Ma, R.; Zhou, Y.; Chen, Y.; Liu, Q.; Peng, G.; Liang, Z.; Wang, J., *RSC Advances* **2015,** *5* (90), 73834-73841.

82. Li, P.; Ma, R.; Zhou, Y.; Chen, Y.; Zhou, Z.; Liu, G.; Liu, Q.; Peng, G.; Wang, J., *RSC Advances* **2015,** *5* (55), 44476-44482.

83. DOEU US Department of Energy, Office of Energy Efficiency and Renewable Energy, Hydrogen, Fuel Cells and Infrastructure Technologies Program (HFCIT): 2010; pp 1-34.

84. O'Hayre, R.; Cha, S.-W.; Colella, W.; Prinz, F. B., John Wiley & Sons, Inc: 2016; pp 117-166.

85. O'Hayre, R.; Cha, S.-W.; Colella, W.; Prinz, F. B., John Wiley & Sons, Inc: 2016; pp 167-202.

86. Seh, Z. W.; Kibsgaard, J.; Dickens, C. F.; Chorkendorff, I.; Nørskov, J. K.; Jaramillo, T. F., *Science* **2017,** *355* (6321).

87. Fabbri, E.; Habereder, A.; Waltar, K.; Kotz, R.; Schmidt, T. J., *Catal. Sci. Technol.* **2014,** *4* (11), 3800-3821.

88. Bratsch, S. G., *Journal of Physical and Chemical Reference Data* **1989,** *18* (1), 1-21.

89. Chi, B.; Li, J.; Han, Y.; Chen, Y., *International Journal of Hydrogen Energy* **2004,** *29* (6), 605-610.

90. Lyons, M.; Brandon, M., 2008; Vol. 3, p 1386-1424.

91. Swierk, J. R.; Klaus, S.; Trotochaud, L.; Bell, A. T.; Tilley, T. D., *The Journal of Physical Chemistry C* **2015,** *119* (33), 19022-19029.

92. Doyle, R. L.; Lyons, M. E. G., *Journal of The Electrochemical Society* **2013,** *160* (2), H142-H154.

93. Pletcher, D.; Li, X.; Price, S. W. T.; Russell, A. E.; Sönmez, T.; Thompson, S. J., *Electrochim. Acta* **2016,** *188*, 286-293.

94. Marini, S.; Salvi, P.; Nelli, P.; Pesenti, R.; Villa, M.; Berrettoni, M.; Zangari, G.; Kiros, Y., *Electrochim. Acta* **2012,** *82* (Supplement C), 384-391.

95. Merle, G.; Wessling, M.; Nijmeijer, K., *Journal of Membrane Science* **2011,** *377* (1–2), 1-35.

96. Pellow, M. A.; Emmott, C. J. M.; Barnhart, C. J.; Benson, S. M., *Energy Environ. Sci* **2015,** *8* (7), 1938-1952.

97. Ioroi, T.; Oku, T.; Yasuda, K.; Kumagai, N.; Miyazaki, Y., *J. Power Sources* **2003,** *124* (2), 385-389.

98. Ioroi, T.; Kitazawa, N.; Yasuda, K.; Yamamoto, Y.; Takenaka, H., *J. Appl. Electrochem.* **2001,** *31* (11), 1179-1183.

CHAPTER 7

Alkaline Fuel Cells with Gortex-based Electrodes May Be Powered by Hydrogen-Enriched Methane Containing as little as 5% Hydrogen

The text in this chapter is based on a scientific paper published by myself and my supervisors.[1(a)] Also, to note the fact that I contributed at least 30% to this paper[1(a)] in developing a novel approach of Gortex-based alkaline fuel cell technology which is used to test "Power-to-Gas" applications.

7.1 Introduction

Blending hydrogen into the existing natural gas pipeline network in a "*Power-to-Gas*" (P2G) technology is presently being actively pursued by many electrical utilities as a means of increasing the deployment on electrical grids, of renewable energy sources like biomass, solar or wind (Figure 7.1(a)).[1] Not only does P2G help balance such electrical grids, but it also allows for an improved utilization of renewable resources that often generate power when it is least needed. The natural gas network offers a vast potential for hydrogen storage and utilization. It has also been proposed as a means of transporting hydrogen to downstream, end-user markets.[1(b)] As a practical outcome of the P2G strategy, it may be anticipated that future natural gas distribution networks will routinely contain a small

proportion of hydrogen. This is likely to be less than 10% as that is all that natural gas networks can currently tolerate. Natural gas is primarily composed of methane, but also contains ethane, propane and heavier hydrocarbons.

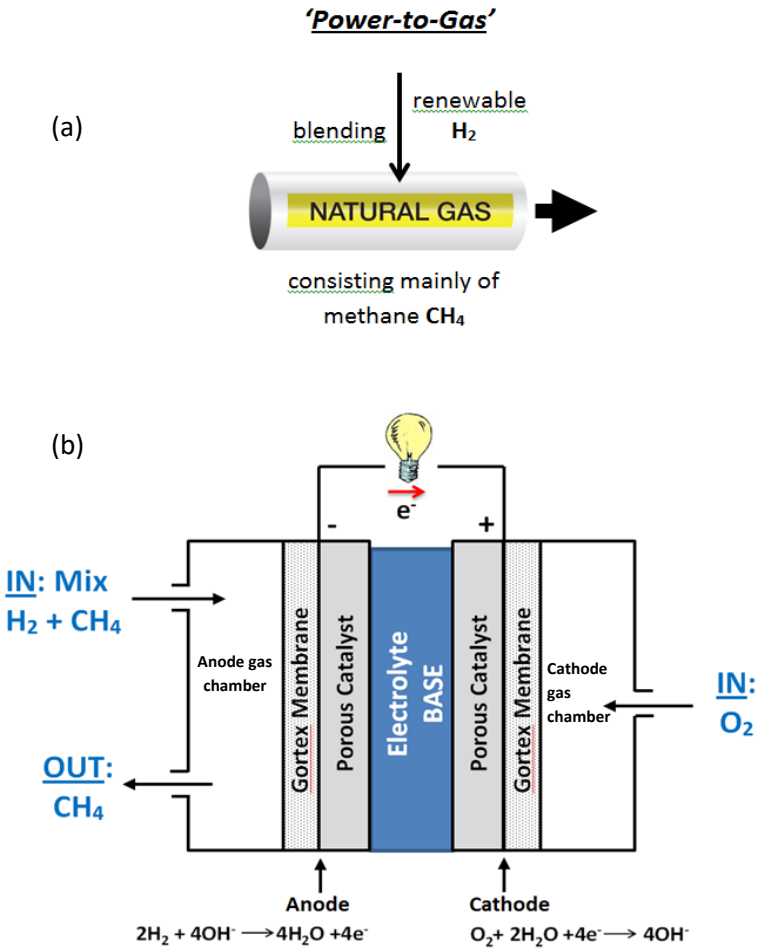

Figure 7.1. *(a) Principle of "Power-to-Gas", in which hydrogen manufactured from excess renewable energy, is injected in existing natural gas pipelines. Natural gas is mainly methane. (b) Schematic diagram of a fuel cell in the present chapter.*

If the hydrogen-enriched natural gas streams of P2G could be used to generate electricity, then this would provide additional economic benefits. A hydrogen-oxygen fuel cell capable of doing so would, however, need to be successfully and sustainably fueled by the low levels

of hydrogen present. That is, the fuel cell would have to be capable of utilizing the <10% hydrogen blend as a fuel.

The most widely used class of hydrogen-oxygen fuel cell at present is the Proton Exchange Membrane (PEM) fuel cell. Studies have demonstrated that methane acts an inert gas when fed through the anode of a PEM.[2(a),(b)] PEM fuel cells have, moreover, been shown to be capable of generating electrical power when fueled with a blend of 5% hydrogen in nitrogen (N_2),[2(c)] which also acts as an inert gas in such cells. However, at such high dilutions, PEM fuel cells are known to experience significant resistances arising from proton diffusion limitations due to the solid-state PEM electrolyte and its interface with the solid catalysts.[2(d)] Thus, for example, the charge transfer resistance in a PEM fuel cell increased from 330 mΩ cm^2 when fueled with pure hydrogen, to 780 mΩ cm^2 when the hydrogen was diluted to 5% by volume with nitrogen - a 240% increase (all feedstock gases humidified to 91%).[2(c)] It is perhaps for this reason that PEM fuel cells capable of operating with 5-10% hydrogen in methane do not appear to have ever been proposed or studied.

Another reason may involve the need to humidify feedstock gases in PEM fuel cells in order to maintain the conductivity of the proton exchange membrane. Natural gas transported by pipeline is routinely extremely dry.[1] If a PEM fuel cell were used to extract electricity from hydrogen-enriched natural gas, then the gas would first have to be humidified before entering the cell. It may then also have to be de-humidified after leaving the cell and before re-entering the natural gas pipeline.

Alkaline fuel cells (AFC) were one of the first fuel cell technologies applied to practical power generation, with initial applications in space. Fueled with pure hydrogen and oxygen, they were introduced in the 1960s, with great success in the Apollo missions and then on the Space Shuttle.[2-3] The limited application of AFCs to space missions was mostly due to a key disadvantage of the alkaline electrolytes employed, namely, carbon dioxide (CO_2) poisoning.[4-5] This problem led to an almost complete termination of activities in alkaline fuel cell research in the beginning of the 1990s.[6] However, more recently, the CO_2 tolerance of AFCs utilizing more modern gas diffusion electrodes has been confirmed and, as the alkaline

electrolyte is easily exchanged, it seems that CO_2 in the air is no longer a major problem for AFCs.[7] Given their simplicity of operation and low cost, AFCs are being reconsidered for commercialization.[8]

AFCs normally employ liquid alkaline electrolytes (typically 6 M KOH), which provides faster reaction kinetics and allows the use of non-noble metals like Ni or Ag as catalysts.[9] All AFCs require porous electrodes, also called gas-diffusion electrodes (GDEs). In order to achieve good performance, a high interfacial contact area is required within the AFC GDEs between three phases: solid (electrode), liquid (electrolyte), and gas (reactant).[3] Hydrogen is fed into the anode, where it is oxidized and combined with hydroxide ions (OH^-) to form water. The hydrogen oxidation reaction (HOR) that occurs on the anode is shown in eq. 7.1:

$$2\ H_2 + 4\ OH^- \rightarrow 4\ H_2O + 4\ e^- \qquad \ldots (7.1)$$

The electrons generated at the anode flow to the cathode, where the oxygen reduction reaction (ORR) takes place (eq. 7.2):

$$O_2 + 2\ H_2O + 4\ e^- \rightarrow 4\ OH^- \qquad \ldots (7.2)$$

The OH^- ions produced at the cathode diffuse through the electrolyte to the anode, to thereby complete the cycle.[10]

In this Chapter, we report that alkaline fuel cells containing two porous-Gortex-based electrodes, layered with suitable catalysts, binders, and a current carrier Ni mesh, are capable of successfully and sustainably utilising hydrogen-methane mixtures as fuels (Figure 7.1(b)). Mixtures containing as little as 5% hydrogen (vol/vol) may be exploited. Fuel cells of this type have the potential to harness the dilute gas mixtures of *Power-to-Gas* for the local generation of electrical power. To the best of our knowledge, beyond these AFCs, only solid oxide fuel cells operating at >800 ºC are presently practically capable of extracting electricity from natural gas pipelines at desktop scale.

7.2 Experimental

7.2.1 Materials

The following materials were used: Carbon black (AkzoNobel) pretreated with ascorbic acid as discussed in chapter 5, 20% Pt-Pd on Vulcan XC-72 (Premetek Co. # P13A200), Poly(tetrafluoroethylene) (PTFE) (60 wt.% dispersion in alcohols/H_2O; Sigma-Aldrich #665800), KOH 90%, flakes (Sigma-Aldrich #484016), Ni mesh, 200 LPI (Precision EForming LLC of Cortland NY) (cleaned using isopropyl alcohol prior to use), and copper tape 6.35 mm width (3M). Polypropylene-backed Preveil^{TM} expanded PTFE (ePTFE) membranes with 0.2 μm pore size sourced from General Electric Energy were used in all experiments.

7.2.2 Preparation of catalyst-coated Gortex

See Chapter 2 section 2.4

7.2.3 Cell Construction

The test cell was a 3D-printed plastic cell with a 3 mm inter-electrode gap, a photograph of which was shown in Chapter 2 section 2.5.

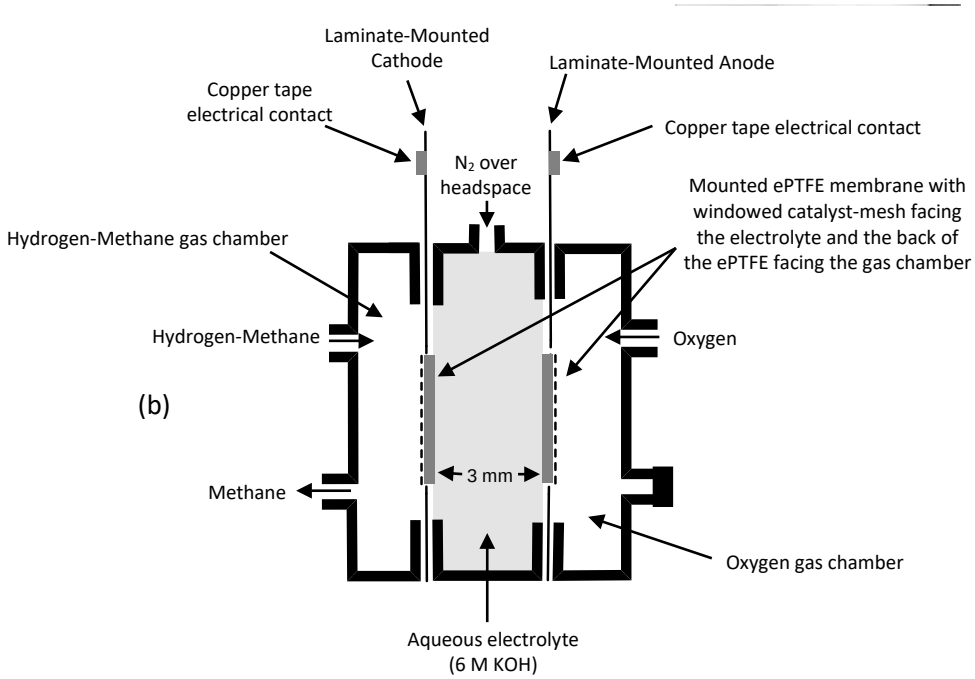

Figure 7.2. *Cross-sectional schematic of the test cell, showing the electrical and gas connections.*

Figure 7.2 shows a cross-sectional view of such a cell and the configuration of anode and cathode along with electrical connections. The gas connections were made using gas-tight fittings. The central cavity of the cell was filled with 6 M KOH.

7.2.4 Reactant Gases and Electrochemical Testing

The hydrogen and methane used in the experiments were stored in high-pressure cylinders connected, via suitable polymer tubing, to the test fuel cell. Calibrated mass flow controllers were used (Aalborg, Stanton Scientific, 10 ml min^{-1} for H_2 and 50 ml min^{-1} for CH_4) to obtain the desired mixtures of hydrogen and methane. As shown in Figure 7.2, the anode compartment of the cell was fed with pure hydrogen or a mixture of hydrogen and methane of varying ratios, while cylinder O_2 gas was supplied to the cathode.

The characterisation of fuel cells were done using steady-state current-voltage (*I*-*V*) curves, chronoamperometry, and chronopotentiometry. The H_2 (H_2 and CH_4 mixture) electrode (anode) was connected as the working electrode and the O_2 electrode was connected as a combined auxiliary/reference electrode. Thus, all reported voltages are *vs.* O_2.

Galvanostatic electrochemical impedance measurements were recorded at open circuit or at the constant current density of 10 mA cm^{-2} conditions between 0.1 Hz and 200 kHz with an AC amplitude of ± 1 mA cm^{-2}. Spectra were analysed and fitted using ZView software version 3.4.

7.3 Results and Discussion

For this Chapter, we fabricated and studied an alkaline fuel cell containing two Gortex-based gas diffusion electrodes. In each of these, the Gortex substrate had been coated with a catalyst layer containing 20% Pd-Pt/CB, CB, dispersed poly(tetrafluoroethylene) (PTFE) as a binder, and a fine Ni mesh as a current carrier (as described in the Experimental section).

Polypropylene-backed *Preveil*^{TM} expanded PTFE (ePTFE) ('Gortex') membranes, produced by General Electric Energy were used in all experiments. These membranes were resistant to flooding at over pressures of >4 bar. The catalyst loading was precisely determined for each electrode; the average was 1.6 g of metal per m^2 (Pt/Pd) loading.

7.3.1 Fuel Cell Operation using Hydrogen-Methane Mixtures in the Range 5%-100%

During the experiments, hydrogen, or mixtures of hydrogen and methane at atmospheric pressure were allowed to slowly flow through the anode gas compartment of the test cell while oxygen gas at atmospheric pressure was slowly passed into the cathode gas compartment. Each of the gases employed were in high purity form. The cell was designed to ensure that each Gortex-based gas diffusion electrode had a 1 cm^2 geometric area. The anode and cathode electrodes were in a facing disposition to each other. No diaphragm, ionomer, or other separator was present in the gap between the electrodes in the cell.

H_2 %	H_2 ml/min	CH_4 ml/min	V_{oc} V	$V_{@10mAcm-2}$ V	P_{max} mW/cm^2	R_{slop_unc} Ω
100	10	0	1.03	0.88	109.3	1.5
50	10	10	1.03	0.88	93.4	1.8
40	8	12	1.03	0.88	87.4	1.9
30	6	14	1.02	0.87	79.9	2.1
20	4	16	1.01	0.87	67.4	2.8
10	2	18	1.00	0.85	39.2	4.9
5	1	19	0.99	0.82	21.6	7.8
100*	10	0	1.04	0.89	96.7	1.8

* after methane exposure

Table 7.1. *Flow parameters of H_2 and CH_4 in examined mixtures. Columns: open circuit voltage (V_{oc}), potential upon applying current density of 10 mA cm^{-2} ($V_{@10mAcm-2}$), the highest power density (P_{max}) and ohmic resistance (R_{slop_unc}) from uncorrected polarization curves.*

The performance of the above-described alkaline fuel cell was initially examined with mixtures of hydrogen in methane of: 50%, 40% 30%, 20%, 10% and 5%. The total flow of the H_2-CH_4 mixture in these experiments was kept constant at 20 ml min^{-1}. Detailed flow conditions are summarised in Table 7.1. Comparative experiments using pure hydrogen, were performed before and after the experiments with the hydrogen mixtures, in order to assess the stability of the system to the methane.

A voltage drop of only 40 mV in the open circuit potential (V_{oc}) was observed when cells were supplied with pure hydrogen compared with cells supplied with a methane blend containing 5% hydrogen. A 60 mV voltage drop was seen at a low current density of 10 mA cm^{-2} (Table 7.1).

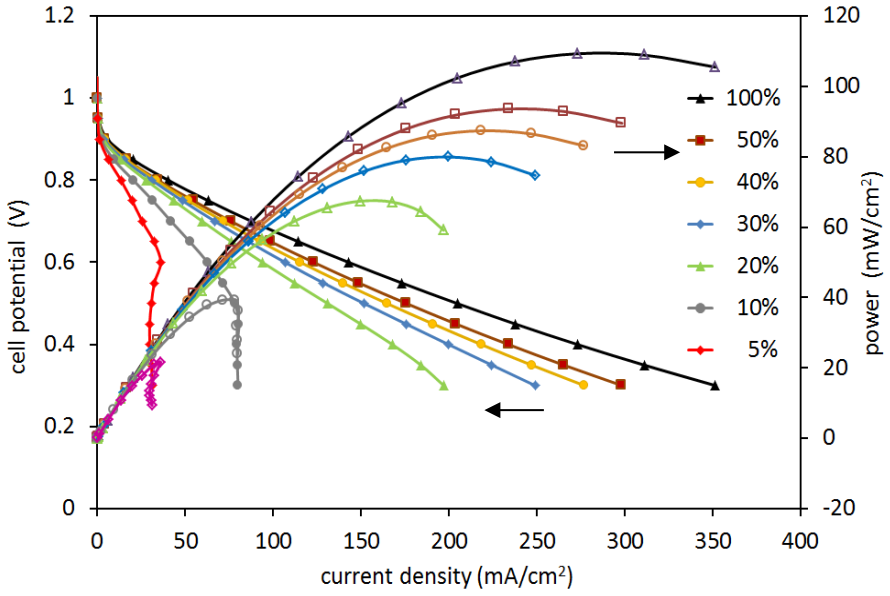

Figure 7.3. *Current density – voltage curves, (j-V) on left axis and current density–power density (j-P) curves, on right axis for a fuel cell operating between 5% and 100% of hydrogen in a gas mixture.*

7.3.3 Polarisation Curves

To characterize the overall fuel cell performance, polarization curves were measured. Figure 7.3(b) displays the polarization curves (filled markers), and power curves (empty markers) of the gas mixtures investigated. Cell potentials were measured between the cathode and anode, meaning that the polarization curves represent the combination of the polarizations of these two electrodes.

For the gas mixtures above, the linear part of the polarization curves displayed a gradual increase in slope with declining hydrogen proportions, from 1.5 Ω for pure hydrogen to 7.8 Ω for 5% H_2. This indicates a concomitantly increasing resistance according to Ohm's law (equation 7.3):

$$U = iR \qquad \ldots (7.3)$$

where i is the current flowing through the cell, and R is the total cell resistance, which includes electronic, ionic, and contact resistance). The estimated resistances from uncorrected polarization slopes for all gases are given in Table 7.1.

The mass transport limitations in the polarization curves are obvious for the 5% and 10% hydrogen mixtures, with the onset occurring earlier for 5% (Figure 7.3(b)). When the cell voltage was 0.6 V, the hydrogen in the 5% mixture became almost depleted, which noticeably impaired the performance of the cells.

The losses due to concentration occur over the entire range of current densities, but become more prominent at high currents densities, where the reaction rates are higher, causing faster consumption of reactants. A concentration gradient was formed if the mass transport was not fast enough to supply the reactant from the bulk of fluid into the electrode interface, which

caused the potential decline. Several processes may contribute to this, such as slow diffusion in the gas phase into the electrode pores, solution/dissolution of reactants/products into/out of the electrolyte, or diffusion of reactants/products through the electrolyte to/from the electrochemical reaction site.

It can be seen that the percentage of hydrogen in the mixture had an impact on the maximum power density. With pure hydrogen, the highest power density was 109.3 mW cm^{-2}, dilution of the hydrogen decreases the highest power density to 21.6 mW cm^{-2} at 5% hydrogen in mixture (Table 7.1).

To extract information about kinetic and mass transport losses and the ohmic resistance of the cell, the cell overpotential using pure hydrogen, was plotted as a function of current density (Figure 7.4).

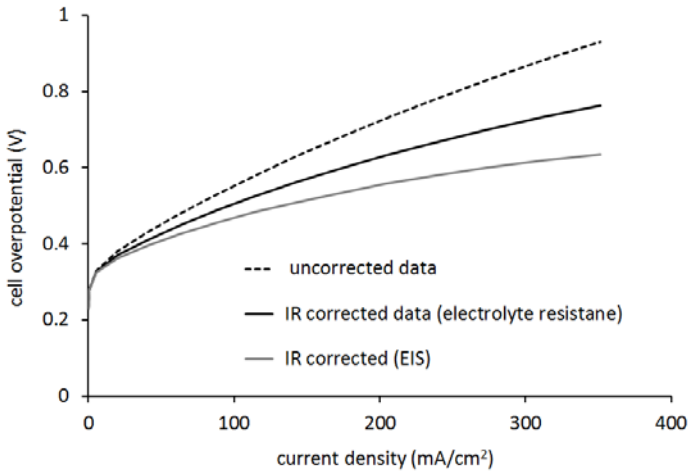

Figure 7.4. *Polarization curves for pure hydrogen, uncorrected data (dash line), corrected by: (i) taking into account the electrolyte resistance (black line) and (ii) using EIS (grey line)).*

The Ohmic resistance of the supporting electrolyte (E_{el}) depends on the anode-to-cathode spacing or the charge-transport length (d), cross-sectional area of charge transport (A) and the ionic conductivity (σ) (eq. 7.4)

$$E_{el} = \frac{d}{\sigma A} \quad \ldots (7.4)$$

The E_{el} of the 6 M KOH electrolyte was calculated as 0.48 Ω (d = 0.3 cm, σ = 0.63 S cm^{-1},[12] 20 and A= 1 cm^2). Polarization curves were then iR-corrected by adding the current multiplied by the electrolyte resistance. Figure 7.4 shows the uncorrected polarization curve for pure hydrogen (Figure 7.4; dashed line) and the same curve corrected for the solution resistance (Figure 7.4; black line). The slope was still significant however.

To better isolate the kinetic losses, the ohmic resistance ($R_Ω$=0.90±0.01) from electrochemical impedance spectroscopy (EIS) was applied to the correction in the same fashion (Figure 7.4; grey line). Impedance corrected polarization curves were later also used for the generation of the Tafel plots.

7.3.4 Tafel Plots

At low current densities, the kinetics are commonly modelled by the Tafel equation, given in eq. 7.5.

$$\eta = Aln\left(\frac{i}{i_o}\right) \quad \ldots (7.5)$$

where η defines the overpotential, which is the difference between the electrode potential E and the standard potential E_0 ($\eta = E - E_0$), i denotes the current density, i_o is the exchange current density, and A is the Tafel slope. The Tafel slope provides insight into the reaction kinetics and also the mechanism, to thereby elucidate the elementary steps and the rate

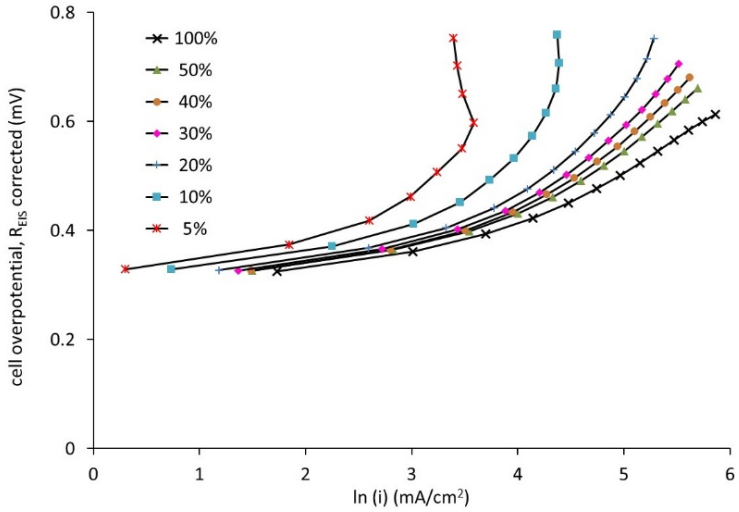

Figure 7.5. *Tafel plots for the fuel cell operating between 5% and 100% of hydrogen in methane.*

determining steps. A is higher for an electrochemical reaction that is slow, since slow reaction leads to a higher overvoltage and the exchange current density i_o can be considered as the current density at which the overvoltage begins to move from zero. If i_o is high, then the surface of the electrode is more 'active' and a current in one particular direction is more likely to flow. It is desired to have as high a value of i_o as possible, and as rapid kinetics as possible (low A).

H_2 %	A mV/dec	*io* mA/mg_{PtPd}	$R_{(ct)}$ Ω	$C_{(ct)}$ F	$Z_{(d)}$ Ω
100	124	18	0.22	$1.1 \cdot 10^{-4}$	2.67
50	155	32	0.26	$8.9 \cdot 10^{-5}$	2.75
40	169	37	0.26	$8.8 \cdot 10^{-5}$	2.79
30	190	32	0.27	$8.6 \cdot 10^{-5}$	2.85
20	165	22	0.28	$8.4 \cdot 10^{-5}$	3.04
10	160	11	0.28	$8.2 \cdot 10^{-5}$	3.80
5	175	8	0.29	$8.0 \cdot 10^{-5}$	7.11

Table 7.2. *Parameters obtained from the Tafel plots: slope A, and the exchange current density i_o; from electrochemical impedance, double-layer capacitance within the catalyst layer $C_{(ct)}$, charge transfer resistance $R_{(ct)}$, diffusional resistance $Z_{(d)}$.*

Figure 7.5 provides impedance-corrected Tafel plots for all investigated gas mixtures. Table 7.2, gives slopes (*A*) (in units of mV dec^{-1}) and exchange current densities (i_o) (in units of mA/mg_{cat}) calculated from the catalyst loading.

The estimated Tafel slope for pure hydrogen was 124 mV dec^{-1}. This is consistent with the reported literature; Tafel slopes of around 120 mV dec^{-1} and higher are frequently reported for both the hydrogen oxidation reaction (HOR) and the oxygen reduction reaction (ORR) in alkaline medium, and on and platinum supported carbon (Pt/C).[13,14] The slopes for all hydrogen-methane mixtures are higher in comparison to pure hydrogen and vary between 155-190 mV dec^{-1}, which suggest slower kinetics.

The exchange current density i_o estimated from the Tafel plots were higher for the mixtures with 20-50% hydrogen and lower for 10% and 5% compared to the i_o of pure hydrogen (Table 7.2). The reasons for this increase are not clear, however as noted by Almutairi and colleagues,[15] the Gibbs free energy (ΔG°) and standard equilibrium voltage (E^0) in eq. 7.6, considered as the V_{oc}, are higher for methane than for hydrogen. This was used by this author to explain higher voltages observed with the addition of methane into hydrogen.

$$E^0 = -\frac{\Delta G^0}{zF} \qquad \ldots (7.6)$$

(Methane: ΔG°= –818 kJ mol^{-1}, *E*°= 1.41 V versus hydrogen: ΔG°= –237 kJ mol^{-1}, *E*°=1.23 V, z is the molar number of electrons being transferred and F is Faraday's constant)

The lower i_o for the 5-10% gas mixtures can possibly be explained by the reduced access of hydrogen to the 3-way solid-liquid-gas interface in the electrode, while competing with the methane flow. However, as can be seen in Figure 7.4, the Tafel plots are strongly influenced

by concentration losses in these diluted mixtures, and as recognised by Shinagawa et al,[14] the contribution of mass-transport can lead to misinterpretation of the kinetics due to inaccurate Tafel slopes.

Perhaps the key insight that can be derived from the i_o and *A* values in Table 7.2 is the fact that, despite the differences, they are all of similar order. This is, in fact, rather stunning given the enormous differences in the proportion of hydrogen present in the mixtures fed into the cells. It indicates that all of the fuel cells depicted in Table 7.2 (5%-100% hydrogen) operate in a very similar way. That is, while the kinetics may slow somewhat at high dilutions of hydrogen in the reactant gas mixture, the operation of the fuel cell is, in essence, the same. This seems to be a quite extraordinary outcome.

7.3.5 Electrochemical Impedance Spectroscopy

To break down the total cell resistance into individual polarization contributions, electrochemical impedance spectroscopy (EIS) was applied. EIS has proved to be very useful in distinguishing processes with different time constants. The preliminary EIS measurements were taken with symmetrically supplied hydrogen (H_2/H_2) and oxygen (O_2/O_2) at the two electrodes of the cell and the results were shown earlier in Figure 5.2(a)-(b) in Chapter 5. These experiments were done to determine the anode and cathode transfer functions at the open circuit potential (V_{oc}) and compare it with cells operated with either H_2 or O_2 at the same conditions.[16] Based on the charge transfer resistances (R_{ct}) and double-layer capacitance within the catalyst layer (C_{ct}) from Table 7.3, H_2/H_2 displayed a faster electrochemical reaction kinetics. Another feature, relaxation time t_0 (eq. 7.7), which is related to the recovery rate of the steady-state when a perturbation is applied to the system, was evaluated from Bode plots in Figure 5.2 (b). The shorter value of t_0 indicates faster kinetics. As seen from Table 7.3, t_0 is shorter for H_2/H_2 than for O_2/O_2 and H_2/O_2, which

points out facile reaction kinetics at anode (electrode supplied by H_2) when compared to much slower reaction kinetics at cathode (electrode supplied by O_2).

$$t_o \approx \frac{1}{\omega_{min}} = \frac{1}{2\pi f} = RC \qquad \ldots (7.7)$$

where ω_{min} is the frequency at which the phase shift is minimum.

H_2 %	$R_{(ct)}$ Ω	$C_{(ct)}$ F	i_0 mA/mg_{PdPt}	t_o ms
H_2/H_2	0.23	8.0E-05	158	0.2
O_2/O_2	0.67	4.0E-05	160	0.3
H_2/O_2	0.76	3.7E-05	172	0.3

Table 7.3. *Parameters obtained after fitting data from Nyquist and Bode plots to equivalent circuit (Nyquist, Bode plots and equivalent circuit shown in Figure 5.2); charge transfer resistance (R_{ct}), double layer capacitance (C_{ct}), exchange current density (i_o) and relaxation time t_o calculated from R_{ct}. Electrochemical cells were supplied with symmetrically supplied hydrogen (H_2/H_2), oxygen (O_2/O_2) and (H_2/O_2), at the two electrodes of the cell, at open circuit potential (OCV).*

However the exchange current density i_o, calculated from the charge transfer resistance R_{ct} at open cell voltage (eq. 7.8), was equal for the anode and cathode: $i_{o\ anode}$ =0.16 A per mg_{PdPt} and $i_{o\ cathode}$ = 0.16 A per mg_{PdPt}.

$$R_{ct} = \frac{RT}{zFi_0} \qquad \ldots (7.8)$$

where z is the number of electrons involved in overall reaction, R the gas constant, T the temperature and F the faradaic constant.

Sheng and co-workers[17] reported somewhat higher numbers (albeit using a 3-electrode system), that were, nevertheless, close for HOR/HER and ORR in 0.1 M KOH and on Pt carbon support ($i_{o\ anode}$=0.35 A per mg_{pt} and $i_{o\ cathode}$ =0.26 A per mg_{pt}).

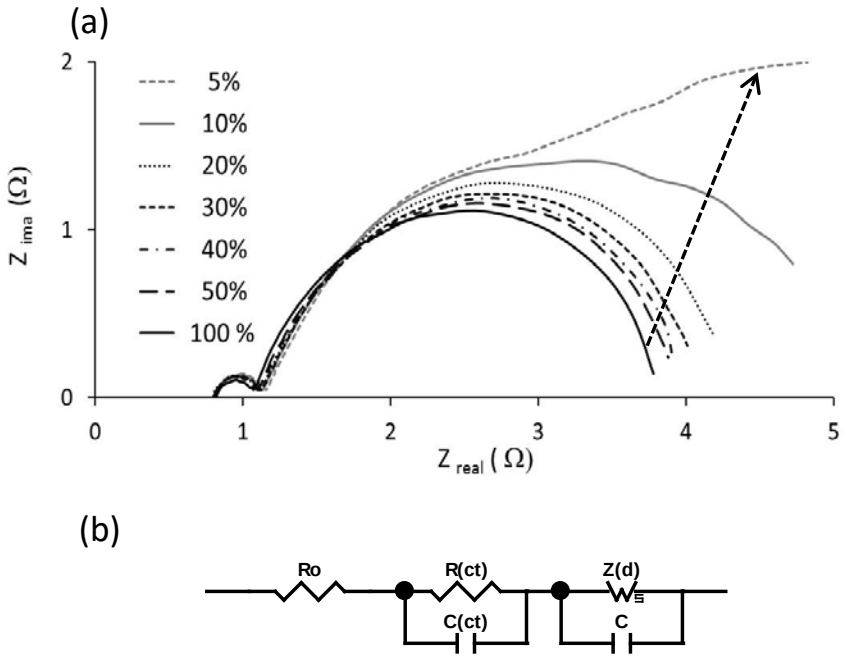

Figure 7.6. *Nyquist spectrum of impedance measurements for cell (1 cm^2) supplied with pure hydrogen and 50%, 40%, 30%, 20%, 10%, and 5% hydrogen and methane mixture. (a) The total flow was kept constant at 20 ml min^{-1}, constant current density of 10 mA cm^{-2} was applied; (b) the equivalent circuit.*

Thus, it can be concluded that the charge transfer resistances of both electrodes significantly contribute to the impedance of a fuel cell (H_2/O_2) at open circuit potential (V_{oc}). One can also see in the H_2/H_2 case, finite diffusion as an additional loop at the lowest part of the frequency range and infinite diffusion as a straight line with a slopes close to 1 in the O_2/O_2 and H_2/O_2 spectra.

To investigate the EIS of the gas mixtures, spectra were collected at a constant current density of 10 mA cm^{-2} (close to the V_{oc}, see Table 7.1) for: 100%, 50%, 40% 30%, 20%, 10% and 5% hydrogen in methane mixtures. The results are depicted as Nyquist plots in Figure 7.7(a). Two arcs are visible for the cell operating with pure hydrogen, which corresponds to two relaxation times; namely, the smaller, charge transfer arc at high frequencies (40 kHz-200 Hz,) and a larger, finite diffusion arc at lower frequencies (200 Hz-0.1 Hz), also known as the Nernst impedance. To estimate all resistances of the cell from the EIS measurements, the data were fitted to an equivalent electrical circuit, displayed in Figure 7.7(b), with the results given in Table 7.2.

In general, the intercept of the arc with the real axis at the high-frequency end represents the total ohmic resistance (or electrolyte resistance, often used in fuel cell literature), R_{Ω}. The ohmic resistance is recognized as the sum of the contributions from uncompensated contact resistance and the ohmic resistance of cell components such as electrolyte (electrolyte ionic resistivity) and electrodes.

For all measured mixtures including pure hydrogen R_{Ω}=0.90±0.01 Ω remained constant. The charge transfer arc changed only slightly with a decrease of the hydrogen proportion in the gas mixture. Thus, the charge transfer resistance changed only from 0.22 Ω cm^2 when using pure hydrogen to 0.29 Ω cm^2 when the hydrogen was diluted to 5% using methane (Table 7.2). This equates to an ca. 30% increase in the key resistance feature of the cell that essentially determines its overall efficiency. The Gortex-based alkaline fuel cell was clearly highly efficient.

However the diffusion arc significantly expands as the H_2 proportion decreases (Figure 7.7(a) and Table 7.2). Increased resistances estimated from this arc indicate longer relaxation times with hydrogen dilution (see. eq. 7.7), which corresponds to a lower freedom of diffusion within the cell. The diffusion arc was readily diminished and the associated

diffusion resistance reduced by simply increasing the overall flow of H_2/inert gas through the anode without changing the diluent proportion.

After the completion of all of the above measurements with the hydrogen-methane mixtures, the cells were again fed with pure hydrogen and the (j-V) and EIS were compared with the first results obtained with pure hydrogen (Table 7.1 and Figure 7.8(a)-(b)).

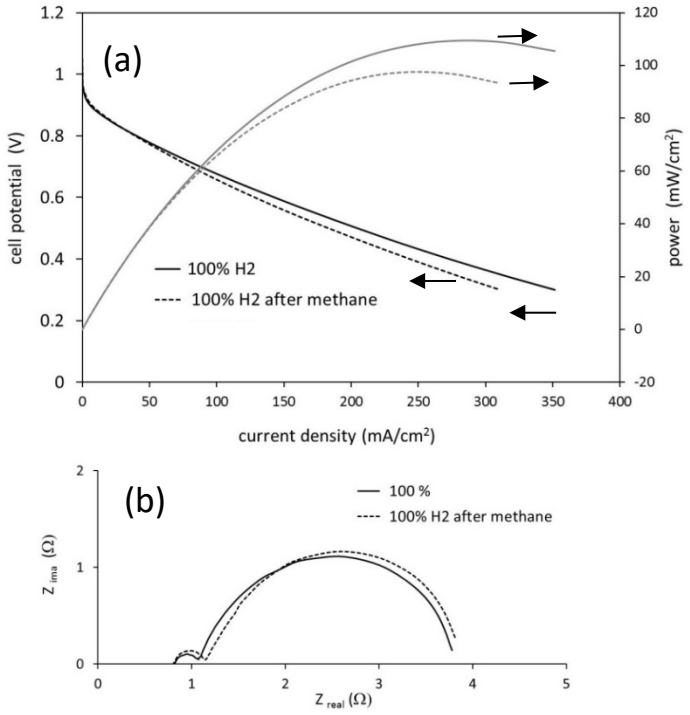

Figure 7.7. *(j-V), j-P) (a) and GEIS at 10 mA cm^{-2}, (b) characteristics for a fuel cell operating with pure hydrogen before (solid lines, black for j-V and grey for j-P) and after measurements with hydrogen and methane mixtures.*

The (j-V) results show, that after the cells were exposed to methane, there was a slight increase in the overvoltage at higher current density. Thus, 40 mA cm^{-2} less current was generated at the cell voltage of 0.3 V (Figure 7.8(a)). The highest power density of 109.3 mW cm^{-2} (Figure 7.3(a)) also decreased to 96.76 mW cm^{-2} (Figure 7.8(a)). This may be a result of the reaction being "starved" while collecting the data for 5% and 10%, at higher

current density range. However, both (j-V) and (j-P) curves in the range up to 50 mA cm^{-2} did not change (Figure 7.8(a)), indicating that the system was, effectively, fully reversible in this range. That is, it essentially recovered its full performance after being treated with the hydrogen-methane mixtures. Full reversibility of the cell in the low current density range was also confirmed with EIS performed at 10 mA cm^{-2} (Figure 7.8(b)), and the cell demonstrated a fully recovered performance (stable potential of 0.89V at 10 mA cm^{-2}, Table 7.1).

These results are similar to those of Ibeh et al,[18] who used PEM cells and Pt supported carbon electrodes to separate hydrogen from its mixture with methane. It can be concluded that, methane does not appreciably deactivate the anode catalyst surface under experimental conditions.

7.3.6 Hydrogen-Methane Mixtures in the Range 2%-5%

To probe further, to lower concentrations of the hydrogen, below 5%, a further set of experiments was performed with a fixed flow rate of hydrogen/methane of 1 ml min^{-1} (Table 7.3). In these experiments the cell potential was limited to 0.6 V to avoid cell starvation.

H_2 %	H_2 ml/min	CH_4 ml/min	V_{oc} V	$V_{@10mAcm-2}$ V	P_{max} mW/cm^2	$R_{(j-V)slop\_unc}$ Ω
100	1	0	1.04	0.86	44.2	4.0
5	1	19	0.99	0.79	15.4	10.1
4	1	24	0.99	0.77	12.0	12.9
3	1	32	0.98	0.74	9.4	15.8
2	1	49	0.97	0.67-0.59**	6.9	20.1
100*	1	0	1.02	0.88	36.9	4.8

* after methane exposure,** within 30 min

Table 7.4. *Parameters of the flow of H_2 and CH_4 in examined mixtures, and obtained: open circuit voltage (V_{oc}), potential upon applying current density of 10 mA cm^{-2}($V_{@10mAcm-2}$), the highest power density (P_{max}) and ohmic resistance (R_{slop_unc}) from uncorrected polarization curves.*

As with the previous set of results, the slopes of the polarization curves (j-V) and (j-P) were found to gradually change with hydrogen dilution, indicating a further increase in the cell resistances. (Table 7.4 and Figure 7.9(a)). The potentials monitored at the cell with an applied current density of 10 mA cm^{-2}, were lower by 70 mV (5%), 90 mV (4%), and 120 mV (3%). All of these were stable. The mixture having 2% hydrogen however (Table 7.4) originally exhibited a voltage of 0.67 V but after 30 min this gradually changed to 0.59 V which indicates that it was at the border of stability. Galvanostatic EIS measurements at 10 mA cm^{-2} also showed an increase of resistance deriving from mass transport (Figure 7.9(b)).

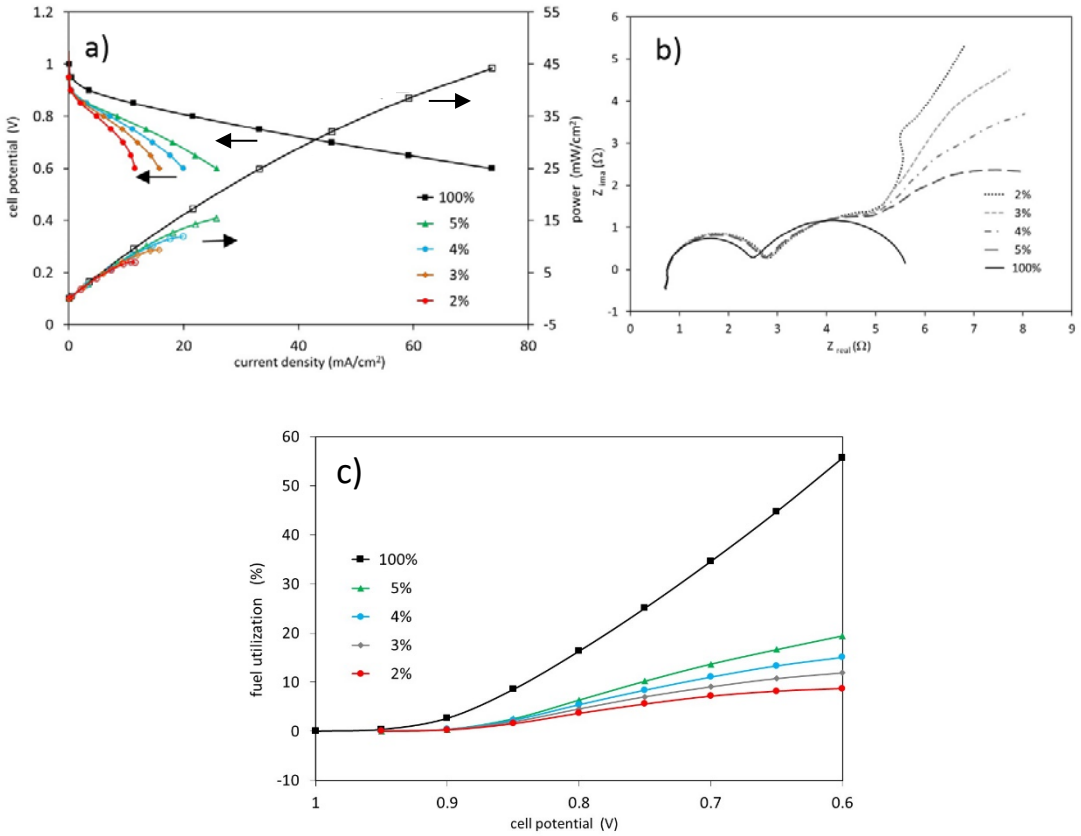

Figure 7.8. *(j-V) and (j-P) characteristics (a) fuel utilization (b) and GEIS at 10 mA cm^{-2} for the cell (1 cm^2) operating with: 100%, 5%, 4%, 3% and 2% hydrogen in the gas mixture.*

The extent of fuel utilization (FU) was calculate from eq. 7.9 and plotted (Figure 7.9(c)); in all cases the cell was fed with the same amount of hydrogen or hydrogen/methane of 1ml min^{-1}.

$$FU = \frac{Hc}{Hf} * 100 \quad [\%] \qquad \ldots (7.9)$$

where H_c is the theoretically produced hydrogen on the basis of the current intensity and H_f is fed hydrogen. At the low current density of 10 mA cm^{-2} (0.8 V) the fuel utilization was $FU_{100\%H2,0.8V=}$16% for the pure hydrogen and $FU_{5\%H2,0.8V=}$6% for the 5% mixture.

As expected for the highest current density and the applied potential of 0.6 V, the difference increased, as does the increased mass transport resistances. For pure hydrogen $FU_{100\%H2,0.6V=}$56% and for 5% mixture only $FU_{5\%H2,0.6V=}$19%. With the further dilution of hydrogen below 5%, the values of FU decrease further.

These results imply that with a more dilute mixture, more hydrogen was wasted. Lower currents generated by the cell with the same amount of fed hydrogen suggest again, that the hydrogen access to the catalyst surface is reduced. However when compared to pure hydrogen, this drop of FU does not follow the percentage of dilution. One of the reasons could be the difference in kinetic diameters, which is quite often invoked in discussing gas permeation in porous materials; these are smaller for hydrogen when compared to methane (2.9 Å vs 3.8 Å).[19]

7.3.7 Water Balance in the Fuel Cell

While studies did not examine the issue of water balance, it should be noted that water is produced in the Gortex-based fuel cell. Its potential accumulation within the aqueous 6 M

KOH electrolyte would therefore need to be considered. The electrolyte is also in direct contact (through the Gortex interface) with the flowing gases, meaning that a humidification equilibrium would be created in the gas chambers. This equilibrium would depend on the operating temperature of the fuel cell and the excess heat it generates. In the process, water vapour from the electrolyte would be taken up by the gases, potentially depleting the water content of the 6 M KOH electrolyte. In a cell fuelled by hydrogen-enriched natural gas, the competing processes of water accumulation and water depletion would ideally be balanced. If that could be achieved, the outlet gas from the anode would contain water vapour and would have to be de-humidified prior to re-entering the natural gas pipeline. In a perfectly balanced system however, the de-humidification step would, effectively, be removing the excess water created during the cell reaction.

7.4 Conclusions

Utilisation of a novel alkaline fuel cell having Gortex-based gas diffusion electrodes for power generation from dilute mixtures of hydrogen and methane, has been unequivocally demonstrated in this chapter. Mixtures of between 2% and 100% of hydrogen were examined. The following conclusions can be drawn from this study:

1. *Hydrogen dilution:* At a low current density of 10 mA cm^{-2}, the studied class of AFC can operate efficiently with dilution of hydrogen down to 5% and with an overvoltage of only 60-70 mV above the potential required when the cell is fed with pure hydrogen. Indeed, Tafel plot studies show that, in terms of the fundamental operation, there is essentially no difference between a 5% hydrogen mixture and 100% hydrogen. In particular, the key measure of charge transfer resistance, which sets the overall efficiency of the cell, displays only an ca. 30% increase in going from pure hydrogen as a fuel, to 5% hydrogen. This seems to be an extraordinary result.

2**.** *Cell losses:* Mass transport losses, which are dominant in this system, start to appear at low current densities, when the hydrogen concentration goes below 20%. But the increased resistance provided by the mass transport limitations are only mild down to ca. 5% mixtures of hydrogen. Moreover, they can, effectively, be circumvented by simply increasing the overall flow rate of the dilute hydrogen-methane mix through the cell. The cell can operate successfully under this condition. The limitation at higher current densities involves depletion of the hydrogen from the mixture. For 5% hydrogen and a flow of 1 ml min^{-1}, above potentials of 0.6 V the cell reaction begins to starve, with the highest power density achieved for this mixture is 21.6 mW cm^{-2}.

3. *Reversibility:* The cells were fully reversible after exposure to methane, which indicates that the methane gas has an inert behaviour in the cell and that no catalyst deactivation occurs.

4. *Gortex electrodes:* The novel Gortex substrate of the electrodes clearly provides a remarkably active interface that allows the fuel cell to selectively extract the hydrogen from the methane and utilize it as a fuel.

5. *Ability to extract electricity from methane enriched with hydrogen:* As natural gas is mostly methane, the present cell offers a potential means of generating electrical power locally by utilizing the dilute 5-10% hydrogen-methane mixtures envisaged for power-to-gas technologies. To the best of our knowledge, only solid oxide fuel cells operating at >800 ^{o}C are presently practically capable of extracting electricity from natural gas pipelines at a local scale. The present technology potentially provides a future alternative.

References

1. (a) K. Wagner, P. Tiwari, G. F. Swiegers, G. G. Wallace, *Adv. Energy Mater.* **2018**, *8*, 1702285 (b) Goetz, M.; Lefebvre, J.; Moers, F.; McDaniel Koch, A.; Graf, F.; Bajohr, S.; Reimert, R.; Kolb, T. *Renewable Energy* **2016**, *85*, 1371; (c) M. W. Melaina, O. Antonia, M. Penev, in "*Blending Hydrogen into Natural Gas Pipeline Networks: A Review of Key Issues*" Technical Report NREL/TP-5600-51995, National Renewable Energy Laboratory, March 2013, and refs therein (https://energy.gov/eere/fuelcells /downloads/blending-hydrogen-natural-gas-pipeline-networks-review-key-issues); (d) "*Power-to-Gas: The Case for Hydrogen - White Paper*", California Hydrogen Business Council, Los Angeles, CA 90049, 2015 and refs therein (https://californiahydrogen.org /sites/default/files/CHBC%20Hydrogen%20Energy%20Storage%20White%20Paper%20FINAL.pdf)
2. (a) Ibeh, A.; Gardner, C.; Ternan, M. *Int. J. Hydrogen Energy* **2007**, *32*, 908; (b) See also studies of contaminant gases in hydrogen feed-gas, for example: X. Cheng, Z. Shi, N. Glass, L. Zhang, J. Zhang, D. Songa, Z.-S. Liu, H. Wang, J. Shen *J. Power Sources* **2007**, *165*, 739, and refs therein; (c) See, Fig. 4 in M. Boillot, C. Bonnet, N. Jatroudakis, P. Carre, S. Didierjean, F. Lapicque *Fuel Cells 06* **2006**, *1*, 31; (d) See, for example: M. T. Dinh Nguyen, S. A. Grigoriev, A. A. Kalinnikov, A. A. Filippov, P. Millet, V. N. Fateev, *J. Appl. Electrochem.* **2011**, *41*, 1033.
3. Perry, M. L.; Fuller, T. F. *J. Electrochem. Soc.* **2002**, *149*, S59.
4. Lin, B. Y. S.; Kirk, D. W.; Thorpe, S. J. *J. Power Sources* **2006**, *161*, 474.
5. Cifrain, M.; Kordesch, K. V. *J. Power Sources* **2004**, *127*, 234.
6. Tewari, A.; Sambhy, V.; Urquidi Macdonald, M.; Sen, A. *J. Power Sources* **2006**, *153*, 1.
7. Guelzow, E. *J. Power Sources* **1996**, *61*, 99.
8. Gulzow, E.; Schulze, M. *J. Power Sources* **2004**, *127*, 243.
9. Thyberg, S. *J. Electrochem. Soc.* **1990**, *137*, 2654.

10. McLean, G. F.; Niet, T.; Prince-Richard, S.; Djilali, N. *Int. J. Hydrogen Energy* **2002**, *27*, 507.
11. Verhaert, I.; De Paepe, M.; Mulder, G. *J. Power Sources* **2009**, *193*, 233.
12. Gilliam, R. J.; Graydon, J. W.; Kirk, D. W.; Thorpe, S. J. *Int. J. Hydrogen Energy* **2007**, *32*, 359.
13. Genies, L.; Faure, R.; Durand, R. *Electrochim. Acta* **1998**, *44*, 1317.
14. Shinagawa, T.; Garcia-Esparza, A. T.; Takanabe, K. *Sci Rep* **2015**, *5*, 13801.
15. Almutairi, G.; Dhir, A.; Bujalski, W. *Fuel Cells (Weinheim, Ger.)* **2014**, *14*, 231.
16. Wagner, N.; Schnurnberger, W.; Muller, B.; Lang, M. *Electrochim. Acta* **1998**, *43*, 3785.
17. Sheng, W.; Gasteiger, H. A.; Shao-Horn, Y. *Journal of The Electrochemical Society* **2010**, *157*, B1529.
18. Ibeh, B.; Gardner, C.; Ternan, M. *International Journal of Hydrogen Energy* **2007**, *32*, 908.
19. Mehio, N.; Dai, S.; Jiang, D.-e. *J. Phys. Chem. A* **2014**, *118*, 1150.

CHAPTER 8

Summary and Perspectives

8.1 Summary

This research work comprehensively studied the use of *Gortex* membranes as novel substrates for leak-proof GDEs together with range of catalyst layers for developing highly efficient, low-cost novel alkaline-based electrolysers and fuel cells.

Initially, we reported the fabrication, characterization, and operation of Gortex membrane-based GDEs overcoated with a catalyst layer comprising either sputter-coated Pt or 10% Pt on Vulcan XC72 incorporating carbon black and PTFE binder, with fine Ni meshes as a current carrier. Capillary flow porometry indicated that the electrodes only flooded/leaked when the excess of pressure on their liquid-side over their gas-side was 4.3-5.7 bar, which is an order of magnitude greater than the previously reported best for a GDE of 0.2 bar. When particulate-coated Gortex electrodes was used in desktop AFCs with low Pt loadings and at 20 ^{o}C, it yielded notable current and power densities. These AFCs worked efficiently without an ion-permeable, gas-impermeable diaphragm between the electrodes and were robustly tolerant of CO_2 over extended periods of operation. These results indicate that it is now possible to use Gortex-based GDEs in many industrial electrochemical processes without the problem of flooding/leaking.

In the next set of experiments, the performances of various well-known, conventional water-splitting catalysts, layered on Gortex membrane substrates, in AWE were reported. The results indicated that the use of Gortex drastically reduced the activation overpotential of the

catalysts during water-splitting at temperatures of 80 ^{o}C and above. In particular, the activation overpotential for O_2 formation from water is decreased to near negligible proportions. This phenomena was mainly attributed to the powerful capillary action exhibited by the Gortex, where newly-formed oxygen bubbles are vigorously drawn into and through the Gortex. Among all catalyst layers, best performances were obtained for AWE employing a cathode comprising of a mixture of Raney Ni, CB and PTFE, with a Ni mesh current collector, deposited on Gortex. When a catalyst layer comprising of mixture of $NiCo_2O_4$, PTFE, and a Ni-mesh deposited on Gortex, in 6 M KOH with a 10 mm inter-electrode gap, the resulting AWE required only 1.23-1.27 V to achieve 10 mA cm^{-2} over 1 h at 80 ^{o}C. The combined cathode and anode activation overpotential (η_{Cell}) of the cell after 1 h was a mere 0.09 V. To the best of our knowledge, this cell may constitute the most energy efficient water electrolyser yet reported. Then an equivalent, high-performing AFC was tested using 20%Pt-Pd/CB, CB, PTFE, and a Ni-mesh, deposited on Gortex at both anode and cathode, and generated 0.88 V at 10 mA cm^{-2} in the reverse direction after 1 h at 80 ^{o}C. The combination of the above AWE and AFC has resulted in a notional round-trip energy efficiency of 72.4% at 10 mA cm^{-2} and after 1 h at 80 ^{o}C in each direction, assuming complete conservation of heat.

This work also included an application of novel Gortex substrates for developing alkaline-based DRFC which are highly efficient and extremely tolerant to CO_2 poisoning. In first set of experiments, a range of precious metal and its alloys as catalysts were investigated for DRFC application. Among all the precious metal and its alloys investigated, the AFC containing 20% Pd-Pt/CB+PTFE+Ni-mesh/Gortex was the most efficient cathode; with an AWE unit containing IrO_2 was the most efficient anode, both AFC and AWE operating at 80 ^{o}C, to form an alkaline-based DRFC. When abovementioned most efficient AFC and AWE was used in combination, it displayed a notional round-trip energy efficiency of 64.3% after 1 h at 10 mA cm^{-2} in each direction, assuming full conservation of heat.

Other highly efficient catalysts based on low cost transition metal oxides (having perovskite or spinel structure) were also investigated for alkaline-based DRFC applications using novel Gortex substrates. Perovskite, such as $La_{0.8}Sr_{0.2}MnO_3$, when employed as a catalyst on Gortex, as a fuel cell cathode ('$La_{0.8}Sr_{0.2}MnO_3$+CB+PTFE+Ni-mesh/Gortex'), at 10 mA cm^{-2}, it exhibited a voltage of 0.85 V at 20 ^oC and 0.9 V at 80 ^oC. This indicated that the temperature increase led to an increase in current densities and led to improvement in ORR activity. Spinel, such as $NiCo_2O_4$, when tested in fuel cell cathode ('$NiCo_2O_4$+CB+PTFE+Ni-mesh/Gortex'), delivered currents of 10 mA cm^{-2} at almost same voltage (0.85 V), both at RT and 80 ^oC. Temperature had little to no influence on fuel cell performance made of $NiCo_2O_4$ as cathode catalyst. We have combined AFC employing $La_{0.8}Sr_{0.2}MnO_3$+CB+PTFE+Ni-mesh/Gortex as the most efficient cathode, with an AFC unit comprising $NiCo_2O_4$+PTFE+Ni-mesh/Gortex as the most efficient anode, both AFC and AWE operating at 80 ^oC, to form an alkaline-based DRFC. The resulting electrolyser required 1.27 V to achieve 10 mA cm^{-2} after 1 h at 80 ^oC. The notional round-trip energy efficiency of this DRFC was 70.9% after 1 h at 10 mA cm^{-2} in each direction, assuming full conservation of heat.

In another application of novel Gortex-based electrodes, AFC was tested for a *"Power-to-Gas"* (P2G) technology, which involves using unwanted, excess renewable energy to manufacture hydrogen gas that is then injected into the existing natural gas pipeline network in 5-10% by volume. The results indicated that these types of AFC has the potential to harness such gas mixtures for downstream generation of electric power. The AFC, with novel Gortex-based electrodes layered with Pd/Pt catalysts, generates electricity remarkably efficiently when fuelled with methane (CH_4) containing 5% hydrogen. Methane constitutes the major component of natural gas. The AFC was studied over a range of hydrogen to methane ratios using Tafel plots and EIS measurements. The results indicated that, in terms of fundamental operation, there is, astonishingly, almost no difference between using pure hydrogen and 5% hydrogen in methane, as the fuel. The Gortex electrodes and alkaline

electrolyte are clearly able to utilize the diluted hydrogen as a fuel with remarkable efficiency. The methane acted as an inert carrier gas and was not consumed in this process.

8.2 Perspective

The future work of this research may include development of electrolysis cell which split seawater to generate oxygen at a commercial scale. Electrolysis of seawater normally generates chlorine gas at the anode because of the large bubble overpotential of oxygen. This is because while the half-reaction for chlorine (Cl_2) formation is thermodynamically less favourable than that for oxygen generation, it has a substantially lower bubble overpotential. That is, the additional energy required to form O_2 in the form of bubbles is very much higher than that required to form Cl_2. When performed on the industry standard catalyst, Pt black, the activation overpotential for O_2 formation at 25 ^oC is at least 0.77 V, while that of Cl_2 formation is only ca. 0.08 V. This large additional voltage requirement overwhelms the smaller disparity in E^o between Cl_2 formation reaction and oxygen generation reaction. As a result, in the presence of Cl^- ions in seawater, Cl_2 evolution generally occurs at the anode in standard commercial electrolysers. In so doing, it destroys the reaction efficiency of the cell and generates the undesirable and poisonous Cl_2 product instead of O_2.

Seawater is one of the most abundant and accessible resources on Earth. It contains a multiplicity of inorganic ions, organic molecules and biological materials, whose concentrations vary, often dramatically, around the world. Typical seawater has a pH of 8.4-8.8 and contains common ions like Cl^-, Na^+, Mg^{2+}, SO_4^{2-}, Ca^{2+}, K^+ and HCO_3^- (listed in order of decreasing concentration). Of these, Na^+ and Cl^- (from table salt, NaCl) are the most abundant, with standard mean chemical concentrations of $[Na^+]$ 0.47 M and $[Cl^-]$ 0.55 M, respectively. If subjected to electrolysis, seawater may undergo a variety of oxidation processes, of which the most important is Cl_2 formation at the anode.

Despite a great deal of work, it has therefore not proved possible to develop abiological catalysts that are intrinsically capable of generating bulk quantities of pure O_2 from pH-unmodified seawater at the anode of a water electrolyser.

Gortex electrodes has shown to drastically diminish the oxygen overpotential at the anode in water-splitting. This is because bubble formation is eliminated by using Gortex and thereby also the bubble overpotential of the reaction. The small pores and highly hydrophobic character of the Gortex may create a strong capillary action that may extract O_2 gas out of any newly-formed bubbles, into and through the Gortex substrate. This characteristics of Gortex based electrodes can be investigated in detail in future work.

One of the main areas which could be expanded in the future research is to study the impact of cell operating pressure on the AFC and AWE performances. The application of higher pressure on the gas side improves the efficiency due to faster kinetics in AFCs. It is also anticipated that there would be a significant reduction in costs when operational pressure of the AWE is increased. This would be due to the production of pressurized hydrogen and oxygen which eliminates the need for a compressor for pressurization.

Another area that can be expanded in future research is the selective heating of electrodes. In particular, to achieve higher electrical efficiencies in AWEs, selective heating of the anode can be done as the oxygen overpotential decreases with temperature (however the hydrogen overpotential increases with temperature). This could lead to further performance enhancements.

In this thesis, most of the anodes in AFCs and cathodes in AWEs contained precious metals like 10%Pt/CB as HOR and HER catalyst respectively. However, recently developed earth abundant and cost effective elements such as metal free and transition metal electro catalysts, may be investigated to replace the noble metal catalysts.